VYSOKÉ UČENÍ TECHNICKÉ V BRNĚ
BRNO UNIVERSITY OF TECHNOLOGY

FAKULTA ELEKTROTECHNIKY A KOMUNIKAČNÍCH TECHNOLOGIÍ
ÚSTAV RADIOELEKTRONIKY

FACULTY OF ELECTRICAL ENGINEERING AND COMMUNICATION
DEPARTMENT OF RADIO ELECTRONICS

CONTRIBUTION TO EFFICIENT USE OF NARROWBAND RADIO CHANNEL

PŘÍSPĚVEK K EFEKTIVNÍMU VYUŽITÍ ÚZKOPÁSMOVÉHO RÁDIOVÉHO KANÁLU

DOKTORSKÁ PRÁCE
DOCTORAL THESIS

AUTOR PRÁCE AUTHOR	Ing. MAREK BOBULA
VEDOUCÍ PRÁCE SUPERVISOR	doc. Ing. ALEŠ PROKEŠ, Ph.D.

BRNO 2010

ABSTRACT

The industrial narrowband *land mobile radio* (LMR) devices, as considered in this dissertation project, has been subject to *European standard ETSI EN 300 113*. The system operates on frequencies between 30 MHz and 1 GHz, with channel separations of up to 25 kHz, and is intended for *private, fixed,* or *mobile, radio packet switching networks*. Data telemetry, SCADA, maritime and police radio services; traffic monitoring; gas, water, and electricity producing factories are the typical system applications. *Long distance coverage*, *high power efficiency*, and *efficient channel access techniques* in *half duplex operation* are the primary advantages the system relays on. Very low level of *adjacent channel power emissions* and robust *radio receiver architectures*, with *high dynamic range*, enable for a system's coexistence with various communication standards, without the additional guard band frequency intervals.

On the other hand, the strict limitations of the referenced standard as well as the state of the technology, has hindered the increase in *communication efficiency*, with which the system has used its occupied bandwidth. New modifications and improvements are needed to the standard itself and to the up-to-date architectures of narrowband LMR devices, to make the utilization of more efficient modes of system operation practically realizable.

The main objective of this dissertation thesis is therefore to find a practical way how to combine the favorable properties of the advanced nonlinear and linear digital modulation techniques in a single digital modem solution, in order to increase the efficiency of the narrowband radio channel usage allocated to the new generation of the industrial LMR devices.

The main attention is given to the particular areas of digital modem design such as proposal of the *new family of the Nyquist filters minimizing the adjacent channel interference*, design and analysis of the *efficient algorithms for frequency discrimination*, *fast frame and symbol timing recovery* as well as to *the analysis of the software defined receiver performance* under *additive white Gaussian noise* (AWGN) and *multipath fading* radio channel conditions. There are also main results presented from the practical part of this dissertation project, while designing and analyzing two prototyping architectures of the narrowband software defined radio modems. In this part, in addition, the conditions and practical recommendations towards using spectrally efficient modulation techniques in future narrowband LMR devices are provided.

ABSTRAKT

Předkládaná práce se soustředí na problematiku využívání úzkopásmového rádiového kanálu *rádiovými modemy,* které jsou určené pro *průmyslové aplikace pozemní pohyblivé rádiové služby*, specifikované v dominantní míře *Evropským standardem ETSI EN 300 113*. Tato rádiová zařízení se používají v kmitočtových pásmech od 30 MHz do 1 GHz s nejčastěji přidělovanou šířkou pásma 25 kHz a ve většině svých instalací jsou využívána ve *fixních nebo mobilních bezdrátových sítích*. Mezi typické oblasti použití patří zejména datová telemetrie, aplikace typu SCADA, nebo monitorování transportu strategických surovin. Za hlavní znaky popisovaného systému lze označit komunikační pokrytí značných vzdáleností, dané především vysokou výkonovou účinnosti datového přenosu a využívaní efektivních přístupových technik na rádiový kanál se semiduplexním komunikačním režimem. Striktní požadavky na elektromagnetickou kompatibilitu umožňují těmto zařízením využívat spektrum i v oblastech kmitočtově blízkým jiným komunikačním systémům bez nutnosti vkládání dodatečných ochranných frekvenčních pásem.

Úzkopásmové rádiové komunikační systémy, v současnosti používají převážně exponenciální digitální modulace s konstantní modulační obálkou zejména z důvodů velice striktních omezení pro velikost výkonu vyzářeného do sousedního kanálu. Dosahují tak pouze kompromisních hodnot *komunikační účinnosti*. Úpravy limitů příslušných rádiových parametrů a rychlý rozvoj prostředků číslicového zpracování signálu v nedávné době, dnes umožňují ekonomicky přijatelné využití spektrálně efektivnějších modulačních technik i v těch oblastech, kde je prioritní využívání úzkých rádiových kanálů.

Cílem předkládané disertační práce je proto výzkum postupů směřující ke sjednocení výhodných vlastností lineárních a nelineárních modulací v moderní konstrukci úzkopásmového rádiového modemu. Účelem tohoto výzkumu je efektivní a „ekologické“ využívání přidělené části frekvenčního spektra.

Mezi hlavní dílčí problémy, jimiž se předkládaná práce zabývá, lze zařadit zejména tyto: *Nyquistova modulační filtrace, navrhovaná s ohledem na minimalizaci nežádoucích elektromagnetických interferencí*, efektivní číslicové algoritmy *frekvenční demodulace a rychlé rámcové* a *symbolové synchronizace*. Součástí práce je dále analýza navrhovaného řešení z pohledu celkové konstrukce programově definovaného rádiového modemu v rovině simulací při vyšetřování robustnosti datového přenosu *rádiovým kanálem s bílým Gaussovským šumem* nebo *kanálem s únikem* v důsledku mnohacestného šíření signálu.

Závěr práce je pak zaměřen na prezentování výsledků praktické části projektu, v níž byly testovány, měřeny a analyzovány dvě prototypové konstrukce rádiového zařízení. Tato finální část práce obsahuje i praktická doporučení, vedoucí k vyššímu stupni využitelnosti spektrálně efektivnějších komunikačních režimů v oblasti budoucí generace úzkopásmových zařízení pozemní pohyblivé rádiové služby.

Keywords

Spectrum efficiency, power efficiency, adjacent channel power, constant envelope modulation, linear modulation, Nyquist filters, rapid frame synchronization, symbol synchronization, software defined digital radio, narrowband land mobile radio, ETSI EN 300 113, dynamic range, FPGA

Klíčová slova

Spektrální účinnost, výkonová účinnost, nežádoucí vyzařování do sousedního kanálu, modulace s konstantní modulační obálkou, lineární modulace, Nyquistova filtrace, rychlá rámcová synchronizace, symbolová synchronizace, softwarově definované rádio, radiostanice pozemní pohyblivé služby, ETSI EN 300 113, dynamicky rozsah, FPGA

Bibliografická citace

BOBULA, M. *Příspěvek k efektivnímu využití úzkopásmového rádiového kanálu.* Brno: Vysoké učení technické v Brně, Fakulta elektrotechniky a komunikačních technologií, 2011. 175 s. Vedoucí dizertační práce doc. Ing. Aleš Prokeš, Ph.D.

The manuscript of this thesis is deposited and available:

at the Department of Radio Electronics
Faculty of Electrical Engineering and Communication
Brno University of Technology
Purkyňová 118, 612 00 Brno, Czech Republic

Tel.: +420 541 149 105
Fax: +420 541 149 244
E-mail: urel@feec.vutbr.cz

Declaration

I hereby declare that the work in this thesis is my own, except for quotations and summaries, which have been duly acknowledged. The thesis has not been accepted for any degree and is not concurrently submitted for award of any other degree.

In Brno, ...   …………………………
(Signature)

ACKNOWLEDGEMENT

Je mojou milou povinnosťou na tomto mieste poďakovať doc. Ing. Alešovi Prokešovi, PhD. za cenné pripomienky a za to, že prevzal záštitu nad touto prácou.

Ďalej by som chcel poďakovať Ing. Karlovi Daňkovi, PhD. za jeho originálny pohľad nielen na svet rádioelektroniky. Jeho cenné rady a životný príklad v mnohých ohľadoch ďaleko presahujú rámec tejto práce.

Ďakujem taktiež mojím kolegom z firmy RACOM, Ing. Lubošovi Křížovi, Ing. Pavlovi Říhovi, Ing. Martinovi Kaštánkovi, Ing. Marekovi Prášilovi, Ing. Renému Samkovi a ďalším. Bez názorov a práce týchto ľudí by nevzniklo mnoho z prakticky nameraných výsledkov prezentovaných v tejto práci. Ing. Milanovi Tannenbergovi, PhD. ďakujem za skvalitnenie textu dizertačnej práce. Ing. Jiřimu Hruškovi patrí poďakovanie za to, že RACOM, ako spoločnosť tvorivých ľudí, existuje a za možnosť sa k nej pridať.

Veľmi pekne ďakujem mojím rodičom za postoj ku vzdelaniu, za morálnu a finančnú podporu počas mojich predchádzajúcich štúdii.

Túto prácu by som však chcel venovať ako poďakovanie za nesmiernu podporu svojej manželke Mgr. Alexandre Bobulovej a synovi Adamovi.

TABLE OF CONTENTS

1 INTRODUCTION

Steadily increasing demand for frequency spectrum, driven in recent years by an overwhelming public interest in wireless communication, has led to an even-greater importance on the spectrum efficiency utilization. The effort to use the spectrum effectively can, however, be traced back to as early as 1922 [3], [4]. From the very advent of the radio transmission, it was evident that a radio device should not only use its occupied channel bandwidth effectively, but, in addition, should also avoid any unnecessary interference with other systems. Since then the frequency spectrum had been proving its importance and has become a scarce resource nowadays. It can be "widened" just by the technical advancements towards its more and more efficient usage. Although it is a technical propriety, such a practice is also covered in numerous regulation documents and directives [5].

> *…radio equipment shall be so constructed that it effectively uses the spectrum allocated to terrestrial/space radio communication and orbital resources so as to avoid harmful interference…* *([5], Article 3.2, Directive 1999/5/EC)*

Such an attitude yields to never-ending ambition for designing, still more advanced, radio devices. This dissertation thesis describes one such approach to enhance the spectrum usage of the *land mobile radio* (LMR) system, operating on frequencies between 30 MHz and 1 GHz, with channel separation of up to 25 kHz intended for *private mobile radio* (PMR) networks. This frequency range and especially the VHF band is very well suited for long *distance coverage* as a primary concern of the LMR communication systems. The PMR systems are mainly used for telemetry, SCADA systems, maritime radio service and are operated by a wide range of users, such as police, companies producing or transporting gas, water, electricity, and in other industrial applications. Although the data traffic, generated per user in PMR network is relatively low compared to other wireless systems, there is also a significant need for spectrally efficient modulation techniques which would afford higher network capacity within the same available bandwidth in the future LMR systems.

The narrowband radio devices under consideration are specified mostly by the *European standard ETSI EN 300 113* [1]. Such radio equipments have to face challenging environmental and radio conditions all over the world. The dynamic range in the vicinity of 100 dB, very strict adjacent channel transmitted power attenuation requirements, high data sensitivity, adjacent channel selectivity, high level of radio blocking or desensitization and high co-channel rejection [1], [2] are its most important radio characteristics to mention. It is no wonder that for such high dynamic range demands, super heterodyne receiver structures with a majority of analog components are still widely used. But yet the radio transceiver has to be small in dimensions, consumes low power and remains all its parameters over the wide industrial temperature range and over extensive period of time for reasonable price. At the same time, it should provide enough flexibility to accommodate different channel bandwidths, digital modulation formats, data rates, and techniques, to combat negative effects of the radio channel. From this point of view, the *software defined radio* (SDR) concept is, indisputably, a prospective alternative and has not been widely used by these systems [6], [3]. The rapid expansion of the digital signal processing, together with the advancements in signal analog-to-digital converters technology have, in recent years, made such projects economically manageable.

To the best of author knowledge today's LMR systems, being subject to [1], use mostly exponential constant envelope modulations GMSK and 4-CPFSK. The application of the continuous phase modulations is mainly due to the extreme *adjacent channel transmitted power* (ACP) attenuation requirements, and inherent robustness against channel nonlinearities. Relatively simple implementation of the non-coherent demodulators and synchronization algorithms also significantly contributes to the efficient channel usage, especially in packet-based switching networks. The systems thus maintain good power efficiency while the spectral efficiency reaches compromising values not exceeding 1 bit/s/Hz.

The communication system utilizing the narrowband radio channel uses exclusively packet or frame based multiple channel access techniques. It is either *stochastic multiple channel access* or *carrier sense multiple access* (CSMA) with collision detect, acknowledgements and reservation. There are various frame lengths used, ranging from couple of bytes e.g. 12, up to a maximum of 1500 bytes. For half duplex operation, the typical *receive-to-transmit attack times* are around 1 ms. Compared to circuit switching networks, the frame switching communication systems are recognized for their inherent efficiency which also contributes to efficient use of a given bandwidth. However, such concept forces very strict demands upon the synchronization algorithms, which have to extract all the possible information about frequency offset, frame and symbol synchronization within the first few bytes of incoming frame. It is obvious that the shorter the overall acquisition time the higher the communication efficiency of the LMR system that can be achieved. From this point of view, the efficient synchronization algorithms are needed for new modes of system operation, and as such, they are considered an important part of this thesis.

Another example of the LMR radio system, with great emphasis on the spectral utilization, can be seen in a system complying with the *terrestrial trunked radio* (TETRA) standard, especially with the new *TETRA enhanced data service* (TEDS) specification [11], [12]. Such systems benefited from the technologies developed for second cellular systems – namely GSM and IS-95 – and incorporate many similar features. The TEDS standard defines a complete structure of the physical layer and imposes the use of linear digital modulation schemes π/4-DQPSK, π/8-D8PSK, and *filter bank multi-carrier modulation* (FBMCM) to reach higher data rates. As a result of the trade-off between power and spectrum efficiency, the system can, at least, achieve this goal within the limited coverage of its cells. The implementation of the linear digital modulation has resulted in new standard definitions [36], [40] with considerably-less strict limits for adjacent channel power attenuation and new limits for other essential radio parameters.

As will be shown in this thesis, the specific aspects of the LMR under consideration are driven by different objectives. However, the wise use of the favorable properties of the advanced nonlinear and linear digital modulations implemented in a single digital modem is now feasible, due to the software defined platform. *It is the main ambition of this dissertation work to find a practical way of how to combine such signaling techniques together with the modern digital methods for fast frame and symbol synchronization and channel impairments compensation algorithms*, *needed to increase the efficiency of the narrowband radio channel usage allocated to the new generation of the industrial LMR devices.*

1.1. Thesis organization

This dissertation work is organized as follows. *Chapter 2* contains more detailed description of the LMR physical layer technical parameters and requirements. They are considered crucial for comparison of the particular modes of system operation and create objectives for the whole transceiver design and analysis.

Section 3 reviews the signal models for intended digital modulations. The core of this chapter can be seen in digital pulse shaping filter analysis and proposal of the new family of Nyquist filters.

The analysis of the exponential modulations creates a significant part of this thesis as these techniques are still the major modulation formats used by the LMR radios. Therefore, *Chapter 4* is focused on a closer description of the digital algorithms for frequency discrimination as a core algorithm of the software defined modem. Two refinements to the techniques available in technical literature are presented which can improve the signal-to-noise ratio of the demodulated signal.

In the following *Chapter 5*, the problem of fast frame and symbol synchronization is analyzed. A complete frame and symbol timing recovery concept suited for burst mode communication system which utilizes selected modulation techniques is proposed. The approach is based on a *sample wise pattern correlation technique* with a combination of a *decision directed adaptive synchronization algorithm*, and forms a fast synchronization method. Its main building blocks, especially the timing error detectors for acquisition and tracking phase are covered in details. The design and analysis of the *fractional interpolation filters* as a timing adjustment mechanism is also included in this chapter. For the exponential modulation techniques, the symbol synchronization method based on digital frequency discrimination is derived. The performance of its *data aided* (DA) and *non-data aided* (NDA) mode of operation is compared. The last part of *Chapter 5* is dedicated to the overall performance evaluation of the digital receiver, utilizing the proposed frame and symbol synchronization scheme. The evaluation criterion in form of power efficiency has been selected. In the first part, the radio channel convolving the incoming signal is assumed to have fixed and constant frequency characteristic and be corrupted only by the presence of the *additive white Gaussian noise* (AWGN). In the second part, the robustness of the proposed system against the *multipath fading process* of chosen parameters is simulated and evaluated.

The aim of *Chapter 6* is to summarize the main results and experiences from the practical part of this dissertation project while designing, testing and analyzing two prototyping architectures of the narrowband software defined radio modems. The main attention is given to describe the main limitation and compromises influencing the instantaneous dynamic range performance of the *intermediate frequency* (IF) sampling digital receiver, with a main emphasis on its practical implementation. In the second part, the measurement results of the *essential radio parameters* as required by [1] are given to empirically confirm the proposed radio modem structures, including majority of the algorithms that have been derived in the theoretical part of this thesis. Also in this section, the conditions and practical recommendations towards using spectrally efficient modulation techniques in future narrowband LMR devices are provided.

Chapter 7 concludes this dissertation work by summarizing the main contributions that have been achieved through the project and discusses the possible future improvements of the narrowband LMR system studied.

1.2. Main dissertation contributions and publications

The main contributions of the work behind the dissertation thesis presented can be seen mainly in the following areas:

- Analysis and application of the enhanced digital modulation formats for the next generation of narrowband LMR system in order to improve its spectral efficiency, while respecting its specific characteristics in form of high power efficiency, robustness against interference and fast signal acquisitioning needed for rapid packet switching. The work towards meeting this general objective had begun in 2005, and has required some original ideas that are formulated and analyzed in this dissertation thesis. Besides that, the work included a significant amount of engineering work which is not covered in this thesis.

- In order to effectively fulfil very strict limits of adjacent channel power, new class of Nyquist filters called Nyquist δ-filters has been formulated and analyzed in detail. The main results of this work can be found in *Chapter 3* and has also been published in [91]:

BOBULA, M., PROKEŠ, A., DANĚK, K. Nyquist Filters with Alternative Balance between Time- and Frequency-domain Parameters. In *EURASIP Journal on Advances in Signal Processing.* Volume 2010, Accepted for publication 2010-10-28.

- The problem of rapid frame and symbol synchronization applicable for exponential and linear mode of narrowband LMR system operation creates a significant part of the thesis contributions. The algorithm formulation and analysis is covered in Chapter 5, and towards the end of 2010, it has been implemented successfully in a new generation of radio modems utilizing 2-CPFSK, 4-CPFSK and π/4-DQPSK modulations. Although the final version of the algorithm presented in this thesis differs from the one published in [23], the publication covers its important part of synchronization acquisition in form of a sample wise pattern correlation technique.

BOBULA, M., DANĚK. K., PROKEŠ, A., Simplified frame and symbol synchronization for 4–CPFSK with h=0.25. In *Radioengineering*, vol.17, no. 2, June 2008. [Online] Cited 2010-10-20. Available at:
http://www.radioeng.cz/fulltexts/2008/08_02_108_114.pdf

- Design and analysis of the two prototyping architectures for IF *(intermediate frequency)* sampling software defined narrowband radio modems. Giving the complete measurement results of the essential radio parameters of the two possible architectures, this part of the work identifies the main factors influencing the instantaneous dynamic range performance, and gives several practical design recommendations in order to increase the efficiency of the narrowband radio channel utilization. Several results from this work have also been published in [13]:

BOBULA, M., DANĚK, K., PROKEŠ, A. Implementation of Industrial Narrow Band Communication System into SDR concept. In *Radioengineering*, vol. 17, no. 4, December 2008. [Online] Cited 2010-10-20. Available at:
http://www.radioeng.cz/fulltexts/2008/08_04a_086_092.pdf

- Other work and publications concerning design and analysis of the narrowband LMR systems.

BOBULA, M., Design of the fractional delay interpolators based on Farrow structure. (in Czech), [Online] Cited 2010-06-13. Available at:
http://www.elektrorevue.cz/cz/clanky/zpracovani-signalu/5/navrh-cislicovych-filtru-se-spojite-promennou-hodnotou-zpozdeni-na-bazi-farrowova-interpolatoru/

BOBULA, M. OFDM Performance Simulation for Narrow Bandwidth Radio Channel of 200 kHz. *Final technical report.* Manipal Academy of Higher Education. MIT India. 2006.

BOBULA, M. *Use of Radio Channel 200 kHz for data transmission.* MSc. Diploma Thesis, University of Technology BRNO, 2006.

BOBULA, M. FPGA Implementation of an SDDR Core for Radio Transceiver. In *STUDENT EEICT 2006*. vol. 2. VUT BRNO, 2006. p. 14 - 16, ISBN-80-214-3161-X.

2 THESIS OBJECTIVES

To understand the motivation behind the main objective of the thesis presented, it is, first, necessary to briefly describe the essential technical parameters – particularly their limits – required upon the LMR system. First of all, the characteristics of the radio receiver and transmitter are given, followed by the main characteristics of the narrowband communication channel as a physical medium through which the signal passes from the transmitter to the receiver.

2.1. LMR receiver characteristics

The most important parameters which have a strong influence on how the land mobile radio receiver is designed are a *maximum usable (data) sensitivity*, *co-channel rejection*, *adjacent channel selectivity* and *blocking* or *desensitization*. In this work their definitions and requested limits are a subject to European standard ETSI EN 300 113 [1]. It is important to note that all the following radio parameters and limits are requested for conformity testing only, to ascertain if the radio device under consideration is capable of *listen-before-talk* (LBT) mode. While it is the case of the intended narrowband radio system, the radio parameters are considered essential in this work.

Where needed, the test signals and all other details, such as measurement procedures, are also assumed to be the subject of referenced standard, unless otherwise noted.

2.1.1. Maximum usable data sensitivity

The maximum usable data sensitivity is the minimum level of the signal (emf) at the receiver input, produced by a carrier at the nominal frequency of the receiver, modulated with a normal test signal, which will, *without interference*, produce, after demodulation, a data signal with a specified *bit-error-ratio* (BER) of 10^{-2} or a specified *successful message ratio* (SMR) of 80%.

> *The maximum usable sensitivity shall not exceed an electromotive force of* ***3.0 dBμV*** *under normal test conditions.*

Assigning this value as S, one can readily express what *signal-to-noise ratio* (SNR) can be expected in relation to *noise figure* (NF) transformed to the receiver input

$$SNR = S - \left(10\log(kT) + 10\log\left(B_N\right) + NF\right)\ [\mathrm{dB}]. \qquad (2.1)$$

In (2.1), k is the Boltzmann's constant, T is the absolute temperature in Kelvins and B_N is the receiver noise bandwidth of 25 kHz, unless otherwise noted. Besides the maximum usable sensitivity, all other receiver parameters can be classified as the measures of the *receiver degradation parameters* used to analyze the degradation of its performance due to the presence of unwanted (interfering) signals. In this case, the level of the wanted signal for all degradation measurements shall be **3 dB** above the limit of the maximum usable sensitivity.

2.1.2. Co-channel rejection

The co-channel rejection is a measure of the receiver capability to receive a wanted modulated signal without exceeding a given degradation due to the presence of an unwanted modulated signal, both signals being at nominal frequency of the receiver. The co-channel rejection is expressed as a ratio (dB) of the level of the unwanted signal to the level of the wanted signal, for which the BER of 10^{-2} – or the SMR of 80 % – or better is obtained. Both signals are referred to the receiver input.

> *The value of the co-channel rejection ratio shall be between* ***-8.0 dB*** *and* ***0 dB****, for channel separations of* ***25 kHz****.*

Although, no limitation has been imposed by the standard on the type of modulation to be used in the system, the above regulation limits of data sensitivity and co-channel rejection do cause the utilization of the higher order modulation to be difficult [13].

2.1.3. Adjacent channel selectivity

The adjacent channel selectivity is a measure of the receiver capability to receive a wanted modulated signal without exceeding a given degradation due to the presence of an unwanted signal which differs in frequency from the wanted signal by an amount equal to the channel separation, for which the equipment is intended. The adjacent channel selectivity is expressed as a ratio (dB) of the level of the unwanted signal to the level of the wanted signal, for which the BER of 10^{-2} – or the SMR of 80 % – or better, is obtained.

> *The value of the adjacent channel selectivity for channel separation of* ***25 kHz*** *shall not be less than* ***70 dB****.*

2.1.4. Blocking or desensitization

Blocking is a measure of the receiver capability to receive a wanted modulated signal exceeding a given degradation due to the presence of an unwanted input signal at any frequencies other than those of the spurious responses or the adjacent channels. The blocking or desensitization is expressed as a ratio (dB) of the unwanted signal level to the level of the wanted signal, for which the BER of 10^{-2} – or the SMR of 80 % – or better is obtained. Both signals are, again, referred to the receiver input.

> *The blocking ratio for any frequency within the specified ranges shall not be less than* ***84 dB****, except at frequencies on which spurious responses are found.*

As will be shown later in this work (Chapter 6), the adjacent channel selectivity and blocking level of the receiver are the fundamental parameters which force challenging requirements upon the dynamic range of the whole receiver, including the effective dynamic range of the digital receiver structure and selection of the main channel selectivity filters [13]. Moreover, the high dynamic range requirement also makes the design of the local oscillator signal generators as well as the sampling generators difficult. The oscillators would, in this case, need to exhibit an extremely low level of the *phase noise* not to cause the degradation of the receiver noise floor due to the phenomenon called *reciprocal mixing* [15].

Communication system with specified limits of maximum data sensitivity and co-channel rejection can be according to [14] classified as *power-limited*. With the assumption that today's LMR systems already use the most spectrally efficient modulation, the only way to increase the data rate – in a given coverage area – seems to be to widen the system bandwidth together with the transmitted signal power. As is shown in the next paragraph, due to the strict transmitter characteristics, this primary assumption cannot be the case for the narrow band LMR system.

2.2. LMR transmitter characteristics

In this section, two essential radio transmitter parameters are identified to have a crucial influence on an overall system performance. Those are *the adjacent channel power* and *the* *transmitter power efficiency,* [1]. The first has a direct impact on the spectrum efficiency of the LMR system and the latter is considered an important issue in order to minimize the overall system power consumption.

2.2.1. Adjacent channel power

The adjacent channel power or *adjacent channel interference* (ACI) is that part of the total output power of a transmitter under defined conditions of modulation, which falls within a specified pass-band centred on the nominal frequency of either of the adjacent channels. This power is the sum of the mean power produced by the modulation, hum and noise of the transmitter. Adjacent channel power is usually referenced to the un-modulated carrier power.

> *For a channel separation of 25 kHz, the adjacent channel power shall not exceed a value of* ***60 dB*** *below the transmitter power without the need to be below -37 dBm.*

It is important to note that, until 07/2007, the standard strictly demanded the adjacent channel power ratio of -70 dB. The ACP parameter is particularly important in LMR systems, since it influences the density of the radio channels that can be used in a given area. Its value originated in the use of the traditional analog *frequency modulated* (FM) radio systems. Ironically, it was one of the main limitations for why those systems were – for many years – not able to utilize spectrally more efficient modulation schemes [9]. This paradox can also be found in the relevant ETSI documents, reasoning the decision to lessen the ACP requirement [16]:

> *The limits for 25 kHz systems are excessive, especially for non-constant envelope modulation. While these limits* ***may*** *make sense for historical constant-envelope modulation****,*** *the gross discrepancy between the 12.5 kHz limit (-60 dBc, -99 dBc/Hz) and 25 kHz limit (-70 dBc, -112 dBc/Hz) is a constraint on modern highly spectrally efficient systems. Note that this limit is also covered by existing sharing studies in ECC on* ***TETRA TEDS*** *and no concern anymore.*

The TETRA has followed this concept from the very beginning, setting the limit at -60 dB[1] rather than -70 dB, which has been left to be beyond the state of the present linearization technology for equipments production [17].

It is therefore reasonable to suppose that such obliging step will open up a closed door for TETRA system into the frequency bands initially planned for LMR systems with -70 dB of ACP attenuation. However, this would give TETRA a significant advantage over the LMR specified by [1] in form of the higher user data rates applicability. That is another reason for why the systems designers of LMR systems should respond to that question by utilizing more advanced modulation techniques.

2.2.2. Transmitter power efficiency

Although the evaluation of the *transmitter power efficiency* is not required to fulfil the regulation requirements [1] so far, it is considered a key aspect of the modern LMR radio equipment design. It is either to minimize the overall power consumption while the LMR – sourced from a battery or a solar panel – is transmitting the required power level, or in order to transmit the highest possible output power using the input power available to the system and thus to increase the system coverage.

> *The practical way of evaluating the transmitter efficiency is to find the ratio of the transmitted output power and the overall input power level of the transmitting system,*

---

[1] The standard [40] specifying the conformity testing for TETRA-like devices allows -55 dBc in normal or -50 dBc in extreme temperature conditions. However, the measurement procedure making use of the spectrum analyzer rather than measuring receiver is recommended.

while the transmitter is operating under defined conditions of modulation and the ACP requirements are satisfied.

In the systems, where the transmitter power efficiency is of primary importance, the *transmitter non-linearity* also creates an important issue. Generally speaking, the higher the transmitter non-linearity, the higher the transmitter efficiency can be reached. Unfortunately, the device with a non-linear transfer function also tends to distort the spectrum of the transmitted signal, especially if the modulated signal exhibits the non-constant modulation envelope. In contrast, it is also true that only the non-constant envelope modulation can withstand a strict band limitation – by means of modulation filtering [14]. In other words, if the signal has a constant modulation envelope, it has an unlimited spectrum, and, if it has a band limited spectrum, it experiences the amplitude variations, which after passing through the non-linear power amplifier, would be suppressed, but would also regenerate the side-lobes of the modulated signal spectrum [9], [14]. The phenomenon is known as the *spectral re-growth*, and it depends mainly on the three transmitter characteristics. Those are *peak to average power ratio* (PAPR) of the digital modulation scheme in use, *transmitter non-linearity* and *the efficiency of the power amplifier linearization* or *pre-distortion technique* and all have to be considered when selecting the digital modulation technique for the system, where both power and spectrum are the key issues.

As it was written in Section 2.1.4, the LMR under consideration can be classified as a power limited system. By a closer examination of the demanding limits of ACP it has to be regarded also as *strictly bandwidth limited*. For such systems, the only way to increase the data rate is to use more bandwidth-efficient modulation schemes [14], [7]. One can now either take back the early assumption that today's LMR system already utilizes the most spectrally efficient modulation techniques possible and try to find more suitable signaling techniques, or one can compromise the data rate over the decreasing signal level – similarly to the TETRA system. With the partial lessening in ACP parameter requirement to -60 dB, both of the assumptions should be practically applicable.

2.3. LMR channel characteristics

It is an uneasy task to reasonably separate the characteristics of the communication system from the communication channel, through which the information is transferred. In this work the main parameters describing the communication channel in form of *channel capacity*, and *channel fading characteristics* have been selected. Eventually it is up to the communication system – and especially the radio receiver – quality, on how well it deals with all aspects of the data transmission over the selected channel.

2.3.1. Shannon bound on the channel capacity

The most fundamental bound on the radio channel capacity for a given bandwidth allocation was specified by Shannon in its milestone paper [18], [19]. Its most remarkable implication is an inherent trade-off between the bandwidth efficiency and the power budget in form of *bit-energy to noise power spectrum density ratio* requirement of a signaling (meaning modulation and coding) technique [14]

$$\frac{E_b}{N_0} \geq \frac{2^{\eta} - 1}{\eta}, \qquad (2.2)$$

where the bandwidth efficiency η is defined (2.3) as the ratio of the gross data rate R_b and occupied bandwidth B – which can be, for simplicity, equal to the noise bandwidth of the receiver

$$\eta = \frac{R_b}{B} . \tag{2.3}$$

The Shannon bound is graphically shown in Figure 2.1. Although it is very difficult to approach this limit for practical communication systems, it represents the never-ending ambition to move towards this theoretical bandwidth and power efficiency by making use of the new modulation and coding techniques.

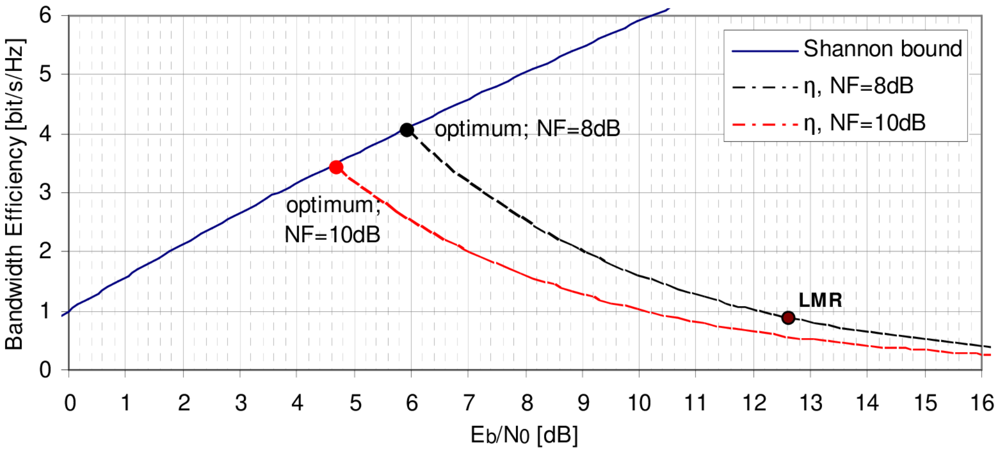

Figure 2.1: The graphical comparison of the LMR system against the Shannon limit of channel's capacity.

The above defined received signal level S=-110 *dBm,* (data sensitivity limit for BER=10^{-2}) and typical value of the radio receiver noise figure NF=8 *dB* can be used to analyze today's LMR system performance in relation to the Shannon limit. The maximum bandwidth efficiency of any signaling technique, but, requiring particular value of $(E_b/N_0)_{req}$ can be written as

$$\eta_{\max} = \frac{(S/N)_{avail}}{(E_b / N_0)_{req}} , \tag{2.4}$$

where the *signal-to-noise ratio* (SNR) available in the receiver can be calculated using (2.1) as

$$\left(\frac{S}{N}\right)_{avail} = -110 \text{ dBm } - \left(-174 \text{ dBm/Hz } + 44 \text{ dBHz } + 8 \text{ dB}\right) = 12 \text{ dB} . \tag{2.5}$$

If the η_{max} is plotted as a function of E_b/N_0 required for a signaling technique to reach sufficiently small BER (10^{-2}), the optimum value of bandwidth and power efficiency of the ideal system can be found. This has been done in Figure 2.1 for two edge values of NF typical for LMR systems. As expected, the higher the NF of the LMR receiver, the lower the available spectrum efficiency of the system is possible. The optimal signaling technique, according to Shannon criterion, would reach approximately 4 bit/s/Hz and would require E_b/N_0 = 6 dB – assuming that S=-110 *dBm* and NF=8 *dB.* Current modulation and coding schemes do not approach this limit very closely. However, any communication system with the same value of data sensitivity, noise figure and channel bandwidth as described above, should fall within the selected region in Figure 2.1. As an example[2], the parameters of the particular LMR system of R_b=21.68 *kb/s*, B=25 *kHz*, S=-110 *dBm* (BER=10^{-2}), NF=8 dB can be used.

It can be readily seen from Figure 2.1 that the distance between the ideal system and the chosen LMR is significant, and it is the main ambition of the thesis presented to lower this distance, as it would mean that the system uses the allocated spectrum more effectively.

2.3.2. Channel fading characteristics

In the previous section it was assumed that the channel is ideal in a sense that the transmitted signal is only attenuated by *a free space loss factor* and corrupted by the AWGN. Such radio channel has a totally flat transfer function with a linear phase characteristic, and does not cause any unwanted *channel-induced inter-symbol interference*. In a real radio communication system, the signal propagates over the multiple paths and scatters on various objects which give rise to partial waves arriving at the receiver with different amplitudes and phases due to the various paths' attenuation and delay. Summed in the receiver, the resulting signal will experience variation in amplitude and phase. In this case the *multipath fading* channel conditions have to be taken into consideration when comparing the system performance [20], [21], [12].

According to the time spreading mechanism due to the multipath signal propagation, the radio channel can be classified as experiencing *a small scale frequency selective fading*, or, *a small scale frequency flat fading*. Due to the time variant mechanism of the relative transmitter and/or receiver motion, the channel can be classified to exhibit *fast fading* or *slow fading* condition.

Although the LMR receiver performance under the fading condition is not specified by the referenced standard [1], it creates an important aspect of the modern radio device design and, as such, it is also covered in this dissertation (Chapter 5.7.2).Respecting the small scale multipath fading categorization published in [20] the radio channel under consideration is assumed as *time-variant*, experiencing *slow frequency flat fading* mechanism. When viewed in the time domain the radio channel is said to be frequency flat if all of the significant received multipath components of a symbol arrive within the symbol time duration T_s. And, the channel is referred to as introducing slow fading if the channel state remains virtually unchanged during the time of the modulation symbol [21].

For practical radio channel simulation in this work, the simplified radio channel models TU50 and HT200 at reference frequency of 400 MHz – defined in [12] – are used. The models exhibit a few discrete paths which are mutually statistically independently fading. The signal tap in each path is assigned its relative delay and its average relative power of the complex tap-gain process. The fading process in each path is assumed to be stationary Gaussian process with a power density function equal to the classical Doppler spectrum (Section 5.7.2).

---

[2] In fact, this example is not completely rigorous, because of the other factors taking place in the system such as the selection of *modulation index*, *forward error correction* (FEC), *synchronization sequences redundancy*, *push-to-talk* (PTT) delays etc., which also contribute to bandwidth efficiency either positively or negatively

3 DIGITAL MODULATIONS FOR NARROWBAND RADIO CHANNEL

In this chapter a brief analysis of the digital modulations intended for the narrowband transmission is given. To analyze the properties of the enhanced digital modulation techniques and their relations to the studied parameters of the LMR system, the signal models of the exponentially (Section 3.1) and linearly (Section 3.2) modulated signals are provided.

Although the linear digital modulation techniques in general are widely used in wireless communication systems [56], [52] and their properties are well established in technical literature [14], [7], [52], their wider utilization into the narrowband LMR systems, as specified by [1], was considered economically unfeasible for practical realization, mainly due to the strict limits of ACI attenuation. In fact, to the best of author's knowledge, there were no radio modems utilizing linear digital modulations while fulfilling [1] available at the time of the work at this project (2005-2010). The relaxation of this limit in 2008 has opened up a possibility for practical utilization of the spectrally efficient digital modulation techniques. In 2010, also the ASIC based modem solution for 25 kHz narrowband radio channel, making use of linear modulation, emerged [90]. However, a number of technical problems had been solved already, and, the solution based on flexible software reprogrammable platform while respecting specific aspects of the LMR systems makes this topic original.

From a practical point of view, the chapter presented proposes software defined transmitter structure and gives a comparison of the most important parameters of modulation techniques selected. It contains several practical recommendations to be respected in new generation of LMR design.

3.1. Exponential digital modulations

The use of exponential digital modulations and particularly the *continuous phase modulation* (CPM) has been motivated mainly due to the extreme ACP attenuation requirements and inherent robustness against the channel nonlinearities. Relatively simple implementation of the non-coherent demodulators and synchronization algorithms also significantly contributed to the efficient channel usage, especially in packet based switching networks. The M-CPFSK in this case is recognized as a general class of the non-linear or exponential digital modulation.

3.1.1. M-CPFSK signal model

Following the typical signal notations e.g. [63] the information – modulation – signal to be transmitted can be written as

$$m(t,\alpha_k)=\sum_{k=-\infty}^{\infty}\alpha_k h(t-kT), \qquad (3.1)$$

where α_k are the data symbols taking on the values from the real symbol alphabet ±1, ±3,..., $\pm M-1$, T is the symbol period and $h(t)$ is the frequency pulse or an impulse response of the pulse shaping filter [35]. Obviously, the modulation signal $m(t,\alpha_k)$ is a superposition of the modulation impulses weighted by the information symbols. Due to the requirement for continuous phase change, the relation between the frequency pulse *h*(*t*) and phase pulse *q*(*t*) in all CPM modulations is defined as

$$q(t) = \int_{-\infty}^{t} h(\tau)d\tau \,, \tag{3.2}$$

thus the resulting continuous phase $\psi(t,\alpha_k)$ of the modulated signal changes in time according to

$$\psi(t,\alpha_k) = 2\pi h \sum_{k=-\infty}^{\infty} \alpha_k q(t-kT), \tag{3.3}$$

where *h* is the *modulation index* describing the relation between the *maximum frequency deviation* Δf and the *symbol rate R* according to

$$h = \frac{2\Delta f}{R(M-1)} \,. \tag{3.4}$$

It also defines how much the phase changes during the symbol period respecting the symbol value of α_k. The resulting complex envelope *s*(*t*) of the M-CPFSK modulated signal can be then written as

$$s(t) = \exp\left\{ j2\pi h \left[\sum_{k=-\infty}^{\infty} \alpha_k q(t-kT) \right] \right\}, \tag{3.5}$$

which can be further modified into (3.6) corresponding to the conventional analog FM signal

$$s(t) = \exp\left\{ j2\pi k_{FM} \int_{-\infty}^{t} \left[\sum_{k=-\infty}^{\infty} \alpha_k h(\tau-kT) \right] dt \right\}, \tag{3.6}$$

where k_{FM} is a frequency modulator sensitivity per modulation state defined as

$$k_{FM} = \frac{\Delta f}{(M-1)} \,. \tag{3.7}$$

Equation (3.5) or (3.6) can be used directly, to generate a complex representation of exponentially modulated signal in baseband. The block diagram of the modulator is shown in Figure 3.1. By closer examination of (3.5) we see that to optimize the characteristic of the M-CPFSK modulation, we can basically modify the symbol alphabet α_k, improve the phase pulse shape *q*(*t*) or alter the modulation index. There have been many investigations in the recent past covering the influence of all of these parameters on the characteristics of the exponential modulations. In [8] authors deal with a symbol alphabet modification by comparing the duo-binary and 4-level signaling for narrowband LMR and come to the conclusion that the full-response 4-level CPFSK outperforms the duo-binary signaling technique.

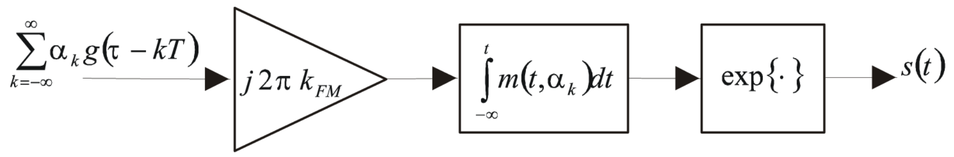

Figure 3.1: M-CPFSK general signal model used for the exponential modulation analysis.

Although a proper channel coding can significantly improve the power efficiency of the M-CPFSK modulation – as shown mainly by Rimoldi [36] and his followers [38] – this topic is not covered in this thesis.

The selection of the modulation index in most practical applications of LMR has been driven by compromising requirements between the modulation rate, receiver sensitivity and adjacent channel power level. Its value usually converges to $1/M$ with a well known example of MSK, particularly GMSK where $M=2$ and $h=0.5$ as the lowest value needed to maintain an orthogonal signaling [7]. *Multi-h CPFSK* digital modulation as reported for instance in [39] provides higher minimum *Euclidian distance* between the two successive symbols, but tends to widen the signal spectrum, and thus, the ACI. Significant effort was spent by author to optimize either the symbol alphabet of M-CPFSK or the modulation index distribution. However, none of the modifications yielded higher spectrum efficiency of the M-CPFSK modulated signal. Therefore, the symbol alphabet assumed in this work is uniformly distributed and the modulation index is a constant for selected modulation setting.

Although the spectrum of the exponentially modulated signal cannot be strictly band limited, the shape of the frequency pulse significantly influences [35] the spectrum of the transmitted signal (3.5). Therefore, there is a detailed analysis of the more recent pulse shaping filters given in Section 3.3, in order to select suitable modulation filter minimizing the ACI of the narrowband LMR.

3.2. Linear digital modulations

This chapter introduces the general superposition model of the linearly modulated signal. It also describes the signal constellations of the selected modulation techniques which can be used to improve the spectral efficiency of the LMR systems. Two main criteria are chosen to evaluate the proper modulation techniques, and those are *spectrum efficiency*, and *peak-to-average-power-ratio*.

3.2.1. Linear digital modulation signal model

Similarly to the modulation signal used for exponential modulation, the complex modulation envelope of the linearly modulated signal can be written as a linear superposition of the modulation impulses weighted by the information symbols

$$s(t) = m(t,\alpha_k) = \sum_{k=-\infty}^{\infty} \alpha_k h(t-kT) = s_I(t) + js_Q(t). \qquad (3.8)$$

In case of linear modulation, α_k is the train of the *complex* modulation symbols as oppose to the *real* symbols in (3.1). The complex modulation symbols α_k are usually plotted in complex plane, regardless of the time scale, and form *a constellation* of the digital modulation. For a given modulation pulse shape $h(t)$ that defines the spectrum of the modulated signal, it is just the modulation constellation and the allowed transitions between the constellation points that distinguishes between various modulation techniques. Thus, innumerable modulation formats exist. However from the prospective of the narrowband radio design, the constant envelope constellations are of the utmost importance, since they minimize the amplitude variations of the modulated signal. It can be shown [14], that the lower the modulation envelope variations, the lower the amount of the spectral re-growth and self interference due to the channel nonlinearities. As the evaluation criterion the PAPR of the modulation envelope (3.8) of the given modulation scheme can be calculated as

$$PAPR = \frac{\max\left\{\left|m(t,\alpha_k)\right|^2\right\}}{E\left\{\left|m(t,\alpha_k)\right|^2\right\}}, \qquad (3.9)$$

where E assigns the expectation function over the sufficiently long signal interval.

If the modulation symbols α_k result from a differential encoding, the digital modulation format is called differential. The differential encoding and decoding is known [57] to be very robust against fast signal fading effects and has the advantage of non-coherent detection at the receiver. On the other hand, at the same SNR ratio the differential encoded modulation format typically experiences higher BER than its non-differentially encoded counterpart. The combination of both properties – minimum modulation envelope amplitude variations and differential encoding – yields to the widely used [56] single carrier modulation techniques named π/4-DQPSK, π/8-D8PSK. In order to further improve the bandwidth efficiency (3.10)

$$\eta = \frac{R_b}{B} \cong \frac{\log_2(M)}{1+\alpha}, \tag{3.10}$$

where α assigns the *excess bandwidth* parameter (Section 3.3), the 16-QAM modulation, with a star constellation diagram [57], can be used. It has an advantage in that the star ordering of the constellation points can carry a differentially encoded modulation signal. Such a modulation format is therefore referred to as 16-*state differentially encoded quadrature amplitude modulation* (16-DEQAM). In Table 3.1, there is a comparison of the theoretical spectrum efficiencies and PAPR values for two levels of excess bandwidth parameter.

Table 3.1: Comparison of the linear digital modulation techniques. The PAPR parameter (3.9) is stated for two excess bandwidths.

Modulation	η	*PAPR* (α=0.25)	*PAPR* (α=0.35)	non-coherent
[-]	[bit/s/Hz]	[dB]	[dB]	[-]
QPSK	2	5	3.7	no
OQPSK	2	4	3	no
DQPSK	2	5	3.7	yes
π/4-DQPSK	2	4.3	3.2	yes
π/4-FQPSK	2	3.7	2.7	yes
8DPSK	3	4.5	3.5	yes
π/8-8DPSK	3	4.5	3.5	yes
16-QAM	4	6.5	5.5	no
16-DEQAM	4	5.5	5	yes

For the prospective narrowband LMR design, the π/4-DQPSK, D8PSK and star 16-DEQAM have been selected based on the above comparison. In the following sections, the selected modulation techniques and their constellations are briefly described.

3.2.2. π/4-DQPSK and π/4- FQPSK signal model

As it was written above, the modulation symbols α_k in differential modulations result from the differential encoding. This means that α_k is obtained by applying a phase transition $\Delta\varphi(k)$ to the previous modulation symbol $\alpha_{(k-1)}$. Hence, in vector notation [12], [58]

$$\begin{aligned} \alpha_k &= \alpha_{k-1} e^{j\Delta\varphi(k)}, && k \geq 1 \\ \alpha_k &= 0, && k = 0 \end{aligned}. \tag{3.11}$$

In (3.11), the α_0 is the phase reference before the start of the information signal sequence $b(2k)$. For the π/4-DQPSK, the allowed phase changes are shown in Table 3.2. The constellation plot can be found in Appendix B; Figure B.8. In Table 3.2, the symbol sequence α_k is already *Gray encoded* from the bit sequence $b(2k)$ to minimize bit errors.

The π/4-DQPSK system maintains a spectral efficiency of the conventional QPSK modulation while reducing amplitude variation. Other improvements to the π/4-DQPSK have been proposed in literature by Feher et al inventions [58]. By utilization of the *quadrature cross-correlation processor*, the envelope fluctuations can be further reduced. However, the π/4-FQPSK is a subject to various US patents [58] and cannot be used freely in commercial applications.

Table 3.2: Phase transitions of the π/4-DQPSK modulation [12].

α_k		$\Delta\varphi_k$
$b(2k\text{-}1)$	$b(2k)$	[rad]
0	0	+π/4
0	1	+3π/4
1	1	-3π/4
1	0	-π/4

3.2.3. D8PSK (π/8-D8PSK) signal model

The same concept of the differential encoding as in the case of π/4-DQPSK takes place in spectrally more efficient π/8-D8PSK modulation [12]. Despite its wide spread in communication systems [12], [57] the basic concept of D8PSK – however π/8 phase shifted – is recommended for the LMR systems. The reason for that can be seen in Table 3.1. When relatively-low excess bandwidths are selected, the constellation shifted version does not bring the system any significant advantage in form of PAPR reduction compared to D8PSK constellation, but increases the effective constellation size. The phase transitions of the D8PSK are shown in Table 3.3.

Table 3.3: Phase transitions of the D8PSK modulation [57].

α_k			$\Delta\varphi_k$
$b(3k\text{-}2)$	$b(3k\text{-}1)$	$b(3k)$	[rad]
0	0	0	0
0	0	1	+π/4
0	1	1	+π/2
0	1	0	+3π/4
1	1	0	-π
1	1	1	-3π/4
1	0	1	-π/2
1	0	0	-π/4

3.2.4. Star 16-DEQAM signal model

In order to further improve the spectral efficiency, the 16-state modulation that can be differentially encoded and decoded has been proposed [57] for the systems requiring fast non-coherent detection. In this work, the signal notation of the star 16-DEQAM has been adopted according to [57]. Three least significant bits of the 4-bit symbols are mapped onto the differential phase (3.11) with a particular phase steps shown in Table 3.3. The most significant bit is then mapped onto an amplitude change, such that the logic “1” changes the amplitude, while logic “0” does not change the amplitude of the transmitted signal. The constellation diagrams of the D8PSK and 16-DEQAM can be seen in Appendix B; Figure B.8.

3.3. Digital pulse shaping filter optimization

3.3.1. Objective of the new pulse shaping filter

The spectrum of the exponentially modulated signal cannot be considered strictly band limited – similarly to the most linear digital modulation formats. However, the shape of the phase or frequency pulse significantly influences [35] the spectrum of the transmitted signal (3.5). A truncated version of the *square root raised cosine* (RRC) pulse shaping filter as a typical representation of the Nyquist filter for the excess bandwidth greater than zero is usually implemented in LMR systems when using 4-CPFSK modulation. Such filters typically have limited stop-band attenuation and thus the designers are forced to use very low roll-off factors approaching the value of 0.2 and therefore higher group delays of more than 8 symbols [53].

The demand for the matched pulse shaping filters with high stop-band attenuations is even more severe in case of the linear modulation techniques. It can be shown (Figure 3.2) that the typical truncated version of the RRC filters can reach the ACI levels of -60 dBc required, with very high group delays and therefore very high orders of the digital filters.

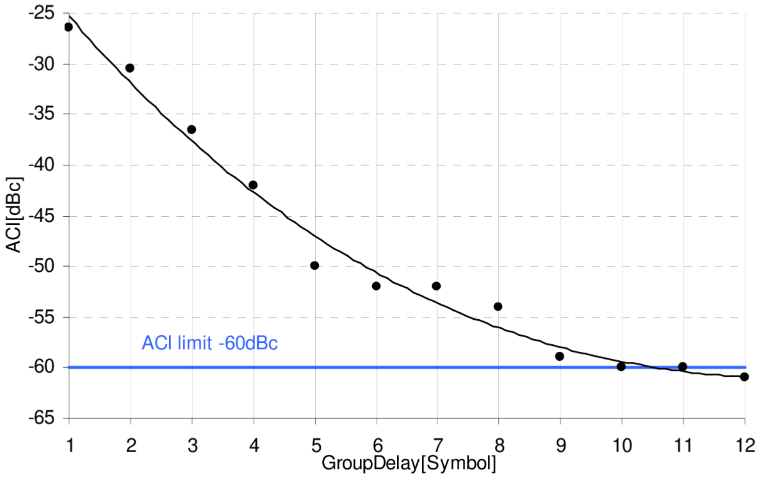

Figure 3.2: ACI as a function of the truncated version of the RRC filter group delay. 16-DEQAM, 25 kBaud, 25% excess bandwidth, ACI measured as described in Section 2.2.1.

Designing matched pulse shaping filters with their cascade satisfying the Nyquist condition for minimum ISI thus becomes an uneasy task. Despite their practical importance, there are only a few design techniques that can be used to directly devise the matched combination of the Nyquist filters. The MATLAB software and its *Digital Filter Design* application [50] provides the Nyquist filters based on a truncated version of the RC filter. Such filters create a single version of balance between the time- and frequency-domain parameters. The designer can use a wide range of weighting windows to trade off the out-of-band suppression for the excess bandwidth; however, the coefficients of the square root filter version cannot be explicitly calculated and for most of the windows, the minimum excess bandwidth is typically limited by the equivalent noise bandwidth of the window being used [48]. The same is true for the case when the designer chooses to calculate the coefficients of the RRC filter directly and limits the impulse response by the appropriate window; moreover, the residual ISI is increasing rapidly, because such design technique significantly violate the *Nyquist first condition*, which is becoming an issue with high order digital modulations.

Other techniques to design the pulse shaping filters that have been reported are based on optimization algorithms with a specific objective functions such as maximizing the robustness to timing jitter [41], [42], [43], minimizing the duration of the impulse response [45], [46] or minimizing the PAPR *peak to average power ratio* at the transmitter filter output [44]. Besides the complex way of calculating the filter coefficients, filters that are obtained by optimization techniques are usually of non-linear phase [45], [46] or they cannot be directly partitioned into matched filter pairs [41], [42], [44]. A well-written reference concerning the problem of designing matched pairs of digital Nyquist (M) filters with balanced performance can be found in [47]. The method is based on numerical calculation and does not provide an exact definition of the filter characteristic, which complicates the design of matched filter pairs with different values of the group delay parameter and over-sampling ratio; however, it offers a wide range of communication filters and is also used for comparison.

3.3.2. Nyquist filters design analysis

If the digital receiver processes a data signal on the sample-by-sample basis, a typical problem which arises from the strict band limitation of the signal spectrum is ISI. To lower the amount of ISI to zero, the overall transmitter-channel-receiver frequency response should fulfil the first Nyquist criterion defined in the time domain as [14], [41], [43]

$$g(kT)=\begin{cases}1, & for\ \ k=1\\ 0, & otherwise\end{cases}. \qquad (3.12)$$

The frequency domain equivalent of this criterion in a sense of *integral Fourier transform* can be written as

$$\sum_{k=-\infty}^{\infty} G\left(f+\frac{k}{T}\right)=T, \qquad |f|\leq\frac{1}{2T}. \qquad (3.13)$$

It states that the sum of the copies of the spectrum shifted by the baud rate must add to a constant value over the frequency range -1/2*T* to 1/2*T*. As shown in [14], the first Nyquist criterion for zero ISI level has two important implications for the modulation filter design. First, the double-sided bandwidth of the processed data signal cannot be less than *1/T* without introducing the ISI. Second, the spectrum of the signal should be symmetrical around the centre frequency and it should also embody an odd *vestigial symmetry* around the frequency of *1/2T*. Neglecting this condition in any sense would cause an increase in ISI. For a minimum double-sided signal bandwidth equal to the Nyquist frequency *1/T* – recalling that *T,* is the unfiltered modulation symbol period – the Nyquist condition yields a unique solution with its time representation being a *sinc* pulse. For the signal bandwidth exceeding the Nyquist frequency, innumerable filter characteristics should exist [14]. However, to the best of the present author's knowledge, there are only two sets of filter frequency responses explicitly defined by their continuous piecewise function definitions [47], [42]. The first one and perhaps the most widely used one follows the *raised cosine* (RC) frequency characteristic as defined by (3.14)

$$G_{RC}(f)=\begin{cases}1, & 0\le f\le B(1-\alpha)\\ \dfrac{1}{2}\left\{1+\cos\left(\dfrac{\pi}{2B\alpha}\left[f-B(1-\alpha)\right]\right)\right\}, & B(1-\alpha)<f\le B(1+\alpha)\\ 0, & B(1+\alpha)<f\end{cases}, \qquad (3.14)$$

where *B,* is the single-sided filter bandwidth corresponding to 1/2*T,* and *α* is the *excess bandwidth* parameter usually called *roll-off factor*. The corresponding continuous time impulse response of the RC filter can be written as

$$g_{RC}(t)=\mathrm{sinc}\left(\frac{t}{T}\right)\frac{\cos\left(\pi\alpha\dfrac{t}{T}\right)}{1-4\alpha^2\left(\dfrac{t}{T}\right)^2}. \qquad (3.15)$$

The lower the roll-off factor, the narrower is the occupied bandwidth of the signal. However, with a low roll-off factor the original modulation (modulated) signal becomes more vulnerable to *timing jitter* as the eye pattern of the received signal narrows down and becomes practically almost undetectable for the roll-off factor equalling zero. The second negative effect resulting from lowering of the roll-off factor is related to the practical aspects of the digital filter design and that is the length of the filter impulse response or the decay of its tails to zero. The lower the roll-off factor, the longer the impulse response of the RC filter has to be taken into account when designing a digital filter with comparable stop-band attenuation.

It is only recently that another set of modulation filters has been reported [42]. In [42], modulation filters marked as "better" than Nyquist filter [3] is defined in frequency domain as

$$G_B(f)=\begin{cases}1, & 0\le f\le B(1-\alpha)\\ \exp\left\{\dfrac{\ln 2}{\alpha B}\left[B(1-\alpha)-f\right]\right\}, & B(1-\alpha)<f\le B\\ 1-\exp\left\{\dfrac{\ln 2}{\alpha B}\left[f-B(1+\alpha)\right]\right\}, & B<f\le B(1+\alpha)\\ 0, & B(1+\alpha)\le f\end{cases}, \qquad (3.16)$$

with a corresponding scaled time function

$$g_B(t)=2B\sin c(2Bt)\frac{4\beta\pi t\sin(2\pi B\alpha t)+2\beta^2\cos(2\pi B\alpha t)-\beta^2}{4\pi^2t^2+\beta^2}, \qquad (3.17)$$

where

$$\beta=\frac{\ln 2}{\alpha B}. \qquad (3.18)$$

The excess bandwidth parameter *α* can be used to trade off the occupied bandwidth and the time duration of the pulse.

The problem with designing a modulation filter can be noticed, in that the designer needs to carefully consider both representations of the signal – the time and the frequency one. Therefore, when designing modulation filters, one representation has to be

---

[3] However, the present author disagree with the attribute "better" – because any filter fulfilling the Nyquist criterion can be regarded as a Nyquist filter, thus there cannot be a better filter in this filter family – the B index is used for all the related characteristics of this filter in the following text.

compromised at the expense of the other and it is a particular application that defines the final compromise.

Moreover, in a complete radio system, the overall Nyquist modulation filter is typically split into its transmitter (TX) and receiver (RX) parts to fulfil the matched filtering condition for maximizing the signal-to-noise ratio at the decision stage [14]. The matched filter condition can be written in the frequency domain as (3.19)

$$H_{RX}(f) = H_{TX}(f)\exp(-j2\pi fT), \tag{3.19}$$

or in the time-domain as

$$h_{RX}(t) = h_{TX}(T - t). \tag{3.20}$$

It says that the matched filter impulse response should be the time reversed variant of the signaling pulse, where T is its time duration. Thus, to meet all these conditions, the transmitter and receiver filter frequency characteristic should follow a square root version of the Nyquist filter (3.21)

$$|H_{RX}(f)| = |H_{TX}(f)| = \sqrt{G(f)}. \tag{3.21}$$

Although both filters are assumed to be the same, there are different requirements placed on the design of each of them. They can be summarized into the following four conflicting requirements [47]:

- The length of the impulse response $h(t)$ should be kept as small as possible to minimize the implementation cost and the propagation delay of the DSP part of the radio transceiver.
- The Nyquist criterion should be satisfied as closely as possible to minimize ISI.
- At the transmitter side, the primary issue is the transmission bandwidth defined by the ACP requirements (Section 2.2.1). Thus the adjacent channel, and alternate channel power limits, dictate the stop-band attenuation of the transmitter filter $H_{TX}(f)$.
- The lower the magnitude of the impulse response side-lobes**,** the better is the eye-opening, hence the better timing jitter immunity can be reached [43].
- At the transmitter side there is also a demand to minimize the PAPR of the transmitted pulses [44], [47]. Such an optimization of the transmitter and receiver filters typically yields a filter pair that is no longer mutually matched (3.19), (3.20).

From an analysis of (3.15) it is evident that the impulse response of the RC filter differs from the minimum bandwidth Nyquist filter by the window function used to truncate the *sinc* pulse. The design of the digital filter, thus, boils down to selecting an appropriate window function [43]. The same holds true for most of the modulation filters with the zero ISI property. An example of the impulse response decomposition for the RC, B-filter and weighted RC filter is shown in Figure 3.3.

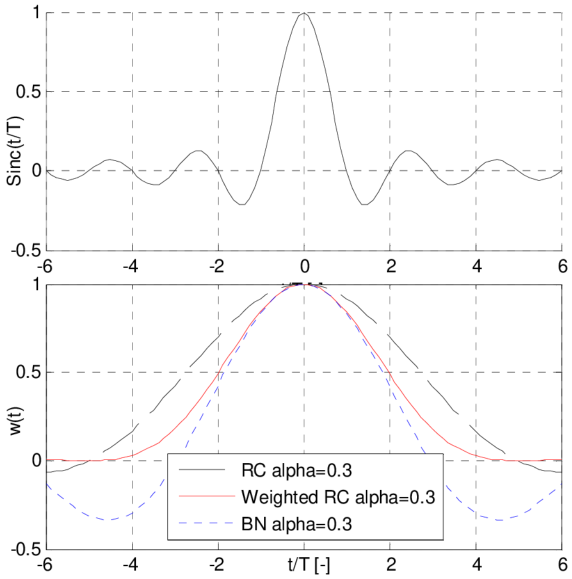

Figure 3.3: Decomposition of the impulse response of the studied modulation filters. **(Top)** *sinc*(*t/T*) function, the ideal Nyquist's filter. **(Bottom)** Typical windowing functions used to limit the impulse response.

In the above example, the group delay of the filters has been chosen to be six modulation symbols, $G_D = 6$. It should be noted that this delay also determines the length of the filter impulse response L, as well as the filter order N_0 according to

$$N_0 = L - 1 = 2NG_D, \qquad (3.22)$$

where N is the number of samples per one modulation symbol. In narrowband LMR systems based on fast packet switching, it is preferable to lower the group delay parameter as well as the filter order to the minimum values, since it means lower propagation delay times and simpler hardware realization structures.

It can be seen from Figure 3.3 that both the RC and the B-filter windowing functions for the chosen parameters are in fact a cascade of the two windows, where the second window, denoted $w(t)$ in (3.23), is a rectangular pulse which causes a widening of the amplitude frequency characteristic and a relatively high level and slow decay of its side lobes,

$$g(t) = g_{RC}(t)w(t). \qquad (3.23)$$

A different second window can be selected in order to improve these negative effects. In Figure3.4, there is an example of the RC filter with the roll-off parameter set to 0.3, weighted by the Hann window[4]. For the sake of comparison, the truncated version of the RC filter with equivalent excess bandwidth (α=0.47) has been added to the plot. It can be seen that for the same filter order (N_0=96), the weighted version of the RC filter has a better stop-band attenuation, because its time domain characteristic (Figure 3.5) goes smoothly to the zero level and it is minimally influenced by the truncation operation. However, as is shown in Figure 3.5, there is an increase in the impulse response side lobes level.

---

[4] The name Hann – instead of Hanning – has been adopted in this work according to MATLAB Digital Filter Design [50] and also because it is considered a correct name of the window named after the *Austrian meteorologist Julius Von Hann* [48].

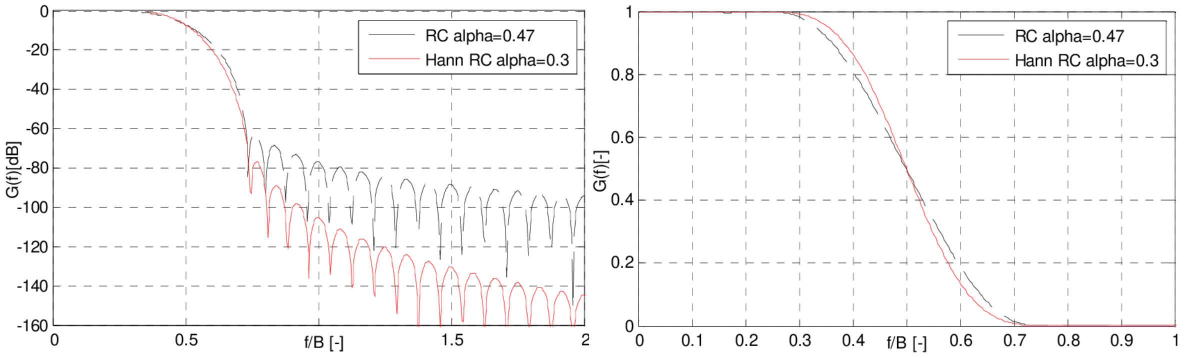

Figure 3.4: Amplitude frequency characteristics of the truncated RC filter with α=0.47 and its Hann window weighted variant with α=0.3. For the same filter order and excess bandwidth, the weighted version of the RC filter reaches better stop-band attenuation by a factor of 13.8 dB.

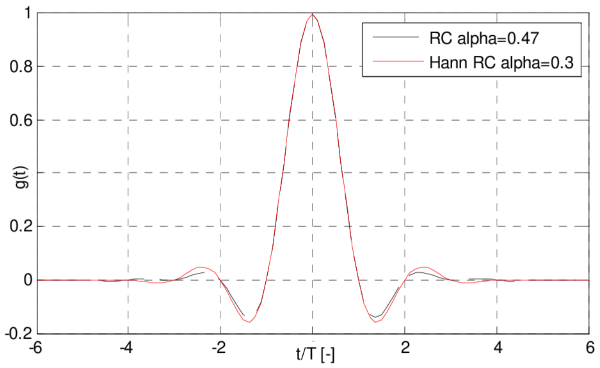

Figure 3.5: Graphical comparison of the impulse responses of the studied filters.

Larger tails of the impulse response typically result in a higher sensitivity to timing jitter [43]. Hence, the weighted version of the RC filter cannot be classified as a better filter; it represents an alternative balance between the studied parameters. A major obstacle of the described design method – one of the few methods available in MATLAB software [50] – is that the frequency response *G*(*f*) is not known and it is a problem to calculate the *H*(*f*) (3.21) as well as the matched filters coefficients. The numerical method based on *sampling the frequency response* [51] can be an option, however, such an approach yields to approximated results with a high level of residual ISI. It is therefore reasonable to start from the filter definition in the frequency domain, derive all the coefficients by calculating its *inverse Fourier transform,* and limit the resulting impulse response in a certain interval. In fact, the term “raised cosine filter” also originates from its definition in the frequency rather than the time domain.

3.3.3. Nyquist δ-filter formulation

A closer analysis of equation (3.10) unveils the fact that the frequency response of the RC filter is a convolution of a rectangular pulse of duration 1/2*T* and a RC window modified by the roll-off parameter. As shown in [48], there are other window shapes that can converge to zero more smoothly. A good alternative is a generally defined *Blackmann window*, which can be continuously changed to the *Blackmann*, *exact-Blackmann*, *Blackmann-Harris* and $cos^4(x)$ windows by changing the values of a_0, a_1 and a_2 in its definition

$$w(x)=a_0+a_1\cos(\pi x)+a_2\cos(2\pi x) \tag{3.24}$$

From the comparison shown in Figure 3.6 it can be seen that although the general Blackmann window smoothly converges to zero level, it does so at the expense of the window width, and its shape does not satisfy the vestigial symmetry property. Nevertheless, there is still the possibility of decomposing the window into its upper and lower parts, as shown in Figure 3.6, and using these functions to construct a Nyquist filter by shifting them to the right by a distance marked δ. Respecting the typical notation of the Nyquist RC filters, a general *Nyquist δ-filter* defined in the frequency domain can thus be written as [91]

$$G_\delta(f)=\begin{cases} 1, & 0 \le f \le B(1-\alpha) \\ 1-a_0-a_1.\cos\dfrac{\pi[B(1+\alpha_0)-(f+\delta)]}{2B\alpha_0} \\ -a_2.\cos 2\dfrac{\pi[B(1+\alpha_0)-(f+\delta)]}{2B\alpha_0}, & B(1-\alpha)< f \le B \\ a_0+a_1.\cos\dfrac{\pi[B(1+\alpha_0)-(f-\delta)]}{2B\alpha_0} \\ +a_2.\cos 2\dfrac{\pi[B(1+\alpha_0)-(f-\delta)]}{2B\alpha_0}, & B< f \le B(1+\alpha) \\ 0 & B(1+\alpha)\le f \end{cases}, \qquad (3.25)$$

where

$$\delta = 0.5 - B(1-\alpha_0) - \frac{2B\alpha_0}{\pi}\left[\pi - \arccos\left(\frac{1}{4}\,\frac{a_1-\sqrt{a_1^2+8a_2^2+4a_2-8a_2a_0}}{a_2}\right)\right]. \qquad (3.26)$$

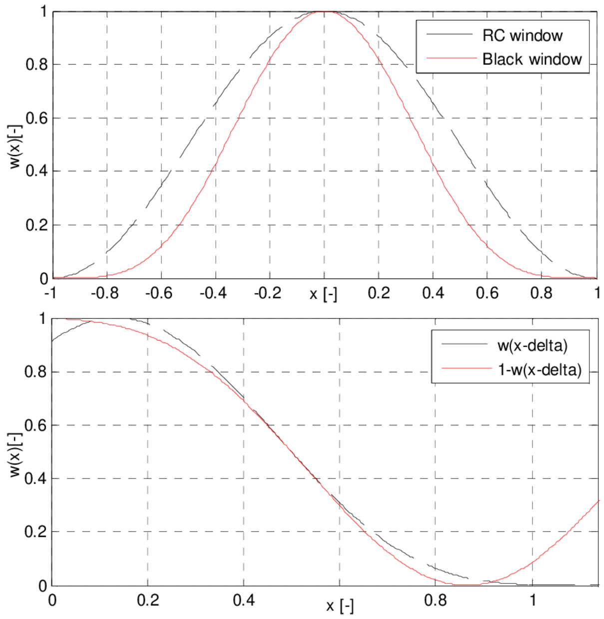

Figure 3.6: (top) RC window versus general Blackmann window (a_0=3/8; a_1=4/8; a_2=1/8;). **(bottom)** Decomposition of the Nyquist δ-filter (3.25, α_0=1) frequency response into its upper and lower part.

For the special case, where the parameters a_0, a_1, a_2 equal 3/8, 4/8 and 1/8 respectively, the equations (3.25) and (3.26) can be effectively reduced to (3.27)

$$G_\delta(f)=\begin{cases} 1, & 0\le f\le B(1-\alpha) \\ 1-\cos\left\{\dfrac{\pi[B(1+\alpha_0)-(f+\delta)]}{4B\alpha_0}\right\}^4, & B(1-\alpha)< f\le B \\ \cos\left\{\dfrac{\pi[B(1+\alpha_0)-(f+\delta)]}{4B\alpha_0}\right\}^4, & B< f\le B(1+\alpha) \\ 0 & B(1+\alpha)\le f \end{cases}, \tag{3.27}$$

and (3.28)

$$\delta=0.5-B(1-\alpha_0)-\frac{4B\alpha_0}{\pi}\arccos\left(\frac{1}{2^{\frac{1}{4}}}\right). \tag{3.28}$$

The quoted values of $a_{0\text{-}2}$ parameters are preferred in this paper because they represent the boundary case for which the Blackmann window approaches zero level without a discontinuity. It is important to note that the Nyquist δ-filter defined by (3.25) to (3.28) differs from the RC filter also in the starting point of its stop-band region – and its first null bandwidth. Therefore, to get the filter definition directly comparable to that of the RC filter, its notation is adopted where

$$\alpha_{RC}=\alpha=\alpha_0+\delta, \tag{3.29}$$

which means that when comparing both filters (Section 3.3.5), the RC filter will have an equivalent roll-off factor adjusted by the value of the δ parameter.

From (3.25) to (3.28) the digital filter coefficients can be calculated *(see the Maple script in Appendix C)* by the inverse Fourier transform of the frequency response (3.30)

$$g_\delta(t)=\frac{\pi}{2}\int_{-B(1+\alpha)}^{B(1+\alpha)} G_\delta e^{j2\pi ft}\,df, \tag{3.30}$$

and equidistantly sampling the continuous impulse response of the filter (3.31) over the limited time interval, which is defined by the group delay parameter G_D

$$g_{\delta\_S}(t)=g_\delta(t)\delta_{T_S}(t)=\sum_{n=-G_DN}^{G_DN} g_\delta(t).\delta(t-nT_S), \tag{3.31}$$

where T_S is the sampling period defined in relation to the modulation symbol period T

$$T_S=\frac{T}{N}, \tag{3.32}$$

and $\delta_{T_S}(t)$ is the train of the unit impulses. In order to keep the notation simple the coefficients of the Nyquist δ-filter impulse response have been denoted $g_\delta[n]$.

The matched filter pair (3.15), (3.16) can be calculated analogously as a square-root version of the Nyquist δ-filter

$$h_\delta(t)=\frac{\pi}{2}\int_{-B(1+\alpha)}^{B(1+\alpha)} \sqrt{G_\delta}\, e^{j2\pi ft}\,df, \tag{3.33}$$

and its sampled version

$$h_{\delta\_TX}[n] = h_{\delta\_RX}[-n] = h_{\delta}[n] = h_{\delta}(t)\delta_{T_S}(t), \qquad (3.34)$$

can be used for the transmitter and receiver filter directly, since the impulse response $h_{\delta}[n]$ is symmetrical, and therefore linear-phase. *(see the Maple script in Appendix C)*

It is important to note that all the definitions of the Nyquist and square root Nyquist filters, either in the frequency, or the time domain, were given in their non-causal form and thus zero phase characteristics were implicitly assumed [51]. Such filters are not practically realizable and therefore all the impulse responses of the studied filters have to be time shifted to begin at a zero time instant.

3.3.4. Nyquist filter evaluation criteria

Although all the studied filters calculated by their generic relations (3.14), (3.16) and (3.27) have a negligible level of ISI, when used as a cascade of the transmitter and receiver filters of their truncated square root versions, residual ISI appears and cannot be omitted. To compare this property among different filters, the relative level of residual ISI can be calculated as [47]

$$\rho_{ISI} = 10\log\frac{\sum\limits_{n=mN,m\neq 0} g_{RC}^{2}[n]}{\sum\limits_{n=mN,m\neq 0} g_{\delta}^{2}[n]}. \qquad (3.35)$$

In addition to (3.35), it is also reasonable to compare the cascaded filter impulse response side lobes level according to

$$\rho_{SL} = 10\log\frac{\sum\limits_{n=N+1}^{G_D N+1} g_{RC}^{2}[n]}{\sum\limits_{n=N+1}^{G_D N+1} g_{\delta}^{2}[n]}. \qquad (3.36)$$

From the frequency-domain parameters, the transmitter stop-band attenuation is of utmost importance. The difference in stop-band attenuation between two filters can be evaluated according to [47]

$$\rho_{SB} = 10\log\frac{\int_{f_0}^{1-f_0}\left|H_{RRC}\left(e^{j2\pi f}\right)\right|^2 df}{\int_{f_0}^{1-f_0}\left|H_{\delta}\left(e^{j2\pi f}\right)\right|^2 df}, \qquad (3.37)$$

where the stop-band of the Nyquist and also the square root Nyquist filters is typically [14], [7] considered to start at the normalized frequency f_0

$$f_0 = \frac{1+\alpha}{2N}, \qquad (3.38)$$

and to end at the normalized frequency 1-f_0.

3.3.5. Matched Nyquist filters evaluation

Firstly, the proposed Nyquist δ-filter has been compared with the truncated version of the RC filter. To get the numerical results presented in Table 3.4, the over-sampling ratio of the filters has been set to 5 and the group delay parameter, as well as the excess bandwidth, has been varied. It can be seen that the square root Nyquist δ-filter reaches better stop-band attenuation and its cascade experiences lower residual ISI level for the same filter order, but it does so in expense of a higher impulse response side lobes level.

Secondly, the group delay parameter was set to 6 and the over-sampling ratio N was changed from 4 to 6. The results shown in Table 3.5 express that the difference in performance of both filters is approximately the same when compared to the respective values shown in Table 3.4, and do not change significantly with the over-sampling factor.

Table 3.4: Numerical values of ρ_{SB}[dB], ρ_{ISI}[dB], ρ_{SL}[dB]. Square root RC filter versus square root Nyquist δ-filter. The over-sampling factor N=5 is fixed and the group delay parameter G_D and roll-off parameter α of the filters vary.

RRC Filter / root Nyquist δ-filter; N=5										
G_D	α_0[-]	0.2	0.25	0.3	0.35	0.4	0.45	0.5	0.55	0.6
	δ[-]	0.027	0.034	0.040	0.047	0.054	0.061	0.068	0.075	0.082
	α[-]	0.227	0.284	0.340	0.397	0.454	0.511	0.568	0.625	0.682
5	ρ_{SB}[dB]	0.1	5.9	10.9	8.8	8.0	8.6	8.4	7.2	7.2
	ρ_{ISI} [dB]	-4.2	5.9	6.7	0.6	7.8	5.2	2.6	9.7	0.2
	ρ_{SL}[dB]	-0.7	-0.9	-1.2	-1.5	-1.9	-2.3	-2.7	-3.3	-0.9
6	ρ_{SB}[dB]	4.2	10.8	8.5	8.2	8.6	7.5	6.8	6.7	5.1
	ρ_{ISI} [dB]	3.9	6.8	4.6	6.6	4.3	5.9	11.3	11.8	7.0
	ρ_{SL}[dB]	-0.7	-0.9	-1.2	-1.5	-1.9	-2.3	-2.7	-3.3	-3.9
7	ρ_{SB}[dB]	9.9	8.9	8.3	8.4	7.2	6.8	5.8	4.3	4.5
	ρ_{ISI} [dB]	10.4	2.0	6.7	3.8	11.4	10.4	6.6	7.8	8.4
	ρ_{SL}[dB]	-0.7	-0.9	-1.2	-1.5	-1.9	-2.3	-2.8	-3.3	-3.9
8	ρ_{SB}[dB]	10.2	8.0	8.6	7.2	6.8	5.2	4.5	3.6	2.4
	ρ_{ISI} [dB]	5.0	7.6	4.3	10.9	10.6	7.1	8.2	15.4	14.2
	ρ_{SL}[dB]	-0.7	-0.9	-1.2	-1.5	-1.9	-2.3	-2.8	-3.3	-3.9

Next, there is a set of results provided in Table 3.6 to compare the proposed Nyquist δ-filters with the digital filters, designed according to [42]. It is evident that the B-filters in contrast to the Nyquist δ-filters, move a balance in favor of the time domain parameters and thus the difference in stop-band attenuation and residual ISI is even greater than in the case of the RC filter described before. Since all the values are given in their relative form, one can easily make a comparison between the RC and the B- filter.

The results presented express that the Nyquist δ-filter represents an alternative balance between the parameters studied, and can be an option in applications that require higher stop-band attenuation as well as a low level of residual ISI. It should be noted that the proposed filter set has been devised using a heuristic approach, and as such, cannot be considered a globally optimal solution. In fact, other filters might provide even better stop-band attenuation, but as it has been shown, at the cost of the higher residual ISI and/or worst side lobes level. Table 3.7 gives a comparison of the Nyquist δ-filter with the filters devised by an iterative algorithm [47] for several choices of its design parameters. It can be seen that the stop-band attenuation of the Nyquist δ-filter can be reached, or can even be overcome, at the additional cost of increased side lobes level or ISI.

Table 3.5: Numerical values of ρ_{SB}[dB], ρ_{ISI}[dB], ρ_{SL}[dB]. RRC filter versus square root Nyquist δ-filter. The group delay parameter of the filters is fixed G_D=6 and the over-sampling N varies.

RRC Filter / root Nyquist δ-filter; G_D =6										
N	α_0[-]	0.2	0.25	0.3	0.35	0.4	0.45	0.5	0.55	0.6
	δ[-]	0.027	0.034	0.040	0.047	0.054	0.061	0.068	0.075	0.082
	α[-]	0.227	0.284	0.340	0.397	0.454	0.511	0.568	0.625	0.682
4	ρ_{SB}[dB]	4.6	10.8	8.4	8.3	8.6	7.4	6.8	6.7	4.9
	ρ_{ISI} [dB]	4.3	6.5	5.8	6.4	4.1	7.1	10.9	12.4	7.0
	ρ_{SL}[dB]	-0.7	-0.9	-1.2	-1.5	-1.9	-2.3	-2.8	-3.3	-4.0
5	ρ_{SB}[dB]	4.2	10.8	8.5	8.2	8.6	7.5	6.8	6.7	5.1
	ρ_{ISI} [dB]	3.9	6.8	4.6	6.6	4.3	5.9	11.3	11.8	7.0
	ρ_{SL}[dB]	-0.7	-0.9	-1.2	-1.5	-1.9	-2.3	-2.7	-3.3	-3.9
6	ρ_{SB}[dB]	4.1	10.8	8.6	8.2	8.6	7.6	6.8	6.7	5.2
	ρ_{ISI} [dB]	3.7	7.0	3.7	6.7	4.4	5.1	11.5	11.5	6.9
	ρ_{SL}[dB]	-0.7	-0.9	-1.2	-1.5	-1.9	-2.3	-2.7	-3.3	-3.9

Table 3.6: Numerical values of ρ_{SB}[dB], ρ_{ISI}[dB], ρ_{SL}[dB]. Square root B-filter versus square root Nyquist δ-filter. The over-sampling factor N=5 is fixed and the group delay parameter G_D of the filters varies.

Root B-filter / root Nyquist δ-filter; N=5										
G_D	α_0[-]	0.2	0.25	0.3	0.35	0.4	0.45	0.5	0.55	0.6
	δ[-]	0.027	0.034	0.040	0.047	0.054	0.061	0.068	0.075	0.082
	α[-]	0.227	0.284	0.340	0.397	0.454	0.511	0.568	0.625	0.682
5	ρ_{SB}[dB]	8.2	15.4	19.5	18.2	19.6	19.9	19.1	19.6	27.3
	ρ_{ISI} [dB]	3.2	8.8	6.9	12.8	13.4	8.3	10.1	17.6	16.8
	ρ_{SL}[dB]	-2.2	-2.9	-3.8	-4.9	-6.1	-7.3	-8.3	-8.5	-8.6
6	ρ_{SB}[dB]	13.7	15.4	18.3	19.9	19.5	19.4	13.0	19.0	18.5
	ρ_{ISI} [dB]	5.5	12.3	14.7	11.1	7.4	15.1	17.5	17.4	16.0
	ρ_{SL}[dB]	-2.2	-1.5	-3.9	-5.0	-6.1	-7.3	-6.6	-8.6	-7.8
7	ρ_{SB}[dB]	18.8	18.3	13.1	19.3	19.8	19.6	18.5	18.6	17.9
	ρ_{ISI} [dB]	11.9	12.2	11.7	8.4	18.9	14.8	17.9	14.0	16.4
	ρ_{SL}[dB]	-2.2	-3.0	-2.4	-5.0	-6.2	-7.4	-8.4	-8.7	-7.9

Table 3.7: Numerical values of ρ_{SB}[dB], ρ_{ISI}[dB], ρ_{SL}[dB]. Square root Nyquist (M) filter versus square root Nyquist δ-filter. The N parameter is fixed and the group delay parameter G_D of the filter varies; γ and γ_T are the design parameters of the iteration algorithm [47].

root Nyquist (M) / root Nyquist δ-filter									
		G_D =5; N=5; g_T=0				G_D =5; N=5; g_T=0.05			
α_0[-] ; δ[-]	γ[-]	0.5	1	2	10	0.5	1	2	10
0.25; 0.034	ρ_{SB}[dB]	-1.2	-0.5	-0.3	0.0	-0.1	0.1	0.1	0.2
	ρ_{ISI} [dB]	1.4	-2.6	-5.0	-6.6	3.5	-1.3	-4.6	-6.9
	ρ_{SL}[dB]	0.0	0.1	0.2	-0.2	-0.3	-0.3	-0.2	-0.2
		G_D =6; N=5; g_T=0				G_D =6; N=5; g_T=0.05			
α_0[-]; δ[-]	γ[-]	0.5	1	2	10	0.5	1	2	10
0.25; 0.034	ρ_{SB}[dB]	-2.6	-2.2	-2.1	-1.0	1.1	0.6	0.3	0.9
	ρ_{ISI} [dB]	-0.1	-3.1	-4.1	-5.2	8.5	3.2	-1.1	-5.0
	ρ_{SL}[dB]	0.2	0.2	0.2	0.1	-0.4	-0.1	0.0	0.0
		G_D =7; N=5; g_T=0				G_D =7; N=5; g_T=0.05			
α_0[-]; δ[-]	γ[-]	0.5	1	2	10	0.5	1	2	10
0.25; 0.034	ρ_{SB}[dB]	-9.6	-9.3	-9.3	-4.9	4.6	4.7	4.6	3.6
	ρ_{ISI} [dB]	-1.4	-2.2	-2.5	-4.1	11.8	6.4	1.6	-5.0
	ρ_{SL}[dB]	0.4	0.4	0.4	0.3	-0.9	-0.4	-0.3	-0.1

To further explore the absolute levels of the parameters studied, one particular combination of filters from the studied examples has been selected and their respective characteristics have been calculated. In Figure 3.7, and Figure 3.8, there are amplitude frequency characteristics of the square root Nyquist filter variants clearly unveiling the significant differences in stop-band attenuation. It is interesting to note also the pass band ripple (Figure 3.8) of the characteristics from which the B-filter is the worst due to the discontinuity already in first derivative of its frequency characteristic function (3.16). On the other hand, Figure 3.9 depicts the impulse responses of the filters, from which the increase in the side lobes level is evident. Since this is only the transmitter part of the Nyquist matched filter pair, it is useful to evaluate the side lobes level after the cascade of both filters as shown in Figure 3.11 to Figure 3.13. The respective amplitude frequency characteristics of the filter cascade are shown in Figure 3.10 Seen in a linear scale, they should embody the vestigial symmetry to fulfil the Nyquist condition in the frequency domain (3.13). It can be seen from Figure 3.10 that this condition is not reached fully for any of the filters; however, the Nyquist δ-filter is approaching the symmetrical shape very closely. From the eye diagrams shown in Figure 3.12 and Figure 3.13, the two facts are evident that were predicted by measurement results. Firstly, the residual ISI level is the lowest for the Nyquist δ-filter and the highest for the B-filter, the difference being 14.5 dB. And secondly, the B-filter reaches the widest eye opening and should, therefore, be the most robust from the three studied filters as regards the timing jitter.

As was summarized in the above sections, the directly conflicting requirements placed on a design of the digital matched Nyquist filter pair make the task complicated. From this point of view, the typical truncated RC filter represents a single balance between the time- and frequency-domain parameters. The Nyquist δ-filter set, which was defined throughout this chapter, enlarges the family of Nyquist filters, and when compared with the truncated

RRC filter cascade, it strikes the balance towards the frequency domain parameters while reaching a low level of residual ISI. It does so at the cost of a higher side lobes level of the impulse response. An exact symbolic definition of the Nyquist δ-filter in the frequency domain gives the designer scope to choose freely the arbitrary filter parameters such as equivalent excess bandwidth, group delay and over-sampling parameters and derive coefficients for either the "normal" or the square root filter variants. The filters generated are of linear-phase having symmetrical impulse responses, which directly contribute to efficient hardware realization structures.

From the LMR design point of view, the stop-band attenuation influences the amount of ACI, which is one of the strictest restrictions placed on a transmitter (Section 2.2.1) and therefore the Nyquist δ-filter represents an elegant option, how to reach the required limit without increasing the ISI, violating the matching condition between transmitter and receiver filters and with low group delay of the filter impulse response.

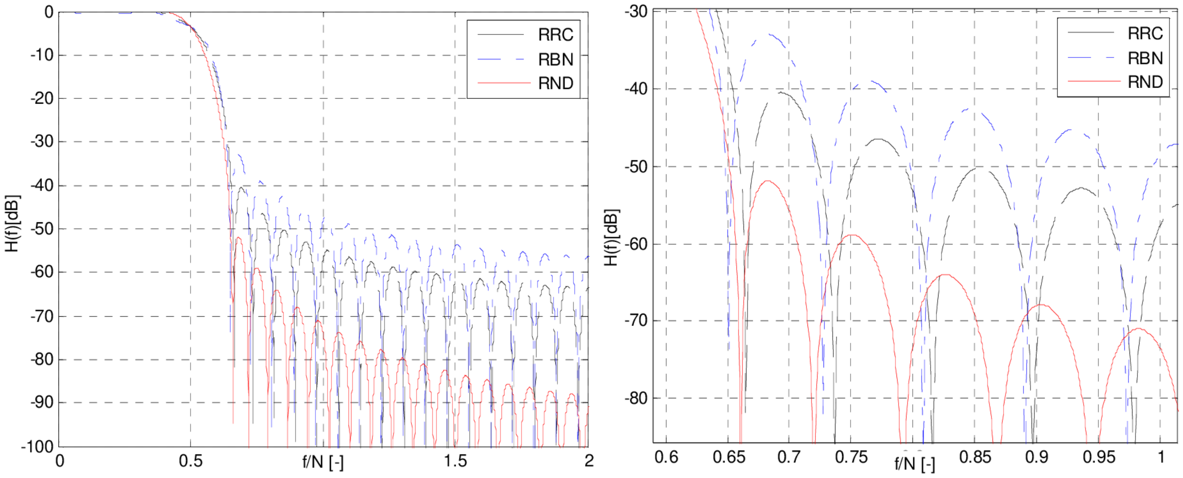

Figure 3.7: Amplitude frequency characteristics (log scale) of the truncated square root RC filter (RRC); square root B-filter (RBN); square root Nyquist δ-filter (RND) of the same filter order and equivalent excess bandwidth α=0.284; G_D=6; N=5; N_O=60.

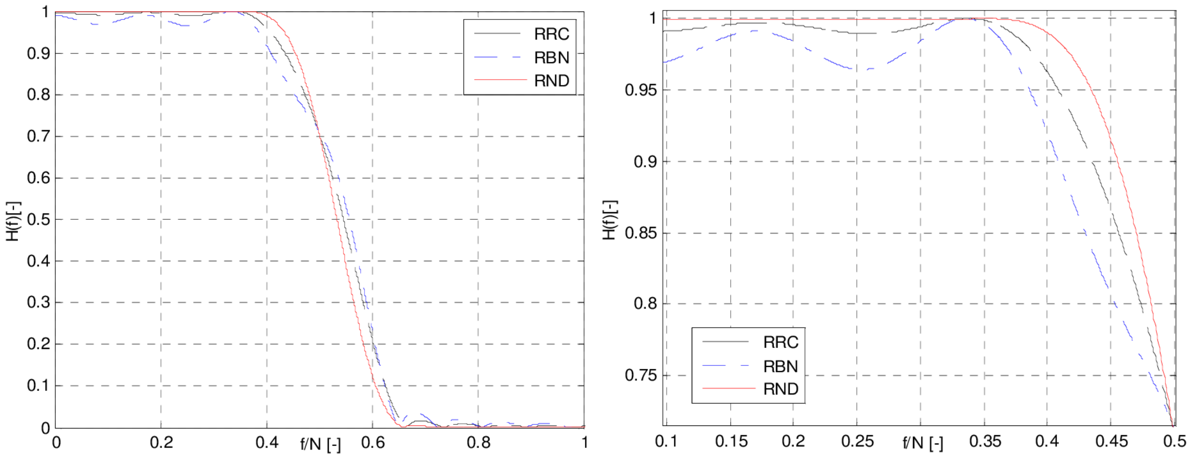

Figure 3.8: Amplitude frequency characteristics (linear scale) of the truncated square root RC filter (RRC); square root B-filter (RBN); square root Nyquist δ-filter (RND). α=0.284; G_D=6; N=5; N_O=60.

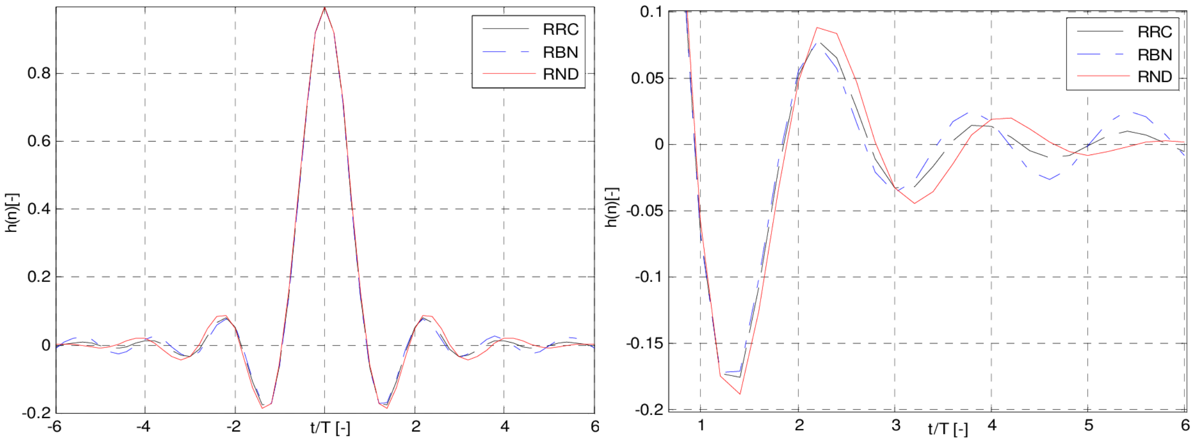

Figure 3.9: Normalized impulse responses of the truncated square root RC filter (RRC); square root B-filter (RBN); square root Nyquist δ-filter (RND). α=0.284; G_D=6; N=5; N_O=60.

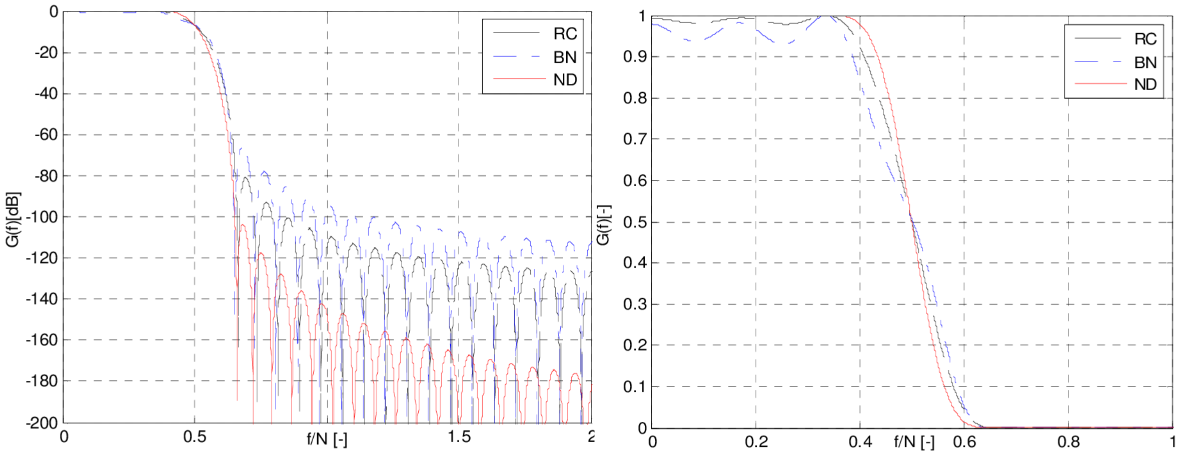

Figure 3.10: **(left)** Amplitude frequency characteristics of the cascade of transmitter and receiver RC filter (RC); B-filter (BN); Nyquist δ-filter (ND); α=0.284; G_D=2x6; N=5; N_O=2x60. **(right)** Amplitude frequency characteristics plotted in linear scale.

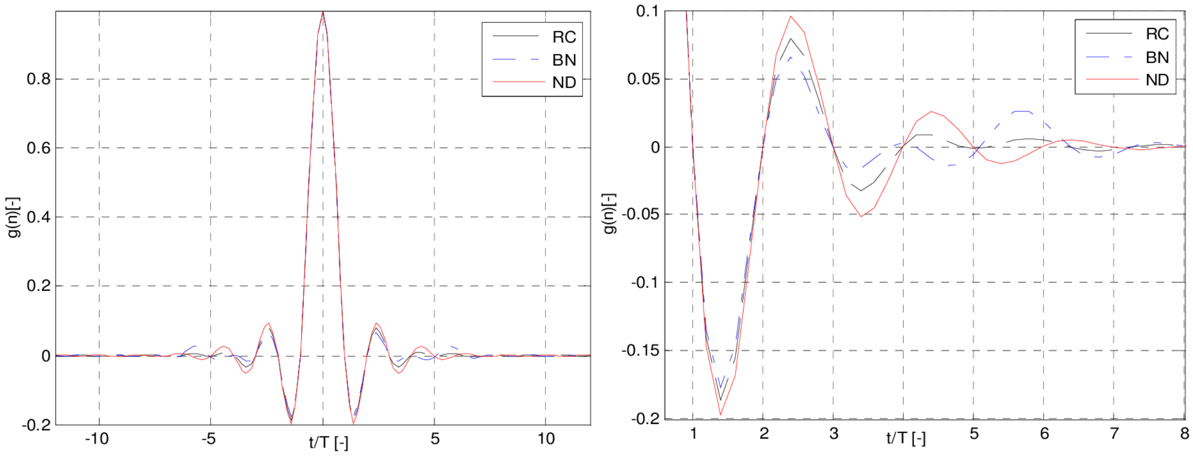

Figure 3.11: Normalized impulse responses of the cascade of transmitter and receiver RC filter (RC); B-filter (BN); Nyquist δ-filter (ND). α=0.284; G_D=2x6; N=5; N_O=2x60.

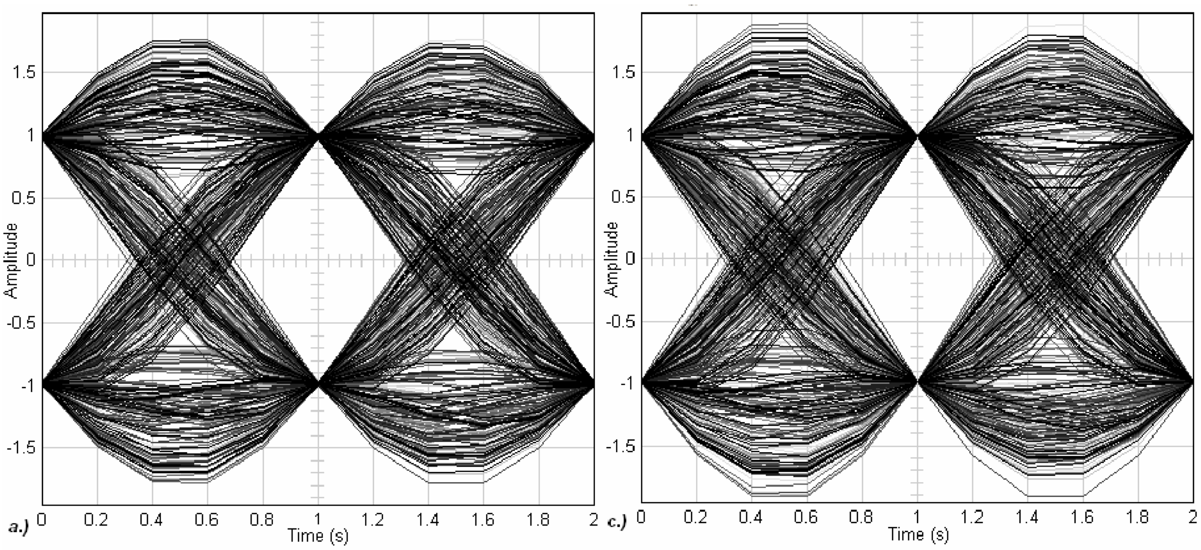

Figure 3.12: Eye diagrams of the transmitter and receiver cascade a.) RC filter; c.) Nyquist δ-filter, α=0.284; G_D=12; N=5; N_O=120.

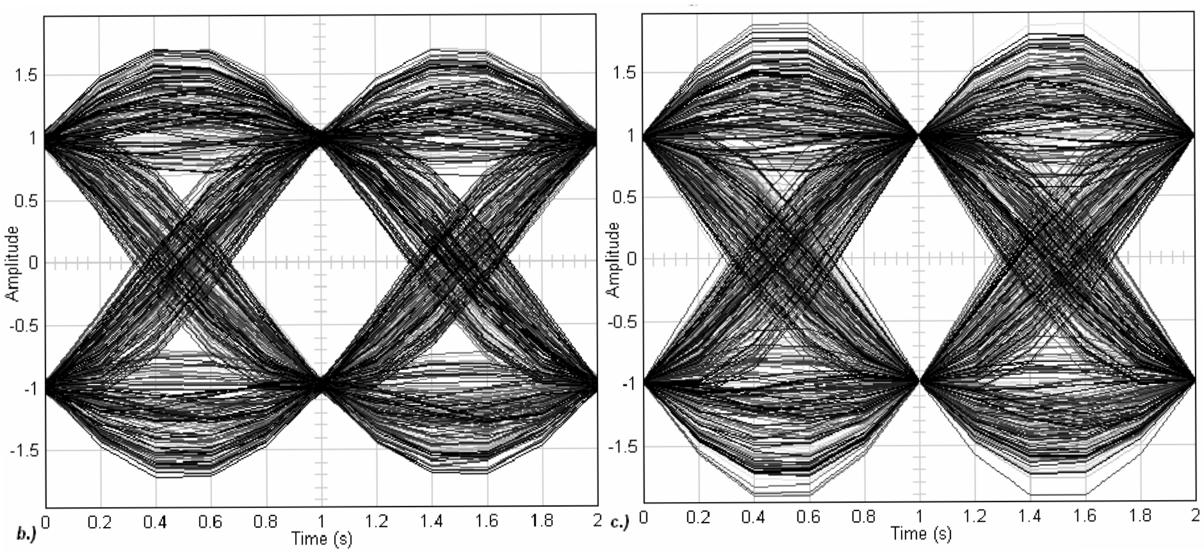

Figure 3.13: Eye diagrams of the transmitter and receiver cascade b.) B-filter; c.) Nyquist δ-filter, α=0.284; G_D=12; N=5; N_O=120.

3.4. ACI limited spectrum efficiency

If the limits of the receiver degradation parameters (Section 2.1) are not assumed for the moment, the main limitation that defines the narrowband LMR system spectrum efficiency (2.3) is the allowed level of the ACI. Therefore, the theoretical limits of the spectrum efficiency limited by the amount of ACI for the selected digital modulations are given in the following sections.

3.4.1. Pulse shape filtering and ACI of exponential modulations

Firstly, a digital transmitter simulation (based on block diagram shown in Figure 3.20) has been set to evaluate the trade-off between the equivalent excess bandwidth of the modulation signal, and the level of the residual ACI for the 4-CPFSK modulation with the chosen symbol rate of 12 kBaud, and with a modulation index of *1/M*. Other parameters of the simulation are as follows:

- The group delay parameter of the modulation filter (truncated version of the RRC filter) $G_D=6$.
- The over sampling factor $N=10$.
- The attenuation frequency characteristic of the ACI measurement filter follows the characteristic required by [1].
- The mean value of the ACP was calculated for 10^6 symbols of the transmitted signal.

The rather high value of the over sampling factor in this example is chosen intentionally, not to influence the results by an additional digital interpolation filters. The result of the analysis is plotted in Figure 3.14. It is important to note that the characteristic is not monotonous as one would expect and experiences a minimum at 20%. This phenomenon is caused by an increasing peak-to-average ratio of the modulation signal as it is shown in Section 3.4.2. Higher the peak level of the modulation signal tends to increase the peak frequency deviation which, in turn, widens the signal spectrum.

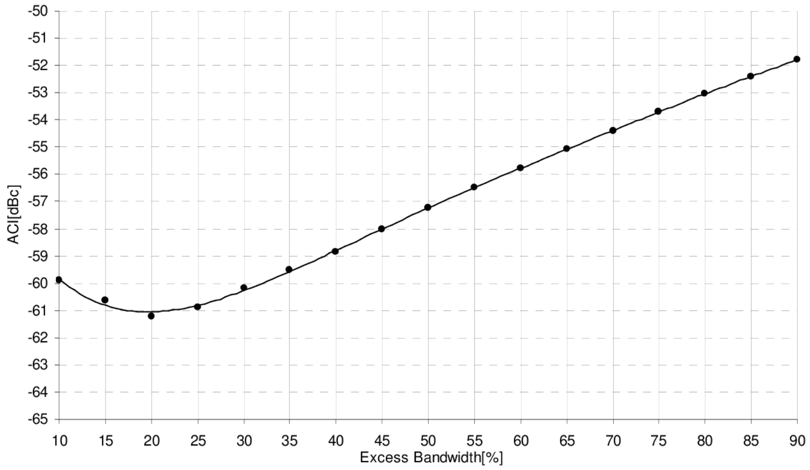

Figure 3.14: ACI as a function of the modulation filter excess bandwidth. The modulation index is set to *1/M*, symbol rate 12 kBaud

Therefore selecting a modulation filter with roll-off factor lower than 0.2 does not make sense since it does not bring the LMR system any advantage in return. As written in Chapter 3.3, for low values of the modulation filter roll-off factor the modulation signal is more vulnerable to timing jitter. For the studied example of the exponential modulation with

h=1/M, the excess bandwidth of the modulation filter between 20 to 30 % can therefore be considered a reasonable choice.

Secondly, a digital transmitter simulation has been set up to analyze the influence of the pulse shaping filters on ACI for a given modulation index (3.4) and over the adjusted symbol rate of the modulation signal (3.1). The pulse shaping filters studied in the previous section, namely the truncated versions of RRC filter and square root Nyquist δ-filter with an excess bandwidth of 28.4%, have been selected for comparison. Other parameters of the simulation were set as in the previous example.

Referring to Figure 3.15 it can be seen, that the stop-band attenuation of the filter has a significant influence on ACI level in the range, where ACI is better than -70 dBc. For higher symbol rates, the contribution of the filter with better out of band rejection is moderate, mainly due to the fact that both filters have the same equivalent excess bandwidth which determines also the bandwidth of the exponentially modulated signal. The examples of the 4-CPFSK modulated signal spectrums for the symbol rate of 12 kBaud, and both pulse shaping filters having the same excess bandwidth, are compared in Figure 3.16.

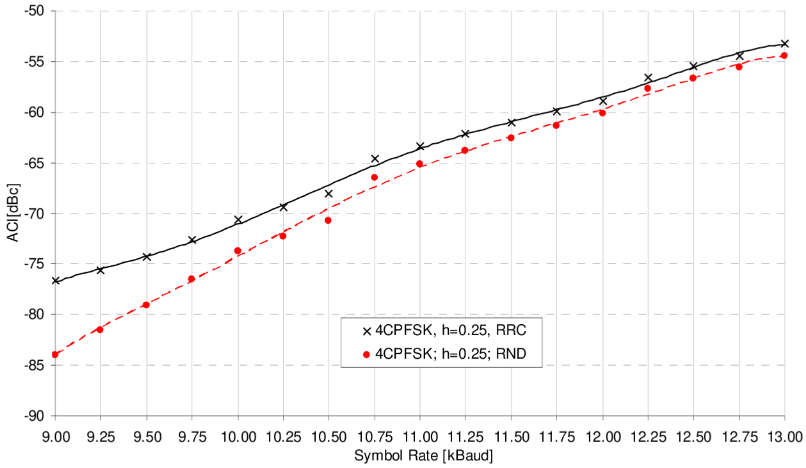

Figure 3.15: Adjacent channel power as a function of modulation rate for 4-CPFSK and two Nyquist filters with the same parameters ρ_{SB}=10.5 dB, ρ_{ISI}=7.5 dB, ρ_{SL}=-0.9 dB. The modulation index is set to 1/M.

In case the LMR system can tolerate higher level of ISI or incorporates the memory based symbol decoder, as is usually the case for the two state minimum shift keying MSK modulation, even more strict pulse shaping filters can be used. Any digital filter with a scalable cut off frequency can be an option; however, the *Gaussian modulation filtering* is typically selected, because it provides an exact definition of the cut-off frequency, while reaching exceptional stop-band attenuations. The continuous time impulse response of the Gaussian filter can be written as [50]

$$h_G(t)=\frac{\exp\left[\dfrac{-t^2}{2\dfrac{\ln(2)}{(2\pi BT)^2}}\right]}{\sqrt{2\pi}\,\dfrac{\sqrt{\ln(2)}}{2\pi BT}}, \qquad (3.39)$$

where *BT* is the main filter parameter called *BT product* used to trade-off the occupied signal bandwidth and the amount of ISI; *B* is the -3 dB filter bandwidth and *T* is an unfiltered symbol interval.

In Figure 3.17, there is a comparison of the ACP for the MSK modulation filtered either by the Nyquist δ-filters and the Gaussian filter with a *BT* factor of 0.3. This value of *BT* product is considered the lowest limit in this work, since lower values yields to troublesome symbol decoding at the receiver side and degrade, significantly, the power efficiency. It can be seen from Figure 3.4 that at the ACI level of -60 dBc the additional contribution to modulation rate cannot be expected higher than approximately 2%.

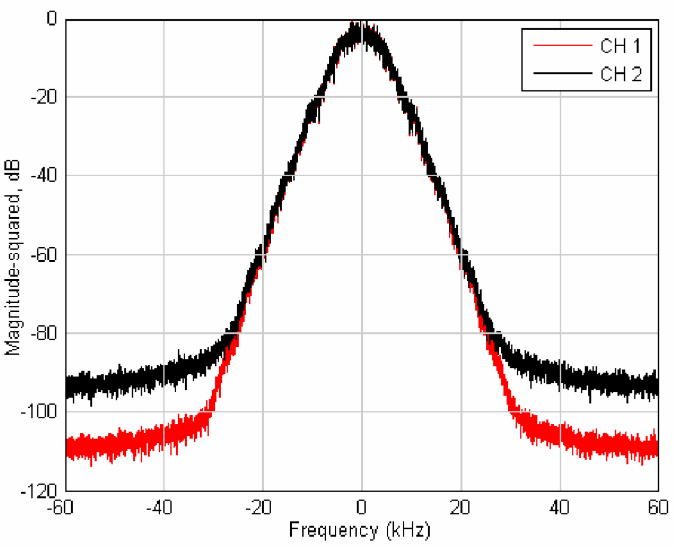

Figure 3.16: 4CPFSK modulated signal spectrum comparison. The modulation index is set to $1/M$, symbol rate to 12 kBaud. CH1: Square root Nyquist δ-filter α=0.284. CH2: RRC filter α=0.284.

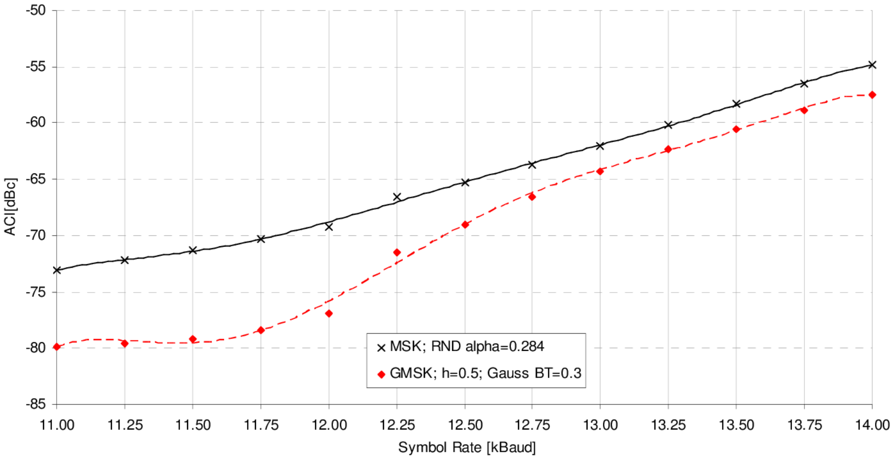

Figure 3.17: Adjacent channel power as function of symbol rate for different pulse shaping filters and MSK modulation.

3.4.2. Pulse shape filtering and ACI of linear modulations

Referring to the linear superposition model of the linearly modulated signal (3.8), it is evident that a pulse shaping filter with its impulse response representing the modulation pulse directly influences the LMR system parameters. Contrary to the ideally constant modulation envelope of the exponentially modulated signal where the ACI can be evaluated straightforwardly, the amplitude variations quantified by the PAPR parameter becomes a crucial issue. As it is shown in [14] any channel nonlinearity has, in general, three negative effects on linear modulation schemes with Nyquist filtering causing amplitude variations:

- The nonlinearity generates a self interference due to the in-band inter-modulation products. This phenomenon can be seen as an increase in ISI level.
- It gives rise to *amplitude-to-amplitude* (AM-AM) and *amplitude-to-phase* (AM-PM) non-linear conversion which needs to be equalized at the receiver side.
- It gives rise to spectral re-growth due to the inter-modulation products which would cause an increase in ACI.

It is therefore highly desirable to minimize the amplitude variations in linearly modulated signal. In Figure 3.17, there is a result of the system simulation for the selected modes of modulation, from which the dependency of the PAPR parameter over the signal excess bandwidth can be analyzed.

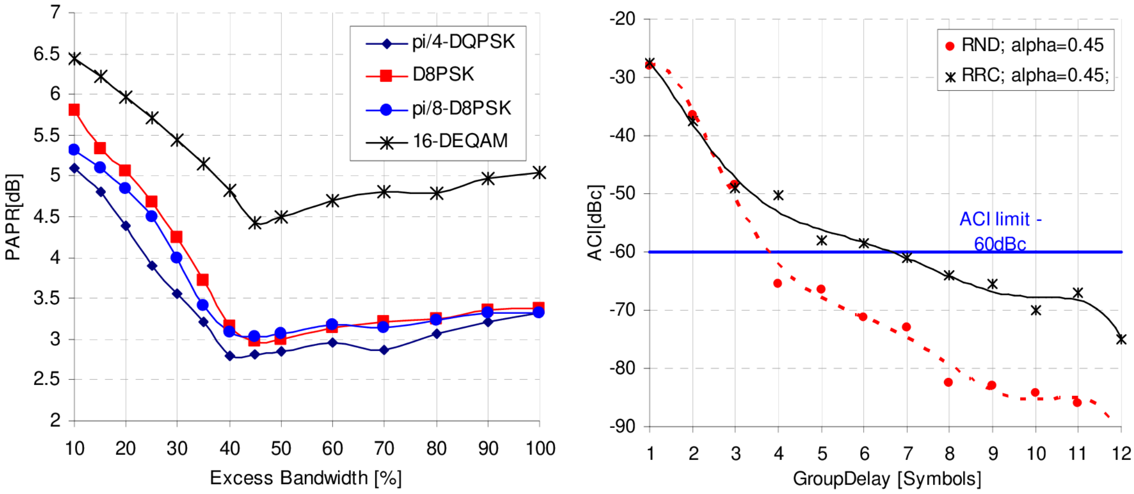

Figure 3.18: (Left) PAPR as a function of the pulse shaping filter excess bandwidth. **(Right)** ACI as a function of the group delay parameter of the transmitter pulse shaping filter. 16-DEQAM, 18 kBaud, ACI measured according to Section 2.1.3.

Compared to Figure 3.14, where the optimum laid around the excess bandwidth of 20%, it is clear that to minimize the amplitude variations the excess bandwidth of the transmitter pulse shaping filter shall be selected between 40 and 45%. Using these values, a Nyquist δ-filter according to Section 3.3 for various group delays of its impulse response can be designed. In Figure 3.18, there is also a comparison of the ACI simulation of the LMR system utilizing 16-DEQAM modulation with a symbol rate of 18 kBaud being shaped by the truncated version of the RRC filter and optimized square root Nyquist δ-filter. Both filters having the same equivalent first null bandwidth. From this comparison the advantages of the later one can be seen. Not only has it provided the digital model with better ACI suppression, but it does so with only the half group delay of the filter impulse response, which is the main contribution to signal propagation delay in the digital processing part. Another advantage becomes clear when comparing the shapes of the filter frequency responses as shown in Figure 3.19. In order to compare the proposed filter to the one recommended by the TETRA standard [12], (RRC filter with excess bandwidth of 35%) it has also been added to the plot.

The 99% occupied bandwidth of the signal spectrum shaped by the Nyquist δ-filter remains the same as for the square root RC filter (35%) which enables to use a high symbol rates of up to 18 kBaud, while the first null bandwidth encloses to the RRC filter having 45% of excess bandwidth. It positively influences the PAPR, which remains very close to the optimal values shown in Figure 3.18, contrary to the values corresponding to excess bandwidth of 35%. Another advantage, especially when higher order modulation techniques are consider can be seen in the reduction of ISI which is more than 4 dB (Table 3.4) in favor of the Nyquist δ-filter. The numerical comparison of the PAPR parameter for all the selected modulation techniques is given in Table 3.8.

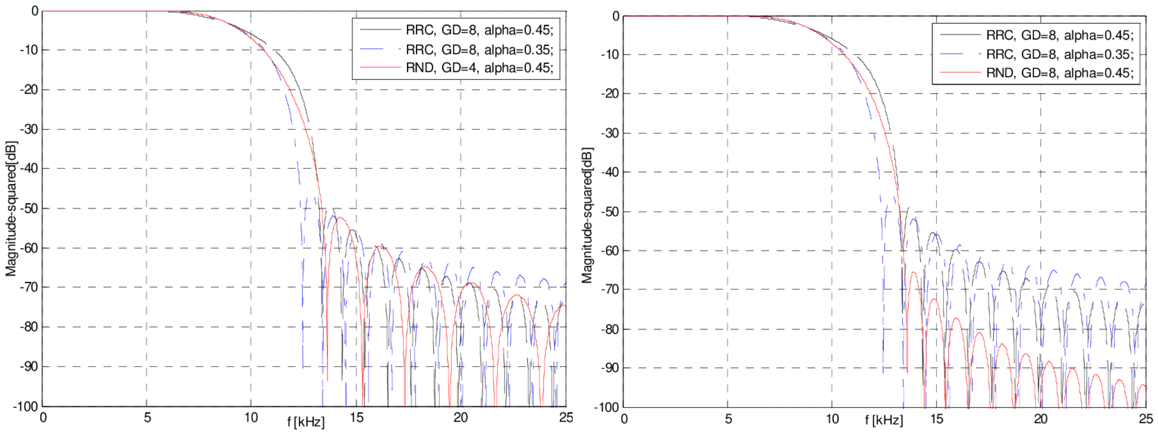

Figure 3.19: Normalized amplitude spectrums of the linearly modulated signal shaped by the analyzed pulse shaping filters. **(left)** Square root Nyquist δ-filter G_D=4. **(right)** Square root Nyquist δ-filter G_D=8.

Table 3.8: Numerical comparison of the adjacent channel interference and *PAPR* values for selected linear modulation techniques shaped by the studied filters.

		π/4-DQPSK	D8PSK	16-DEQAM
Filter	ACI	*PAPR*	*PAPR*	*PAPR*
[-]	[dBc]	[dB]	[dB]	[dB]
RND (G_D=4; 45%)	-66	2.9	3.3	4.5
RRC (G_D=8; 45%)	-65	2.8	3.1	4.5
RRC (G_D=8; 35%)	-62	3.2	3.7	4.6

3.5. SW defined modem for narrowband LMR transmitter

The conventional way of generating the M-CPFSK signal (3.5), (3.6) in an older generation of the LMR radio modems was based on an analog FM modulator – running directly at the carrier frequency – driven by the modulation signal generated by the digital signal processing unit [53]. The biggest advantage of such architecture can be seen mainly in its simplicity, while providing an exceptionally low level of spurious emissions in near (ACI) and also in far distance from the carrier frequency, limited mainly by the residual phase noise of the transmitter oscillator. The signal thus generated requires no post modulation filtering, which contributed to almost ideally constant modulation envelope. On the other hand, only the necessary amount of the digital signal processing tasks in form of modulation encoding and pulse shaping at the transmitter side makes the architecture oriented purely on exponential modulation techniques, with a minimum degree of flexibility in setting the modulation parameters. Another disadvantage, however, a minor one, is that the modulation index of the modulated signal is set in the analog part resulting in significant variance and aging.

In modern modems, architectures based on all-digital solutions generating the RF signal directly are preferred [54], [55]. This approach minimizes the amount of analog circuitry and maximizes the integration, flexibility and reproducibility of the design. By contrast, a direct adoption of such approach in narrowband LMR transmitter is not economically feasible. Besides the limited and decreasing dynamic range of *digital-to-analog converter* (DAC) over the increasing carrier frequency [27], [28], also the interpolation factors and the amount of the required digital signal processing resources reach impractical levels [13].

The superheterodyne structure, where only the IF modulated signal is provided digitally while the second stage is completely analog, represents the midpoint solution. For the narrowband radio systems it combines both of the disadvantages in form of relatively demanding digital part and a significant portion of analog circuitry comprising of the second mixing stage, with post modulation filtering.

The digital baseband complex modulator in combination with the analog structure of the homodyne transmitter as shown in Figure 3.20 represents a compromising solution for the next generation of the LMR transceivers. The encoded modulation symbols α_k are firstly interpolated to have R_1 times higher sample rate. After the proper pulse shape filtering and numerical integration (Figure 3.20, A), the modulation signal in case of exponentially modulation mode drives the numerically controlled complex oscillator generating the complex baseband replica of the modulated signal (Figure 3.20, B). Before the dual-DAC conversion, the digital baseband signal is, again, interpolated to reach sufficient sample rate of R_1R_2 times the modulation symbol rate $1/T$. In case of linear modulation modes, the encoded *complex* modulation symbols α_k are pulse shaped by the transmitter Nyquist filters and, after proper interpolation, they are fed in to the DAC converters. As a signal processing platform the *field programmable gate array* (FPGA) or *digital signal processor* (DSP) can be used. In this project the FPGA (*Cyclone III EP3C10F256I8, [95]; Cyclone II EP2C8T144I8*, *[29]*) circuit has been adopted.

Using this structure all the parameters of the digital modulations are set by the software defined part, while the analog part effectively converts the baseband signal representation to the desired RF frequency. The relative simplicity of the software modem part, and the flexibility of modulation parameters settings, are, on the other hand, traded-off for the demanding requirements of the *in-phase* (I) and *quadrature* (Q) signal chains matching. Any mismatching in amplitude, phase or DC offsets of I and Q signal paths are giving rise to modulation envelope variation and signal distortion – even in exponentially modulated signal – which is troublesome to compensate, either at the transmitter, or at the receiver side.

In linear modulation mode of operation, the high power amplifier linearization creates a separate and overwhelming chapter [92]. Although this topic had been studied and a proprietary solution based on [93] has been implemented in the prototyping architecture, the closer description of this area has been left out the scope of this thesis; mainly because the author has made no direct contribution to this area. However, there is a summary of the most important measurement results related to the thesis objective, in form of an overall transmitter power efficiency analysis provided in the following Chapter 3.6.

3.6. Transmitter power efficiency analysis

In this section, the measurement results concerning the overall narrowband transmitter power efficiency are presented. It is no ambition to provide exact power efficiency analysis of the particular high power amplifier with the selected linearization circuit proceeded. It is rather to give the example of the practically achievable overall transmitter power efficiencies – in accordance with Section 2.2 – and analyze influence of the selected digital modulation formats. It is also important to note that the amount of adjacent channel power has been measured using spectrum analyzer (Appendix A; I.1) rather than using measuring receiver [1]. This option has been chosen in order to document the measurement values also with the respective spectrum plots, as given in Appendix B.

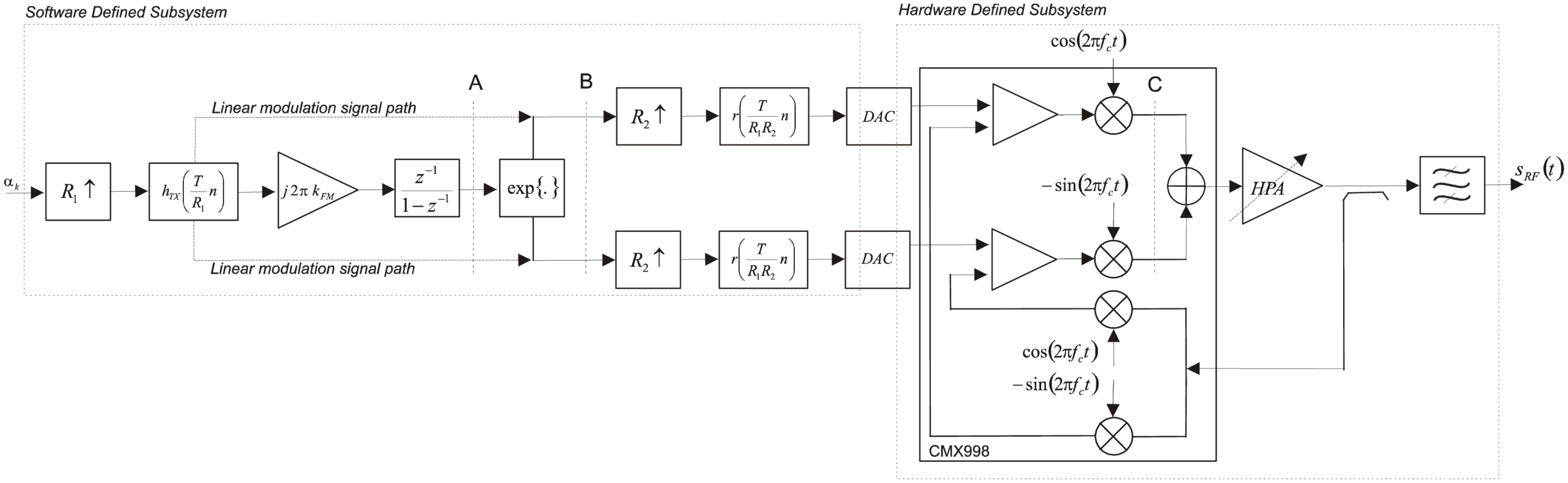

Figure 3.20: Simplified block diagram of the transmitter signal chain.

The measurement values given in Table 3.9 are results of the compromise among several transmitter parameters including maximum output power P_{out}, ACI level, operating mode of the high power amplifier and pre-amplifiers, parameters of the Cartesian feed-back loop [93], overall power consumption of the transmitter etc. Although the compromise has been set by heuristic approach of several trials-and-errors, the final values can be considered as near-balanced and can be taken as a benchmark describing the proposed narrowband transmitter (Figure 3.20) well.

It can be seen from measurement results, that the ACI limit can be maintained for all the selected modes of operation; however, there are two penalties in case of linear modulation schemes that have to be paid for higher spectrum efficiency. Firstly, it is the lower output power level achievable 35 dBm @ π/4-DQPSK, D8PSK and 33 dBm @ 16-DEQAM. Secondly, it is the lower value of the overall transmitter power efficiency (3.40) reached

$$\eta_{TX} = \frac{P_{OUT}}{P_{IN}} 100 \ [\%]. \qquad (3.40)$$

Comparing to exponential modes of operation the efficiency of linear operational modes has decreased to 14% and 10%. Despite this negative trend, the achieved values of output power exceeding 3W, and 2W, respectively, are promising and are considered practically applicable for next generation of narrowband LMR devices. Further improvements can be expected with the advanced PAPR reduction techniques [92] implemented in the software defined part of the transmitter.

Table 3.9: Measurement results of the overall transmitter power efficiency for studied modes of operation. (See Appendix B. for respective spectrum plots).

Modulation Format	**Symbol Rate**	**Mod. Parameter**	P_{out}	**ACI Lower**	**ACI Upper**	**Occupied Bandwidth @ 99.9%**	P_{IN} **(TX)**	η_{TX} **(TX)**	**Spectrum plot**
[-]	[kBaud]	[-]	[dBm]	[dBc]	[dBc]	[kHz]	[W]	[%]	[-]
2CPFSK	10.417	h=0.75, α=0.28	39	-60	-60	20.4	38.4	20.7	Figure B.1
	13.08	h=0.5, α=0.28	39	-60	-59	21.2	38.4	20.7	Figure B.2
4CPFSK	10.417	h=0.25, α=0.28	39	-60	-59	20.0	38.4	20.7	Figure B.3
	13.08	h=0.22, α=0.28	39	-60	-60	20.6	38.4	20.7	Figure B.4
π/4-DQPSK	17.361	α=0.45	35	-61	-60	22.5	22.8	13.9	Figure B.5
D8PSK	17.361	α=0.45	35	-61	-61	22.5	22.8	13.9	Figure B.6
16-DEQAM	17.361	α=0.45	33	-60	-61	22.5	20.4	9.8	Figure B.7
Measurement uncertainty ±2 dB									

3.7. Chapter summary

In this chapter, the analysis of the digital modulation techniques intended for the next generation of narrowband LMR transceivers was given. Using the signal model of the exponentially modulated signal, the current modulation techniques 2-CPFSK and 4-CPFSK were analyzed. Their biggest advantage in form of constant modulation envelope, together with a need for maintaining compatibility to older modem generations, makes their usage inevitable. As was shown in Section 3.1, the higher levels of admissible ACI in addition to proposed pulse shaping technique enable only 10% raise in spectrum efficiency from today's value of 0.87 bit/s/Hz (21.68 kbit/s @ 25 kHz) to a value of 0.96 bit/s/Hz (24 kbit/s @ 25kHz).

Although important, such increase in spectrum efficiency cannot compensate steadily rising demand for system capacity even in the narrowband PMR applications. Due to the limited radio spectrum available, future LMR devices should utilize bandwidth efficient linear digital modulation schemes similarly to the private personal radio standards like, TETRA etc. By the general properties analysis of the selected constellations of linear modulation techniques, the π/4-DQPSK, D8PSK and 16-DEQAM have been selected.

The special attention of this chapter was focused on the analysis and optimization of pulse shaping filters. As was summarized in Section 3.3, the conflicting requirements placed on the design of the digital matched Nyquist filter pair make the task complicated. From this point of view, the typical truncated RC filter represents a single balance between the time- and frequency-domain parameters. The Nyquist δ-filter set, which was defined throughout this chapter, enlarges the family of Nyquist filters, and when compared with the truncated RRC filter cascade, it strikes the balance towards the frequency domain parameters while reaching a low level of residual ISI. It does so at the cost of a higher side lobes level of the impulse response. An exact symbolic definition of the Nyquist δ-filter in the frequency domain gives the designer, scope to choose freely the arbitrary filter parameters, such as equivalent excess bandwidth, group delay and over-sampling parameter and derive coefficients for either the "normal" or the square root filter variants. The filters generated are of linear-phase having symmetrical impulse responses, which directly contribute to efficient hardware realization structures.

From the narrowband LMR design point of view, the proposed Nyquist δ-filter provides the digital modem with better ACI suppression with only a half group delay of the filter impulse response. This parameter determines the digital filter order, and, more importantly, it is the main contributor to the signal propagation delay in a digital signal processing part of the modem. The resultant occupied bandwidth of the linearly modulated signal gives a space to use high symbol rates of up to 18 kBaud while the shape of the main lobe positively affects the PAPR which remains very close to the optimum values simulated.

The software defined transmitter architecture which was described in the last section of this chapter thus represents a potential to rise a spectrum efficiency of the next generation of narrowband LMR systems to the value of 2.88 bit/s/Hz (72 kbit/s @ 25 kHz, 16-DEQAM) while reaching practically applicable output power levels exceeding 2W and maintaining the ACI level of -60 dBc.

4 Digital algorithms for frequency discrimination

4.1. Introduction

The history of the frequency modulated signal, and its processing, can be traced back to the beginning of the 20th century[5] and is closely related to the beginnings of radio broadcasting. However, the digital algorithms for discriminating the instantaneous frequency, as well as their wider practical utilization, was actual only in recent past [33], [34], [80]. From the more general digital signal processing point of view, the demodulation of the signal frequency needs to be classified as a nonlinear system or technique and, as such, the algorithms cannot be analyzed by the "traditional tools" in form of *Z*-transform, impulse response, frequency characteristics [51] etc. Thus, while it was "natural" for the analog circuits – typically consisting of the limiter-discriminator architecture – to demodulate the frequency modulated signal, it is an uneasy task for the digital signal processor to process the frequency discrimination and it is forced to use approximation techniques only. Besides their inherent power efficient characteristics, even the backward compatibility necessitates the modern digital radio devices not only to process the frequency modulated signal, but to process it with a performance approaching the one achieved by their analog counterparts. While the exponential modulations create a significant part of this thesis and are still major modulation techniques used by the narrowband LMR radios, this section is focused on a close description of the digital algorithms of the frequency discrimination. Two refinements to the techniques available in technical literature are presented which can improve the signal-to-noise ratio of the demodulated signal.

4.2. Signal model

Following the signal notations derived in Section 3.1, let us start with a description of the modulated signal seen by the receiver. If only the AWGN is assumed to be corrupting the ideal radio channel, the complex envelope of the received signal can be described as

$$r(t) = s(t-\tau)\exp\left(j2\pi\nu t + \theta\right) + w(t)\,, \qquad (4.1)$$

where ν, θ and τ are unknown values of the frequency offset, carrier phase and symbol timing epoch respectively. The term $s(t\text{-}\tau)$ represents the time delayed complex baseband replica of the exponentially modulated signal. The $w(t)$ is an AWGN noise modelled as a complex independent and identically distributed random signal with independent real and imaginary parts each having two-sided power spectral density $N_0/2$. Its probability density function can be written as [7]

$$p(x) = \frac{1}{\sqrt{2\pi\sigma}}\exp\left(-\frac{x^2}{2\sigma^2}\right), \qquad (4.2)$$

where σ^2 is the mean squared deviation, or variance. In (4.2), the zero mean value is assumed.

From all the operations performed by the receiver, filtering – either anti-aliasing or main selectivity one – and sampling of the received signal have the biggest impact on a digital system performance. Thus, first the complex envelope of received signal after filtering is

---

[5] It was Edwin Armstrong who makes use of frequency modulation to reduce disturbances in radio signaling [81] which is considered the beginning of the FM broadcasting.

$$x(t) = s_r(t-\tau_0)\exp(j2\pi\nu t+\theta)+\upsilon(t)\,, \tag{4.3}$$

where $s_r(t)$ is the transmitted signal shaped by all of the receiver filters and $\upsilon(t)$ is the band limited noise signal with the low pass noise bandwidth B_N. Thus the *SNR* of the studied signal with energy per symbol E_s and symbol rate R can be expressed as

$$SNR = \frac{E_S}{N_0}\left(\frac{R}{B_N}\right), \tag{4.4}$$

where

$$\frac{E_S}{N_0} = \frac{E_b}{N_0} + 10\log_{10}(k) \quad [dB]. \tag{4.5}$$

In (4.5) E_b is the signal energy per one bit of transmitted information and k is the number of information bits per one modulation symbol. In this section, the convention that the E_b/N_0 describes the signal-to-noise ratio in relation to the whole Nyquist zone is used. However, when calculating the *SNR* characteristic, the specific noise bandwidth is considered. The situation is depicted in Figure 4.1. In the later case, the noise bandwidth used to calculate the *SNR* will be explicitly given.

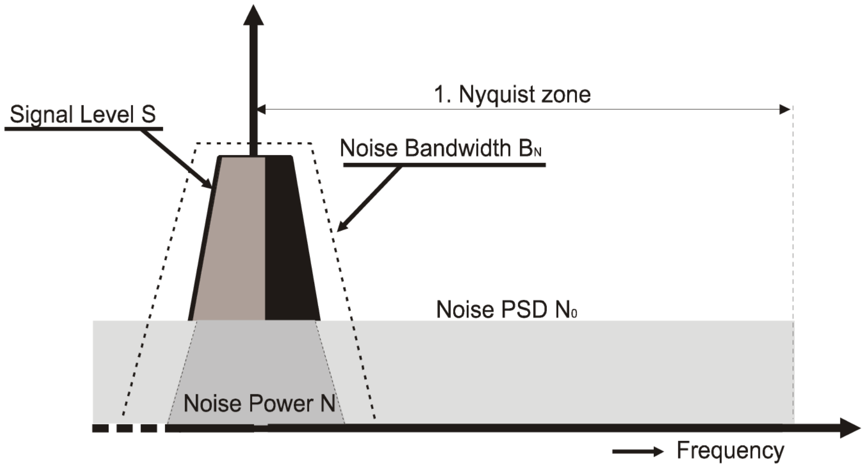

Figure 4.1: Graphical visualization of the signal-to-noise relations.

After the equidistant sampling process with sampling rate of $1/T_S$, the samples $x[i]$ of the $x(t)$ taken at $t=(kT+nT_s)$ are the one seen by the frequency discrimination algorithm

$$x[i] = A(kT+nT_s-\tau_0)\exp[j\psi(kT+nT_s-\tau_0;\alpha_k)]\exp[j2\pi\nu(kT+nT_s)+\theta]+\upsilon[i]$$
$$-\infty \le i \le \infty;\ -\infty \le k \le \infty;\ 0 \le n \le (N-1) \tag{4.6}$$

In (4.6) k is the modulation symbol index, i is the general sample index and n is the digital sample index within the specific interval; in this case it counts the samples within one modulation symbol.

To describe the frequency discrimination algorithms the time delay parameter τ, frequency offset ν and initial phase θ can be omitted without loss of generality. Also the sample indexing can be simplified to

$$i = (kT+nT_s), \tag{4.7}$$

because the algorithms work continuously and do not distinguish symbol intervals. Thus, the equation (4.6) can be rewritten into its reduced form as

$$x[i] = A[i]\exp(j\psi[i]) + v[i], \qquad -\infty \le i \le \infty \tag{4.8}$$

where $\psi[i]$ represents a sampled replica of the instantaneous signal phase defined by (3.3).

4.3. Algorithms for frequency discrimination

In this section, the algorithms for frequency discrimination used to demodulate the M-CPFSK signals are formulated and analyzed. The base principles and naming convention of the algorithms has been adopted from [34] which is a well written reference concerning the audio applications and the main processing engine is a general digital signal processor. The adoption of these techniques and discussion about their implementation in modern FPGA circuits can be found in [33]. The main focus of this section is to discuss the utilization of the algorithms from the narrowband LMR design point of view and to propose modifications that would yield a better performance of the overall system. The evaluation criteria are the output signal-to-noise ratio and the implementation complexity. The simplified block diagram of the digital down-conversion with the frequency discriminator emplaced is shown in Figure 4.2. There are also *SNR* ratios assigned in different position within the down-converter to simplify referencing of the simulated results presented in following chapters.

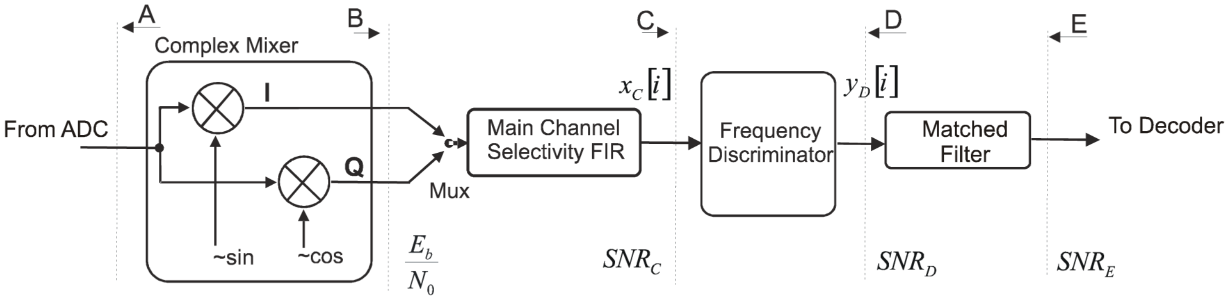

Figure 4.2: Placing the frequency discriminator into software defined digital down-conversion block. Simplified block diagram.

The 4-CPFSK with h=0.25 as the modulation technique and 12 kBaud as the symbol rate has been used as a reference. The input signal with a normalized signal-to-noise ratio in form of E_b/N_0 has been band limited by a digital *main channel selectivity FIR* filter with a low pass characteristic having 3 dB attenuation above the 0.75R frequency offset (~10.85 kHz). Its frequency characteristic is depicted in Figure 4.3.

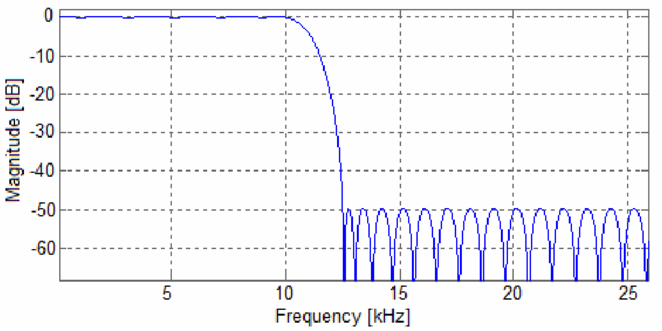

Figure 4.3: Amplitude frequency characteristic of the main channel selectivity filter used to evaluate the frequency discrimination algorithms.

As the pulse shaping filter at the transmitter side and as the *matched filter* at the receiver side the square root Nyquist δ-filter (RND) with an equivalent excess bandwidth of 28.4% has been selected.

4.3.1. Digital frequency discriminator – complex baseband delay model

To describe the frequency modulated signal in baseband (Figure 4.2, C) it is useful to follow a vector notation shown in Figure 4.4. The frequency modulated signal can be seen as a vector rotating either left or right depending whether the instantaneous frequency has been higher or lower than the carrier frequency.

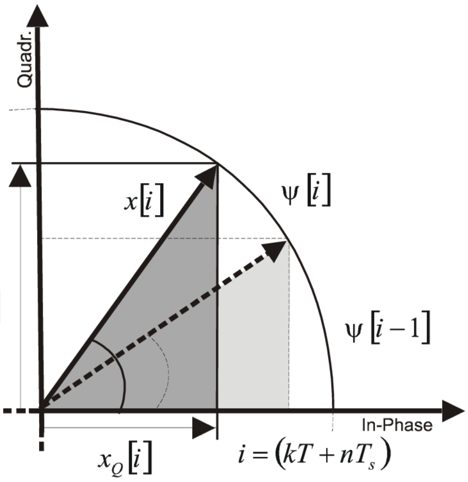

Figure 4.4: Vector representation of the received M-CPFSK signal.

The position of the vector in particular time instant $i=(kT+nT_S)$ is uniquely defined by the instantaneous signal phase $\psi[i]$. However, when the information about the frequency is needed, it is not the instantaneous phase itself, but the instantaneous angular velocity, the required information. Thus, we differentiate the instantaneous phase by discrete time approximation of the derivation – inverse operation to the integration shown in (3.2) and (3.6)

$$\frac{d\psi(t)}{dt} \approx \frac{\psi[i]-\psi[i-1]}{T_s([i]-[i-1])}+\varepsilon[i], \qquad (4.9)$$

where $\varepsilon[i]$ can be seen as the amplitude imperfection caused by the approximation. As it is shown later in this section, if N is chosen sufficiently high *e.g.* 8, the imperfection caused by the approximation has a negligible impact on a system performance.

Referring to (4.6) and (3.5) we can rewrite (4.8) into equation (4.10) that represent the base formula for the digital frequency demodulator and is also suitable for the digital implementation

$$y[i]=\frac{N}{\pi h}\arg\left(x[i]x^{*}[i-1]\right). \qquad (4.10)$$

In (4.10), symbol * assigns the complex conjugate.

The block diagram of the algorithm can be seen in Figure 4.5 – in the following text it is referred to as *complex baseband delay demodulator*, in order to distinguish between the various discrimination architectures.

In reference [34], a similar model of this discriminator is called *baseband delay demodulator*. However, the algorithm has been reduced to its real value architecture and while this modification helps to reduce the algorithm complexity, the output of the algorithm becomes dependent of the input signal amplitude, which is considered a significant disadvantage in the present work. Therefore, in the following, the complex value variant is being analyzed.

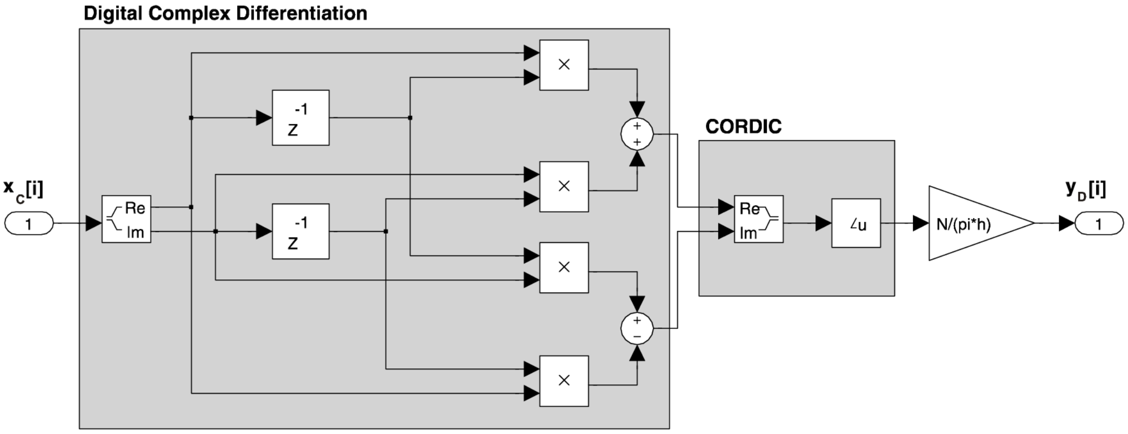

Figure 4.5: Simulation model of the complex baseband delay frequency discriminator used to demodulate M-CPFSK signal. (Floating point model, Matlab Simulink)

It can be readily seen that the demodulator composes of the complex multiplier and of the block that calculates the argument of the new vector. For this purpose the *coordinate rotation digital computer* (CORDIC) is typically selected for implementation. Although the CORDIC algorithm has been studied and implemented into the algorithm simulations as well as into the FPGA design of the demodulator [9], its closer description is not included in this thesis. However, one can find more information about the CORDIC algorithm in references [82] and [83].

If (4.8) is substituted into (4.10), as shown in (4.11), we can write equation (4.12) from which it is obvious that only the first term represents the demodulated signal, while the second term is a noise signal transformed through the demodulation process. It is difficult to describe rigorously, the noise contribution hidden in (4.12). However, as far as it is an additional component to the desired signal, it is possible to run a simulation and calculate the *SNR* before and after the frequency discrimination process. The result of such a simulation is presented in the following section.

$$y[i] = \frac{N}{\pi h}\arg\{(A[i]\exp(j\psi[i]) + \upsilon[i])(A[i-1]\exp(-j\psi[i-1]) + \upsilon^{*}[i-1])\} \qquad (4.11)$$

$$\begin{aligned} y[i] &= \frac{N}{\pi h}(\psi[i] - \psi[i-1]) \\ &+ \frac{N}{\pi h}\arg\{(A[i]\exp(j\psi[i])\upsilon^{*}[i-1]) + (A[i-1]\exp(-j\psi[i-1])\upsilon[i]) + \upsilon[i]\upsilon^{*}[i-1]\} \end{aligned} \qquad (4.12)$$

4.3.2. Simulation results

Since the algorithm is based on a discrete time approximation of derivation operation (4.9), the analysis of the approximation imperfection versus the number of signal samples used per one modulation symbol is covered first. For this purpose, the maximum approximation error has been calculated according to (4.13) where $x[i]$ represents a general input signal while the $y[i]$ represents the output of the differentiation process described by (4.9)

$$\max\left(\varepsilon[i]\right)=\frac{\max\left|x[i]-y[i]\right|}{\max\left|x[i]\right|}\,. \qquad (4.13)$$

As shown in Figure 4.6, for $N \geq 8$ the maximum approximation error $max(\varepsilon[i])$ defined by (4.13) drops down to one percent of the signal amplitude which can be considered acceptable. It is worth stressing, at this point, that by increasing the number of samples per modulation symbol, the performance of most digital algorithms – e.g. synchronization algorithms etc. – is enhanced, but the cost is an implementation complexity and an increase in computational burden. Therefore, in the following simulation N=10 samples per symbol have been selected.

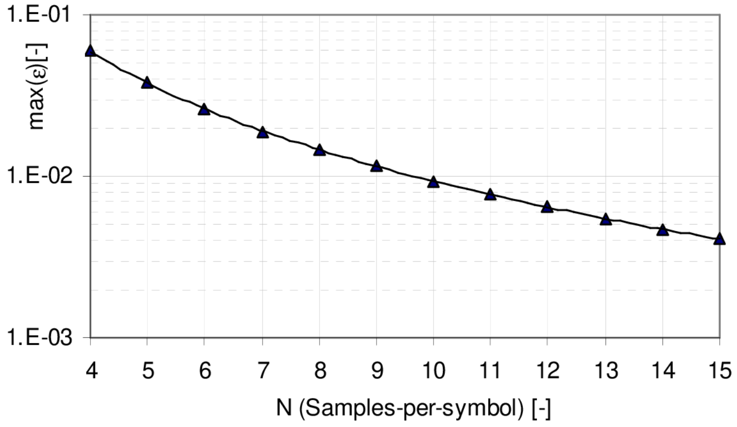

Figure 4.6: Maximum differentiation imperfection $max(\varepsilon[n])$ versus the number of samples per symbol.

Although in the above formulation of the frequency discrimination (4.10) the noise contribution has been omitted, it is the noisy signal that transforms through the nonlinear operation of frequency discrimination. Therefore, a second simulation has been run to study the signal-to-noise ratios before and after the frequency discrimination block. The results are depicted in Figure 4.7.

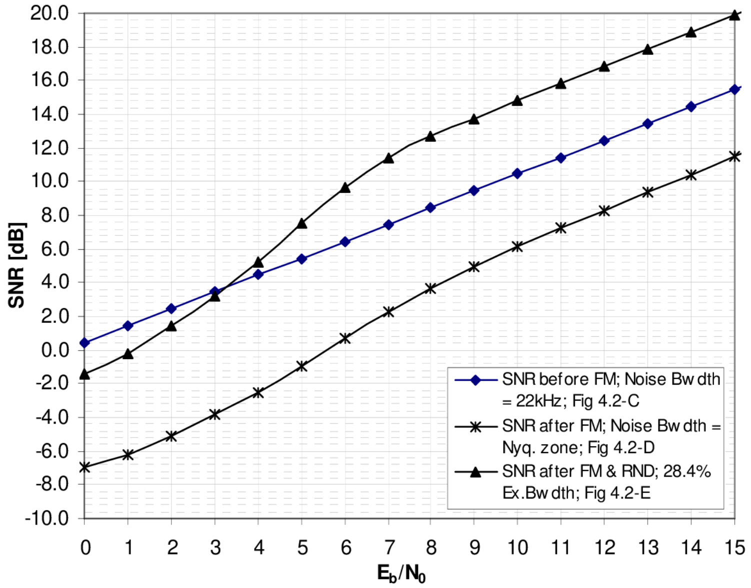

Figure 4.7: The results of the SNR analysis in respective points of the digital receiver chain.

There are three different characteristics shown in Figure 4.7 representing the signal-to-noise ratios in respective points of the digital receiver chain. The reference SNR value is taken at the input to the frequency discriminator Figure 4.2-C and it is assigned as *SNR before FM; Noise Bwdth*=22 *kHz*. This value depends linearly on the E_b/N_0 setting, as well as on the processed bandwidth – in this case it equals approximately 22 kHz (Figure 4.3). After the frequency discrimination the *SNR* depends non-linearly on the above mentioned factors and lowers down for more than 4 dB in average. If the receiver's square root Nyquist filter is selected to reduce the noise bandwidth to optimum level, the *SNR – SNR after FM & RND;* 28.4% *Ex. Bwdth* – overcomes the input value for 4 dB within the region where E_b/N_0 is higher than 7 dB. Below 10 dB the non-linear dependency remains and is clearly visible.
It is important to add that this "gain" is higher than the one given by the simple reduction of the processed bandwidth before and after the frequency discrimination (4.14)

$$G_N = 10\log\left(\frac{B_N}{R(1+\alpha)}\right) \cong 10\log\left(\frac{22\,kHz}{12(1+0.284)kHz}\right) = 1.55\,dB\,. \quad (4.14)$$

For the narrowband LMR systems, the area where the E_b/N_0 is below 5 dB is also of much interest, because it is the exact area of maximum usable data sensitivity (Section 2.1) and where the LMR is forced to operate while degradation parameters are measured. Thus, any frequency discriminator performing better in this region would be preferable option for the narrowband system. As it is shown in the next sections, various algorithms of the frequency discriminations reaches different performance exactly at this particular area, and simple modifications to their architectures exist and improve it.

4.4. Digital phase locked loop model

It is not the purpose of this section to describe the principle of the *phase locked loop algorithm* in detail while this section and the overwhelming descriptions of the *digital phase locked loop* (DPLL) can be found in many references such as [54], [34], [59] etc. It is an evaluation and confrontation of its performance to the other algorithms when used as a main frequency discriminator for the M-CPFSK modulation. A simple modification to the base algorithm is also presented which can help to improve the *SNR* in an interval studied and can be useful also in other application of the DPLL such as carrier recovery, symbol timing recovery etc.

The base DPLL equation modified for the purpose of frequency discrimination can be written as

$$y[i] = \Im\left\{(A[i]\exp(j\psi[i]) + \upsilon[i])\left[\exp\left(-j\pi hR\sum_{n=0}^{i-1} y[n]\right)\right]\right\} \otimes h_{PLL}\,, \quad (4.15)$$

where symbol $\otimes$ assigns the operation of discrete convolution between the output signal of the phase detector $y_{PD}[i\text{-}1]$ and the impulse response of the loop filter h_{PLL}

$$y[i] = \sum_{n=0}^{N-1} y_{PD}[i-n-1]h_{PLL}[n]\,, \quad (4.16)$$

and where N is an order of the loop filter. By closer analysis of the (4.15) it can be seen that the PLL is a feedback system, and, as such, its stability is influenced by the loop filter. In the simplest case the loop filter can be reduced to a single constant. Additional filtering can be done externally as it is shown in Figure 4.2. In this case the (4.15) simplifies into

$$y[i] = \Im\left\{ \left(A[i]\exp\left(j\psi[i]\right) + \upsilon[i]\right) \left[\exp\left(-j\pi hR\sum_{n=0}^{i-1} y[n] \right) \right] \right\} G_{PLL} . \qquad (4.17)$$

Another point of importance is that the output of the DPLL is actually a filtered version of the imaginary part – assigned as $\Im$ – of the phase detector output, and, as such, its absolute value depends on input signal amplitude $A[i]$. This, however, is a problem, since the input signal amplitude varies, either because of the large scale fading, or due to the main channel selectivity filtering, which introduces modulation amplitude variations. The normalization of the signal amplitude can easy this problem, but increases the implementation complexity significantly.

The amplitude signal normalizer follows the equation

$$y[i] = \frac{x_I[i] + jx_Q[i]}{\sqrt{\left(x_I[i]\right)^2 + \left(x_Q[i]\right)^2}} , \qquad (4.18)$$

where in (4.18) the $y[i]$ and $x[i\text{-}1]$ represent a general output and input complex signals respectively.

In fact, placing the signal amplitude normalization in front of the frequency discriminator is nothing exceptional in a world of frequency demodulation and it is used in analog limiter-discriminator architectures widely. What needs to be noted is that the limiter or normalizer of the signal amplitude does have an influence on an output *SNR* exactly in the studied region of E_b/N_0.

The simulation model of the DPLL frequency discriminator that can be directly implemented in an FPGA circuit is shown in Figure 4.8.

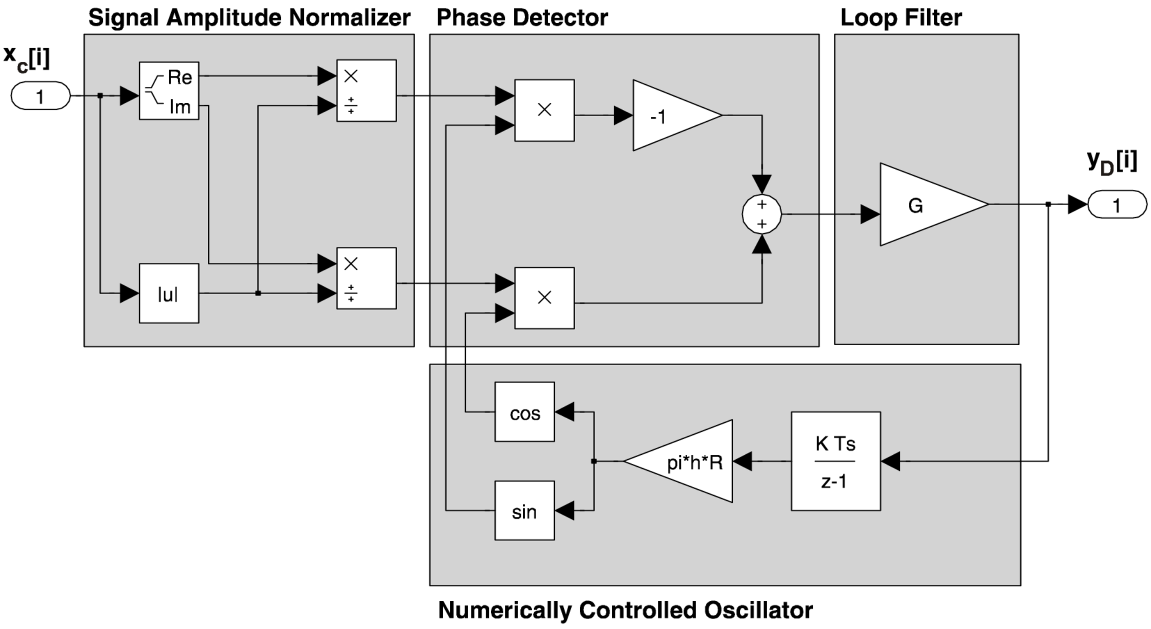

Figure 4.8: Simulation model of the digital phase locked loop frequency discriminator with the signal amplitude normalizer used to demodulate M-CPFSK signal. (Floating point model, Matlab Simulink).

4.4.1. Modification of the algorithm

The modification of the base model of the DPLL, as shown in Figure 4.8, is a result of an assumption that the signal amplitude in a particular time interval should be constant. If this assumption is true and the normalizer does not need to compensate for small scale amplitude variations, an averaging filter can be used to reduce the noise variance presented in the signal amplitude. The moving average filter defined according to (4.19) is a suitable solution for the continuous mode operation; however, any low order FIR filter can also be used

$$y[i] = \frac{1}{N}\sum_{n=0}^{N} x[i-n] - x[i-n-N], \qquad (4.19)$$

where in (4.19) the $y[i]$ and $x[i\text{-}1]$ represent a general output and input real value signals respectively and N is a length of the averaging interval. It is interesting that while the analog limiter circuit cannot distinguish the signal amplitude from the signal itself, its digital counterpart can and this additional information can be used to improve overall performance of the frequency discrimination task. The simulation model of the modified algorithm is shown in Figure 4.9.

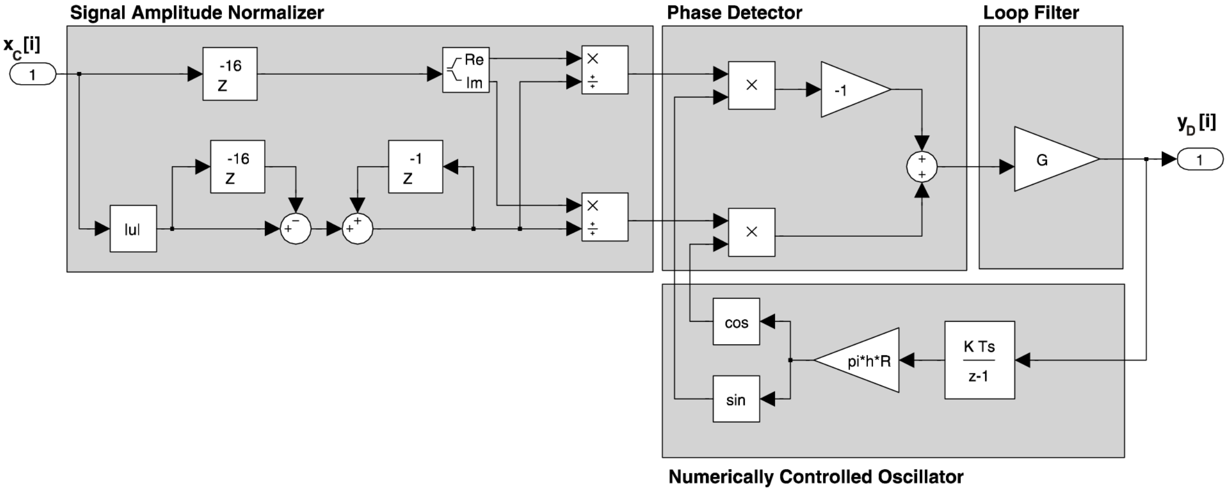

Figure 4.9: Simulation model of the digital phase locked loop frequency discriminator with the modified signal amplitude normalizer used to demodulate M-CPFSK signal. (Floating point model, Matlab Simulink).

4.4.2. Simulation results

In this section, the results of the DPLL performance simulation are presented. All the settings of the simulation are the same as given in Section 4.3. In the first sets of results shown in Figure 4.10, there is a comparison between the DPLL performance with, and without, the normalizer block. As can be seen, in the area where E_b/N_0 is below 5 dB, the algorithm with the normalizer connected performs almost 2 dB worst. Although the normalizer enables the algorithm to work within the wide dynamic range of the input signal amplitude, the 2 dB penalty in *SNR*, is a problem that would yield to lower maximum data sensitivity of the narrowband LMR modem.

The second set of results documents the influence of the averaging filter on an overall *SNR* of the frequency discriminator. Even for the averaging filter processing N=8 signal samples, the *SNR* gain of the frequency discriminator in a required area encloses to the one reached by the base DPLL. It needs to be added that besides the slight increase in algorithm complexity, the averaging filter placed in the signal amplitude normalizer also lengthens a propagation delay of the algorithm therefore its length cannot be increased arbitrarily.

By comparing the respective characteristics (Figure 4.11) of the complex baseband model (Figure 4.7) and model of the DPLL with a modified signal amplitude normalizer

(Figure 4.9), it can also be concluded that the later model performs 2 dB better. The final comparison of all the studied algorithms can be found in Figure 4.14.

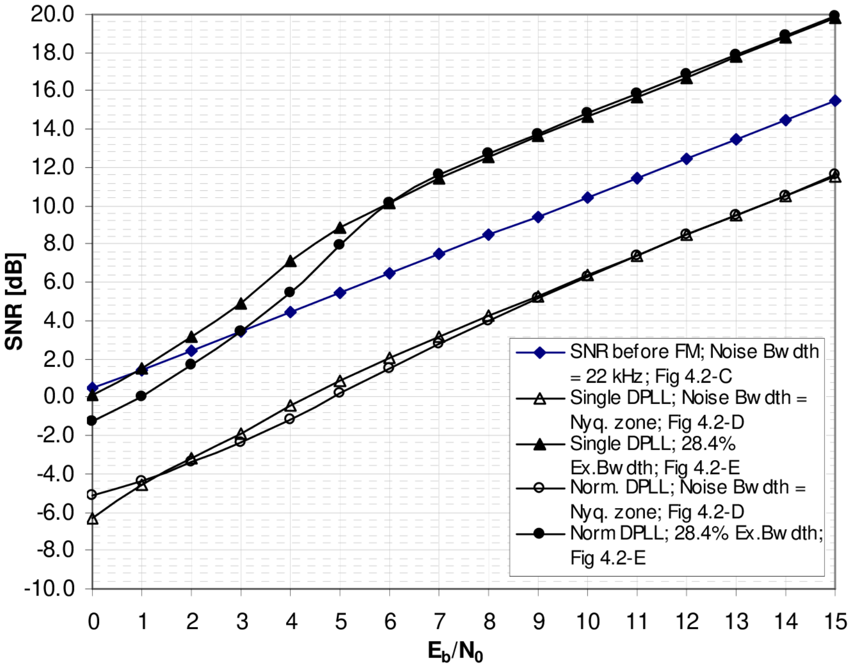

Figure 4.10: Results of the *SNR* analysis in respective points of the digital receiver utilizing the DPLL as a frequency discriminator. The characteristics assigned as *Single DPLL* were simulated for the DPLL without a signal amplitude normalizer.

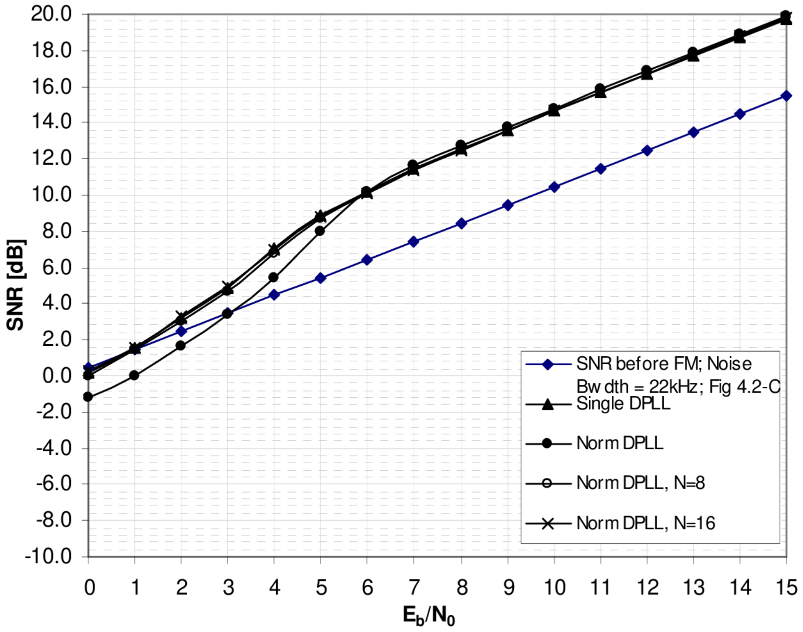

Figure 4.11: Comparison of the *SNR* performance for the DPLL with the base signal amplitude normalizer and modified normalizers utilizing the averaging filter of *N*=8 and *N*=16 signal samples.

4.5. Digital frequency discriminator – mathematic model

In the above Section 4.3, the frequency discrimination method was based on the discrete differentiation with subsequent calculation of signal phase by evaluating the arc-tangent function. The complicated evaluation of the arc-tangent has been a motivation for formulation new algorithms. The digital method described in this section is based on mathematic formulation of the derivation of the arc-tangent function. As is shown in this section, this procedure can be simplified and creates an effective algorithm for frequency discrimination.

Recalling the vector notations shown in Figure 4.4 for the time instant having a simplified notation $[i]$, the instantaneous phase of the received signal (4.6) can be calculated as

$$arctg\left\{\frac{x_Q[i]}{x_I[i]}\right\} = \psi([i-\tau_0];\alpha_k) + 2\pi\nu[i] + \theta. \tag{4.20}$$

In equation (4.20), only the argument of the function describing the received signal is calculated and for the moment, the noise contribution has been ignored altogether. The instantaneous phase should contain all the information about the parameters ν, θ and τ, but again, it can be assumed that the initial phase θ is zero, frequency offset ν is negligible and there is no need to care about the timing offset at this stage of the digital receiver.

We differentiate the instantaneous phase by discrete time approximation of the derivation (4.9) and by using the term for derivation of the *arctg*[*f*(*t*)] of the composite function we can rewrite (4.21)

$$arctg\left\{\frac{x_Q[i]}{x_I[i]}\right\}' = \frac{1}{1+\left(\frac{x_Q[i]}{x_I[i]}\right)^2}\left(\frac{x_Q[i]}{x_I[i]}\right)' \approx \frac{x_I[i-1]x_Q[i] - x_I[i]x_Q[i-1]}{T_S\left[(x_I[i])^2 + (x_Q[i])^2\right]}, \tag{4.21}$$

into (4.22)

$$y[i] = \frac{x_I[i-1]x_Q[i] - x_I[i]x_Q[i-1]}{\frac{\pi h}{N}\left[(x_I[i])^2 + (x_Q[i])^2\right]}, \tag{4.22}$$

which can be used for the instantaneous frequency discrimination [9].

Respecting the constant magnitude character of the M-CPFSK modulated signal, it can be noticed that the whole denominator of the equation (4.22) should be a constant. Although it is true for the transmitted signal – if no additional filtering is performed by the transmitter – the received signal has a significant magnitude variance caused mostly by the main channel selectivity receive filter. This amplitude variance cannot be omitted if the equation (4.22) is used for the frequency demodulation in a digital M-CPFSK baseband receiver. Moreover, it can be seen as the signal amplitude normalizer similarly to the one described in Section 4.4. The main difference is that it is not the absolute value of the vector, but its square power. This fact excludes the possibility to use an averaging filter to potentially improve the performance of such frequency discriminator. In fact, while analyzing its characteristics through the LMR system simulation it was realized that the demodulator performs significantly better if the normalizer uses a square power of the geometric average (4.23)

$$y[i] = \frac{x_I[i-1]x_Q[i] - x_I[i]x_Q[i-1]}{\frac{\pi h}{N}\left(x_I[i]x_I[i-1] + x_Q[i]x_Q[i-1]\right)}, \qquad (4.23)$$

calculated from the two consecutive samples entering the differentiation process rather than a square power of a single sample, as comes from the mathematic formulation (4.22). This discrepancy is a result of an approximation imperfection caused by sampling the input signal in time with a finite sampling frequency. By increasing the sampling frequency or the number of samples per modulation symbol, the approximation approaches its theoretical counterpart.

The simulation model of the modified mathematic frequency discriminator is shown in Figure 4.12. With an exception of the divider it consist of typical HW elements that can be found in modern FPGA circuits, and creates an effective realization structure. From the LMR design point of view also the implementation of the divider can be written effectively by iteration algorithms. It needs to be added however, that as any other division, the algorithms based on (4.22) and (4.23) needs to prevent the situations where the denominator drops to a very low value at very low E_b/N_0 levels. Although this situation is not a critical issue in fixed point digital architectures with inherent bus saturation, the saturation block has been added to the algorithm model in order to complete the description.

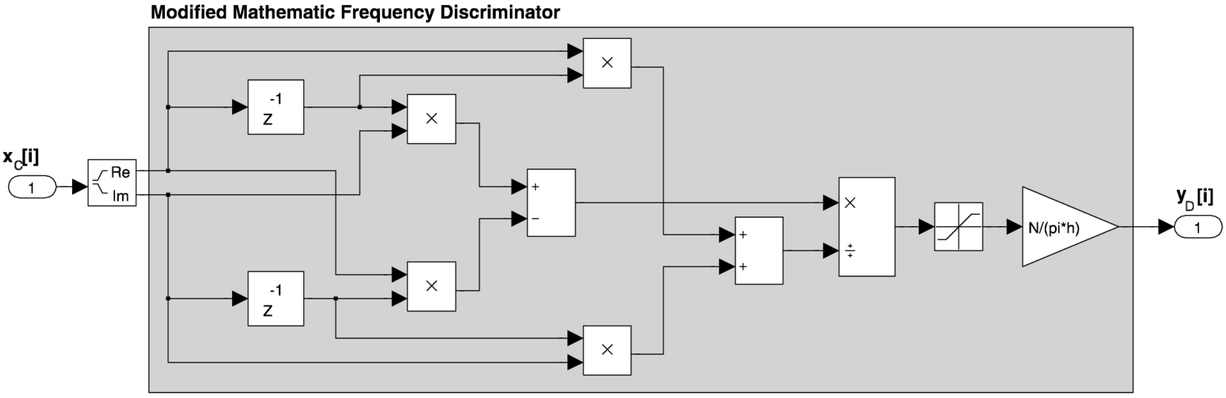

Figure 4.12: Simulation model of the modified mathematic frequency discriminator that can be used to demodulate M-CPFSK signal. (Floating point model, Matlab Simulink).

4.5.1. Simulation results

In this section, the results of the algorithm simulation are presented. All the parameters of the simulation have been set as described in Section 4.3. In the first sets of results presented in Figure 4.13, there is a comparison of the output *SNR* performance for the two algorithms of the mathematic frequency discriminators as given by (4.22) and its modified version by (4.23). The improvement of the SNR in an area where E_b/N_0 is less than 10 dB is obvious. At the particular level, where $E_b/N_0=5$ *dB* the difference reaches the 2 dB wanted. While the proposed modification does not require additional hardware resources, it can be easily judged a better choice when implementing digital frequency discrimination.

Finally, all the algorithms in their modified variants that reach the best *SNR* performance from their family are compared in Figure 4.14. In particular it is the *complex baseband delay model; Normalized DPLL with averaging filter (N=16)* and *modified mathematic* frequency discriminators. It is the modified DPLL version that reaches the best results, however it has the most demanding realization structure in form of combined feedback and feed-forward architecture. The second is the mathematic modified frequency discriminator having an SNR penalty of 0.5dB but since it can be implemented by an effective feed-forward algorithm it can be a preferable alternative.

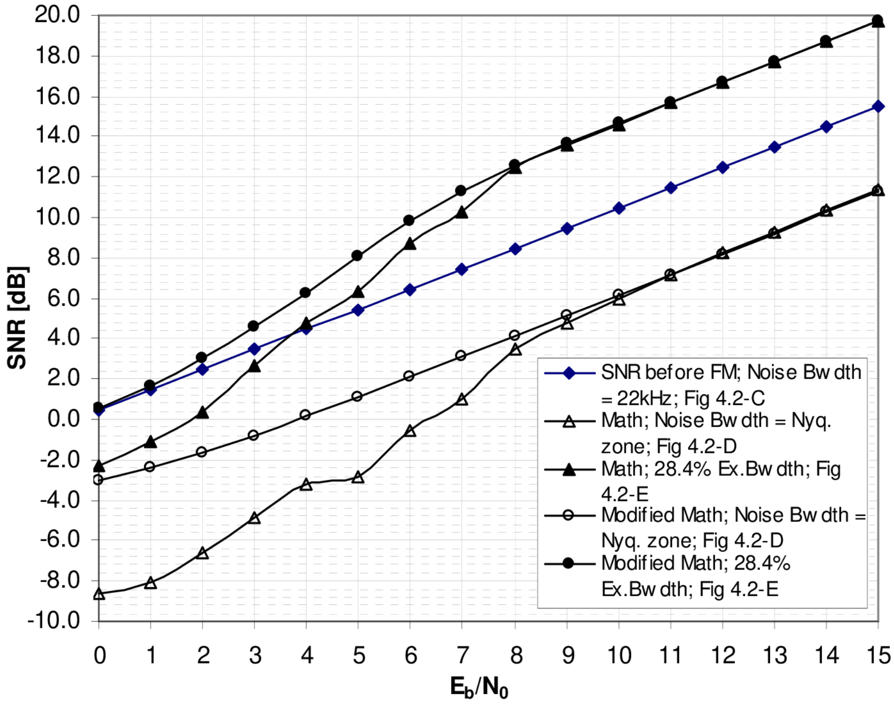

Figure 4.13: Results of the *SNR* analysis in respective points of the digital receiver utilizing the base mathematic (4.22) and modified mathematic (4.23) frequency discriminator.

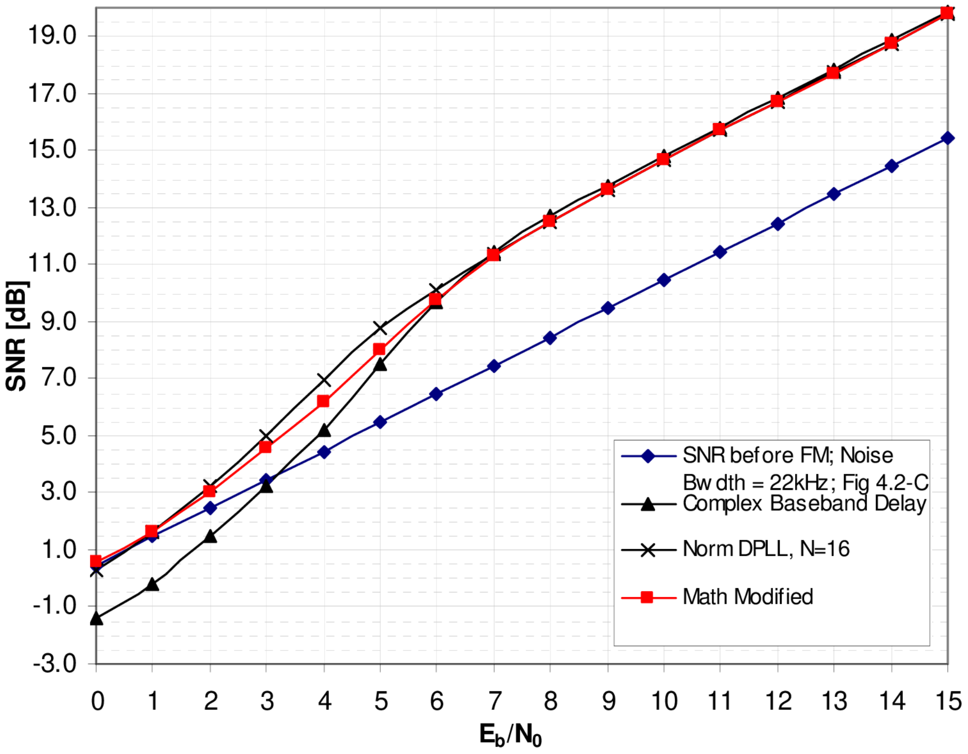

Figure 4.14: Comparison of the *SNR* performance for the three studied algorithms for frequency discrimination.

4.6. Chapter summary

In this chapter, the algorithms for the digital frequency discrimination, as to be used in narrowband LMR, have been formulated and analyzed. The algorithms for frequency discrimination can be considered as the core part of the M-CPFSK digital demodulator. As was shown in this chapter, these algorithms represent a typical class of the non-linear signal processing tasks and, with an exception of the digital phase locked loop with its combined feed-forward and feedback architecture, they use approximation techniques and are limited by a nature of the signal sampling in time. In particular, the approximation of the derivation process by a discrete time differentiation forces the use of higher over sampling rates to reduce the approximation imperfection.

Several remarkable findings can be extracted from the simulation results presented. Referenced to the *SNR* value calculated within the processed bandwidth at the input to the frequency discrimination, the signal-to-noise ratio at its output depends non-linearly on the input SNR and, is on average more than 4 dB lower. If the receiver uses the square root Nyquist filter to reduce the noise bandwidth to the optimum level, the *SNR* in a main E_b/N_0 interval overcomes the input value for 4 dB, in the region where E_b/N_0 is higher than 7 dB. Below the E_b/N_0=10 dB level, the non-linear dependency remains and limits the discriminator performance. It has been important to realize that this noise margin is higher than the one given by the simple reduction of the processed bandwidth before, and after, the frequency discrimination.

Two main modifications to the more general formulations of the frequency discriminators have been proposed. As it was shown by the simulation results the modifications improves the behavior of the demodulators at low *SNR* levels that are important for the maximum usable data sensitivity of the narrowband LMR while operating in marginal conditions (e.g. the radio modem being blocked by a strong interferer).

From all the studied algorithms, the normalized DPLL utilizing the proposed averaging filter reaches the best results. However, as was shown, it has the most demanding realization structure combining feedback and feed-forward architecture. The modified mathematic algorithm can be classified a preferable frequency discrimination algorithm for the narrowband LMR radio modem, since it can be effectively implemented by a feed-forward architecture and has the *SNR* penalty of 0.5 dB comparing to the normalized DPLL algorithm with the averaging filter.

5 Rapid frame and symbol synchronization

5.1. Objective for the new synchronization techniques

The communication system – for which the narrowband LMR equipment is intended – exclusively uses a packet or frame based multiple channel access. It is, either stochastic multiple channel access technique, or *carrier sense multiple (channel) access* (CSMA) with collision detect and acknowledgements. In this case, the radio receiver's only priory information about the opposite transmitter(s) is the information about the nominal frequency and the symbol rate selected. There are various frame lengths used, ranging from a couple of bytes e.g. 12, up to the maximum of 1500 bytes. The typical receive to transmit attack time is around 1 ms.

Such requirements place very strict demands on the synchronization algorithms, which have to extract all the possible information about frequency, frame and symbol synchronization within the first symbols of the incoming frame. It is obvious that, the shorter the acquisition time the higher the communication efficiency of the LMR system can be achieved. However, in case the system does not, or cannot, have all the realizations of the random process, the only way of estimating its parameters is to make use of the time demanding ensemble average of the required parameter [51]. This basically means that the higher the accuracy of the estimated parameter, the longer the averaging periods are needed. This is a major reason that hinders the use of the non-data aided synchronizers in radio data packet switching systems. Methods based on an a priori known preamble symbols are preferred since the preamble represents a single realization of the random process of known parameters, however corrupted by the radio channel. With today's digital signal processing capability these tasks can be enhanced further by developing more and more sophisticated algorithms, but care must be taken when trading off the performance gained by such algorithms and their complexity.

Some synchronization algorithms can be found in literature [61] to [68] but only few of them e.g. [65], [66] and [68] focus on rapid synchronization techniques based on specific preamble, as is often the case in narrowband communication systems. In reference [62], the synchronization method is proposed for orthogonal M-CPFSK and as such cannot be adapted to systems with $h=1/M$ and non-orthogonal signaling.

Synchronization techniques described in [61], [63] and [64] are non-data aided and to suppress significant pattern jitter introduced in recovered timing estimate, long integration periods starting from 128 symbols are needed. Significant processing power is also required for their practical implementation.

The synchronization method described in reference [65], [67] based on specific preamble pattern, are declared as a well suitable for burst mode communication systems with only 16 symbols required to synchronize from the receiving frame. Although this method can provide system with information about the symbol timing estimation, the exact moment when the value of timing estimate is valid becomes unknown to the receiver in case it tries to synchronize from the received noise. Since this is always the case, the problem of rapid symbol timing recovery is very closely related to the frame synchronization and the preamble structure should provide the system with all the information needed to synchronize for the incoming frame.

Digital symbol timing recovery techniques intended for linear digital modulations of low order are studied in a well written reference [59]. There are three different *timing error* *detector* (TED) methods – *Gardner*, *Amplitude directed* and *Watkins decision directed* TED – compared in AWGN as well as in Rayleigh fading channel conditions while using QPSK modulation. All the presented methods are non-data aided and typically it takes more than 40 symbol periods of the incoming noiseless signal to acquire symbol timing information. Moreover, the synchronization performance of these methods varies significantly with constellation order and excess bandwidth of the modulation signal and as such cannot be used in symbol timing acquisition of the narrowband LMR. The same holds true for the timing error detector based on nonlinearity e.g. [87], since the significant amount of pattern jitter requires long integration periods to lower the timing estimate variance. From a more general point of view, algorithms that are based on ensemble average of the estimated parameter do not provide sufficient timing accuracy during the short acquisition phase of the synchronization process. The initial symbol timing information, as well as the frame synchronization, can be estimated through the *cross correlation function* of the received signal. Such algorithms are known in literature [51], [60], [23], [79] as correlation detectors or matched filters.

It is the aim of the present chapter to propose and analyze a complete frame and symbol timing recovery concept suited for narrowband burst mode communication system utilizing modulation techniques chosen in Chapter 3, and to analyze in details its main building blocks needed for acquisition and tracking phase. For the exponential modulation techniques, the method based on digital frequency discrimination as an alternative technique to the one introduced in [65] and [66] is also derived. The synchronization performance of its *data aided* (DA) and *non-data-aided* (NDA) modes of operation is compared. It is shown, that the method, however straightforward it is, gives comparable results to the one presented in [65], [67], but the computational burden is reduced. For LMR systems, where the computational power is always very limited and the frame and symbol timing synchronization is to be combined in rapid synchronization algorithm, *the sample wise pattern correlation technique* with a combination of *the decision directed adaptive synchronization algorithm* is proposed in later chapter. The proposed concept can be simply modified for all digital modulation techniques chosen, and yields satisfactory results, as it is shown by the overall system simulation under AWGN and fading channel conditions.

5.2. Rapid frame and symbol synchronization concept

Following the signal model derived in Section 4.2, the received signal at the input to the synchronization algorithm can be described as

$$x[i] = A(kT + nT_s - \tau_0)\exp[j\psi(kT + nT_s - \tau_0;\alpha_k)]\cdot\exp[j2\pi\nu(kT + nT_s) + \theta] + \upsilon[i]$$
$$-\infty \le i \le \infty;\ \ -\infty \le k \le \infty;\ \ 0 \le n \le (N-1) \quad .$$
$$(5.1)$$

In (5.1) we recall that k is the modulation symbol index, i is the general sample index and n is the digital sample index within the specific interval. N is the over sampling ratio describing the number of samples within one modulation symbol. The parameters assigned as ν, θ and τ are unknown values of the frequency offset, initial carrier phase and symbol timing epoch respectively. The $\upsilon[i]$ assigns a single realization of the band-limited noise process.

It is the purpose of the synchronization algorithms to extract and compensates for initial timing offset τ_0 and to follow its characteristic in time as precisely as the single realization of the random process forming the receiving frame permits.

The simplified block diagram of the proposed symbol and frame timing recovery scheme is shown in Figure 5.1. The input to the algorithm is the baseband representation of modulated signal $x[i]$. For the case that the signal is modulated by the nonlinear modulation technique, the *frequency discrimination* block (Chapter 4) together with the *matched filtering* is needed prior to the synchronization process itself. In case of the linearly modulated signal entering the *differential demodulator*, it is assumed that the signal has already been filtered by the receiver matched filter. The common feedback algorithm of the symbol timing recovery comprising the timing adjustment block *(Fractional Interpolator)*, timing error detector *(Symbol Timing Error Detector)* and loop filter [59] is proposed to be supplemented by the sample wise pattern correlation [23] block *(Frame Synchronization, Symbol Timing Acquisition)* to acquire frame synchronization and to provide the initial timing estimate for the feedback algorithm. In the following sections, the main blocks of this concept are analyzed and several modifications are proposed to optimize the structure for the narrowband LMR receiver.

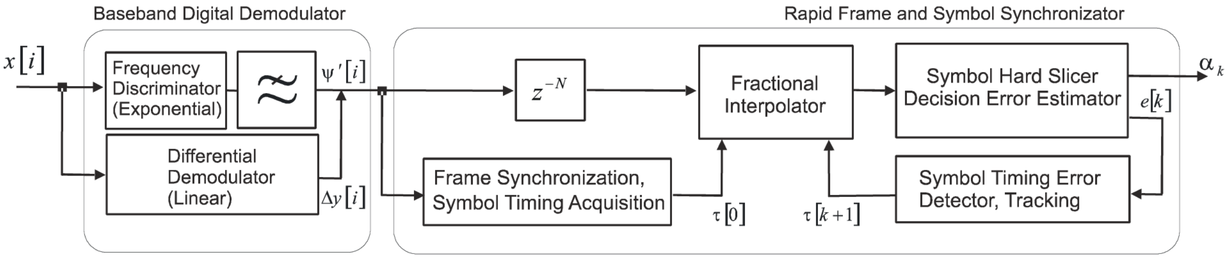

Figure 5.1: Simplified block diagram of the rapid frame and symbol synchronization concept with its main part.

5.3. Timing error detectors – acquisition

5.3.1. Algorithms based on digital frequency discrimination

In this section, the timing error detectors intended particularly for constant envelope modulation formats M–CPFSK with modulation index $h=1/M$ are discussed. The data-aided and non-data-aided versions of the algorithm based on digital frequency discrimination are compared against the synchronization techniques found in literature.

According to [65], and [66], the timing estimation can be calculated by using 4th order autocorrelation over the L_0 symbols α_k of the specific preamble α_k= (...0 0 1 1 0 0 1 1 ...)

$$\xi[n]=\frac{1}{L_0}\sum_{k=0}^{L_0-1}\left(x_k[n]x_k^*[n]\right)^4 \qquad 0\le n\le (N-1), \tag{5.2}$$

where * denotes a complex conjugate. The $\xi[n]$ contains information about the timing epoch which can be extracted by calculating the Fourier transform of its absolute value

$$\tau_0=\frac{T}{2}-\frac{T}{2\pi}\arg\left(\sum_{n=0}^{N-1}\left|\xi[n]\right|e^{\frac{-j2\pi}{N}n}\right) \tag{5.3}$$

For L_0=16 the algorithm is considered to recover symbol timing information which is supposed to be constant over the entire incoming frame. The practical implementation obstacles of this equation can be seen in significant computational burden required to calculate the forth power of the correlation function as well as the non-symmetrical preamble structure which does not fulfil the symbol alphabet.

In the following, a comparable algorithm is derived using the frequency discrimination method and with reduced complexity it provides sufficiently small timing *mean square error* (MSE) [63], [69].

Following the same reasoning as in Section 4.5, the instantaneous phase of the received signal can be calculated as

$$arctg\left(\frac{x_Q[i]}{x_I[i]}\right) = \psi([i-\tau_0];\alpha_k) + 2\pi\nu[i] + \theta\,. \tag{5.4}$$

In equation (5.4), the noise contribution has been ignored in order to simplify the description. The instantaneous phase should contain all the information about the parameters ν, θ and τ. Although it is possible to calculate the timing information right from (5.4), it is convenient to proceed with the frequency discrimination to get rid of the frequency and phase offsets and to extract the timing information by using an equation that is more suitable for hardware realization.

Using the same procedure as in Section 4.5, the description of the received signal after the frequency discrimination can be derived as

$$y[i-\tau_0] = \frac{x_I[i-1]x_Q[i] - x_I[i]x_Q[i-1]}{\frac{\pi h}{N}\left(x_I[i]x_I[i-1] + x_Q[i]x_Q[i-1]\right)}\,. \tag{5.5}$$

Although the transmitted signal experiences only negligible level of amplitude variance, the received signal, as given by (5.5), exhibits magnitude variance caused mostly by the main channel selectivity filter. As was mentioned in Section 4.5, this amplitude variance cannot be omitted if (5.5) is used for the frequency demodulation in digital M-CPFSK baseband receiver. However, for the symbol timing estimation, the information about the demodulated signal amplitude is not needed and (5.5) can be considerably reduced to

$$y[i-\tau_0] \approx x_I[i-1]x_Q[i] - x_I[i]x_Q[i-1]\,. \tag{5.6}$$

By calculating the discrete differentiation, the frequency offset ν transforms into small constant with negligible impact on a timing estimate and the initial phase θ vanishes altogether.

From now on, extracting the timing estimate is similar to the procedure described in [65], [66]. The expectation function of the signal carrying the synchronization information is calculated. In this case however, it is the expectation function of an absolute value of the demodulated signal (5.6) over the specified signal interval of L_0 symbols

$$\xi[n] = \frac{1}{L_0}\sum_{k=0}^{L_0-1}\left|x_{I,k}[n-1]x_{Q,k}[n] - x_{I,k}[n]x_{Q,k}[n-1]\right|,\quad 0 \le n \le N-1 \tag{5.7}$$

and finally, the timing estimate can be by calculated by the Fourier transform

$$\tau_0 = \frac{T}{2\pi}\arg\left(\sum_{n=0}^{N-1}\left|\xi[n]\right| e^{\frac{-j2\pi}{N}n}\right). \tag{5.8}$$

By comparing (5.7) to (5.2) it can be noticed that the forth power has reduced to a single complex multiplication which can be effectively implemented especially in modern FPGA circuits.

For NDA operation, the length of the observation interval L_0 needs to be chosen large enough to suppress significant amount of pattern jitter presented. However, if the rapid synchronization is preferred, the preamble based estimation can be used and thus significantly shorten the observation interval L_0. As it is shown by the simulation results presented in the next section, when simple harmonic preamble pattern in form of α_k=-(M-1),

(M-1)... -(M-1), (M-1) is chosen, the length of the observation interval can be reduced to L_0=16 or even 8 symbols and still reach acceptable *MSE* of the timing estimate for the practical purposes of the narrowband LMR as demonstrated in next section.

5.3.2. Simulation results

In this section, the performance of the proposed timing error detector is analyzed. The 4-CPFSK with h=*0.25* as a modulation technique and 12 kBaud as a symbol rate has been selected for simulation. The input signal with a normalized signal-to-noise ratio in form of E_b/N_0 has been band limited by a digital main channel selectivity FIR filter with a low pass characteristic shown in Figure 4.3. As a pulse shaping and matched filter the square-root Nyquist δ-filter with equivalent excess bandwidth of 28.4% and oversampling ratio of N=10 has been used (Section 3.3).

Figure 5.2 illustrates the performance of the DA operation of the suggested algorithm depicting the *normalized timing mean square error* (MSE_τ)

$$MSE_\tau = E\left\{\left[\frac{(\tau-\tau_0)}{T}\right]^2\right\} \qquad (5.9)$$

as a function of E_b/N_0. It can be seen in Figure 5.2, that the suggested preamble structure enables to decrease its length to 16 or even 8 and timing detector still reaches sufficiently small MSE_τ. Using longer preamble structures increases the number of traces to average and naturally the noise contribution is reduced. In order to compare the results more objectively, the *modified Cramer-Rao bound* ($MCRB_\tau$) calculated according to (5.10) [69], [63]

$$MCRB_\tau = \frac{T\left(\frac{E_b}{N_0}\right)^{-1}}{2\pi^2\xi_g L_0}, \qquad (5.10)$$

where

$$\xi_g = \int_0^{2G_D T} g^2(t)dt \qquad (5.11)$$

has been added to the plot as a benchmark. In (5.11), the $g(t)$ represents the frequency pulse shaped by the transmitter and receiver filters (Chapter 3.3).

It can be seen from the above comparison that the timing error estimator working in DA mode encloses to optimal performance and extracts almost all information available in the observation interval. The near optimum performance of such synchronizer was also a main motivation to use a transparent and orthogonal tone in band to help the system tracking the timing epoch over the received frame. However, it was found that although the pilot tone is orthogonal to the modulation signal at the optimum sampling points, it is not the case in its close vicinity and it causes a significant signal distortion. This approach requires further investigation while it might be a good option for narrowband LMR system operating in linear modulation mode.

For NDA operation of the timing synchronizer much longer Figure 5.3 observation interval, starting at least at 128 symbols are needed, and the distance between the $MCRB_\tau$ is still substantial. As demonstrated also in Figure 5.3, this fact is in accordance with the results available in literature [62], [63].

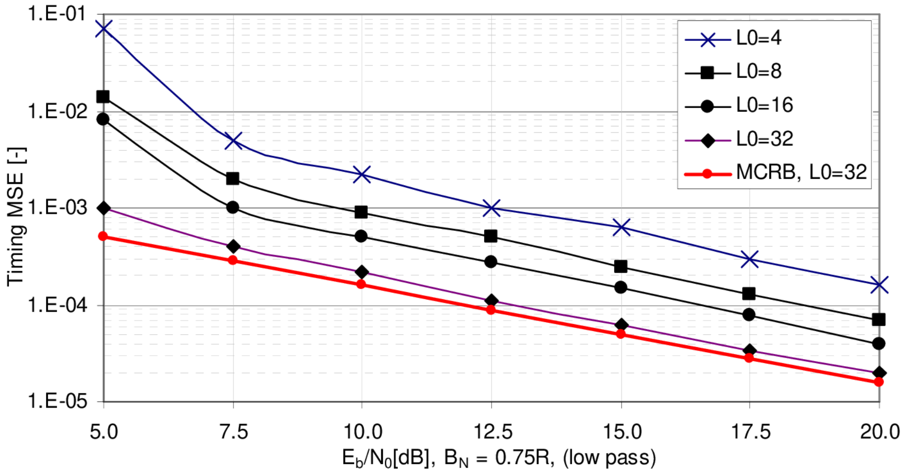

Figure 5.2: Timing estimation MSE_τ for different length of the preamble L_0=4,8,16,32. DA operation.

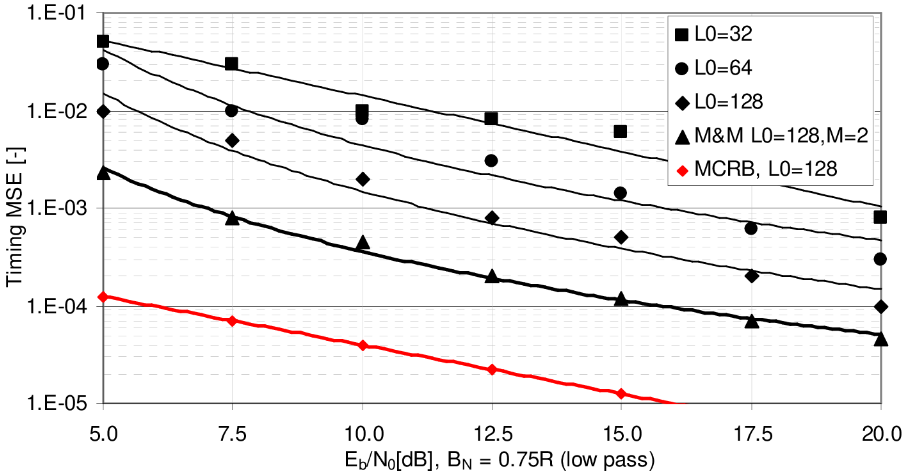

Figure 5.3: Timing estimation MSE_τ for different length of the preamble L_0=4, 8, 16, 32; M&M L_0=128, M=2 [63].

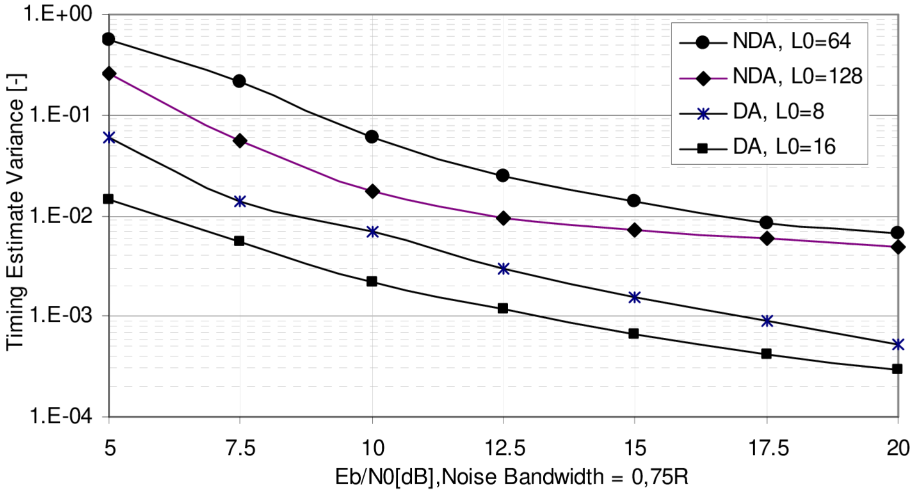

Figure 5.4: Timing estimation variance for DA and NDA mode of the algorithm operation for different lengths of the observation interval.

5.3.3. Drawbacks of the algorithm

Despite the encouraging results presented in the previous section, especially for the DA mode of operation, some drawbacks of the described approach can be seen mostly in the following points:

- Although the original algorithm [65] has been simplified significantly, there is still need for Fourier transform calculation in order to complete the synchronization algorithm.
- Relatively high number – e.g. 8 to 10 – of samples per symbol is needed to approximate the derivation operation, Figure 4.6.
- Significant variance of the timing estimate in situations when E_b/N_0 is low (e.g. $E_b/N_0 < 10$ dB) and the observation interval L_0 is not long enough to average the noise contribution, (Figure 5.4, Figure 5.5).
- For the frame based communication, the exact moment when the timing estimate has the lowest MSE_τ with respect to its optimum value remains unknown and needs to be further calculated. The timing estimate convergence to its optimum value over the receiving preamble is depicted in Figure 5.6

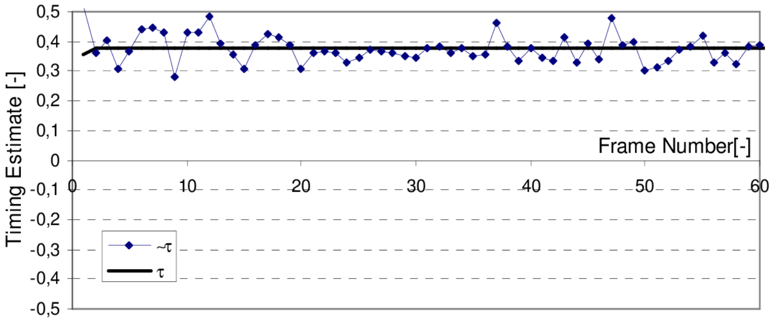

Figure 5.5: Instantaneous timing estimates over the received frames. E_b/N_0=10 dB; DA operation, preamble length L_0=16.

5.4. Sample wise pattern correlation

The last problem mentioned in the previous section is critical, especially in the frame based communication systems, where the only source of the timing information is the receiving frame itself. It is important to note that such assumption needs to be made with almost all similar algorithms described in [62] to [66], regardless the fact, how accurate they estimate the timing information. Some pattern recognition technique would easy the problem but at this point the symbol timing has not been recovered.

Besides calculating the mean value of the stochastic process by using ensemble average as was the case in the previous section, the symbol timing information as well as the frame synchronization can be estimated through the cross-correlation function of the received signal. Such algorithms are known in literature [51], [60], [23], [79] as correlation detectors or matched filters. Opposed to the matched filters described in Chapter 3.3, where this assignment meant that the impulse response of such filters is matched to the signaling pulse, in the theory of signal restoration by correlation techniques the term “matched” is referred to the situation where the filter impulse response represents the entire interval of the wanted signal.

The aim of this section is to describe, optimize, and analyze, signal correlation techniques to be used in symbol and frame timing acquisition process of the narrowband communication system. The main contribution can be seen in the simplified formulation of the digital algorithm that is independent of the threshold detection and with a proposed modification can be used for all the modulation techniques studied. The analysis of its main characteristics, by using a system level simulation of the LMR transceiver, is also provided in the last part of this section.

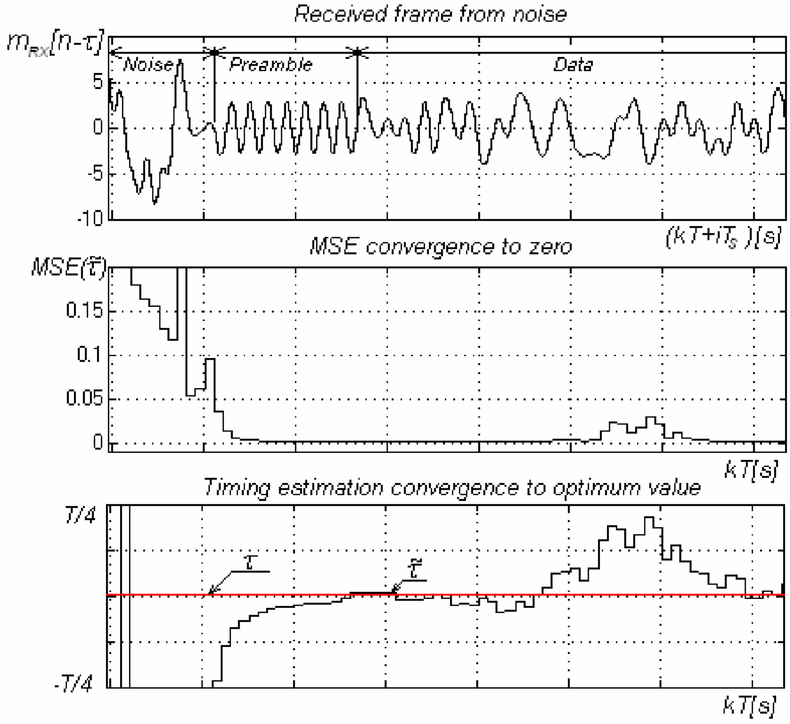

Figure 5.6: Example of the timing estimate calculation over the receiving frame from a band limited noise. E_b/N_0=25 dB, L_0=16, 4-CPFSK.

5.4.1. Algorithm formulation

Let suppose that the distortion less frequency discrimination according to (4.23) is already employed in the system as well as the matched filtering by a square root Nyquist filter of any of the characteristics studied in Section 3.3. The incoming signal can be written in simplified general notation as

$$y[i] = \begin{cases} A(i-\tau_0)x(i-\tau_0)+\nu[i] & 0 \le i \le (L_0 N - 1) \\ \nu[i] & otherwise \end{cases}, \tag{5.12}$$

where $x(i-\tau_0)$ is the original preamble signal with the symbol length of L_0, which optimal sampling instant τ_0 is to be estimated. The $\nu[i]$ represents the realization of noise process which is statistically independent from the preamble signal $x(i-\tau_0)$. N is the over sampling factor. $A(i)$ is the general time variant amplitude of the incoming signal.

As shown in [51], the cross-correlation function between the incoming signal and its local replica $x(i)$ can be written as

$$R_{xy}(\tau) = E[x(i)\,y(i+\tau)] = E[x(i)Ax(i+\tau-\tau_0)] + E[x(i)\nu(i+\tau)],$$

$$R_{xy}(\tau) = A\,R_{xx}(\tau-\tau_0) + R_{x\nu}(\tau). \tag{5.13}$$

In (5.13) E represents the mean value or the expectation function and R denotes the correlation function. If the noise signal is independent of the preamble, the second term approaches zero and the correlation reaches its maximum exactly at $\tau=\tau_0$.

In practical applications, the calculation of (5.13) can be approximated by a FIR filter which calculates the convolution between the incoming signal and the finite impulse response $h[n]$ – where index n is from $0 \le n \le (L_0N\text{-}1)$ – according to (5.14)

$$R_{xy}(\tau) \approx R_{xy}[i] = \sum_{n=0}^{L_0N-1} y[i-n]h[n], \qquad (5.14)$$

where the impulse response of the FIR filter is the time reversed replica of the sampled preamble signal $x(n)$ having finite length of L_0N-1 samples

$$h[n] = x[L_0N - n - 1], \quad 0 \le n \le L_0N - 1. \qquad (5.15)$$

Basically, two main problems that are also identified in [51] have to be resolved when implementing this technique in practice. Firstly, it is the dependency of the correlation function maximum upon the incoming signal amplitude $A[n]$

$$R_{xy}(\tau_0) \approx R_{xy}[0] = \frac{1}{(L_0N-1)} \sum_{n=0}^{L_0N-1} A[n]\left|x[n]\right|^2 . \qquad (5.16)$$

This dependency complicates the detection of the precise position of the preamble signal in time.

Secondly, it is the proper selection of the correlation interval L_0 together with a proper choice of the shift parameter τ such that the estimated value of the timing interval is unbiased and experiences low variance.

5.4.2. Correlation maximum normalization

The dependency of the timing estimate of the correlation detector upon the incoming signal amplitude (5.16) makes the detection of the correlation maximum difficult. Therefore, some additional modification can be done to overcome this problem. The modifications make use of the nonlinear transformation of the detected signal, most often its normalization by the calculated signal amplitude [51]

$$R_{xy}(\tau) \approx R_{xy}[i] = \frac{\sum_{n=0}^{L_0N-1} y[i-n]h[n]}{\sum_{n=0}^{L_0N-1} (y[i-n])^2} . \qquad (5.17)$$

Recalling how the $y[n]$ signal has been generated in the proposed receiver (4.23) it can be seen that for the exponentially modulated signal the nonlinear transformation has already been performed and the signal coming to the sample wise pattern correlator represents the instantaneous frequency – derivation of the signal phase (angle)[6] – and as such embodies a normalized signal amplitude within the proposed dynamic range of the digital receiver (Section 6.2).

5.4.3. Simplified formulation of the algorithm

In addition to the above mentioned problems, also the complexity of the algorithm has to be taken into account when implementing a complete synchronization technique. In general, when the correlation detectors are used for frame synchronization [23], [60] there is no need

---

[6] The non-linear matched filters are also called angle or cosine filters.

to calculate the mutual correlation using full signal resolution. In fact, the wanted signal which occurrence is to be detected is a sequence of logic levels rather than an actual signal samples. Since the transmitted symbols have not yet been distinguished at this point of the digital receiver, the oversampling correlation techniques need to be used [23]. On the other hand, this modification increases the complexity of the correlation calculation. For applications with limited amount of signal processing resources the reduction of the signal resolution in amplitude rather than in time by reducing the oversampling factor can be a preferred option. In the utmost situations only the information about the signal polarity can be used to calculate the correlation function with a priori bipolar preamble pattern assign as $h[k] = x[L_0 - k - 1]$

$$R_{xy}(\tau) \approx R_{xy}[i] = \sum_{k=0}^{L_0-1} sign(y[i-kN])sign(h[k]) \quad -\infty \le i \le \infty, \tag{5.18}$$

where i is the sample index, k is the symbol index, N is the number of samples per symbol, and *sign*(.) denotes the bipolar signum function

$$sign(x) = \begin{Bmatrix} 1 & x \ge 0 \\ -1 & otherwise \end{Bmatrix} \tag{5.19}$$

The signum function can be seen as the application of limiter to the incoming signal which normalizes the information about the signal amplitude and thus solves the problem of the cross-correlation maximum dependency on time variant signal amplitude (5.16).

Cross-correlation function $R_{xy}[i]$ achieves its maximum each time it finds out the corresponding preamble sequence. Ideally, for the rectangular modulation pulse, the maximum would spread for N samples. In real systems however, it is less than N due to the intersymbol interference introduced by the respective characteristics of the communication channel including all filters.

The central point of the cross-correlation function maximum is in direct relation to the maximum eye opening of the demodulated signal and represents the optimal sampling point. Thus, it can be used not only for the frame synchronization but also for symbol timing estimation. As it is shown in Fig 5.7, the centre of the correlation peak can be used as the initial time instant τ_0 for symbol timing recovery.

Even though the (5.18) represents already a straightforward approach, it can be simplified even further. In (5.18), the bipolar signalling can be changed into unipolar and the multiplication into the XOR operation denoted as $\oplus$

$$R_{xy}(\tau) \approx R_{xy}[i] = \sum_{k=0}^{L_0-1} sign(y[i-kN]) \oplus sign(h[k]) \quad -\infty \le i \le \infty, \tag{5.20}$$

where, in this case the *sign*(x) denotes the unipolar signum function defined by

$$sign(x) = \begin{Bmatrix} 1 & x \ge 0 \\ 0 & otherwise \end{Bmatrix}. \tag{5.21}$$

Now, the required information about the frame and symbol synchronization is carried in a minimum of the correlation function $R_{xy}[i]$. The main advantages of this modification are that the algorithm is no more dependent on the preamble length L_0, the threshold detection is greatly simplified and the computational requirements are substantially reduced.

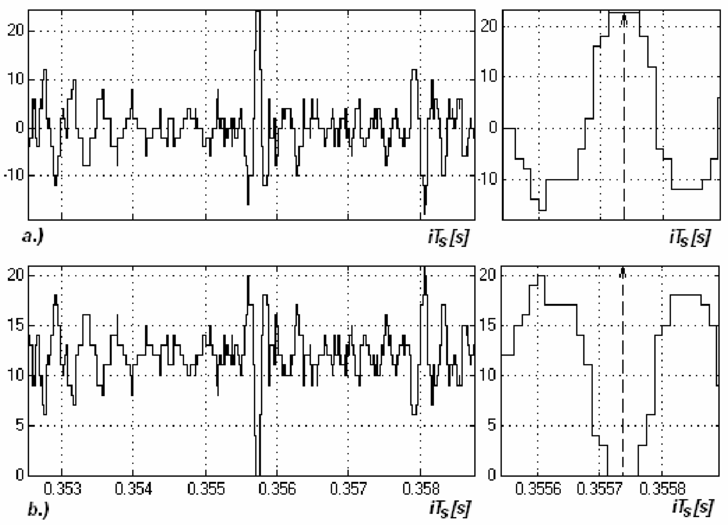

Figure 5.7: **(a)** Result of the sample wise pattern correlation calculation (5.18); L_0=24, E_b/N_0>25 dB. Detailed scan of the correlation maximum, with its centre taken as the timing estimate. **(b)** The result of equation (5.20) with detailed scan of the correlation minimum.

5.4.4. Adoption the algorithm for the linear modulation techniques

Direct adoption of the proposed synchronization mechanism to the linear modulation techniques (Section 3.2) is complicated mainly by the fact that the maximum of cross-correlation function is strictly dependent on the receiving signal frequency offset [60], which is always present at the beginning of the received frame. While this phenomenon was a minor issue for exponentially modulated signal processing, it requires a special attention when implementing the synchronization task for linearly modulated signal.

Let us assume the receive signal has already been down converted to baseband and filtered by a square root Nyquist filter of any of the characteristics studied in Section 3.3. Similarly to (5.12) the receive signal can be written as

$$y[i]=\begin{cases} A(i-\tau_0)x(i-\tau_0)\exp(j2\pi\Delta fT_S(i-\tau_0))+v[i] & 0\le i\le(L_0N-1) \\ v[i] & otherwise \end{cases}, \qquad (5.22)$$

where in case of linear modulation, the $x(i\text{-}\tau_0)$ is representing the original *complex* baseband preamble signal with the symbol length of L_0, which optimum sampling instant τ_0 is to be estimated. The Δf represents the overall frequency offset between the transmitting and receiving radio modem.

In accordance with (5.14), the cross-correlation function can be calculated as

$$R_{xy}(\tau)\approx R_{xy}[i]=\sum_{n=0}^{L_0N-1}y[i-n]h^*[n], \qquad (5.23)$$

now with the difference that it is the convolution of two complex sequences rather than real sequences in (5.14). The symbol * represents the complex conjugate.

To see the negative effect of the frequency offset, we need to substitute for $y[i]$ from (5.22), while omitting for simplicity the term for time variant amplitude, as well as the noise term and assuming also that $\tau_0=0$

$$R_{xy}[i]=\sum_{n=0}^{L_0N-1}x[i-n]\exp(j2\pi\Delta fT_S i)x^*[L_0N-n-1]. \qquad (5.24)$$

In (5.24) there is (5.15) in its complex form used for $h[n]$.

At optimum sampling point where $i=L_0N-1$ we can also assume that each cross-correlation value is a constant

$$x[i-n]x^*[L_0N-n-1]=1 \qquad 0 \le n \le (L_0N-1), \tag{5.25}$$

and get

$$R_{xy}[i]=\sum_{n=0}^{L_0N-1}\exp(j2\pi\Delta fT_S i). \tag{5.26}$$

As shown in [60], we can further use the identity

$$\sum_{i=0}^{N-1} x^i = \frac{1-x^N}{1-x}, \qquad x \ne 1, \tag{5.27}$$

and modify Euler's equation

$$\sin(x)=\frac{e^{jx}-e^{-jx}}{2j}, \tag{5.28}$$

into

$$\frac{2j\sin\left(\frac{x}{2}\right)}{e^{j\frac{x}{2}}}=1-e^{jx}, \tag{5.29}$$

to get

$$R_{xy}[i]=\exp\left[j2\pi\Delta fT_S\left(\frac{L_0N-1}{2}\right)\right]\frac{\sin(\pi\Delta fT_S L_0N)}{\sin(\pi\Delta fT_S)}. \tag{5.30}$$

From (5.30) it is now clear that the cross-correlation maximum depends on the frequency offset. When plotted against the relative frequency offset, as shown in Figure 5.8, it can be noticed that the degradation of the maximum is substantial even for the frequency offsets of few percentage of the symbol rate.

Another important point is that the degradation is more severe for longer sequences [60]. This can be seen in Figure 5.9, by comparing the relative degradation of the two sequences of different lengths.

For the LMR communication system utilizing the selected linear modulation techniques, the problem described can be effectively overcome by the differential encoding and decoding of the preamble sequence in the same manner as the data sequence is encoded (3.11). Assuming that the preamble symbols are now encoded to the transmitted signal parameter change – either phase or magnitude – rather than to the absolute level of the signal parameter itself, the previous example can be rewritten as follows.

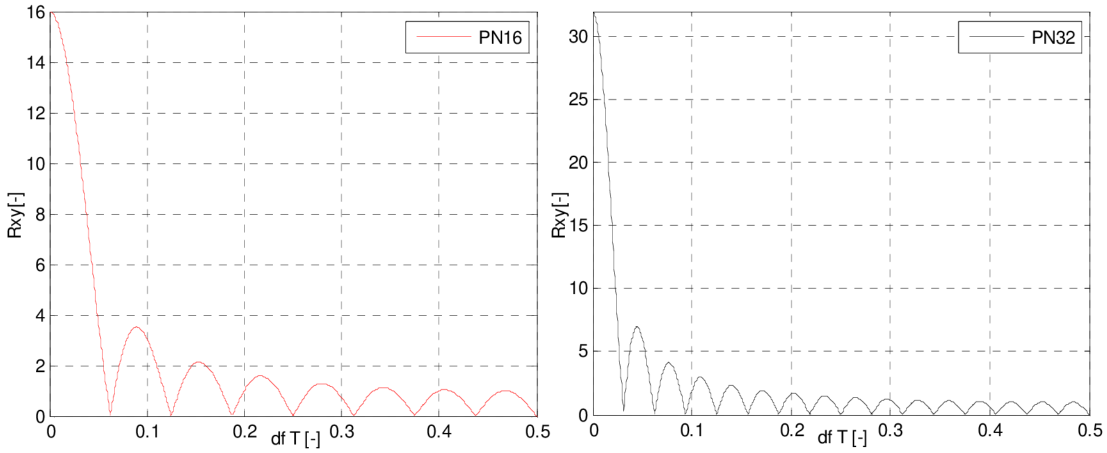

Figure 5.8: Degradation of the cross-correlation maximum due to the frequency offset for two pseudo random binary sequences of length 16 and 32 symbols.

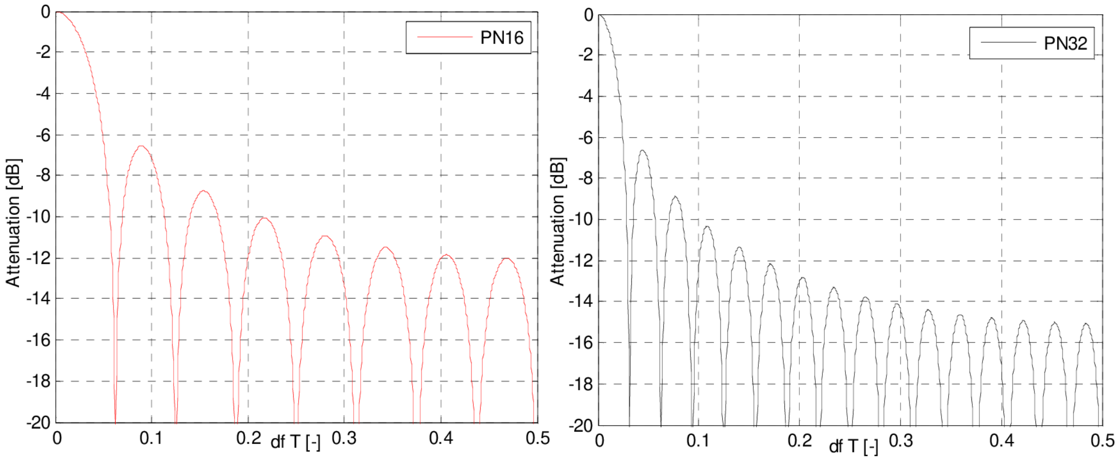

Figure 5.9: Relative attenuation of the cross-correlation maximum as a function of the frequency offset for two pseudo random binary sequences of length 16 and 32 symbols.

The incoming signal is the same as the one given by (5.22) however, prior to the cross-correlation detection we need to calculate the differential demodulation as

$$\Delta y[i] = y[i]y^*[i-N], \tag{5.31}$$

$$\Delta y[i] = \exp(j2\pi\Delta f T_S N)x[i]x^*[i-N] + \Delta\nu[i], \tag{5.32}$$

where

$$\Delta\nu[i] = x[i]\exp(j2\pi\Delta f T_S i)\nu^*[i-N] + x^*[i-N]\exp(-j2\pi\Delta f T_S i)\nu[i] + \nu[i]\nu^*[i-N]. \tag{5.33}$$

It was no ambition of this work to analyze the transformation of the noise process through the differential demodulation and its influence on synchronization performance. In the following, it is therefore assumed that the $\Delta\nu[i]$ is, again, a single realization of the random process with a zero mean value although, it is also reasonable to assume that the spectrum of such process is not white within the processed bandwidth.

Now the cross-correlation with a differentially encoded preamble pattern can be calculated as

$$R_{xy}[i] = \sum_{n=0}^{L_0N-1} \Delta y[i-n]\Delta x^*[L_0N-n-1], \qquad (5.34)$$

$$R_{xy}[i] = \exp(j2\pi\Delta f T_S N)\sum_{n=0}^{L_0N-1} \Delta x[i-n]x^*[L_0N-n-1] + \sum_{n=0}^{L_0N-1} \Delta \nu[i]x^*[L_0N-n-1]. \qquad (5.35)$$

From (5.35) it can be realized that, if the second term in (5.35) is omitted, the cross-correlation maximum is degraded only by a single and constant phasor $exp(j2\pi\Delta T_S N)$. Moreover, the symbol period can be recognized where

$$T = NT_S, \qquad (5.36)$$

and therefore it can be concluded that the degradation of the cross-correlation maximum due to the frequency offset is independent also of the over-sampling factor. This is a preferable property which enables to use either higher number of samples per modulation symbol or use an over sampling to locate the optimum sampling point more precisely without the degradation of the correlation maximum due to the frequency offset.

5.4.5. Simplified formulation of the algorithm

The hardware realization of the complex differential demodulator is straightforward and follows exactly the definition (5.31). However, it is worth a note that the complex differential demodulator is a non-linear algorithm and as such it requires doubled output signal resolution to operate fully over the entire input signal resolution.

When it comes to complex correlator the direct implementation of (5.34) yields to demanding processing structures containing four FIR filters with their output summed together. Besides the complexity, also the previously described problems with cross-correlation maximum variation over the signal level, as well as the correct threshold detection have to be taken into account when (5.34) is used for symbol synchronization.

Following the same reasoning as in Section 5.4.3 the (5.34) can be rewritten into

$$R_{xy}(\tau) \approx R_{xy}[i] = \sum_{k=0}^{L_0-1} sign(\Delta y[i-kN]) \oplus sign(\Delta x^*[L_0-k-1]), \quad -\infty \le i \le \infty, \qquad (5.37)$$

where the $sign(x)$ function is defined as

$$sign(x) = \begin{Bmatrix} [0\ \ 0] & \Re(x) \ge 0; \Im(x) \ge 0 \\ [0\ \ 1] & \Re(x) < 0; \Im(x) \ge 0 \\ [1\ \ 1] & \Re(x) < 0; \Im(x) < 0 \\ [1\ \ 0] & \Re(x) \ge 0; \Im(x) < 0 \end{Bmatrix}. \qquad (5.38)$$

This modification greatly simplifies the overall complex correlation structure and unifies the acquisition mode of the symbol and frame synchronization task for all of the selected linear modulation formats.

5.4.6. Performance simulation results

It is difficult to evaluate the statistical performance of the synchronization algorithm based on a correlation detection of particular signal interval. To the best of author's knowledge, there is no unified way of evaluating the digital correlation algorithms, most likely because its performance depends on a number of parameters including oversampling factor, modulation filtering, threshold detection and the particular correlation properties of the selected random patterns. Also, the sample wise pattern correlation technique and similar correlation based detectors work on discrete sample basis and therefore there is not much sense in calculating the *MSE* of the symbol timing estimation as a continuous function of E_b/N_0 as in the previous Section 5.3.1. However, it is worth a note at this point that the *MSE* of such symbol timing estimation cannot be considered better that the lowest limit defined by

$$MSE_{\tau} \geq \left(\frac{1}{2N} \right)^2 . \qquad (5.39)$$

Therefore, it is no ambition of this section to give an overwhelming performance evaluation of the proposed detector. It is, rather, of intension to give an application-relevant performance indication in form of a timing accuracy of the algorithm. Thus, in the following, the probability that the correlation detector estimates the symbol timing with a deviation greater than the above mentioned limit (5.39) is evaluated. The *pseudo-noise* (PN) sequences with lengths L_0 of 8, 16 and 24 symbols have been selected as the preamble signal. The preambles and their signal representations – the impulse responses of the correlation matched filter – after the Nyquist filtering are shown in Figure 5.10.

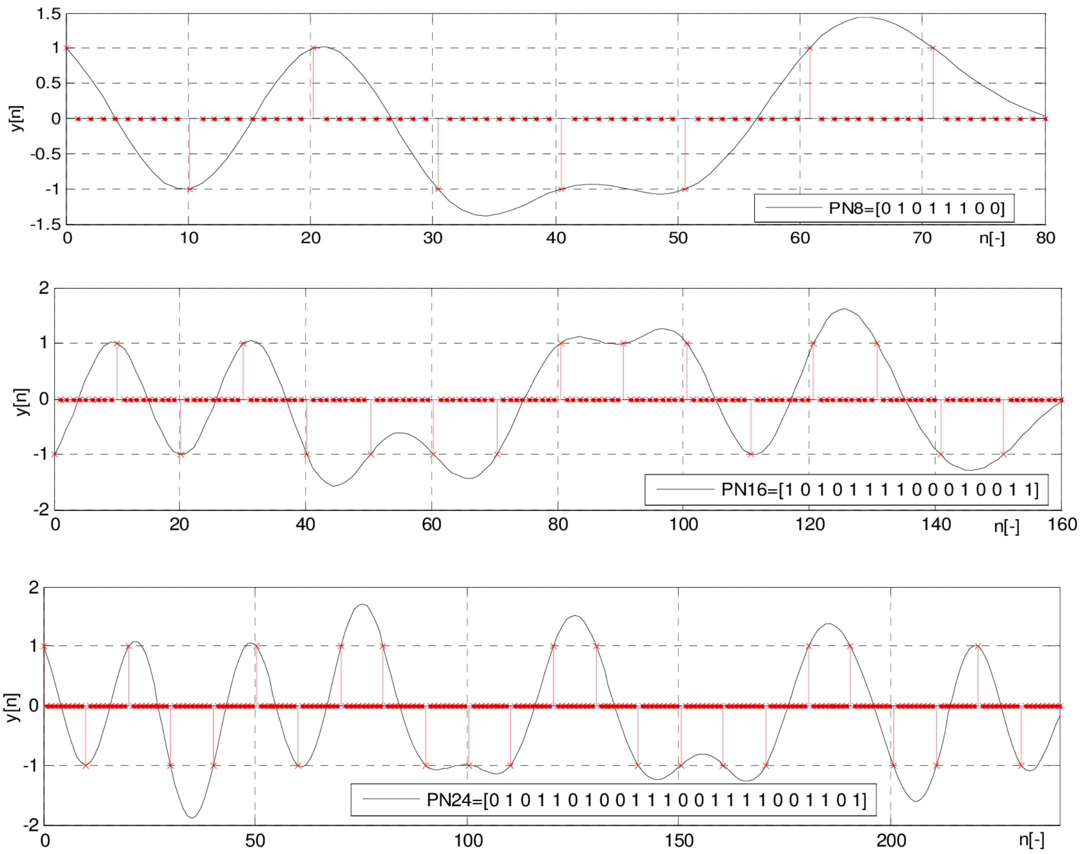

Figure 5.10: Up sampled (N=10) and filtered PN sequences of length L_0=8, 16, 24 used for correlation synchronization analysis.

In Figure 5.11 to Figure 5.15, there are results of the sample wise pattern correlation simulation for the chosen PN sequences. In accordance with (5.39) the *“Sync Deviation Probability”* – as it is given in Figure 5.11 to Figure 5.15 – represents the probability parameter that the recovered clock based on correlation detection differs from the optimum sampling clock by a phase deviation greater than 1/(2N), which in this particular situation equals ±0.05 of the symbol interval T. Note that exceeding the given interval does not necessarily yield to symbol detection errors, it only represents the selected initial synchronization accuracy. For each level of the E_b/N_0 the deviation probability has been calculated over the 10^4 transmitted frames. It can be seen from Figure 5.11 that the timing accuracy of the sample wise pattern correlation technique can be increased be selecting a longer preamble pattern. However, when doubling the preamble length, the synchronization accuracy does not improve for more than 1 dB. A similar observation can be made from Figure 5.13, in a bid to aid the case that the preamble is a complex vector.

There are sets of result shown in Figure 5.12 and Figure 5.14 measured by the respective algorithms simulations for the two values of the excess bandwidth parameter. It can be seen that the lower the excess bandwidth of the signal coming into the correlation calculation, the lower the deviation probability of the correlation maximum. This is a remarkable finding, since the lower the excess bandwidth used in the system, the higher the required synchronization accuracy is needed to process the data without errors. It is interesting that cross-correlation function of the incoming signal refines the synchronization accuracy and extracts the information about the need for more precise synchronization hidden in the signal itself[7].

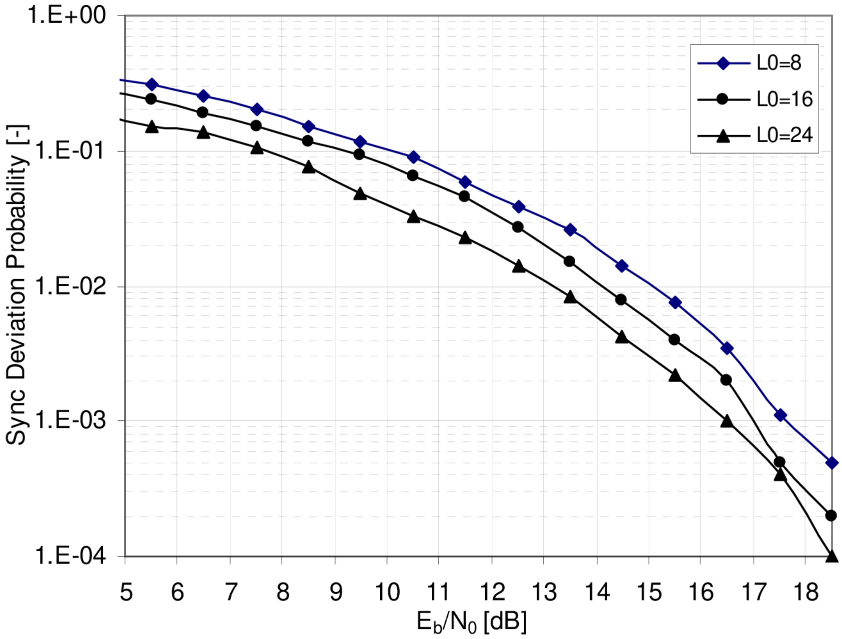

Figure 5.11: Synchronization performance of the correlation synchronizer (5.20) for up-sampled (N=10) and filtered PN sequences of different lengths L_0=8, 16, 24. The noise bandwidth in this case is equal to the occupied signal bandwidth defined as $(1+\alpha)R/2$, where α=0.28.

---

[7] When comparing two signals with different excess bandwidths, one can easily judge which signal needs more precise synchronization, for instance from an eye diagram of the signal, thus the information is present in the signal, indeed.

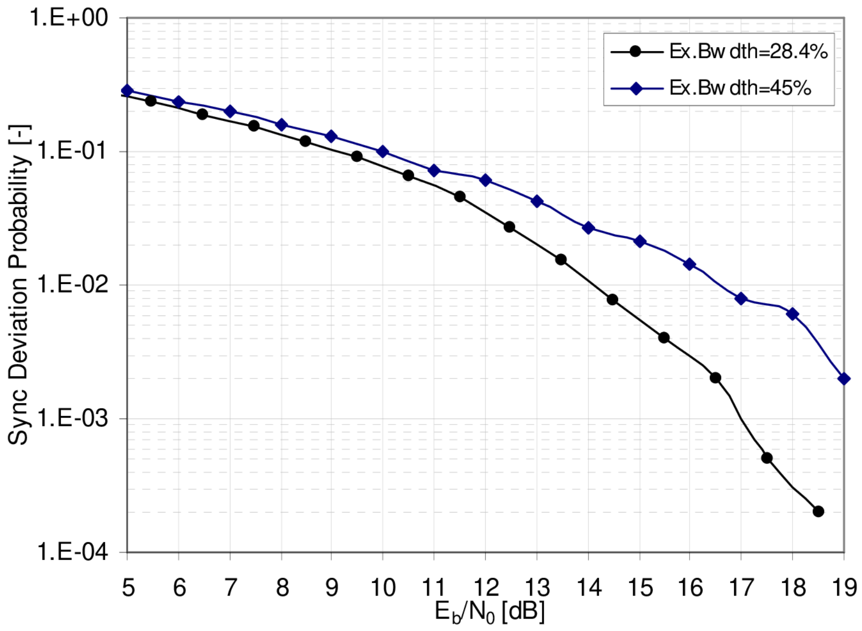

Figure 5.12: Synchronization performance of the correlation synchronizer (5.20) for up-sampled (N=10) and filtered PN sequences of L_0=16 and two values of excess bandwidth. The noise bandwidth in this case is equal to the occupied signal bandwidth defined as $(1+\alpha)R/2$.

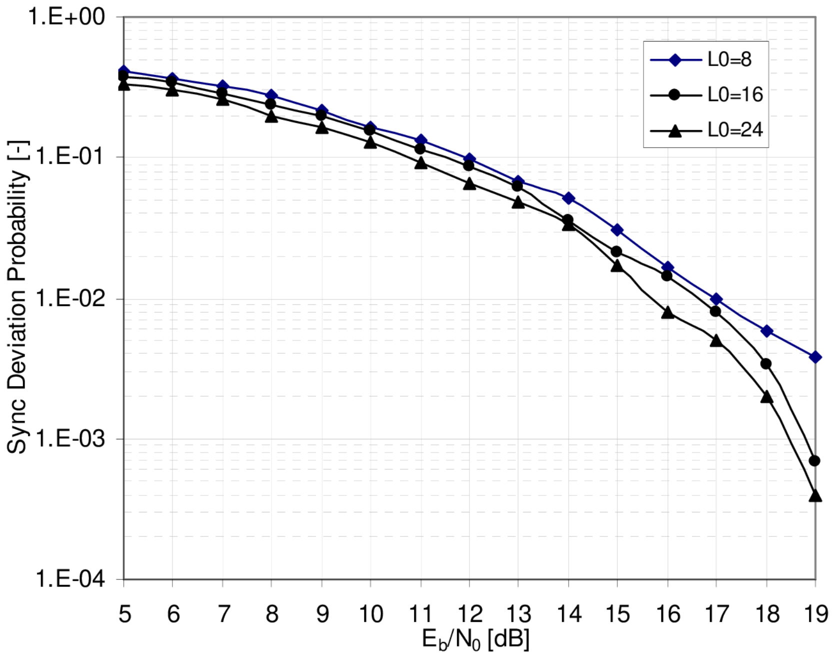

Figure 5.13: Synchronization performance of the correlation synchronizer (5.37) for up-sampled (N=10) and filtered PN sequences of different lengths L_0=8, 16, 24. The noise bandwidth in this case is equal to the occupied complex signal bandwidth defined as $(1+\alpha)R/2$, where α=0.45.

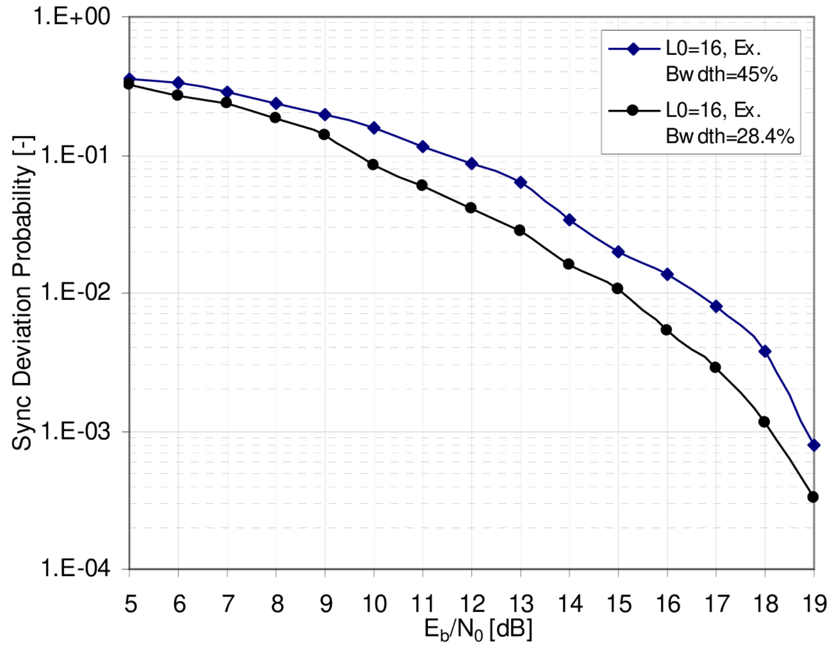

Figure 5.14: Synchronization performance of the correlation synchronizer (5.37) for up-sampled (N=10) and filtered PN sequences of L_0=16 and two values of excess bandwidth. The noise bandwidth in this case is equal to the occupied signal bandwidth defined as $(1+\alpha)R/2$.

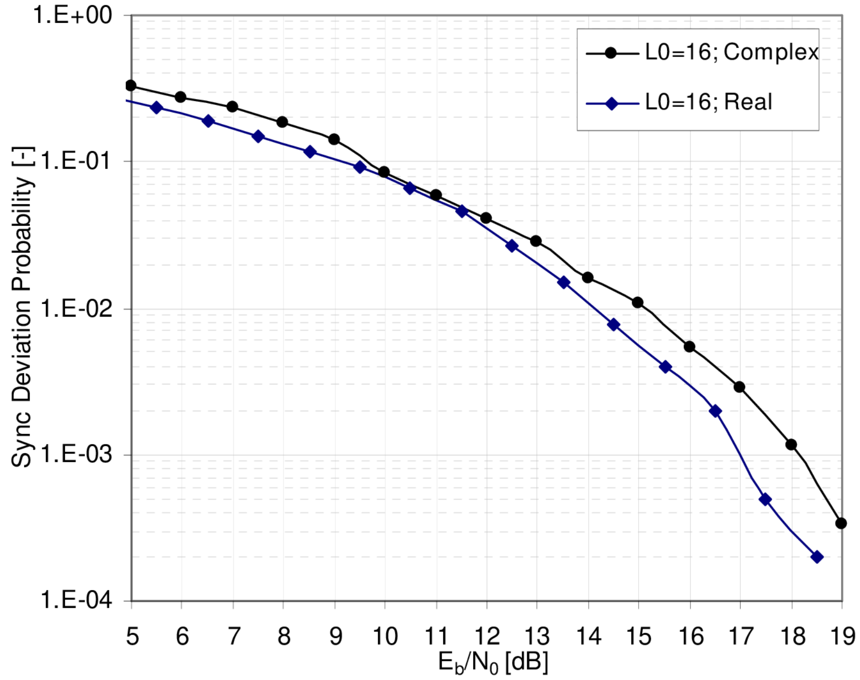

Figure 5.15: Comparison of the synchronization performance of the correlation synchronizers for exponential (5.20) and linear modulation (5.37) for up-sampled (N=10) and filtered PN sequences of L_0=16. The noise bandwidth in this case is equal to the occupied signal bandwidth defined as $(1+\alpha)R/2$,where α=0.28.

5.5. Timing error detectors – tracking

The receiving frame of the physical radio layer can be seen from a more general point of view as a single realization of the stochastic process and the task of the receiver is to gain all the parameters describing its main characteristics. Not only that the transmitted symbols has a random character, but also the character of the radio channel creates an independent stochastic process with its own parameters. The ambition of the synchronization algorithms in particular is to *acquire* an estimate of the phase of optimal sampling instant and also to *track* or to correct the sampling phase over the entire receiving frame upon the current error estimate as precisely as the single realization of such process enables. In signal estimation theory, there are two main approaches how to estimate the parameters of the stochastic process either by means of a signal correlation analysis or adaptive signal restoration based on optimization of a cost or objective function, which in most cases means the minimization of the mean square error signal.

In this section, the main attention is focused on the second approach to be used in symbol timing synchronization process while analyzing the adaptive algorithm for the symbol timing error detection based on non-data aided symbol decisions. While the idea to use the symbol decisions to equalize the time variant character of the radio channel gained much of the interest in the recent past and has found a wide utilization in modern communication systems [54], the modification of the concept to trace the synchronization error in frame based communication together with an initial correlation mechanism in narrowband radio modem can be considered original. The analysis of the synchronization technique performance under a specific condition of the narrowband radio channel creates also a significant part of this section and a portion of the thesis contribution.

5.5.1. Decision directed algorithm formulation

The description of the algorithm can be started from the base concept of the minimization of the mean-squared error MSE of the detected signal [51], [54] where the objective function is defined as

$$\varepsilon_k^2 = \mathrm{E}\left\{ \left| e[k] \right|^2 \right\} \rightarrow \text{min}, \ \forall k, \qquad (5.40)$$

here *k* is the symbol index. Ideally, the error signal can be calculated as

$$e[k] = x[k] - y[kT + \tau]. \qquad (5.41)$$

In this equation, the $x[k]$ is the transmitted data symbol which is either real value signal for the case of exponential modulation or complex signal in case of linear modulation. In the following, the real signal alternative is assumed for the description simplicity. The same assumption is made for the received signal $y[k]$.

Since the receiver does not have the information about the transmitted symbols, the signal $x[k]$ is replaced by its local estimate $\hat{x}[k]$ or the decisions yielding $\hat{x}[k]$. If the initial timing phase τ_0 has been successfully acquired by the previous block (Section 5.4) it is very likely that both symbol sequences are the same.

$$x[k] = \hat{x}[k] \qquad (5.42)$$

As shown in [51] a *stochastic gradient adaptation* can be used to minimize the MSE. Thus, in optimum condition its gradient should converge to zero

$$\nabla \varepsilon_k^2 = \mathrm{E}\left\{ \left| e[k] \right|^2 \right\} \rightarrow 0. \qquad (5.43)$$

Using fact that the instantaneous timing phase is a scalar, (5.43) can be rewritten into

$$\frac{\partial \varepsilon_k^2}{\partial \tau} = \mathrm{E}\left\{ e[k]\frac{\partial e[k]}{\partial \tau} + \frac{\partial e[k]}{\partial \tau} e[k] \right\} = 2\mathrm{E}\left\{ e[k]\frac{\partial e[k]}{\partial \tau} \right\}. \qquad (5.44)$$

Substituting (5.41) into (5.44) and taking into account that $\hat{m}[k]$ is independent on τ yields to

$$\frac{\partial \varepsilon_k^2}{\partial \tau} = -2\mathrm{E}\left\{ e[k]\frac{\partial y[kT+\tau]}{\partial \tau} \right\}. \qquad (5.45)$$

In case we cannot, or do not want to calculate the ensemble average value as in a case of the previous synchronization algorithm (5.7), it can be approximated as an average of a single realization assigned as $\mathcal{E}_k$

$$\frac{\partial \mathcal{E}_k^2}{\partial \tau} = -2\left\{ e[k]\frac{\partial y[kT+\tau]}{\partial \tau} \right\}, \qquad (5.46)$$

and the recursive adaptation algorithm can be used to minimize the MSE of the detected signal while updating the timing phase towards its optimum value

$$\tau[k+1] = \tau[k] - \mu\frac{\partial \mathcal{E}_k^2}{\partial \tau},$$

$$\tau[k+1] = \tau[k] + 2\mu\left\{ e[k]\frac{\partial y[kT+\tau]}{\partial \tau} \right\}. \qquad (5.47)$$

In (5.47) the μ is the step-size parameter influencing the rate of convergence and stability of the algorithm.

Similarly to the frequency discrimination shown in Section 4.3, the derivation of the received signal in (5.47) can be approximated by the discrete time differentiation over the selected time interval and its angular coefficient describes the direction towards the optimum sampling instant. Using this approximation the term for derivation can be rewritten as

$$\frac{\partial y[kT+\tau]}{\partial \tau} \approx \frac{y(kT+\tau+\Delta\tau) - y(kT+\tau-\Delta\tau)}{2\Delta\tau}. \qquad (5.48)$$

In the case of where the differentiation interval is equal to one half of the sampling period T_s, (5.48) reduces further to

$$\frac{\partial y[kT+\tau]}{\partial \tau} \approx \frac{y[kT+\tau] - y[kT+\tau-T_S]}{T_S}, \qquad (5.49)$$

which finally yields an equation suitable for the digital implementation

$$\tau[k+1] = \tau[k] + \frac{2\mu}{T_s} e[k]\{y[kT+\tau] - y[kT+\tau-T_S]\} \quad 0 \le k < \infty. \qquad (5.50)$$

5.5.2. Adoption the algorithm for the linear modulation techniques

There are two ways in general, of processing the signal modulated by the differential linear modulations.

The first one is by processing the in-phase and quadrature signal components separately by using a differential demodulator followed by a decision circuit. An example for the π/4-DQPSK modulation format can be written as

$$\Delta y[i] = y[i]y^*[i-N] \tag{5.51}$$

and assuming that

$$\alpha_k = \begin{Bmatrix} [0\ \ 0] & \Re(\Delta y_k)\geq 0; \Im(\Delta y_k)\geq 0 \\ [0\ \ 1] & \Re(\Delta y_k)< 0; \Im(\Delta y_k)\geq 0 \\ [1\ \ 1] & \Re(\Delta y_k)< 0; \Im(\Delta y_k)< 0 \\ [1\ \ 0] & \Re(\Delta y_k)\geq 0; \Im(\Delta y_k)< 0 \end{Bmatrix}, \tag{5.52}$$

where $\Re(\Delta y_k)$ and $\Im(\Delta y_k)$ assign the in-phase and quadrature signal components respectively.

Following the same principle of MSE minimization as in the previous section, the formulation of the decision directed symbol timing recovery for the signal demodulator (5.51) can be written as

$$\tau(k+1) = \tau(k) + 2\mu\Re\left\{e^*[k]\frac{\partial \Delta y[kT+\tau]}{\partial \tau}\right\} \quad 0 \leq k < \infty, \tag{5.53}$$

where $e[k]$ is the complex error signal defined as

$$e[k] = \Delta x[k] - \Delta y[kT+\tau], \tag{5.54}$$

and

$$\frac{\partial \Delta y[kT+\tau]}{\partial \tau} \approx \frac{\Delta y[kT+\tau] - \Delta y[kT+\tau-T_S]}{T_S}, \tag{5.55}$$

is also the complex signal.

In (5.53), it is important to note that to calculate the update coefficient in each step, another complex multiplication – besides the one in differential demodulator (5.51) – is needed, but since only the real part of the result is used, the two single multipliers instead of four is the actual need.

There are two biggest disadvantages of the differential demodulator designed according to (5.51). The first one is a dependency of the thresholds levels for decoding the in-phase and quadrature modulation symbols on the input signal amplitude. While it is not an issue for the π/4-DQPSK modulation format, the calculation of the signal thresholds for D8PSK and 16-DEQAM becomes a significant problem. The second disadvantage is an asymmetrical distribution of the signal space among the respective constellation points of the modulation. It results to a significant reduction of the symbol timing interval (Figure 5.19) and makes the symbol timing recovery task even more difficult.

The second method to process the signal modulated by the differential linear modulations is by processing the phase of the incoming signal followed by calculating the phase difference and assigning a respective symbol that has most likely been transmitted.

Again, for the case of π/4-DQPSK the tasks needed to be calculated are as follows

$$\hat{\psi}[i] = arctg\left\{\frac{\Im(y[i])}{\Re(y[i])}\right\}, \tag{5.56}$$

$$\Delta\hat{\psi}[i] = \hat{\psi}[i] - \hat{\psi}[i-N], \tag{5.57}$$

$$\alpha_k = \left\{\begin{matrix} [0\ \ 0] & \Delta\hat{\psi}_k \geq 0; \Delta\hat{\psi}_k < \frac{\pi}{2} \\ [0\ \ 1] & \Delta\hat{\psi}_k \geq \frac{\pi}{2}; \Delta\hat{\psi}_k < \pi \\ [1\ \ 1] & \Delta\hat{\psi}_k \geq \pi; \Delta\hat{\psi}_k < \frac{3\pi}{2} \\ [1\ \ 0] & \Delta\hat{\psi}_k \geq \frac{3\pi}{2}; \Delta\hat{\psi}_k < 2\pi \end{matrix}\right\}, \tag{5.58}$$

where $\hat{\psi}[i]$ can be seen as an estimate of the instantaneous signal phase $\psi[i]$.

The formulation of the decision directed symbol timing recovery algorithm can be thus, written as

$$\tau(k+1) = \tau(k) + 2\mu\left\{e[k]\frac{\partial\Delta\hat{\psi}[kT+\tau]}{\partial\tau}\right\} \quad 0 \leq k < \infty, \tag{5.59}$$

where in this case $e[k]$ is the real error signal defined as

$$e[k] = \Delta\psi[k] - \Delta\hat{\psi}[kT+\tau], \tag{5.60}$$

as well as the result of the phase change differentiation

$$\frac{\partial\Delta\hat{\psi}[kT+\tau]}{\partial\tau} \approx \frac{\Delta\hat{\psi}[kT+\tau] - \Delta\hat{\psi}[kT+\tau-T_S]}{T_S}. \tag{5.61}$$

5.5.3. Statistical TED characteristics

It is common in technical literature [59] to describe the statistical behavior of the TEDs by their two main characteristics. The first one is a so-called *S-curve* describing the MSE as a function of a fixed timing offset and the second is a dependency of the square error variance over the fixed timing offset, the *V-curve*. Both characteristics provide information of the statistical behavior of the TED output error signal in response to the input of a large number of random data symbol samples having fixed and known symbol timing error.

The characteristics presented in this section were generated by the algorithm simulations for various settings. By using two edge values of the excess bandwidth parameter, the first set of results documents its effect on the mean and variance of the squared error signal. In Figure 5.16 it is the case for the 4-level modulation signal used in 4-CPFSK modulation while Figure 5.17 shows the respective plots for 2-level modulation signal intended for 2-CPFSK.

It is important to note two implications from these charts presented. The first one is an error free range[8] or the maximum deviation of the sampling clock generator which can be estimated from the monotonous part of either mean or variance characteristics. For the case where M=4 and excess bandwidth of 25%, the range reaches approximately 20% of the symbol interval. Widening the signal bandwidth also broadens this interval to 30% of the symbol interval for M=4 and excess bandwidth of 50%.

---

[8] From the narrowband LMR design point of view, the error free region is considered where bit-error-rate is better than 1e-5.

For the case where M=2 the error free timing interval can be estimated to 60% and 80% for the excess bandwidths of 25% and 50% respectively. These values play an important role and give the maximum admissible interval for the initial timing estimate accuracy of the proceeding symbol timing recovery stage (Section 5.4).

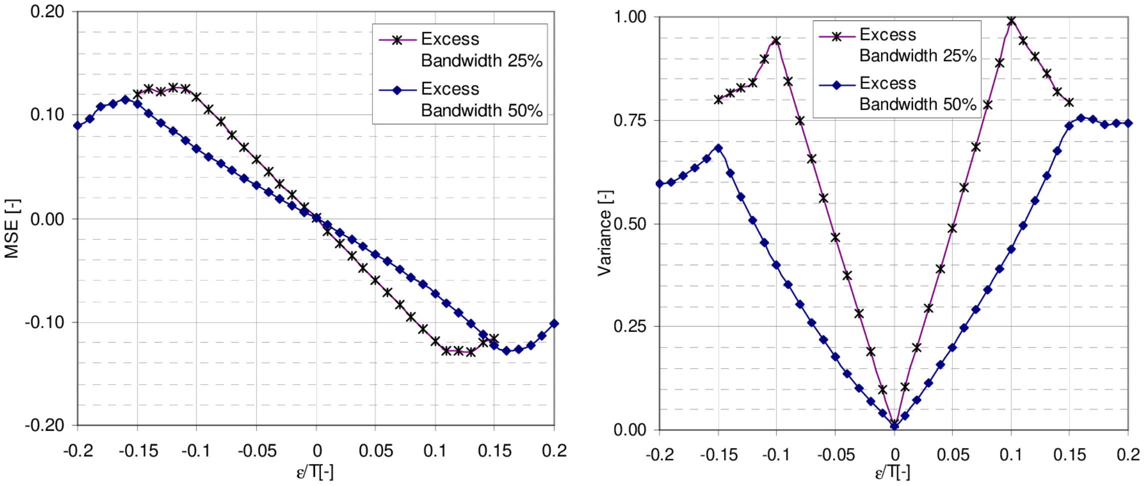

Figure 5.16: Mean square error **(right)** and square error variance **(left)** characteristics of the decision directed TED (5.50) simulated for two values of excess bandwidth. 4-CPFSK, E_b/N_0>50 dB, Mean value calculated over 2048 samples.

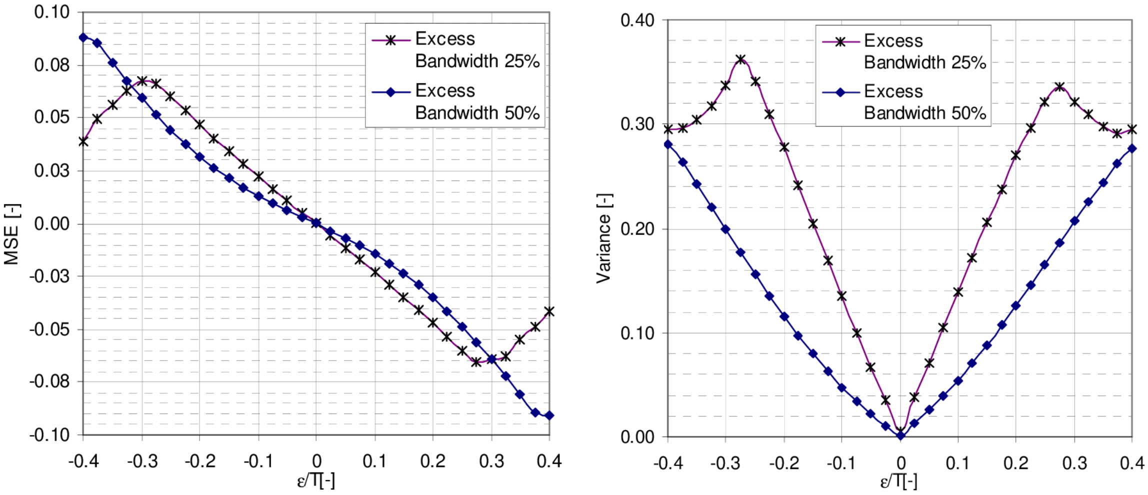

Figure 5.17: Mean square error **(right)** and square error variance **(left)** characteristics of the decision directed TED (5.50) simulated for two values of excess bandwidth. 2-CPFSK, E_b/N_0>50 dB, Mean value calculated over 2048 samples.

On the other hand, the second important finding, resulting from the presented charts, points out that together with lowering the excess bandwidth of the modulation signal the gradient towards the optimum timing instant increases. This is a favorable property improving the convergence rate of the timing algorithm.

In Figure 5.18 and Figure 5.19, there is a graphical comparison of the two TEDs derived in the previous Section 5.5.2 for the differential linear modulations. While for the π/4-DQPSK modulation format the detectors perform almost identically (Figure 5.18), even for the D8PSK modulation, the timing error detector defined by (5.53) performs significantly worse (Figure 5.19). In particular, the error free timing interval can be estimated to 50% of the symbol period in case of π/4-DQPSK and both detectors; 30% for D8PSK and timing error detector 2.; while only less than 15% for timing error detector 1. In all above situations, the excess bandwidth parameter of the pulse shaping filter has been set to 45%.

Therefore, only the statistical characteristics of the timing error detector TED1 based on phase differentiation (5.59) are given in the following figures. In Figure 5.20 to Figure 5.22 there is a comparison of the MSE and normalized square error variance characteristics simulated for two values of the excess bandwidth parameter and constellations of π/4-DQPSK, D8PSK and 16-DEQAM.

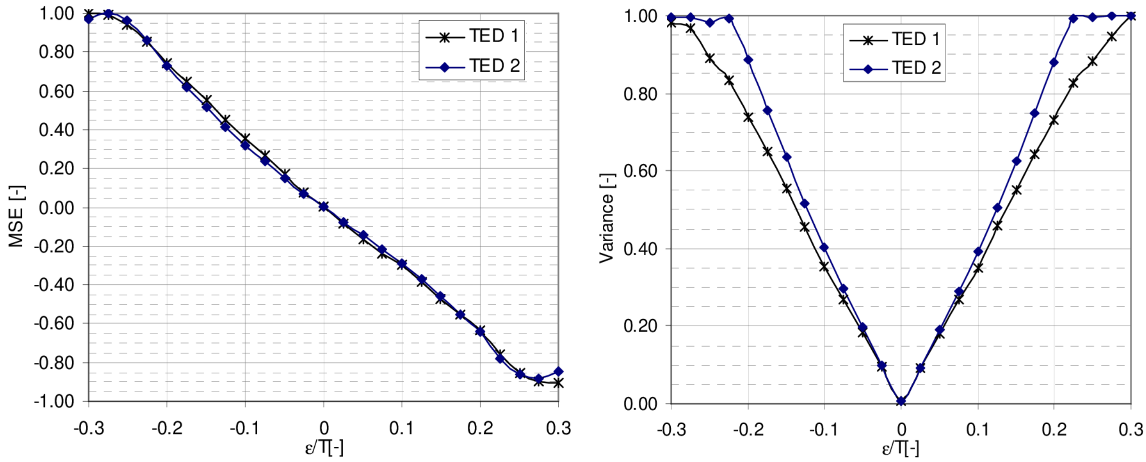

Figure 5.18: Comparison of the normalized mean square error **(right)** and normalized square error variance **(left)** characteristics of the decision directed timing error detectors: TED1(5.59) and TED2 (5.53). π/4-DQPSK, E_b/N_0>50 dB, α_0=0.45.

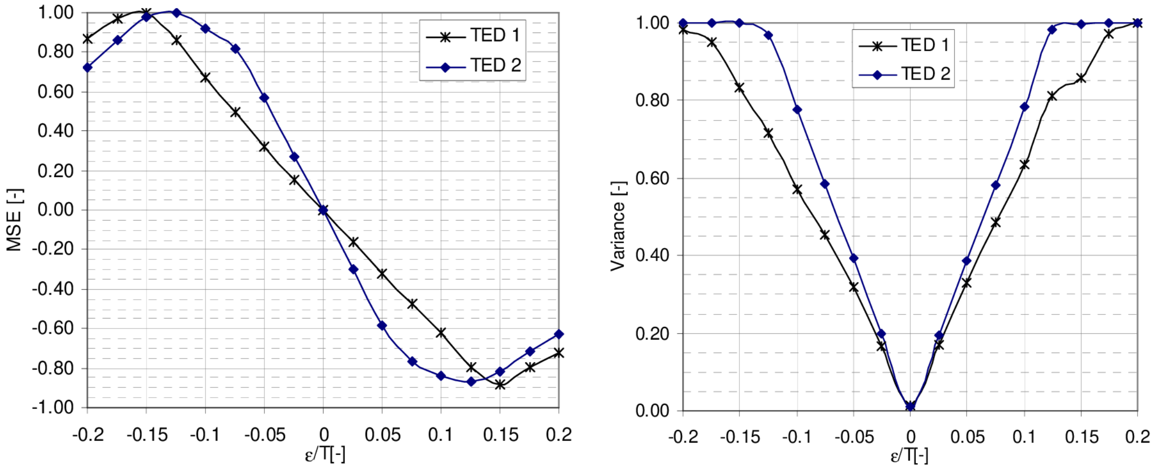

Figure 5.19: Comparison of the normalized mean square error **(right)** and normalized square error variance **(left)** characteristics of the decision directed timing error detectors: TED1(5.59) and TED2 (5.53). D8PSK, E_b/N_0>50 dB, α_0=0.45.

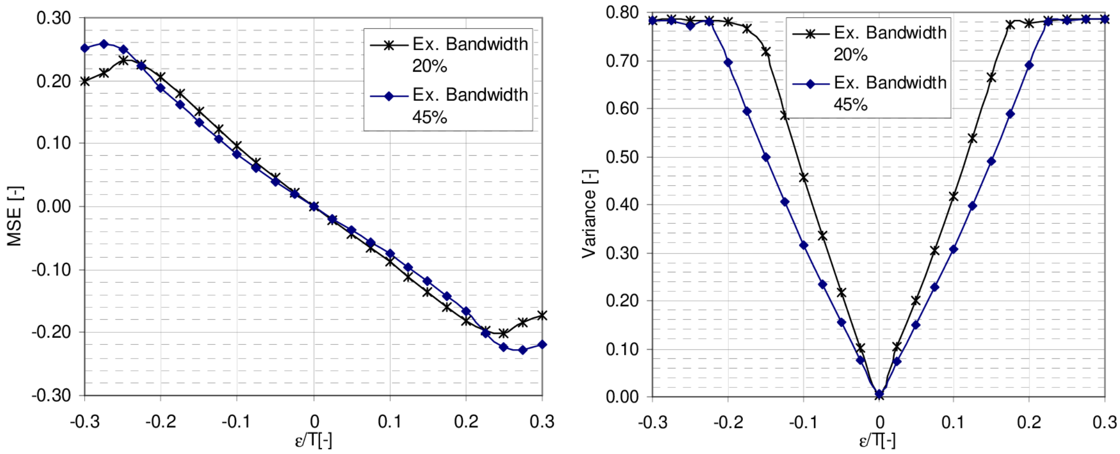

Figure 5.20: Comparison of the mean square error **(right)** and square error variance **(left)** characteristics of the decision directed timing error detector (5.59) simulated for two values of excess bandwidth. π/4-DQPSK, E_b/N_0>50 dB.

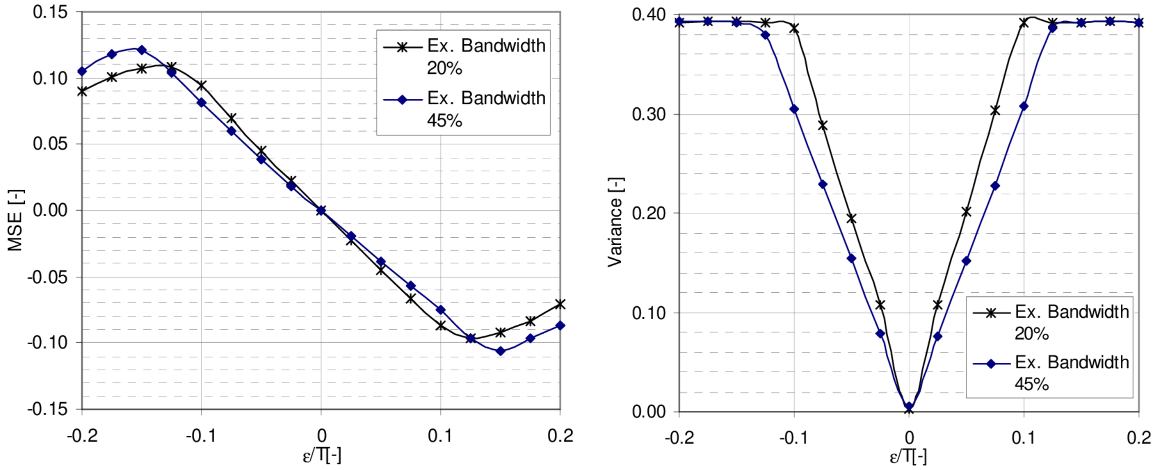

Figure 5.21: Comparison of the mean square error **(right)** and square error variance **(left)** characteristics of the decision directed timing error detector (5.59) simulated for two values of excess bandwidth. D8PSK, E_b/N_0>50 dB.

Based on the results presented it can be concluded, that the error free timing interval lowers down from 50% to 40% with lowering the excess bandwidth for π/4-DQPSK; from 30% to 20% for 8-DPSK and from 20% to 15% in case of 16-DEQAM. It is unfortunate that the higher the number of the modulation states the more precise symbol algorithm is needed. It is also noteworthy that the difference in performance of the TEDs running over D8PSK and 16-DEQAM is low which is caused by the similar constellation arrangement as well as because the error signal is calculated using phase information only and omits the change in amplitude.

One can also note the decrease in the absolute levels of the MSE together with the variance over the increasing constellation order. This is a negative trend since it slows down the convergence rate and limits the interval within which the algorithm works stably. However, as it is shown by the overall synchronization simulation results presented in Section 5.7, together with the initial timing estimate provided by the sample wise pattern correlation algorithm the performance of the synchronizer reach acceptable level for practical implementation.

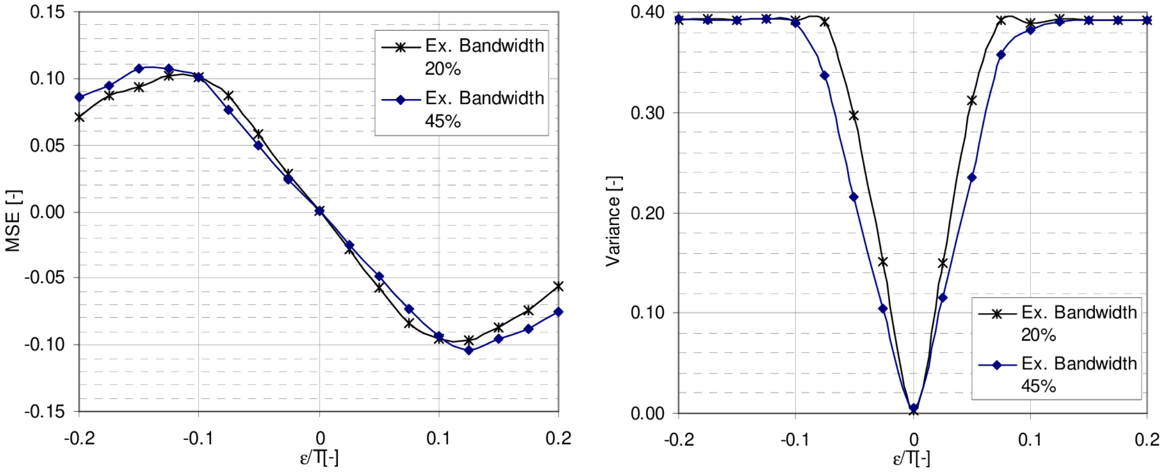

Figure 5.22: Comparison of the mean square error **(right)** and square error variance **(left)** characteristics of the decision directed timing error detector (5.59) simulated for two values of excess bandwidth. 16-DEQAM, E_b/N_0>50 dB.

5.5.4. Simplified formulation of the algorithm

As it is shown by the simulation results in this section a simple modification of the equations (5.50) and (5.59) can be made to reduce an implementation complexity while providing unified performance characteristics for multi state modulation formats. The modification can be written as

$$\tau(k+1) = \tau(k) + 2\mu\left\{e[k]sign\left(\frac{\partial y[kT+\tau]}{\partial \tau}\right)\right\}, \qquad (5.62)$$

where

$$sign(x) = \begin{Bmatrix} 1 & x \geq 0 \\ -1 & x < 0 \end{Bmatrix}. \qquad (5.63)$$

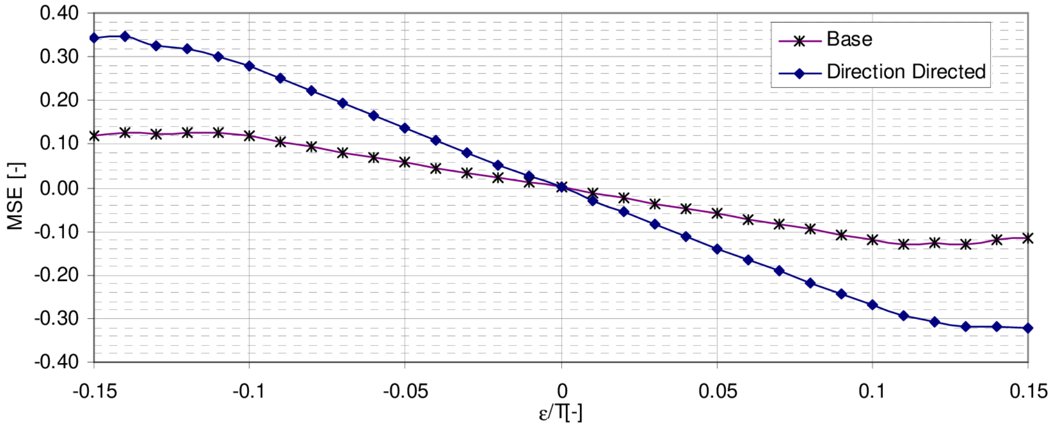

Figure 5.23: Square error variance characteristics comparison for the decision directed TED (5.50) and its direction directed variant (5.62). M=4, E_b/N_0>50 dB, α=25%.

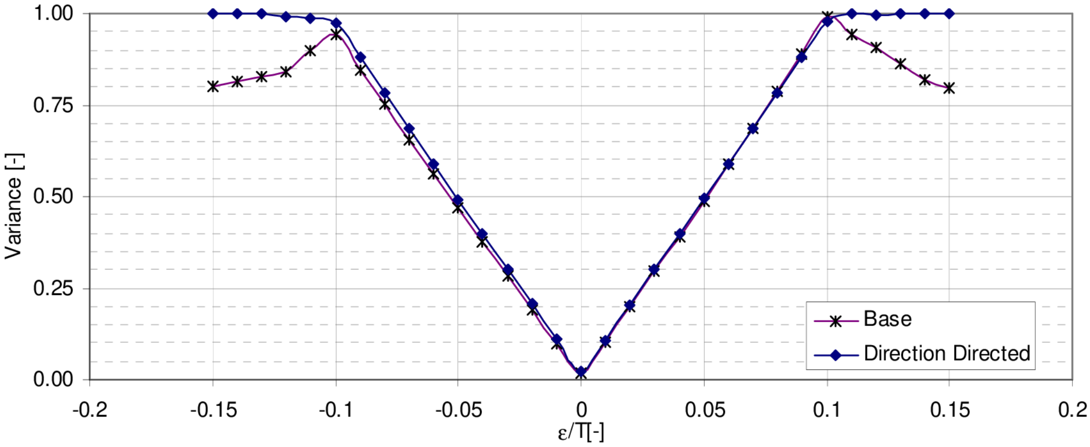

Figure 5.24: Square error variance characteristics comparison for the decision directed TED (5.50) and its direction directed variant (5.62).$M=4$, E_b/N_0>50 dB, α=25%.

The simplification is a result of an assumption that to fulfil the optimization task at each step, one does not need to know the steepness, only the direction of the way towards an optimum is necessary. The resulting algorithm – identified as a *direction directed* in the following text – can thus be seen as an algorithm in between the pure decision directed and the algorithms based on early-late principle [54].

5.5.5. Closed loop performance analysis

In the previous section, all the measured characteristics have been obtained through the open loop simulations and describe the statistical performance of the synchronizers. In the following, the closed loop simulation results are presented.

Firstly, the frequency dependency of the timing estimate variance over the optimum sampling instant oscillation has been simulated. In this case the optimum sampling instant has been periodically shifted within the entire symbol interval in such a way that the instantaneous timing error followed a harmonic function having a selected frequency and amplitude corresponding to one half of the symbol interval. This can be viewed as a simulation of the discrepancy between the transmitter, and receiver, reference oscillators which are used to synchronize the modulation and the demodulated signal respectively. The parameters of the simulation have been set according to the previous chapters, particularly to 4-CPFSK, $h=1/M$, R=12 kBaud and square root Nyquist δ–filter having an excess bandwidth of 28.4%. The simulation results are shown for base decision directed version of the algorithm as well as for its direction directed modification with two levels of the step-size parameter.

There are two important findings that can be extracted from the simulation results shown in Figure 5.25. The first one is the maximum tolerance of the reference oscillators' frequency misalignments that does not exceed a selected error in the symbol decisions. In accordance to the expectation, the lower the step-size parameter the lower the admissible range of frequencies. Even if we select the μ=0.1 and insist on no degradation of the symbol decisions the frequency range of 1 Hz would yield to requirement for the oscillator frequencies accuracies of ±40 ppm, which is easily fulfilled in modern LMR transceivers. The second point to note which goes hand in hand with lowering the step size parameter is the absolute level of the timing estimate variance. As can also be intuitively expected, the lower the step-size parameter, the lower the error variance of the detected symbol. This can be seen in Figure 5.25 for the steady state operation when the oscillation frequency approaches zero.

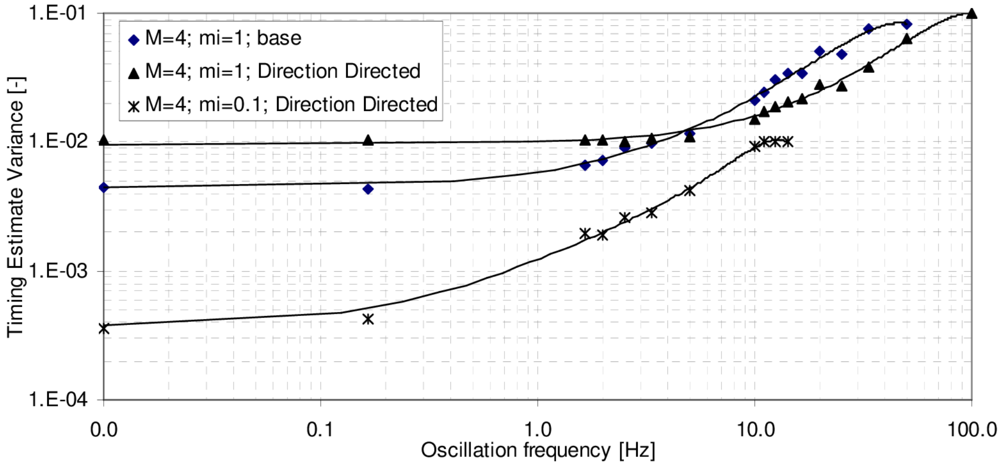

Figure 5.25: Timing estimate variance as a function of the oscillator frequency misalignment. R=12 kBaud, 4-CPFSK, $h=1/M$, E_b/N_0>50 dB, Square root Nyquist δ–filter, α=28.4%.

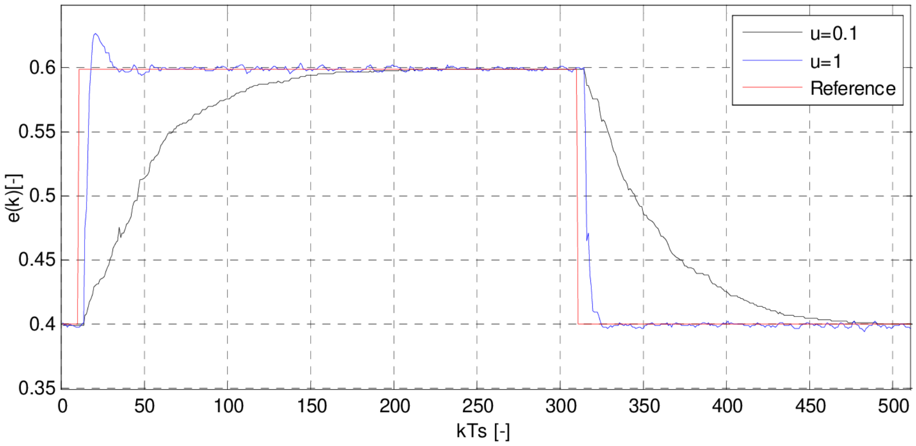

Figure 5.26: Transient responses comparison for two values of step-size parameter μ. R=12 kBaud, 4-CPFSK, $h=1/M$, E_b/N_0>50 dB, Square root Nyquist δ–filter, α=28.4%.

Secondly, the transient responses of the timing estimate for the various levels of the step-size parameter have been simulated. In this simulation, the timing error has been adjusted by a discrete step function and the symbol time intervals needed to converge back to optimum sampling instant has been studied. Examples of the transient responses for the two values of the step-size parameter are shown in Figure 5.26. It can be seen that the acquisition time of the synchronization algorithm is inversely proportional to the step-size parameter and reaches approximately 20 symbols for μ=1 and 200 symbols for μ=0.1.

Thirdly, the performance of the modified decision directed synchronization algorithm in a presence of noise has been simulated. The results are depicted in Figure 5.27. If the performance characteristics of the decision directed TED are compared to respective characteristics of the NDA and DA synchronization algorithms as shown in Figure 5.28 one can conclude that the timing estimate variance of the decision directed synchronizer for a step-size parameter lower than 0.1 lies in between the DA and NDA variants of the synchronization algorithm for the chosen lengths of the observation interval. Since it is assumed that the digital receiver has already acquired symbol synchronization by the correlation process proceeding, this value of the step-size parameter can provide the LMR system with the symbol timing accuracy needed to process even the higher order modulation techniques.

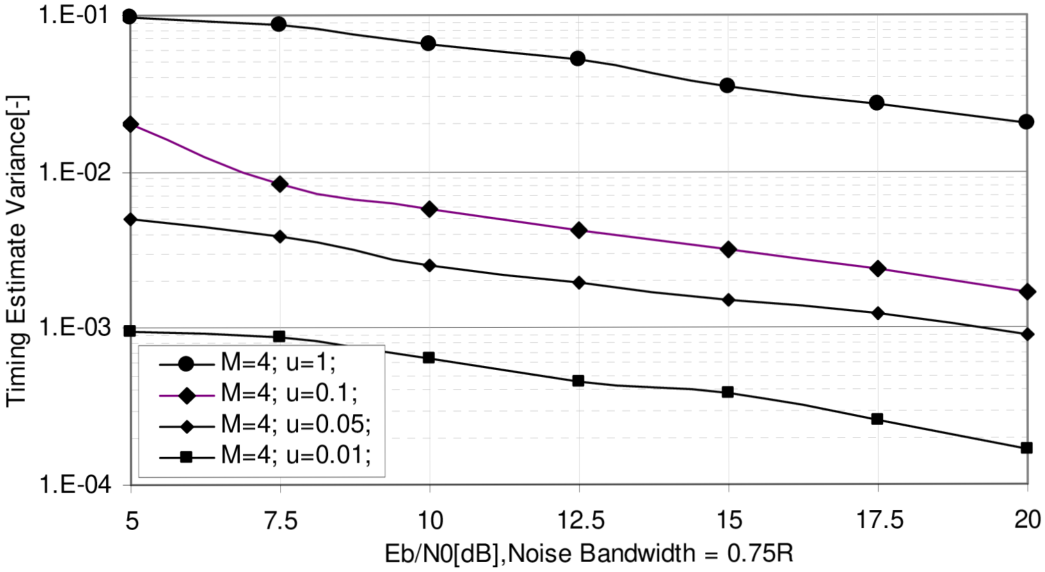

Figure 5.27: Timing estimate variance performance of the decision directed synchronization algorithm for various values of the step-size parameter. $R=12$ kBaud, 4–CPFSK, $h=1/M$, Square root Nyquist δ–filter with excess bandwidth 28.4%.

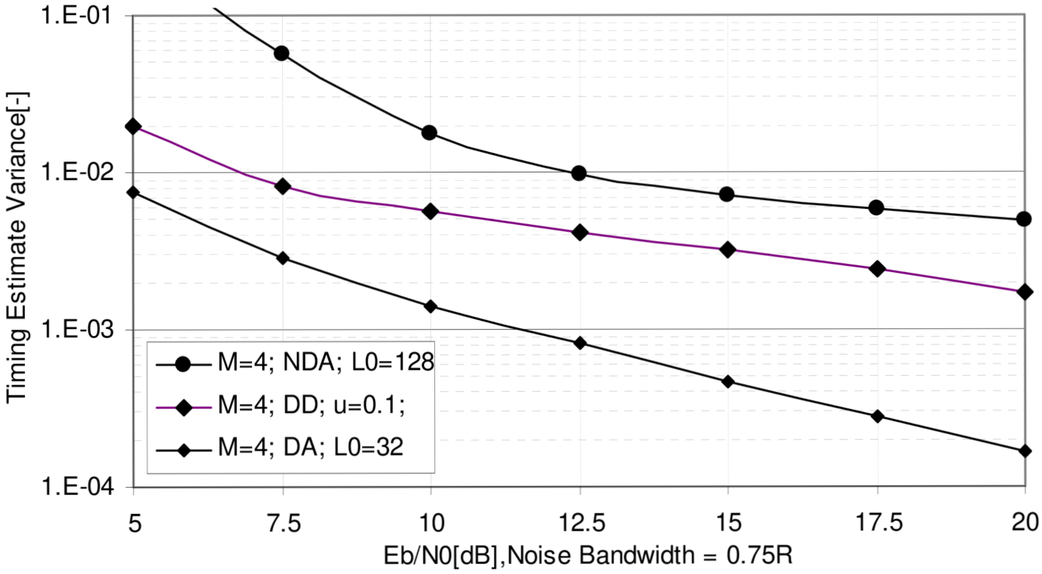

Figure 5.28: Graphical comparison of the timing estimate variance performance of the three studied synchronization algorithms.

5.6. Analysis of the fractional delay interpolators based on Farrow structure

One fact that was hidden in the results of the previous section is that the estimated timing error or offset is a continuous-value parameter representing a distance from the optimum sampling phase. Thus, in order to make use of such a parameter in pure software defined synchronization algorithm, additional timing adjustment algorithms are needed. Basically, there are two methods that can be used for this purpose. One is the poly-phase digital filter (system) representation [76] and the second are the fractional delay interpolators. Since for the narrowband LMR design the complexity of the digital algorithms is also an important issue to consider, the main focus in this section is given to the design and performance analysis of the later timing adjustment mechanism, while it yields to effective digital realization structures [70], [71], [72]. The most of this section has also been published in [72].

5.6.1. General fractional delay interpolator formulation

The basic concept of the fractional delay interpolation has been published by *C.W. Farrow* in his original paper [73]. Since then, the concept has been steadily improved or transformed for a specific applications [74], [75], [77]. The principle of this method results from the fictitious structure shown in Figure 5.29 and it is based on a back transformation to the analog domain.

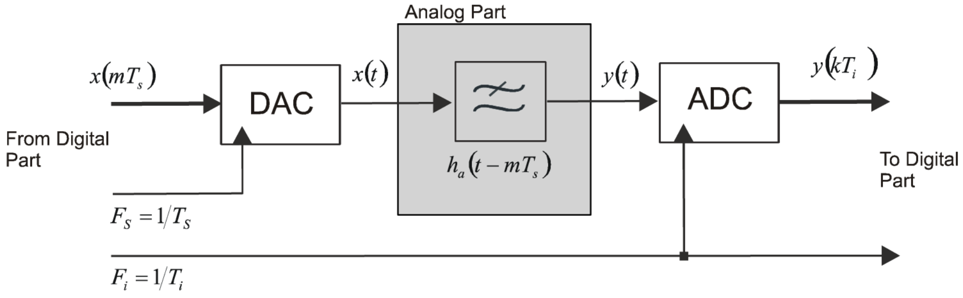

Figure 5.29: Hybrid model of the Farrow interpolator [73], [72].

Referring to Figure 5.29, the stream of digital samples[9] $x(mT_s)$ with the general sampling rate $F_s=1/T_s$ is converted back to original analog domain by the *digital-to-analog converter* (DAC) and after proper analog filtering – with the main task to suppress the higher spectrum replicas only – the signal $y(t)$ is converted back to the digital domain by the *analog-to-digital converter* (ADC) being clocked with a new sampling frequency F_i. Although this structure is not practically feasible it provides a comprehensive conception for the pure digital algorithm.

The signal $x(t)$ at the output of the DAC can be described as [74], [70]

$$x(t) = \sum_{m=-\infty}^{\infty} x(mT_s).\delta(t - mT_s), \qquad (5.64)$$

where $\delta(t-mT_s)$ is the periodic sequence of Dirac impulses. Filtering by the filter having the impulse response $h_a(t)$ influences the analog signal entering the ADC conversion as

---

[9] In this chapter, the sample index “m” instead of “i” as in the previous chapters is used. “i” then assigns the digital filtering index. This notation has been adopted on purpose since it is well-established in this particular area of signal processing algorithms [70] to [74].

$$y(t)=\sum_{m=-\infty}^{\infty} x(mT_s).h_a(t-mT_s), \tag{5.65}$$

and after the ADC, with the sampling rate of $F_i=1/T_i$ which is equal to and therefore commensurate to the symbol rate, it can be rewritten into

$$y(t)=\sum_{m=-\infty}^{\infty} x(mT_s).h_a(kT_i-mT_s). \tag{5.66}$$

To come to an equation suitable for the digital realization it is purposeful to assign indexes as follows [70]

- Signal index:

$$m;\, m=m_k-i \tag{5.67}$$

- Digital filtering index:

$$i=\mathrm{int}(kT_i/T_s)-m \tag{5.68}$$

- Index of the interpolation base-points

$$m_k=\mathrm{int}(kT_i/T_s) \tag{5.69}$$

- Fractional interval:

$$\mu_k=kT_i/T_s-m_k \tag{5.70}$$

In (5.68) and (5.69) the *int*(*x*) function represents the highest integer number not exceeding its argument *x*. All indexes and their relations are shown in Figure 5.30.

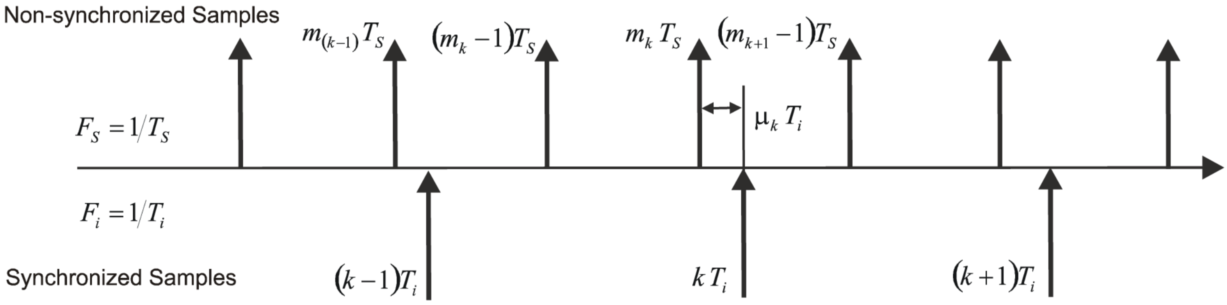

Figure 5.30: Indexing of the digital signal samples [70], [72].

Using relations (5.67) to (5.70), the base equation for the digital fractional interpolation can be written as

$$y(kT_i)=y[(m_k+\mu_k)T_s], \tag{5.71}$$

$$y(kT_i)=\sum_{i=I_1}^{I_2} x[(m_k-i)T_s].h_a[(i+\mu_k)T_s], \tag{5.72}$$

where in (5.72), the digital filtering index is limited from $I_1=-I/2$ to $I_2=I/2-1$ and parameter I is the number digital filter coefficients with an order of I-1. The (5.72) is similar to base definition of the FIR filters by the digital convolution [51] with the difference that the coefficients of the FIR filter are in fact the samples of the analog filter shown in Figure 5.29. This however, is a problem for practical realization since for each value of μ_k there must be new set of filter coefficients. In case an application admits to pre-compute and store all the digital filter coefficient sets, it is possible to choose the corresponding set of coefficients upon the current value of μ_k. This approach yields to memory consuming architectures since it requires a significant portion of embedded memory to store *I* by *N* values of filter impulse response, where *N* is the number of quantization levels of the μ_k.

Different and efficient approach which was proposed in [73] make use of the piece-wise polynomial approximation of the impulse response $h_a(t)$. In this case, the continuous time impulse response $h_a(t)$ is divided by the *I* base-points to the *I*-1 equidistant intervals

$$h_a(t) = h_a[(i+\mu_k)T_s] = \sum_{l=0}^{N=I-1} b_l(i)\mu_k^l \,, \tag{5.73}$$

where $b_l(i)$ are the *Farrow coefficients*. In general case, the Farrow coefficients are constant and independent of the fractional interval μ_k. In each interval, the impulse response is approximated by the polynomial of the same order *N*. Substituting (5.73) into the base interpolation equation (5.72), the equation (5.72) can be written in form of (5.75) that is more suitable for digital filter realization

$$y(kT_i) = \sum_{i=I_1}^{I_2} x[(m_k - i)T_s].\sum_{l=0}^{N} b_l(i)\mu_k^l \,, \tag{5.74}$$

$$y(kT_i) = \sum_{l=0}^{N} \mu_k^l \sum_{i=I_1}^{I_2} b_l(i)x[(m_k - i)T_s] \,. \tag{5.75}$$

To derive the Farrow coefficients it is efficient to make use of the classical formulation of the *Lagrange polynomial interpolation* generally defined as [78]

$$y = f(x) = \sum_{i=0}^{N} y_i C_i(x) \tag{5.76}$$

$$C_i(x) = \prod_{j=0, j\neq i}^{N} \frac{x - x_j}{x_i - x_j} \tag{5.77}$$

It is known that for *I* base-points, the order of the polynomial interpolation *N* can reach, at most, the value of *I*-1. It means that one needs to know at least two base-points to calculate the characteristic equation of the line connecting both points, *N*=1. In (5.57) the x_i, y_i; x_j, y_j are the known base-points. Thus, the value of *y* in an arbitrary position *x* – assuming that the base-points and the order of the polynomial interpolation are known – can be calculated.

In order to calculate the Farrow coefficients using Lagrange polynomial interpolation (5.77) can be rewritten into

$$C_i(x) = \prod_{j=0, j\neq i}^{N} \frac{x - x_j}{x_i - x_j} \Rightarrow C_i(\mu_k) = \prod_{j=I_1, j\neq i}^{I_2} \frac{-\mu_k - j}{i - j} \,, \qquad I_1 \le i \le I_2,\ I_1 = -I/2,\ I_2 = I/2 - 1 \tag{5.78}$$

whereas the approximated impulse response is given by

$$h_a[(i+\mu_k)T_s] = C_i(\mu_k) = \sum_{l=0}^{N=I-1} \mu_k^l b_l(i) \,. \tag{5.79}$$

According to [71] there must be an even number of the base-points in order to get the unique assignment between the interpolant and the base-point sets in the entire range of the impulse response. Moreover, to provide a correct output sample timing, the interpolant has to be calculated in the centre of base-point interpolation interval. This is the reason, why (5.72) or (5.75) is limited within the interval from I_1=-I/2 to I_2=I/2-1. If this is the case, one must subsequently use a negative value of the fractional interval μ_k for the interpolation calculation, as it is shown in (5.78).

An alternative approach – yielding to the same results, naturally – is to select the interval from I_1=-I/2+1 to I_2=I/2. In this case, the coefficients of the filter impulse response are given as

$$C_i(\mu_k) = \prod_{j=I_1, j\neq i}^{I_2} \frac{\mu_k - j}{i - j}, \qquad (5.80)$$

and subsequently, the equation for the output sample changes into

$$y(kT_i) = \sum_{i=I_1}^{I_2} x[(m_k + i)T_s] \sum_{l=0}^{N} b_l(i)\mu_k^l . \qquad (5.81)$$

In the following section, the first definition (5.72) and (5.78) is used, which is also in accordance with the original reference [71].

5.6.2. Digital filters with low order of the interpolation polynomial

Based on the previous section, the formulation of the digital fractional delay interpolator for the lowest and even number of the base-points set I=2; can be written as

$$\begin{aligned} C_{-1}(\mu_k) &= \frac{-\mu_k - (0)}{(-1)-(0)} = b_1(-1)\mu_k + b_0(-1) = \mu_k \\ C_0(\mu_k) &= \frac{-\mu_k - (-1)}{(0)-(-1)} = b_1(0)\mu_k + b_0(0) = 1 - \mu_k \end{aligned} , \qquad (5.82)$$

and substituting (5.82) into (5.74) we can rewrite (5.74) into

$$y(kT_i) = \{x[m_k - (-1)]\}.\{b_1(-1)\mu_k^1 + b_0(-1)\mu_k^0\} + \{x[m_k - (0)]\}.\{b_1(0)\mu_k^1 + b_0(0)\mu_k^0\},$$

$$y(kT_i) = x(m_k) + \mu_k[x(m_k + 1) - x(m_k)]. \qquad (5.83)$$

Equation (5.83) describes the simplest example of the digital filter with a fractional delay element μ_k based on Farrow structure [73] and *linear* polynomial interpolation (Figure 5.31).

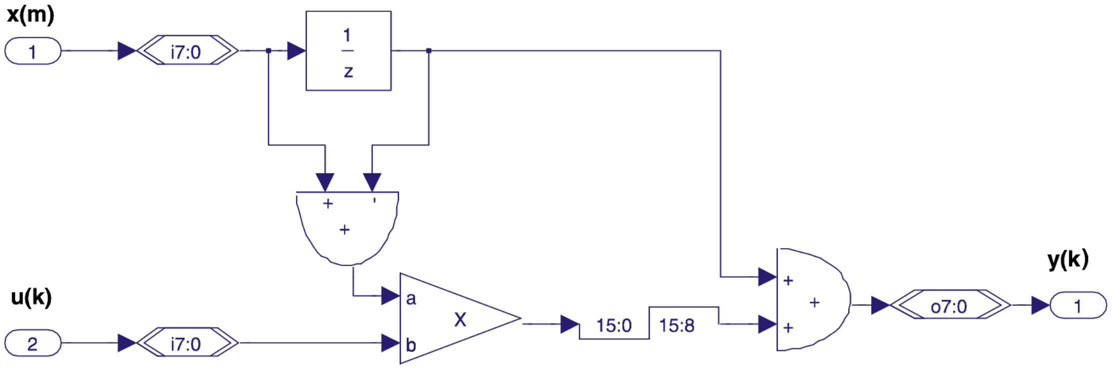

Figure 5.31: Farrow structure of the fractional delay interpolator with a linear polynomial interpolation. (8-bit fixed-point architecture Altera DSP builder blockset in use).

Next higher base-point set with an even number of interpolation base-points is for I=4. Using the same equation (5.78), the Farrow coefficients can be written as

$$C_{-2}(\mu_k) = \frac{1}{6}.\mu_k^3 + 0.\mu_k^2 - \frac{1}{6}\mu_k^1 \ + 0.\mu_k^0$$

$$C_{-1}(\mu_k) = -\frac{1}{2}.\mu_k^3 + \frac{1}{2}.\mu_k^2 + 1.\mu_k^1 + 0.\mu_k^0$$

$$C_0(\mu_k) = \frac{1}{2}.\mu_k^3 - 1.\mu_k^2 - \frac{1}{2}.\mu_k^1 + 1.\mu_k^0$$

$$C_1(\mu_k) = -\frac{1}{6}.\mu_k^3 + \frac{1}{2}.\mu_k^2 - \frac{1}{3}.\mu_k^1 + 0.\mu_k^0 . \qquad (5.84)$$

Substitution of the (5.84) into (5.74) yields a formulation of the fractional delay interpolation filter having a *cubic* polynomial interpolation. The realization structure of the so called *cubic interpolator* is shown in Figure 5.32, which can also be seen as a generalization of the Farrow structure for fractional delay interpolation filters of higher order of the interpolation polynomial. The Farrow coefficient based on the given interpolation polynomial are collectively given in Table 5.1.

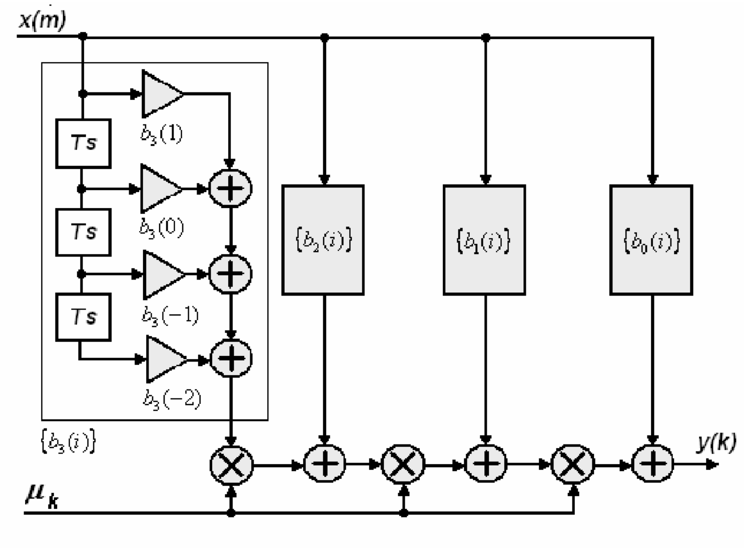

Figure 5.32: Farrow structure of the fractional delay interpolator with a cubic polynomial interpolation.

Table 5.1: Farrow coefficients of the fractional delay interpolators with a cubic and parabolic polynomial interpolation.

	coefficients $b_l(i)$			
i	l=3	l=2	l=1	l=0
-2	1/6	0	-1/6	0
-1	- 1/2	1/2	1	0
0	1/2	- 1	- 1/2	1
1	- 1/6	1/2	-1/3	0
Cubic interpolator				

	coefficients $b_l(i)$		
i	l=2	l=1	l=0
-2	α	$-\alpha$	0
-1	$-\alpha$	$\alpha+1$	0
0	$-\alpha$	$\alpha-1$	1
1	α	$-\alpha$	0
Parabolic interpolator			

According to [71], there is also a possibility to calculate interpolation polynomial of the second order for the base-point set containing 4 base-points. This approach yields a parabolic interpolator. As it is shown in the next section, the parabolic interpolator has the performance very close to the cubic interpolator, but the implementation complexity is significantly reduced. The definition equations of the Farrow coefficients of the parabolic interpolator can be derived from the formulas (5.84) as

$$\begin{aligned} C_{-2}(\mu_k) &= \alpha.\mu_k^2 \quad - \alpha.\mu_k^1 \quad + 0.\mu_k^0 \\ &= b_2(-2)\mu_k^2 + b_1(-2)\mu_k^1 + b_0(-2)\mu_k^0 \\[1ex] C_{-1}(\mu_k) &= -\alpha.\mu_k^2 \quad + (\alpha+1).\mu_k^1 + 0.\mu_k^0 \\ &= b_2(-1)\mu_k^2 + b_1(-1)\mu_k^1 \quad + b_0(-1)\mu_k^0 \\[1ex] C_{0}(\mu_k) &= -\alpha.\mu_k^2 \quad + (\alpha-1).\mu_k^1 + 1.\mu_k^0 \\ &= b_2(0)\mu_k^2 + b_1(0)\mu_k^1 \quad + b_0(0)\mu_k^0 \\[1ex] C_{1}(\mu_k) &= \ \alpha.\mu_k^2 \quad - \alpha.\mu_k^1 \quad + 0.\mu_k^0 \\ &= b_2(1)\mu_k^2 + b_1(1)\mu_k^1 + b_0(1)\mu_k^0 . \end{aligned} \tag{5.85}$$

From (5.85), it is evident that the interpolation of the four base-point set by the second order polynomial is not uniquely defined and depends on α parameter. Selecting $\alpha=1/2$ the implementation complexity of the algorithm is significantly reduced, since there are only two multiplications required. By selecting different values of α parameter, the parabolic interpolator can be changed into linear ($\alpha=0$) interpolator. The realization structure of the parabolic interpolator is shown in Figure 5.33. Again, the Farrow coefficients based on the parabolic interpolation polynomial are given in Table 5.1.

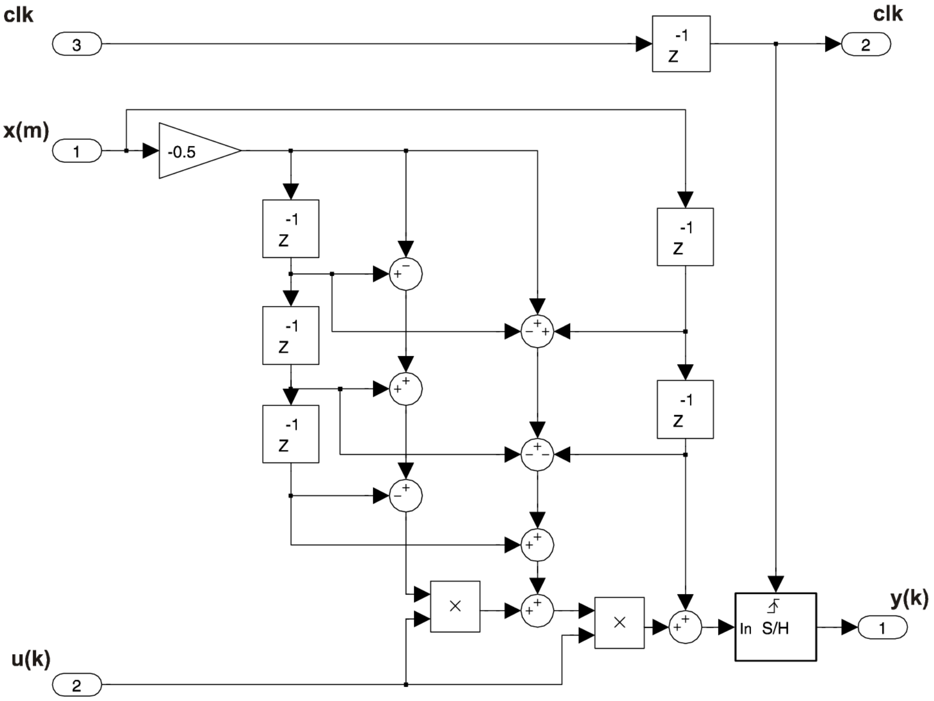

Figure 5.33: Farrow structure of the fractional delay interpolator with a parabolic polynomial interpolation. (Floating point model, Matlab Simulink)

5.6.3. Characteristics of the low order fractional delay interpolators

The fractional delay interpolation filters based on described Farrow structure represent a certain analogy to the hybrid digital-analog system shown in Figure 5.29. As such, the coefficients of the digital filter depend on the fractional interval μ_k. If the quantization of the fractional interval μ_k is not assumed, the infinite number of the digital impulse responses form one continuous impulse response of the analog filter, as shown in Figure 5.34. For the large order of the interpolation polynomial, the resulting impulse response of the digital fractional interpolator would be undistinguishable from its analog counterpart. Even for low order interpolation polynomials the digital filters provides a reasonable trade off between their performance and implementation complexity. In Figure 5.34 there are continuous impulse responses shown for the polynomial approximation of *linear*, *parabolic* and *cubic* interpolation. They represent the sets of all possible coefficients of the particular fractional delay interpolation filter.

Next, the amplitude frequency characteristics, as shown in Figure 5.35, can be evaluated. The biggest signal distortion caused by the fractional delay digital interpolator can be expected in the middle of the signal sample interval, i.e. for the value of the fractional delay parameter μ_k=0.5. Therefore, to compare the amplitude frequency characteristics, this was the chosen value of μ_k and impulse responses coefficients. From the graphical comparison shown in Figure 5.35 it is evident that there is only a slight difference in performance between the cubic and parabolic interpolation. Since the parabolic interpolator requires only two hardware multiplications, ten additions/subtraction operations, it is a preferable choice for the LMR design implementation.

By analyzing the amplitude frequency characteristics of the fractional interpolators – as they are given in a relative frequency scale from zero to Nyquist frequency – it can also be seen that the higher the oversampling ratio, the less distortion is caused to the processed signal. Thus, for the oversampling factor exceeding 5 or 6 signal samples per modulation symbol even the simplest linear interpolator, as shown in Figure 5.31, can be a reasonable choice.

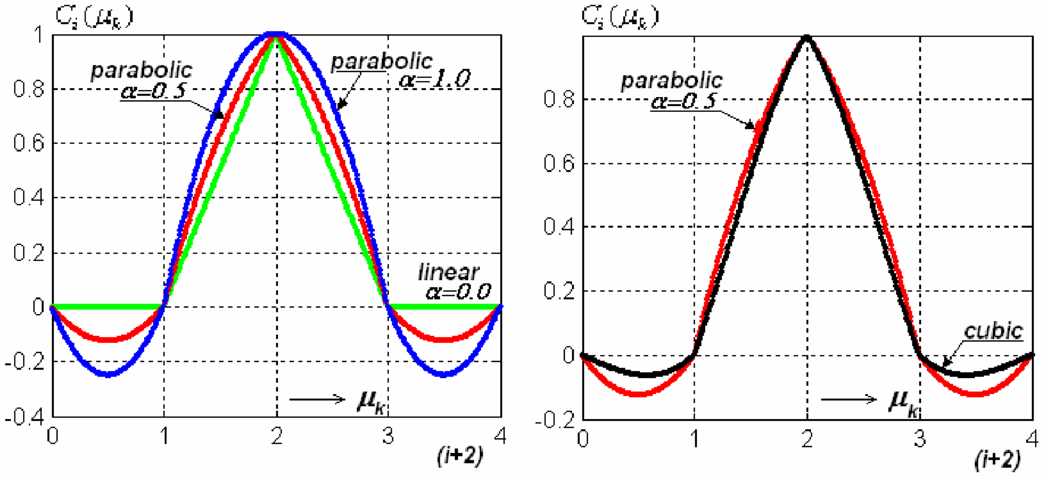

Figure 5.34: The continuous representation of the possible sets of the fractional delay interpolation filters. **(left)** By selecting different values of α=0 the parabolic interpolator can be changed into linear interpolator. **(right)** A direct comparison of the impulse responses (parabolic, and cubic interpolator).

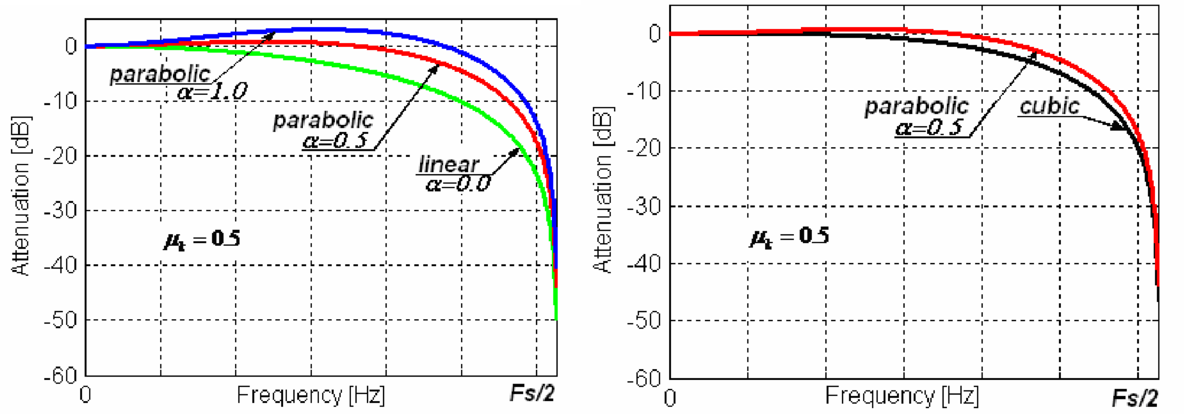

Figure 5.35: (left) Amplitude frequency characteristics of the parabolic interpolator for a selected values of the α parameter and fractional delay of μ_k=0.5. **(right)** Direct comparison of the amplitude frequency characteristics of the parabolic and cubic interpolator for a fractional delay of μ_k=0.5.

5.7. Synchronization algorithm's performance simulation

The scope of this chapter is to evaluate the overall performance of the proposed frame and symbol synchronization scheme, intended particularly for the narrowband LMR utilizing the studied digital modulation techniques. The evaluation criterion in form of symbol-error-rate has been selected. In the first part, the radio channel convolving with the incoming signal is assumed to have fixed and constant frequency characteristics and be corrupted only by the presence of the AWGN having pre-defined parameters. In the second part, the robustness of the proposed system against the multipath fading process of selected parameters is simulated and evaluated.

5.7.1. AWGN channel

The fundamental block diagram of the proposed synchronization scheme to be evaluated can be found in Figure 5.1. The particular parameters that have been used in the simulation are as follows.

- Parameters related to the digital modulations for the selected modes of operation have been set as they were derived in Section 3.4:
    - 2-CPFSK: 13.02 kBaud; modulation index h=0.5;
    - 4-CPFSK: 12 kBaud; modulation index h=0.25;
    - Modulation and matched filter, the square root Nyquist δ-filter with equivalent excess bandwidth of 28.4%, as derived in Section 3.3;
    - π/4-DQPSK, 8DPSK, 16-DEQAM: 17.3 kBaud;
    - Modulation and matched filter, the square root Nyquist δ-filter with equivalent excess bandwidth of 45%, as derived in Section 3.3;
    - Oversampling factor N=10 samples per one modulation symbol.
- Parameters of the physical layer test frames as derived in Section 5.4:
    - Preamble length L_0=16 symbols;
    - Data payload of a given length for each frame has been generated using randomly seeded random generator (Matlab, Simulink).
- The receiver processed bandwidth has been selected as:
    - For exponential modulations, the processed bandwidth ($B_N \approx 10.9$ kHz) has been set by the main channel selectivity FIR filter;
    - For linear modulation the processed bandwidth has been defined by the receiver matched filter and can be approximated by formula $B_N=(1+\alpha)R/2$, where α is the equivalent excess bandwidth parameter and R is the symbol rate, ($B_N \approx 12.5$ kHz).
- Other parameters of the simulations:
    - Correction of the symbol timing has been performed using the fractional interpolator having the Farrow structure of linear interpolation as described in Section 5.6;
    - For exponential modulations the modified mathematic algorithm for digital frequency discrimination has been selected (Section 4.5);
    - Direction directed version of the decision directed TED as derived in Section 5.5 has been used. The step-size parameter μ=0.1, unless otherwise noted.

In the first part, the system under consideration has been ideally synchronized to provide reference power efficiency characteristics for each respective type of modulation. The simulation results can be seen in Figure 5.36 and Figure 5.37. In Figure 5.37, the normalize signal-to-noise ratio has been recalculated using the (4.4) and (4.5) in form

$$SNR\ [dB] = \frac{E_b}{N_0}[dB] + 10\log_{10}(k) + 10\log_{10}\left(\frac{R}{B_N}\right), \qquad (5.86)$$

where k is the number of bits per modulation symbol, R is the symbol rate and B_N is the respective noise bandwidth.

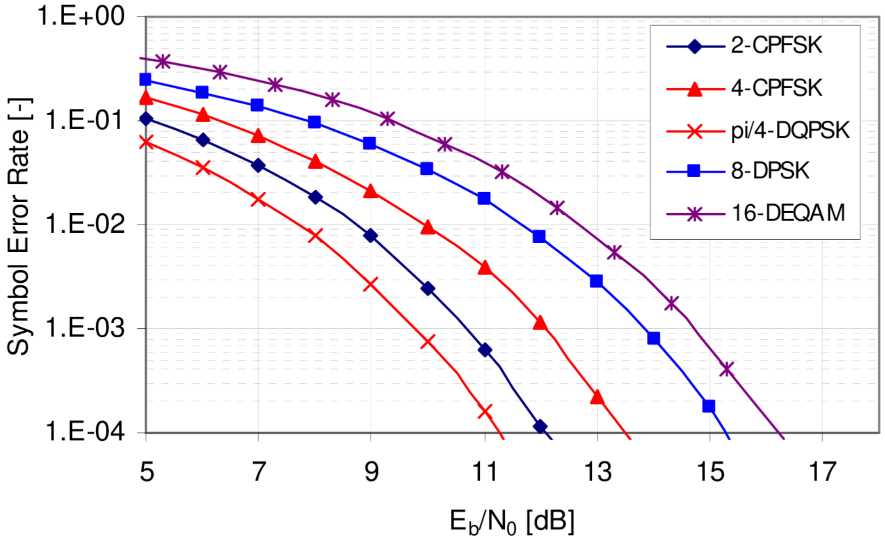

Figure 5.36: Symbol-error-rate characteristics for ideally synchronized digital receiver.

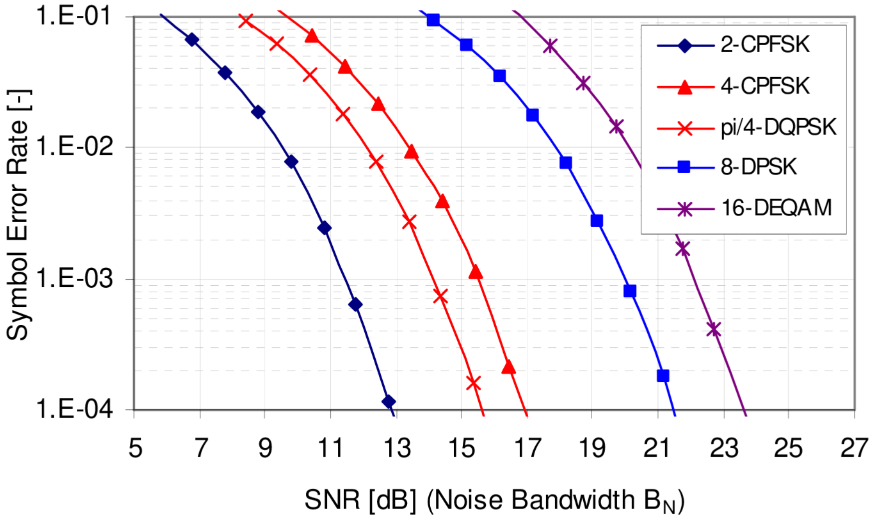

Figure 5.37: Symbol-error-rate characteristics for ideally synchronized digital receiver. The values of SNR have been calculated using (4.4) and (4.5) with respective noise bandwidths and modulation rates.

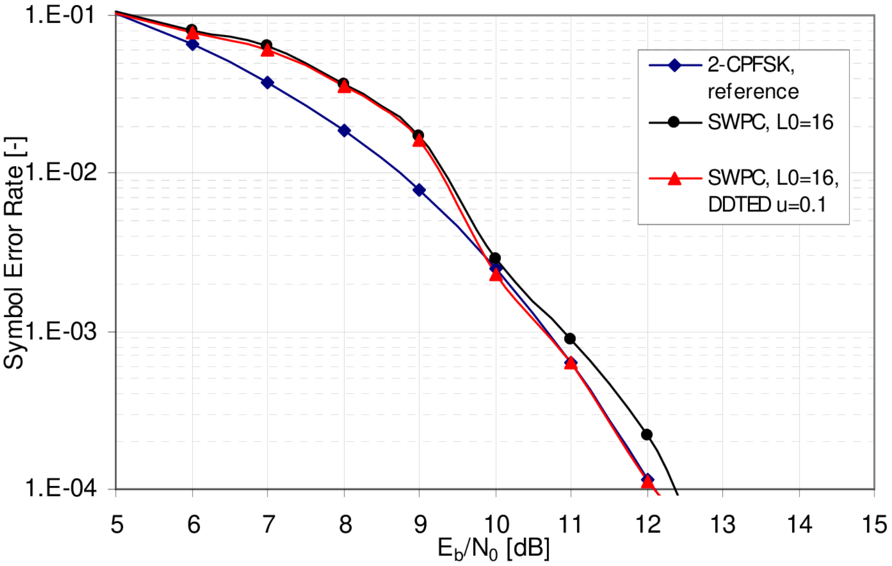

Figure 5.38: Results of the symbol-error-rate analysis for the three modes of the symbol and frame timing synchronization of the narrowband digital receiver. 2-CPFSK modulation technique; frame length 64 B.

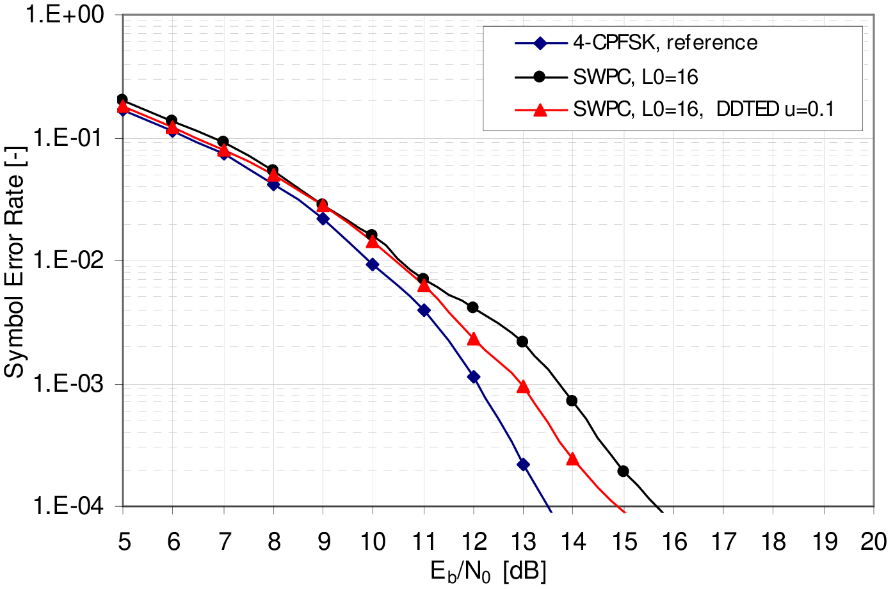

Figure 5.39: Results of the symbol-error-rate analysis for the three modes of the symbol and frame timing synchronization of the narrowband digital receiver. 4-CPFSK modulation technique; frame length 64 B.

Secondly, the behavior of the proposed synchronization scheme has been simulated in two modes. In the first mode, the synchronization task has been achieved using the sample wise pattern correlation technique, as derived in Section 5.4, while the tracking part of the algorithm has been disabled. In Figure 5.38 to Figure 5.43 there are respective power efficiency characteristics of this mode assigned as *"SWPC, L_0=16"*. The second mode represents the complete synchronization scheme utilizing the acquisition and tracking mechanisms as they were formulated in the previous chapters. – The results are assigned as *"SWPC, L_0=16, DDTED μ=0.1"*.

It can be seen from the simulation results (Figure 5.38 to Figure 5.43) that there is a significant influence of initial correlation synchronization precision upon the overall symbol-error-rate of the system within the selected interval. The worsening is more evident for the low constellation ordering modulation – 2CPFSK, 4CPFSK, π/4-DQPSK, while they require lower SNR to reach given SER and the variance of the initial synchronization information as provided by the sample wise pattern correlation is dominant in this region (Section 5.4.6). The tracking part of the synchronization algorithm corrects the symbol timing precision during the time of the receiving frame, but it takes several symbol intervals that have higher likelihood of the incorrect symbol detection.

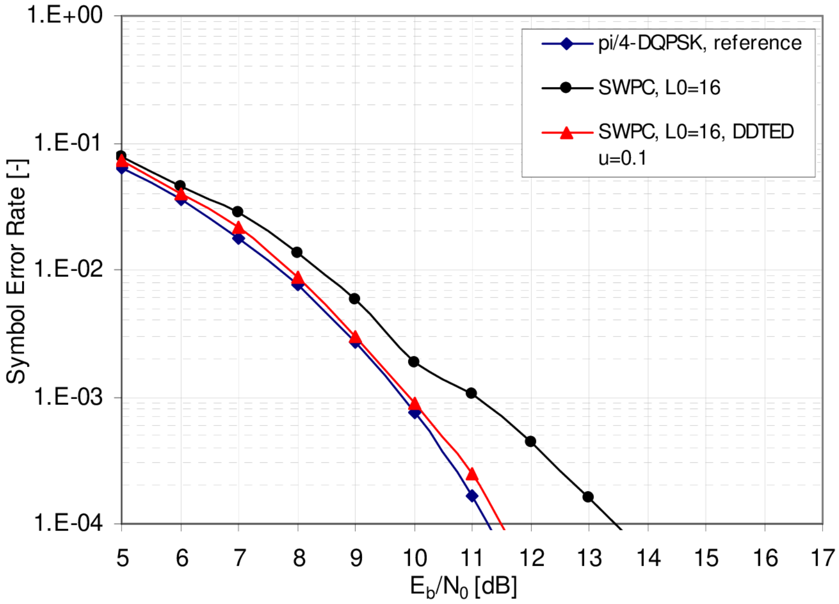

Figure 5.40: Results of the symbol-error-rate analysis for the three modes of the symbol and frame timing synchronization of the narrowband digital receiver. π/4-DQPSK modulation technique; frame length 64 B.

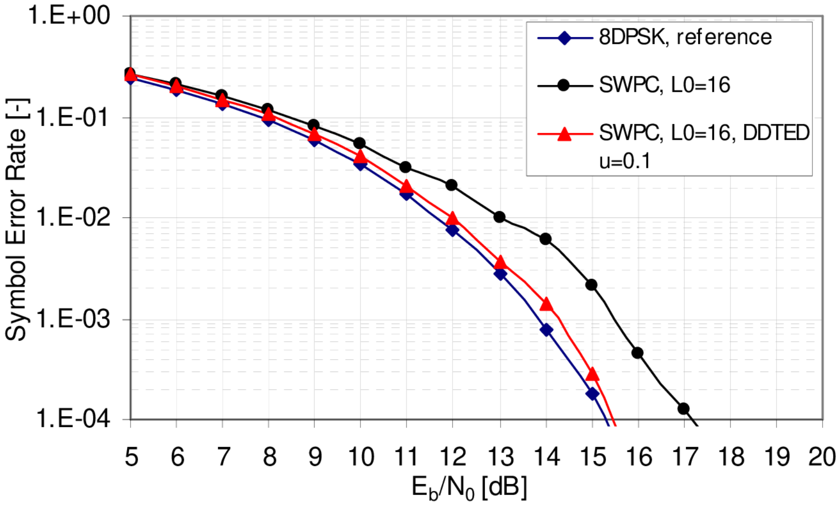

Figure 5.41: Results of the symbol-error-rate analysis for the three modes of the symbol and frame timing synchronization of the narrowband digital receiver. 8-DPSK modulation technique; frame length 64 B.

Fastening the symbol timing recovery loop can improve the transient response, however, at a particular SNRs the inherent variance of the timing estimation would again cause an increase in probability of wrong symbol detection. Thus, to find the optimum value of the step-size parameter for the particular mode of operation it would require running a demanding optimization techniques (Figure 5.46). Nevertheless, even with selected value of the step-size parameter, that has been set from the transient analysis described in Section 5.5.5, the performance penalty compared to optimally synchronized system power efficiency in an analyzed interval of symbol error probabilities reaches 1 dB which can be judged acceptable for practical realization and the performance can be taken as a benchmark for the future synchronization algorithm improvements.

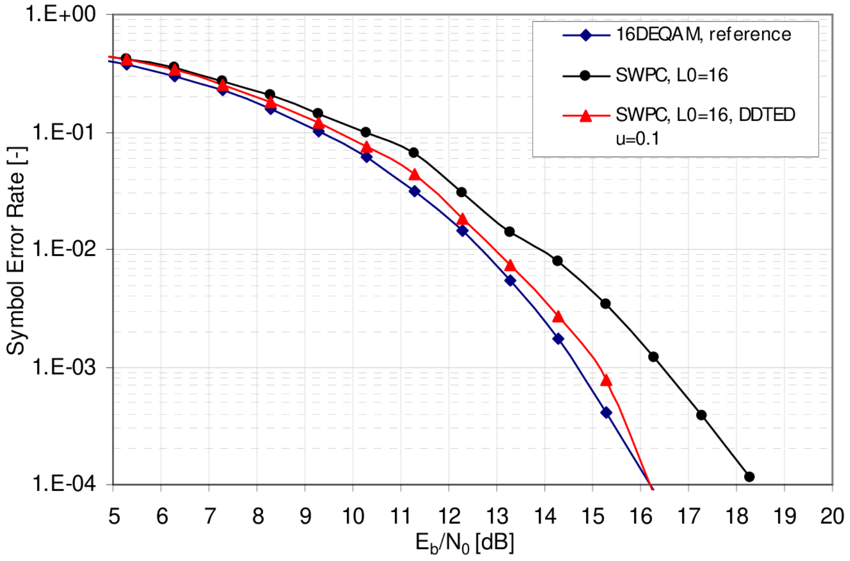

Figure 5.42: Results of the symbol-error-rate analysis for the three modes of the symbol and frame timing synchronization of the narrowband digital receiver. 16-DEQAM modulation technique; frame length 64 B.

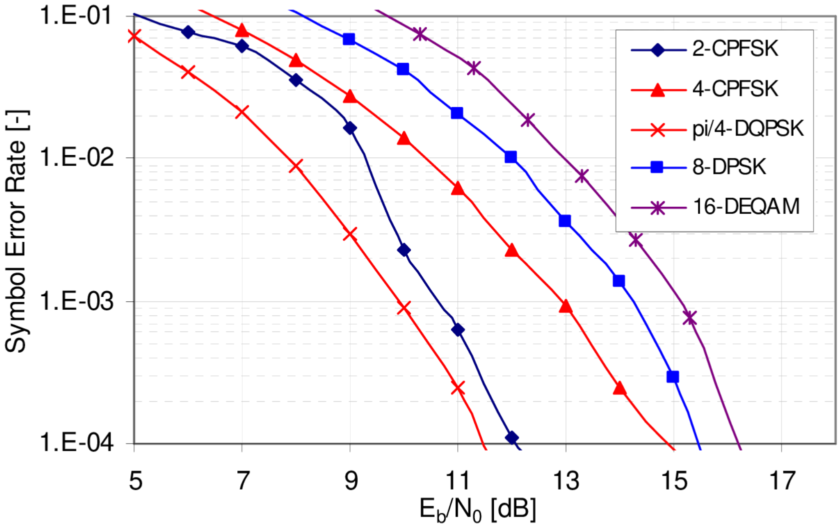

Figure 5.43: Power efficiency characteristics comparison for the selected modulation techniques. The complete synchronization mechanism (SWPC L_0=16, DDTED μ=0.1) has been used; frame length 64 B.

Thirdly, the same system simulations have been run with a fixed SNR corresponding approximately to the SER of ~10^{-3}. This time, the simulations have been run for various frame lengths to examine the algorithm behavior over the different frame lengths. The results are shown in Figure 5.44 to Figure 5.46.

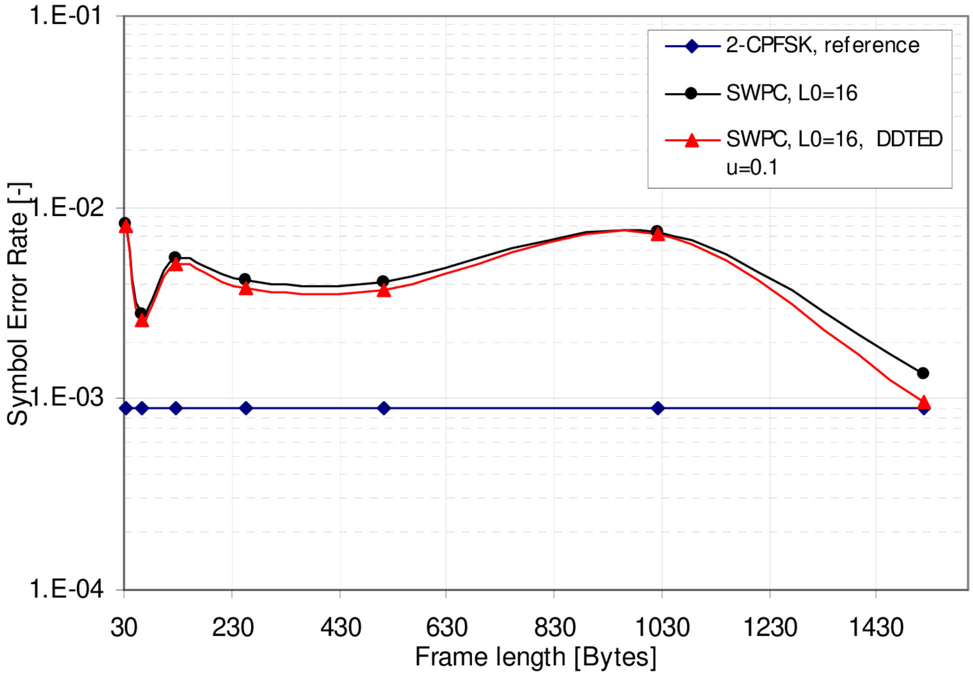

Figure 5.44: Results of the symbol-error-rate analysis of the synchronization algorithm for selected value of E_b/N_0=11dB and different lengths of the test frames. 2-CPFSK

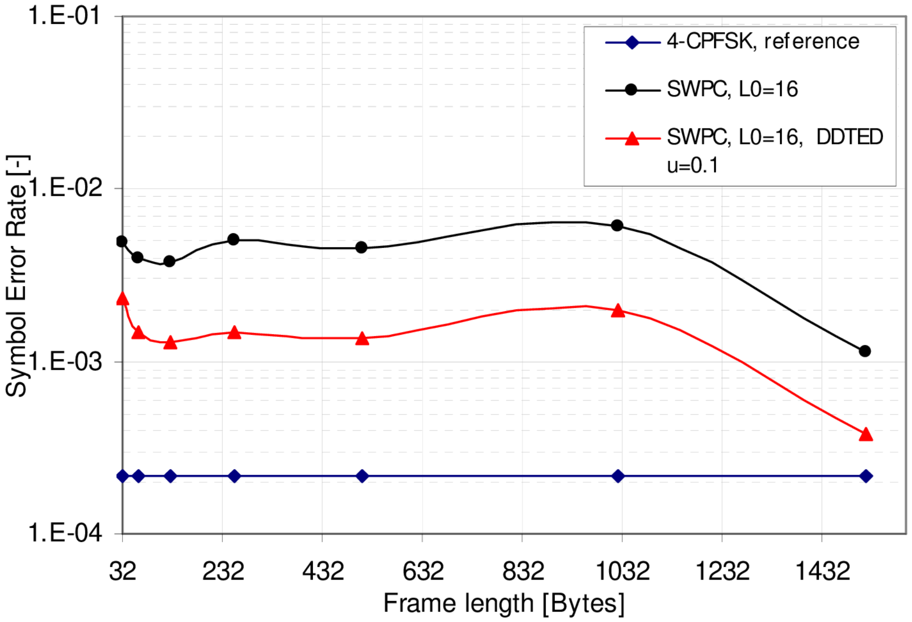

Figure 5.45: Results of the symbol-error-rate analysis of the synchronization algorithm for selected value of E_b/N_0=11dB and different lengths of the test frames. 4-CPFSK

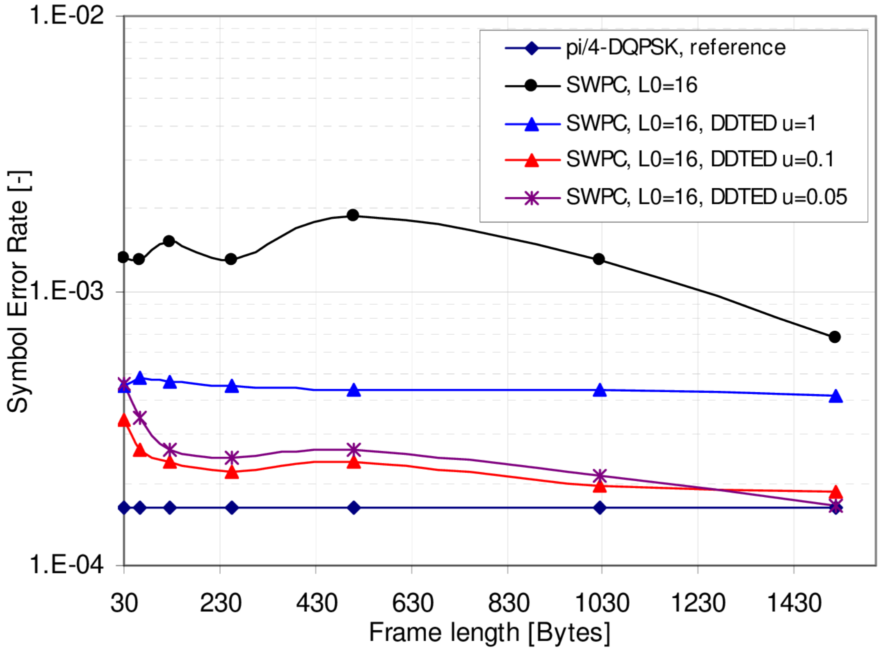

Figure 5.46: Results of the symbol-error-rate analysis of the synchronization algorithm for selected value of E_b/N_0=11dB and different lengths of the test frames. π/4-DQPSK.

At this particular level of SNR, there is a tendency of the symbol-error-rate to decrease over the increasing frame length. This phenomenon can be seen well in Figure 5.46, where the simulations were run with lower values of the step size parameter. Besides that, the example clearly demonstrates that at this particular value of E_b/N_0 lowering the step-size parameter below the selected 0.1 value yields to performance degradation, which is caused by the slowing down the transient response of the timing compensation loop.

5.7.2. Rayleigh fading channel

In the previous analysis, it was assumed that the channel is ideal in a sense that the transmitted signal is only attenuated by a *free space loss factor* (constant) and corrupted by the AWGN. Such radio channel has a totally flat transfer function with a linear phase characteristic and does not cause any unwanted *channel-induced inter-symbol interference*. However, in real radio communication systems, the signal propagates over the multiple paths and scatters on various objects which give rise to partial waves arriving at the receiver with different amplitudes and phase due to the various paths attenuation and delay. When summed in the receiver, the resulting signal experiences variation in amplitude and phase.

In this section, the symbol-error-rate behavior of the digital receiver, synchronized with the proposed synchronization scheme, is therefore analyzed under the *multipath fading* conditions. The suitable channel models are defined first, followed by the analysis of the synchronization algorithm behavior in conditions, where the radio channel experiences modelled fading process and corrupts the incoming signal by channel-induced ISI and by the noisy signal of predefined level.

5.7.3. Rayleigh fading channel models

Respecting the small scale multipath fading categorization published in [20] and [21], the radio channel under consideration is assumed as time-variant, experiencing *slow frequency flat fading* mechanism. When viewed in the time domain, the radio channel is said to be frequency flat if all of the significant received multipath components of a symbol arrive within the symbol time duration T. And the channel is referred to as introducing slow fading if the channel state remains virtually unchanged during the time of the modulation symbol.

Table 5.2: Parameters of the radio channel models [12].

Fading channel models for constant envelope modulation				
Propagation Model	**Tap Number**	**Relative Delay**	**Average relative power**	**Max. Doppler shift**
[-]	**[-]**	**10^{-6}[s]**	**[dB]**	**[Hz]**
Typical Urban TU50	1	0	0	18.5
	2	5	-22.3	
Highly Terrain HT200	1	0	0	74
	2	15	-8.6	

Fading channel models for QAM modulation				
Propagation Model	**Tap Number**	**Relative Delay**	**Average relative power**	**Max. Doppler shift**
[-]	**[-]**	**10^{-6}[s]**	**[dB]**	**[Hz]**
Typical Urban TU50	1	0	-3	18.5
	2	0.2	0	
	3	0.6	-2	
	4	1.6	-6	
	5	2.4	-8	
	6	5	-10	
Highly Terrain HT200	1	0	0	74
	2	0.2	-2	
	3	0.4	-4	
	4	0.6	-7	
	5	15	-6	
	6	17.2	-12	

For practical radio channel simulation in this section, the simplified radio channel models *typical urban* (TU50) and *highly terrain* (HT200) at reference frequency of 400 MHz – defined in [12] – has been used. The models exhibit a few discrete paths which are mutually statistically independently fading. The signal tap (component) in each path is assigned its relative delay and its average relative power of the complex tap-gain process. The fading process in each path is assumed to be stationary Gaussian process with a power density function equal to the classical Doppler spectrum (4.57) normalized by the maximum Doppler shift

$$S(f) = \left\{ \begin{array}{ll} \dfrac{1}{\pi f_d \sqrt{1 - \left(\dfrac{f}{f_d} \right)^2}} & for \; -f_d \le f < f_d \\ 0 & elsewhere \end{array} \right\}, \quad (5.87)$$

where f_d is the maximum Doppler shift frequency, defined as the ratio of the relative transmitter-receiver velocity and the wavelength calculated at a nominal frequency (400 MHz)

$$f_d = \Delta v / \lambda_0 \; . \qquad (5.88)$$

All parameters of the channel models are collectively given in Table 5.2. All other parameters of the simulations were set as described in Section 5.7.

5.7.4. Simulation results

There are two types of results presented for each fading process as given in Table 5.2. Similarly to the previous section, the first set of results, shown in Figure 5.47 and Figure 5.48, depicts the dependency of the SER for the three modes of the symbol and frame timing synchronization of the narrowband digital receiver for selected modulation techniques and fixed frame length. In each plot, there is a reference characteristic for static *"Static"* and fading channel *"REF"* representing the respective modes of operation while the receiver is optimally synchronized. Two more characteristics assigned as *"SWPC"* and *"DDTED"* represent the results achieved by the digital receiver while it was synchronized by the proposed synchronization technique and it is either sample wise pattern correlation technique alone *"SWPC"* or in combination with the decision directed timing recovery algorithm *"DDTED"*.

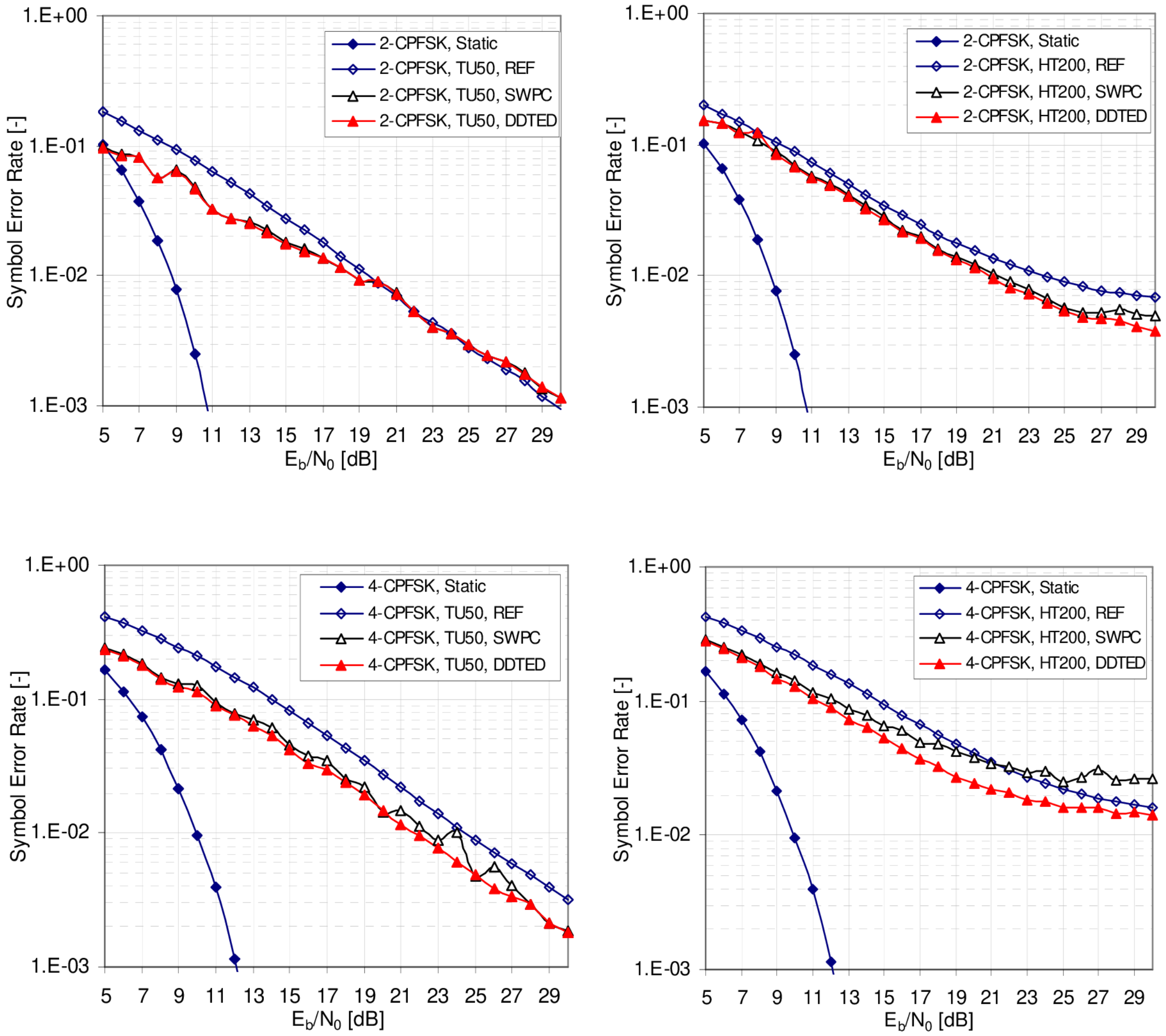

Figure 5.47: Results of the symbol-error-rate analysis for the three modes of the symbol and frame timing synchronization of the narrowband digital receiver under fading condition. 2-CPFSK, 4-CPFSK modulation techniques, frame length 64 B.

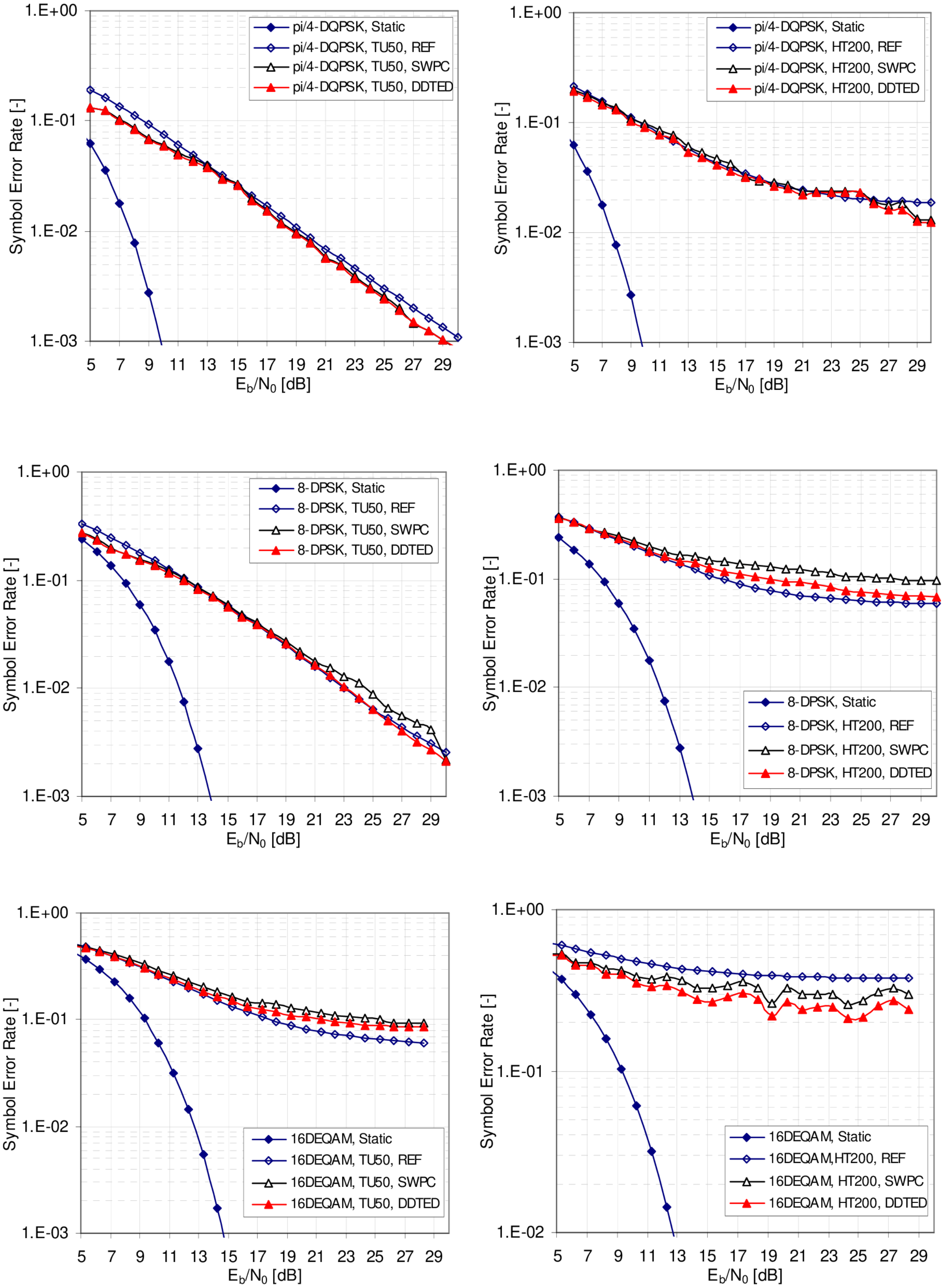

Figure 5.48: Results of the symbol error rate analysis for the three modes of the symbol and frame timing synchronization of the narrowband digital receiver under fading condition. π/4-DQPSK, 8DPSK, 16-DEQAM modulation techniques, frame length 64 B.

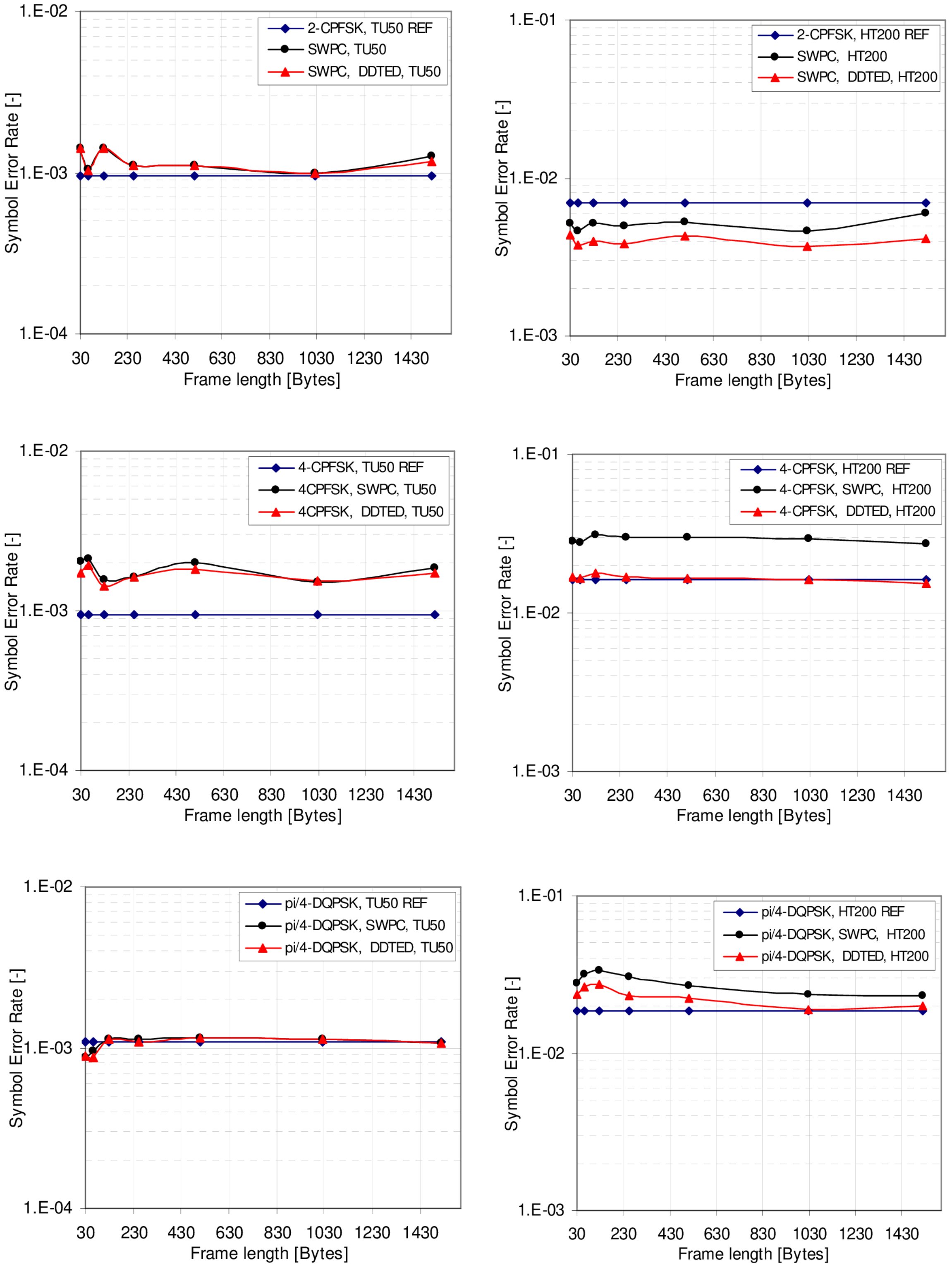

Figure 5.49: Results of the symbol error rate analysis for the three modes of the symbol and frame timing synchronization of the narrowband digital receiver under fading condition. π/4-DQPSK, 8DPSK, 16-DEQAM modulation techniques, frame length 64 B.

It can be seen from the results – Figure 5.47 and Figure 5.48 – that although the fading process significantly degrades the power efficiency of the narrowband receiver, the degradation is caused mostly by the reduction of the signal-noise-ratio while it is evident also in ideally synchronized receiver. The proposed synchronization mechanisms do not contribute to this degradation by any noteworthy portion. It is interesting to note that the adaptively synchronized system reaches in some particular modes of operation even lower values of SER. This phenomenon is most likely caused by the ability of the algorithm to trace the time variant optimum synchronization point. On the other hand, the possibility that the results are influenced by the particular property of the fading process cannot be completely foreclosed, although a significant effort has been spend to mitigate such influences by the long simulation runs and randomization of all simulation parameters including frame bytes, noise and fading processes for each level of E_b/N_0. From the results presented, it is also clearly evident that without redundant information in form of forward-error-correction coding, the digital receiver is not able to reach sufficiently low values of symbol errors (Figure 5.48). This fact becomes a significant problem with increasing spectral efficiency of the modulation techniques in D8PSK and 16-DEQAM.

The second set of results, presented in Figure 5.49, shows the dependency of SER for selected modes of digital receiver operation while receiving frames with various frame lengths at a particular normalized E_b/N_0=30 dB. It can be concluded that there is no significant degradation of the power efficiency caused by the proposed synchronization scheme comparing to the ideally synchronized system.

5.8. Chapter summary

In this chapter, the algorithms for rapid frame and symbol synchronization have been formulated and analyzed by the algorithm and system simulations. The task of the synchronization algorithms in particular is to acquire the phase estimate of the optimum sampling instant within the limited time interval and also to correct the sampling phase over the entire receiving frame upon the current error estimate as precisely as the single realization of the random process forming the receiving frame enables. Thus, the main idea behind the proposed algorithm is to combine two main approaches of the unknown signal parameter estimation in form of *signal correlation* and *adaptive signal parameter estimation based on mean square error minimization* as the objective function.

The key components of the proposed synchronization algorithm that were formulated in this chapter are the *sample wise pattern correlator* in its simplified and effective form (5.18) and (5.37) for the exponential and linear modulation techniques respectively; *decision directed timing estimate detector* in its unified realization structure based on (5.50) and (5.62); and a *fractional interpolator with linear or parabolic interpolation polynomial* given by (5.83) and (5.85) respectively. All parts have been analyzed separately by the algorithm simulations and their respective performance characteristics have been evaluated. In the last part of this chapter, the overall digital receiver utilizing the proposed rapid frame and symbol synchronization scheme has been analyzed under the AWGN and Rayleigh fading radio channel conditions.

The results of the overall system simulations (Section 5.7.1 and 5.7.2) demonstrate that the proposed synchronization algorithm recovers frame and symbol synchronization with practically acceptable penalty in power efficiency – comparing to the optimally synchronized radio receiver – reaching 1 dB in an analyzed interval of the symbol error probabilities. The overall algorithm requires 16 known symbols to acquire the initial timing estimate. Although there is a possibility to decrease the length of the preamble even to 8 symbols and still reach acceptable initial timing estimate precision (Section 5.4.6) the probability of the false synchronization arises and needs to be taken into account. The algorithm can be used for all the digital modulation formats studied and excess bandwidth down to 20%. The performance characteristics of the proposed synchronization algorithm can thus, be taken as a benchmark for future synchronization algorithm enhancements while in general, it should be possible to enhance the performance of the estimation algorithm further by using more redundant information in form of pilot symbols or tones.

The proposed algorithms create a core part of the next generation of narrowband digital receivers and have been implemented in an FPGA software defined digital core. Several results shown in this chapter have also been published in technical articles [13] and [23].

6 RADIO PARAMETERS OF THE NARROWBAND SDR RECEIVER

6.1. Objective

As was written in Chapter 2, the radio parameters and their admissible limits for the narrowband radio device under consideration are specified mostly by European standard *ETSI EN 300 113* [1]. Such radio equipments have to face challenging environmental and radio conditions all over the world. The dynamic range in the vicinity of 100 dB, very strict adjacent channel transmitted power attenuation requirements, high data sensitivity, adjacent channel selectivity, high level of radio blocking or desensitization and high co-channel rejection [1], [2] are the examples to mention (Section 2). For such high dynamic range demands super-heterodyne receiver structures with a majority of analog components is still being widely used. But yet the radio transceiver has to be small in dimensions, consumes low power and remains all its parameters over the wide industrial temperature range and over the extensive period of time for reasonable price. At the same time, it should provide enough flexibility to accommodate different channel bandwidths, digital modulation and coding formats, data rates and techniques to combat negative effects of the radio channel. Such requirements typically create a main motivation behind the redesign of the existing radio architectures and place the need to incorporate still wider part of the device functionality in reconfigurable platform such as DSP or FPGA.

Although the *software defined radio* (SDR) basic principles and various algorithms evaluations have been favored by a great interest in technical literature in recent years, there are only few references discussing the overall system performance when the SDR concept is employed in a narrowband radio transceiver design. The exceptions can be seen in references [2], [84], [85], however, the specific aspects which take place in the design of narrowband communication system according to [1] differ and are not discussed. Moreover to the best of author's knowledge until the year of 2007, there had been no IF sampling digital narrowband radio modem fulfilling the ETSI EN 300 113 available on the market, and no narrowband radio modem utilizing any of the linear modulation schemes. From this point view the work that begun in 2005 [9], [13], [24] can be considered fundamental and creates a significant part of the thesis contribution.

The goal of this chapter is, therefore, firstly to summarize the main results and experiences from the practical part of this dissertation project while designing and analyzing two prototyping architectures of narrowband software defined radio modems. The main attention is given to achieve an understanding of the main limitation and compromises influencing the dynamic range performance of IF sampling digital receiver with a main emphasis on its practical implementation.

In the second part, the measurement results of the radio parameters as required by [1] are given to confirm empirically the proposed radio modem structure including the majority of the digital algorithms that have been derived in the theoretical part of this thesis. This chapter concludes with measurement results proving the contribution to the efficient use of the narrowband radio channel.

6.2. IF sampling digital radio system architecture and its dynamic range

In general, the *dynamic range* (DR) of the radio receiver is a measure of the radio receiver ability to receive a small target input signal with an admissible degradation caused by the presence of large unwanted interfering signal.

Typically, the dynamic range of the radio receiver is determined by the three key radio parameters [30]. The first is the *noise figure*, which is the ratio of the input-referred receiver's noise power spectral density to the thermal noise power spectral density for a given temperature of the radio receiver. The noise figure dominantly limits the radio receiver achievable data sensitivity (Section 2) and the minimum detectable signal power level.

The second key parameter that limits the dynamic range is a *linearity* of the receiver signal chain, which is typically characterized by the *third-order (input) intercept point* (IIP3) characteristic. It describes the ability of the receiver to receive a small target signal without a specified degradation caused by the two strong interfering signal components each having a predefined and specific frequency.

The third parameter that influences the overall dynamic range of the radio receiver – and the major one for this chapter – is a so called *instantaneous dynamic range* (IDR) [30]. In general, the IDR is an essential receiver parameter when the receiver chain utilizes the hard-limiting element, an ADC, in particular. It is a measure of the radio receiver to maintain a given sensitivity limit without a degradation caused by the strong interfering signal clipping the hard-liming device. It is important to note that from the definition of the dynamic range it is a relative measure, which implicitly assumes that the *automatic gain control* (AGC) mechanism cannot improve such characteristic of the radio receiver.

Indisputably, the ADC parameters – such as SNR, *spurious-free dynamic range* (SFDR), effective signal resolution (*ENOB*) etc. – have a primary impact on the overall instantaneous dynamic range performance. The maximum bit resolution of the ADC is driven mainly by two requirements. As shown in [25], one is the minimum signal-to-noise SNR_{req} required for the digital demodulator to process the incoming signal with an acceptable number of errors. The second – and the major aspect here – is an achievable *effective dynamic range* (EDR) [13] of the *digital part of radio receiver*. Its upper limit is determined by the full scale level (the clipping point) of the single ADC as an alternative to a 1 dB compression point of the analog receiver and the lower, by all sources of noise introduced in the quantization process within the frequency band of interest. It needs to be noted that such definition is not the exact equivalent to its analog counterpart mainly because the distortion products of the ADC do not tend to vary as a function of signal amplitude [15]. With a feasibility[10] of the digital receiver design in mind, the EDR_{ADC} of the ADC stage in form of a signal-to-noise ratio within a specified bandwidth can be written as

$$EDR_{ADC}\,[\mathrm{dB}] = 6.02(ENOB) + 1.76 + 10\log_{10}\left(\frac{f_s}{2B_N}\right), \qquad (6.1)$$

where an *effective number of ADC bits* (*ENOB*) [26], rather than nominal number of ADC bits N [25],[27] was taken. The f_s is a sampling frequency and B_N is a noise bandwidth of interest – it is the double sided bandwidth (e.g. 25 kHz) as oppose to the single sided bandwidth as it is used in previous chapters e.g. Chapter 4.2. Their ratio is usually addressed as *over-sampling ratio* (OSR) or *processing gain* in [dB].

---

[10] After several practical experiments with different ADCs it was realized that a well designed ADC stage has an overall self noise (including quantization noise) level of at least 2 to 3 least significant bits (LSB); thus, the effective number of ADC bits better expresses its performance compared to the maximum number of ADC bits.

It is obvious that to increase the EDR_{ADC} of the digital receiver stage having an ADC at its input, one could simply increase the number of effective bits and/or increase the sampling frequency. In real applications both possibilities are strictly limited. As the frequency of the processed IF signal increases (Figure 6.1), it is becoming difficult to reach sufficient signal resolution mostly due to the *aperture jitter* which is a significant ADC signal-to-noise performance limitation [28]

$$SNR_{\text{jitter\_lim}}\,[\text{dB}] = -20\log_{10}\left(2\pi f_{IF}\, t_{j,rms}\right). \qquad (6.2)$$

On the other hand, as the sampling frequency increases, the requirements upon the follow-up digital down conversion and demodulation stage ramp-up significantly. As an example, the typical increase in *logic elements* (LE) [29] count of the digital *cascaded integrator comb* (CIC) filter FPGA implementation versus an increasing decimation ratio R_1 is shown in Figure 6.1. In addition, both operations are directly related to increasing tendency in power consumption, cost and overall dimensions of the radio modem.

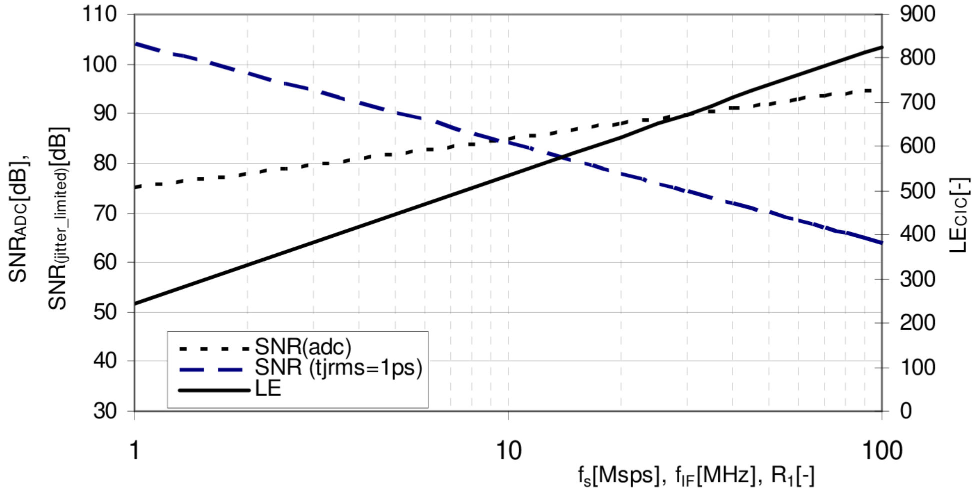

Figure 6.1: **(doted)** Processing gain influenced EDR_{ADC} (6.1) of the $ENOB$=10 bits A/D converter over the increasing sampling frequency. **(dashed)** The tendency of the jitter limited SNR versus input IF frequency (aperture jitter assumed t_{jrms}=1 ps) (6.2), [28]. **(solid)** An example of the trade-off between the decimation CIC filter FPGA logic elements count versus an increase in sampling frequency and decimation ratio R_1.

The practical aspects of the analog front-end design – where the placement of the first IF is typically at frequencies ranging from 40 MHz to 75 MHz, depending for instance on an availability of the *surface acoustic wave* (SAW) or crystal filters – need to be carefully considered as well.

In the following example, there is a calculation of the requested value of the sampling frequency needed for the narrowband LMR system to reach wanted level of its instantaneous dynamic range, in case there is no selectivity implemented in front of the digital receiver stage. Such assumption becomes substantiated when the interferer frequency falls within the close vicinity of the working frequency band and passes through the anti-aliasing filter unchanged. It is also assumed that the LMR should process the incoming signal modulated by the 4-CPFSK with a SER not exceeding the level of 10^{-2} @ ~12 dB SNR_{req} with a presence of a strong interferer which is 84 dB stronger than the useful signal. The situation is graphically depicted in Figure 6.2.

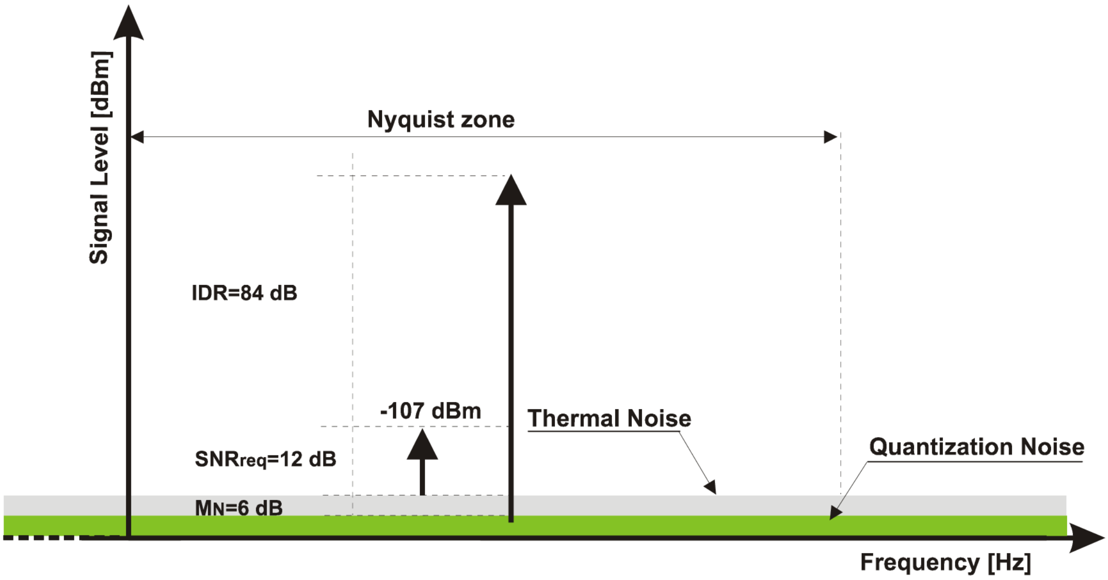

Figure 6.2: To the dynamic range requirements of the narrowband digital receiver.

If we, for the moment, omit the over-sampling ratio in (6.1) and assume the sub-sampling technique at its utmost condition[11], we can calculate the effective number of bits (6.5) of the ADC resolution to fulfil the instantaneous dynamic range requirements of 84 dB. If this is the case, the SNR_{ADC} of the ADC should reach an impressive value of at least 102 dB (6.3)

$$EDR_{ADC}\ [\mathrm{dB}] \cong SNR_{ADC} = IDR + SNR_{req} + M_N\ , \qquad (6.3)$$

where M_N is the noise margin needed to suppress the contribution of the quantization noise below the 1 dB degradation point. In (6.3) and Figure 6.2 the *IDR* is assumed to be equal to the requested blocking ratio of the radio receiver. The (6.3) can be recalculated into effective signal resolution as

$$ENOB = \frac{SNR_{ADC} - 1.76}{6.02} \cong 17\,\mathrm{bits}\,. \qquad (6.4)$$

Such a high value of signal resolution cannot be reached easily. In case the high IF frequency is selected for sampling, the available ADC effective resolution is limited by the timing jitter of the sampling generator – regardless its internal architecture and theoretical bit resolution [86]. Thus for higher IF frequencies of e.g. 45 MHz and the effective value of timing jitter e.g. 1 ps, the effective signal resolution cannot be better than approximately 11.5 bits

$$SNR_{\mathrm{jitter\_lim}} = -20\log\left(2\pi f_{IF} t_{j,rms}\right) \cong 71\mathrm{dB}\,,$$

$$ENOB \cong 11.5\,\mathrm{bits}\,. \qquad (6.5)$$

The additional bits thus need to be obtained by the processing gain which in turn determines the required sampling frequency

$$f_S = 2B_N 10^{\frac{SNR_{ADC} - SNR_{\mathrm{jitter\_lim}}}{10}} \cong 155\,\mathrm{MHz}\,. \qquad (6.6)$$

---

[11] Where the sampling frequency is just twice that of the signal bandwidth to fulfill the Nyquist criterion for the band-pass sampling.

Although theoretically possible, such a high value of the sampling rate is presently impractical for the narrowband radio receiver, mainly due to the price and power consumption of the ADC and following decimating digital down conversion stages[12]. Another important consideration when increasing the sampling frequency is the already mentioned aperture jitter or alternatively a phase noise of the sampling generator [15] that tends to increase or it is more difficult – and therefore more expensive – to reach the same value as for the lower frequencies.

Therefore, for the practical design of the narrowband radio receiver the appropriate combination of the analog front-end design together with the digital receiver is inevitable to improve the data sensitivity, adjacent channel selectivity and to extend the instantaneous dynamic range of whole narrowband receiver.

There were two approaches analyzed in this project, in order to fulfil the design objective of the narrowband radio receiver:

- First approach *(IF sub-sampling architecture)* is an appropriate combination of the analog front-end design together with the digital part of the receiver while still sampling the relatively high IF frequency with a general purpose high speed ADC [89].
- The second approach *(IF over-sampling architecture)* is the implementation of the integrated analog/digital narrowband IF sampling subsystems which includes second analog mixing stage, high performance band-pass sampling sigma delta ADCs in combination with decimation and digital filtering [88].

6.3. IF sampling digital receiver – sub-sampling architecture

The first prototyping architecture of the proposed IF sampling digital receiver with its main parts is shown in Figure 6.3. By concerning all the aspects mentioned in the previous section, the sampling frequency of 1.5625 MHz has been selected to sub-sample the first intermediate frequency of 45 MHz.

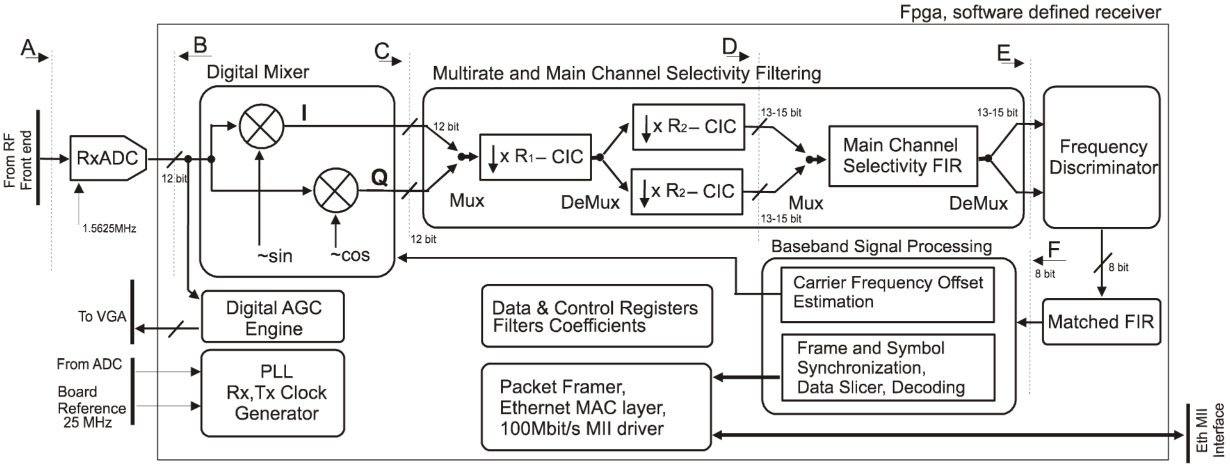

Figure 6.3: Proposed IF sampling digital receiver structure implemented in an FPGA circuit. The capitals denote the main design stages where the bit optimization was performed in order to satisfy the design objectives.

The situation is depicted in frequency domain in Figure 6.4 from which the effective input signal resolution, by using equations (6.7) [27] and (6.1) can be estimated

---

[12] There would be need to decimate the signal samples for the factor exceeding 3000.

$$SNR_{ADC}[\mathrm{dB}] = d - 10\log_{10}\left(\frac{N_{FFT}}{2}\right), \qquad (6.7)$$

where d is the difference between the input signal level and average value of the noise power spectrum density. N_{FFT} is the length of the fast Fourier transform used to calculate the spectrum. The actual number of effective bit resolution is $ENOB \approx 13$ bits. This value includes the processing gain (6.1) which however, does not take place before the filtering stage (Figure 6.3 D,E). Thus at the B stage (Figure 6.3), the input signal has lower effective resolution available of approximately 10 bits ($SNR_{ADC} \approx 58$ dB) in relation to the whole first Nyquist zone.

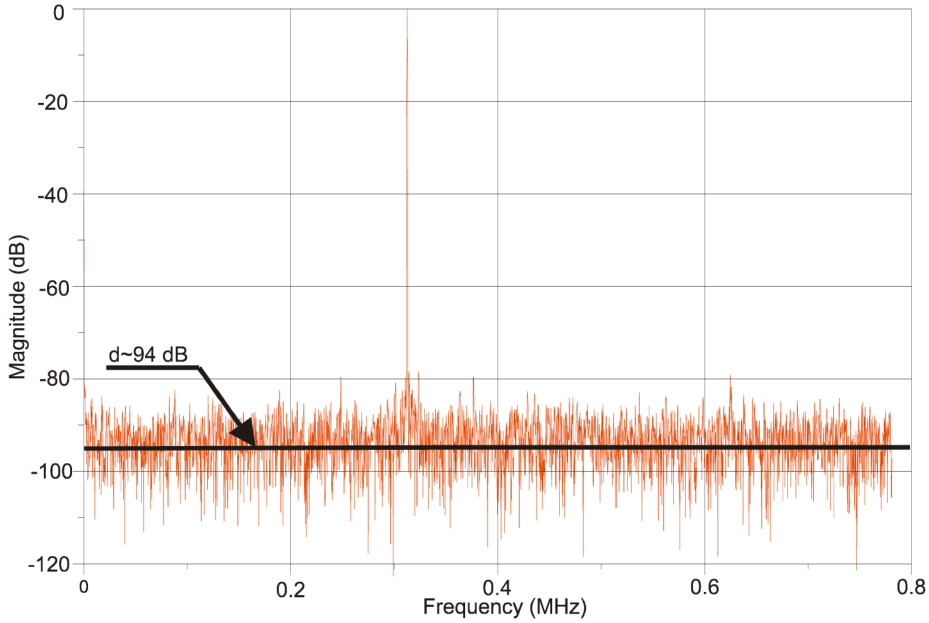

Figure 6.4: Normalized 8k FFT spectrum plot of the sub-sampled IF signal with an input level of (-1 dBFS) of the 12-bit ADC, [89], [13].

This is a key fact for the design of *digital-down-conversion* (DDC) stage comprising the complex *numerically controlled oscillator* (NCO) and embedded multipliers. Since this part runs at the highest clock of the whole digital receiver it makes sense to design it carefully. To realize how the bit resolution of the NCO influences the effective dynamic range of digital receiver, the simulation was set up to measure the noise *power spectral density* (PSD) at the output of the DDC stage (Figure 6.3 B,C). The input signal *ENOB* was assigned to 10 bits which sets the reference level (0 dB) for the normalized noise PSD, as it is shown in Figure 6.5.

The ideal floating point realization of the DDC in this case would yield -3 dB level in each signal path. As can also be seen in Figure 6.5, it is sufficient to choose the NCO resolution with 2 bits exceeding the ENOB resolution without a significant degradation of the effective dynamic range in the digital mixing stage. On the other hand, choosing a higher resolution of the NCO and DDC would not bring any advantage and would cause an additional increase in LEs count and power consumption. The NCO assumed in this example is generating an output frequency not having a fundamental relation to the sampling frequency such as *fs*/4. In this special case, the signal resolution is optimal, even though the NCO is generating <0, 1, 0, -1> values only.

One of the main advantages of the digital receiver architectures can be seen in utilization of precise digital filters of all types. Their usage in the practical narrow band digital receiver is of utmost importance; however, it is followed by two main limitations. First – and the minor one – is a general ramp-up in an implementation complexity with increasing over-sample ratio previously mentioned in relation to (6.1). This problem can be partially reduced by a combination of CIC filters preceding the FIR filter stages, mainly due to their effective realization structures requiring no multipliers or coefficient storage. Further optimization can be done by multiplexing the in-phase and quadrature signal paths together and using one filter structure (Figure 6.3) or using other "DSP tricks" e.g. [31]. In any case the digital filters consume a significant part of the FPGA resources especially if the high demanding fully parallel structures are needed [32].

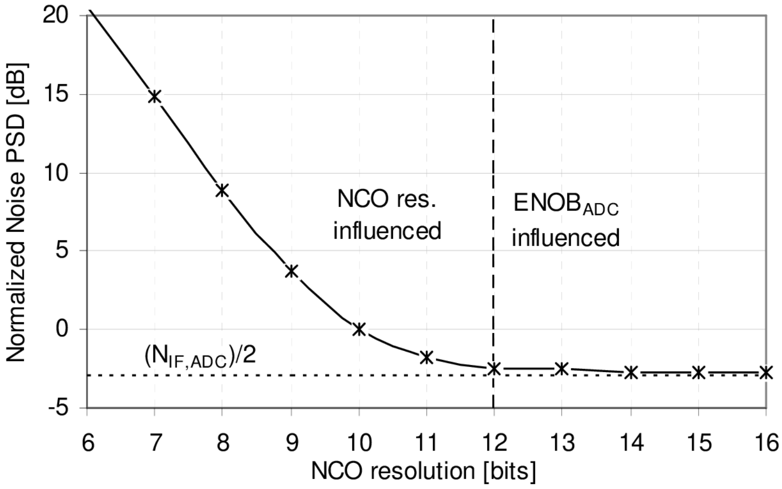

Figure 6.5: Normalized noise power spectral density increase in in-phase (quadrature) signal path after digital mixing (Figure 6.3,C) as a function of complex NCO signal bit resolution.

The second aspect of the digital filters utilization in narrowband digital receiver architecture is that their selectivity and filtering ability does not help to prevent ADC saturation and some kind of AGC algorithm is required to be employed in the system prior to the filtering stage (Figure 6.3). Thus, for high level interfering signals, the digital filtering is helpless, even though there is a FIR filter with the highest stop band attenuation available designed. Placing the AGC block after the main channel selectivity filters would also not easy the problem and the AGC response would need to accommodate the whole impulse response of the preceding signal path to maintain loop stability. Naturally, this fact forces tighter requirements upon the preceding analog filter, which not only needs to provide an anti-aliasing band limitation necessary for the sub-sampling technique, but it also needs to undertake a portion of the main channel selectivity.

The digital filtering is exactly the stage, where the processing gain (6.1) takes place, as shown in Figure 6.6. Thus, depending on a channel bandwidth selected, the signal resolution in D and E stages (Figure 6.3) should have *ENOB* of 13 to 15 bits for the processing gain to take its effect. This is a natural fact which is hidden in equation (6.1) and is sometimes not perceived properly in the digital receiver design, [25].

The proposed digital filtering part of the design is based on four stage multiplexed CIC filter [31] with the decimation factor of R_1=15. It is followed by two stage CIC filters with the decimation factor of R_2=1, 2, 4. Main channel selectivity filter is designed as 42-tap FIR filter having a fully serial filter structure [32] and a -3 dB low pass bandwidth of 0.75*R,* Figure 6.6.

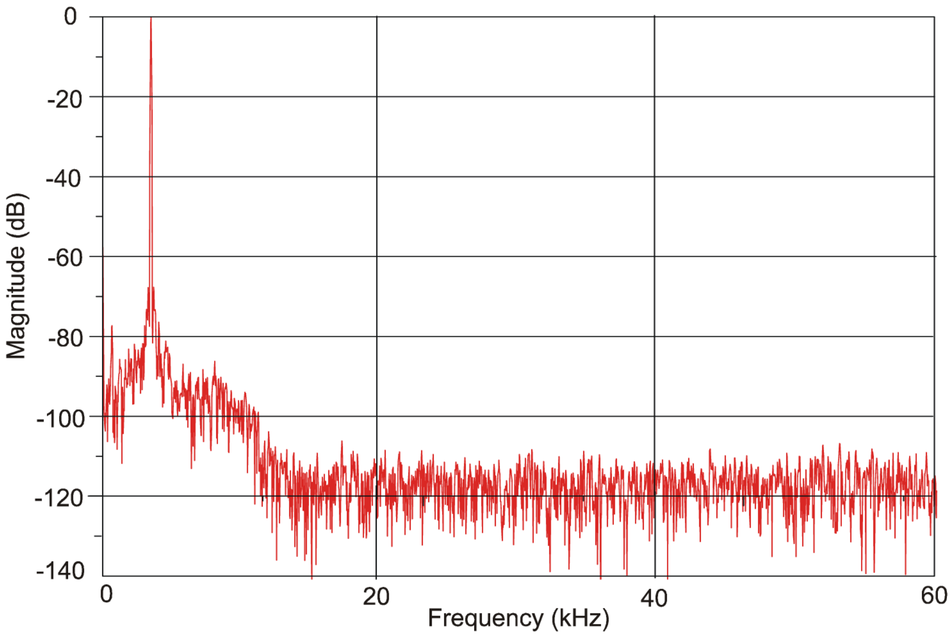

Figure 6.6: 8k FFT spectrum plot of the in-phase signal after the decimation and main channel filtering stage (Figure 6.3, E), [13].

As shown in Section 4, there is a number of ways how to implement a digital frequency discriminator. In this project the modified mathematic model (4.23) of the frequency discriminator – a digital approach based on discrete time signal differentiation as an approximation to the modulated signal phase derivation has been selected. It can also be seen as a digital signal normalizer and it is the last block in the digital receiver chain with a direct impact on the effective dynamic range performance. It therefore consumes a significant part of the FPGA logic resources.

The following stages, particularly the receiver matched filtering, frame and symbol synchronizations, carrier frequency offset compensation and data receiver work with a normalized input signal and as such do not directly influence the dynamic range of digital receiver.

6.3.1. Instantaneous dynamic range analysis

The first simulation was set up to analyze the described structure of the digital receiver using *ALTERA's DSPbuilder toolbox* for MATLAB Simulink software. It was focused on two utmost situations. In the first, the resolution of the input signal has been set up to the value equivalent to a full-scale level of the 12 bit ADC with *ENOB*=10 bits (Figure 6.4). In the second, the input signal level has been set to have an effective resolution of 1 bit above the two least significant "noisy" bits of the ADC. In both cases, the increased level of ADC noise floor has been simulated by an independent noise generator having the signal resolution of the two bits which were added to the input signal. Other parameters of the simulation are as follows:

- 4CPFSK and 2CPFSK modulations with the modulation indexes h=0.25, h=0.75 respectively.
- Symbol rate of R=10.417 ksymbols/s.
- Transmitter modulation and receiver matched filter having excess bandwidth of 28.4%.
- 25 kHz band limited AWGN noise with real power spectrum density N_0.

Figure 6.7 illustrates the symbol error rate performance of the proposed receiver structure over an increasing input E_b/N_0 ratio. It can be seen that for 2-CPFSK modulation the input signal to noise ratio in combination with the processing gain is sufficient for the correct operation and there is almost no degradation in power efficiency even with the 1 bit of effective input signal resolution. On the other hand, for 4-CPFSK modulation the combination of the input and simulated ADC noise levels falls to the area of our interest, where symbol-error-rate is around 10^{-4} and causes a significant degradation in power efficiency. It needs to be noted that the results are also influenced by a finite resolution of the differentiation process, which is supposed to become evident with a lower signal resolution.

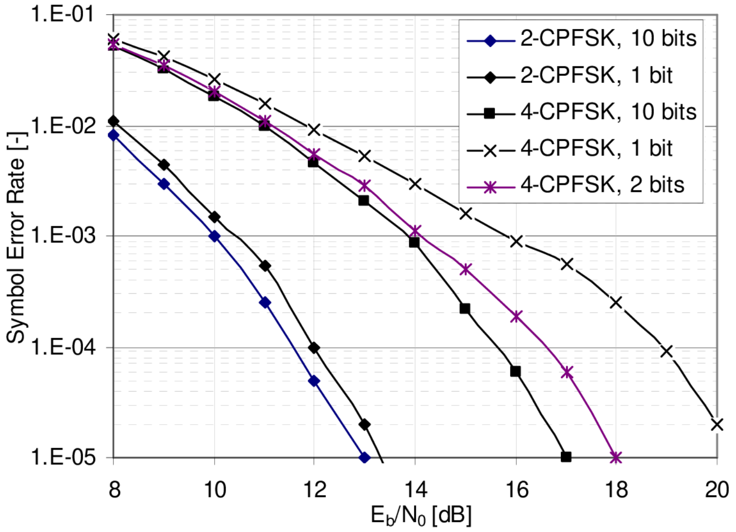

Figure 6.7: Power efficiency characteristics for 4–CPFSK and 2–CPFSK digital narrow band receiver for 1 and 10 bits of effective input signal resolutions.

The second simulation was designed to analyze the co-channel rejection, adjacent channel selectivity, radio blocking and desensitization parameters as defined in Section 2.1. The procedures to measure the essential radio parameters of the radio receiver are thoroughly described in [1] including block diagrams, measurements methods and test signals definitions. For the purpose of the digital radio performance simulation the procedure can be adopted and described in the following three steps:

- Firstly, the signal level of the wanted signal yielding a particular (bit) symbol-error-rate of 10^{-2} is found. In this case the error rate of the data transmission is caused mainly by the simulated ADC noise signal including the quantization noise.
- Secondly, the level of the wanted signal is adjusted to a level which is 3 dB above the level yielding a required symbol-error-rate limit 10^{-2}.
- Thirdly, the unwanted signal with a selected nominal frequency depending on a particular measurement is adjusted to a level until the initial symbol-error-ratio of 10^{-2} is reached again. The relative difference of the wanted and interfering signal levels is the required level of the measured parameter. As the unwanted signal an A-M3 [1], consisting of an RF signal, modulated by an audio signal of 400 Hz with a frequency deviation of 12% of the channel separation has been used.

As can be seen in Figure 6.8, only the IF sub-sampling digital receiver itself cannot and does not fulfil all the requirements, mainly because of the limited instantaneous dynamic range influenced mostly by the respective characteristics of the ADC. The widening of the processed Nyquist zone and thus increasing the effective dynamic range by additional processing gain (6.1) might be an option here, but for the additional cost in complexity – hence power consumption and price – of the ADC, digital down converter and demodulation stages.

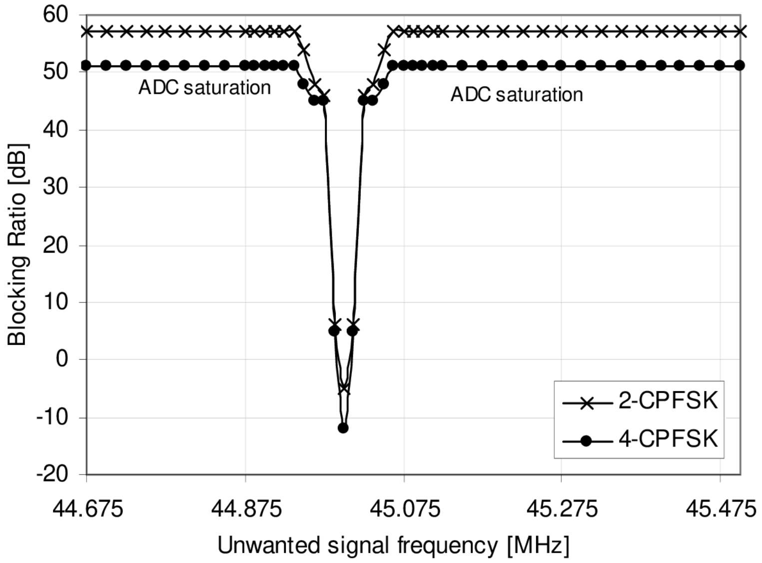

Figure 6.8: The results of the co-channel rejection, adjacent channel selectivity, radio blocking and desensitization simulations for the frequency band of one Nyquist's zone of 0,78125 MHz around the IF frequency of 45 MHz.

6.4. IF sampling digital receiver – Over-sampling architecture

The main advantage of the previous digital system architecture based on a general purpose high speed ADC [89] and the general purpose FPGA [29] circuit can be seen in its flexibility. The ADC as well as the following digital stage is not inherently band limited and the same concept can be used for the different channel bandwidths. However as it was concluded, the instantaneous dynamic range of the digital part of the receiver was limited mainly by the parameters related to the analog-to-digital conversion and without a selective analog front-end part it does not fulfil the essential radio receiver requirements.

The above mentioned implementation complications can be partially overcome by using proprietary ADC converters or the hybrid analog/digital narrowband IF sampling subsystems which includes second analog mixing stage, high performance *band-pass sampling Σ-Δ modulator* ADC in combination with the decimation and digital filtering, [88]. In accordance with the Section 6.2, the main idea behind such architectures is to lower the frequency of the sampled signal by proceeding analog mixing stage, but still band-pass sample the incoming signal. Substantially over-sample the useful signal bandwidth using a relatively high sampling frequency and to make use of the processing gain of the decimation digital filters upon the resulting efficient signal bit resolution. Mixing to zero frequency is then performed digitally.

The simplified block diagram of the prototyping digital receiver is shown in Figure 6.9. The closer description of the AD9874 can be found in [88]; at this place, the main intention is to describe the adoption of such receiver block into the architecture of the narrowband radio receiver and evaluate its influence on the instantaneous dynamic range as defined in Chapter 6.2. It can be seen, that comparing to the block diagram shown in Figure 6.3, the decimation filtering stage has been shifted to the proprietary block, while, this time, it is considered an inherent part of the Σ-Δ analog-to-digital converter in order to reach sufficiently high level of effective dynamic range within the selected part of the Nyquist zone.

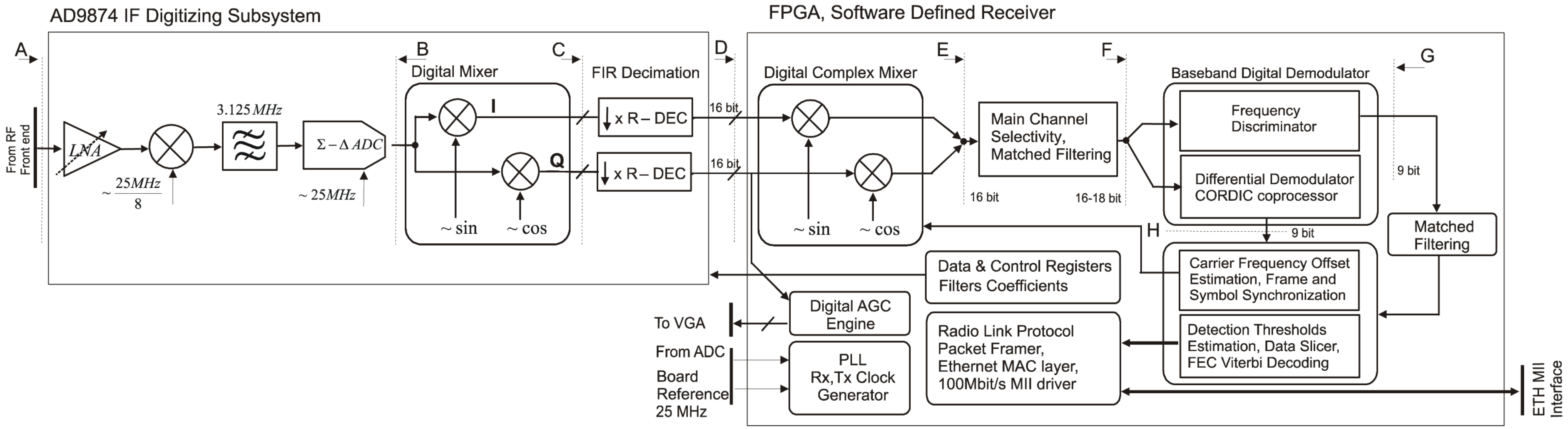

Figure 6.9: Proposed IF over-sampling digital receiver structure with IF sampling subsystem and software defined receiver implemented in an FPGA circuit.

For illustration of this principle, there is a spectrum plot taken at the output of the Σ-Δ modulator ADC shown in Figure 6.3. This figure has been adopted from [88]. It is evident that the efficient dynamic range within the limited bandwidth around the processed signal frequency is substantially higher than the overall EDR_{ADC} in respect to the whole Nyquist zone.

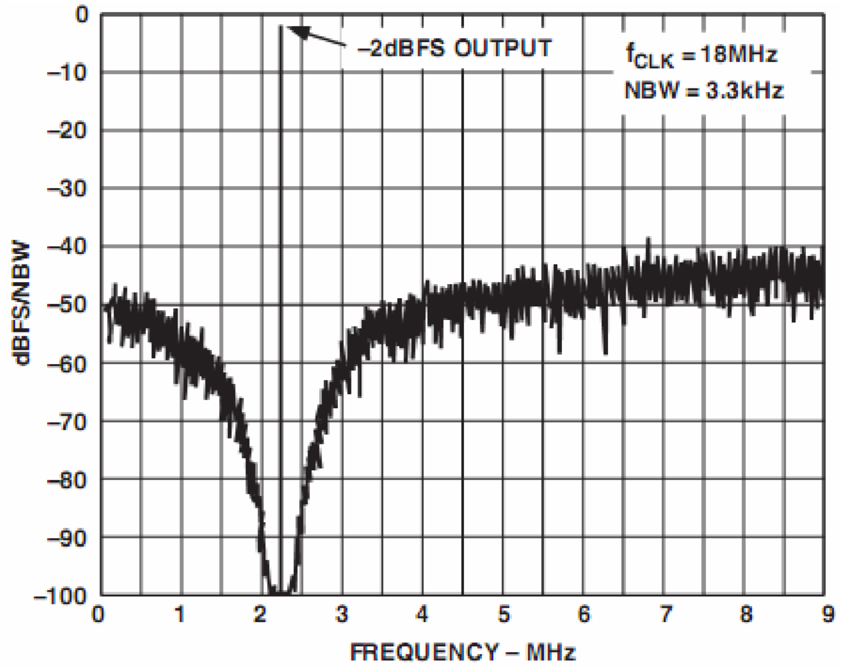

Figure 6.10: Un-decimated spectral output of the Σ-Δ modulator ADC (AD9874) [88]; Figure 6.9, B. Sampling frequency f_S=18Msps; Noise bandwidth of 3.3 kHz. Reprinted from [88] with permission.

It is important to note at this place that the similar system characteristics can be reached with architectures utilizing a dual low pass high performance Σ-Δ modulator ADCs sampling the zero IF complex signal. Except the need for dual ADCs, drivers and filters, such concept has almost the same implementation complexity. There is a significant disadvantage in form of the signal conditioning of the low pass in-phase and quadrature signal components that require two almost identical analog designs to prevent signal distortion. However, with the recent advancements in analog integrated circuit designs that integrate dual matched signal paths into one integrated circuit, such architectures are gaining on their importance even though the architectures utilizing zero IF signal sampling are generally considered far from the concept of the pure software defined radio – pushing the sampling process as close to antenna as possible [55].

The described modification of the general architecture enables to use significantly-higher sampling frequency of 25 MHz, while the digital processing can be designed to operate at relatively low sample rate, in particular the N times the selected modulation rate, as needed. In Figure 6.11, there is a spectrum plot calculated from the input signal (-1 dBFS) samples coming to the FPGA circuit as an in-phase signal component (Figure 6.9 D). If the same approach is used as in the previous chapter, one can estimate the effective signal resolution using (6.7) at the digital receiver input. It reaches approximately 13 bits (d=113 dB, N_{FFT}=4096). It is important to note that the spectrum plot has been taken from a real prototyping device and the result is affected by the phase noise which is clearly visible in close vicinity of the processed signal component. However, as the signal passes through the analog anti-aliasing filter having a -3dB bandwidth of approximately 25 kHz, it is reasonable to assume that at the frequency offset near the Nyquist frequency, the ADC noise is dominant. Moreover, the phase noise level decreases with the input signal level, thus, when calculating the efficient dynamic range of the digital receiver its influence can be omitted.

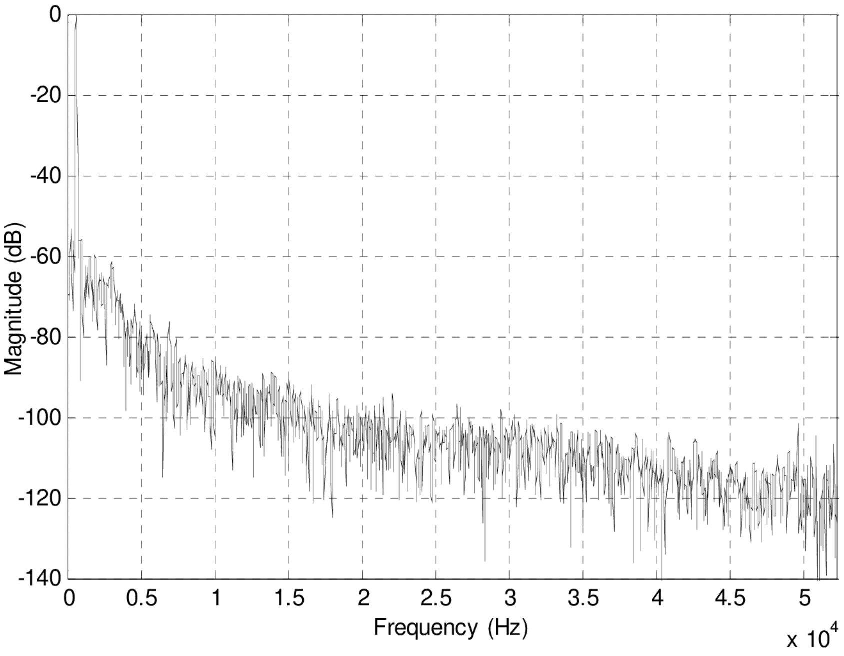

Figure 6.11: Normalized 4k FFT spectrum plot of the In-phase signal component Figure 6.9, D with an input level of (-1 dBFS), Input signal nominal frequency 70.05 MHz, sampling frequency 25 MHz, decimation ratio 240, resulting sample rate 104.167 ksamples/s.

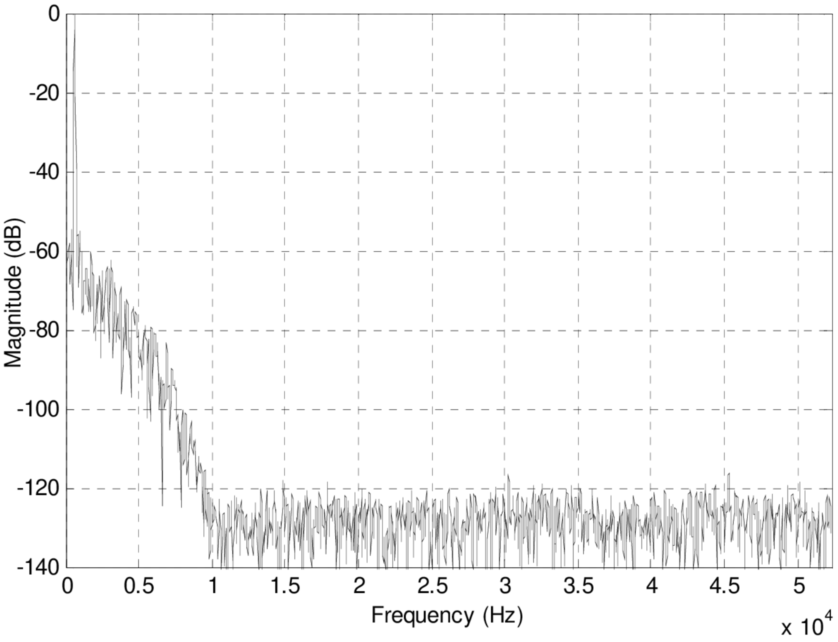

Figure 6.12: Normalized 4k FFT spectrum plot of the in-phase signal component after the main channel selectivity digital filtering Figure 6.9, F; the processing gain is clearly visible. Output signal resolution is 16 bits.

In case the over-sampling ratio of N=10 samples per modulation symbol is assumed, the processing gain widens the effective dynamic range of the digital receiver for another 7 dB. The situation is depicted Figure 6.12. The effective dynamic range with respect to the processed bandwidth widens to approximately 87 dB

$$EDR_{ADC}\,[\mathrm{dB}] = 6.02(ENOB) + 1.76 + 10\log_{10}\left(\frac{f_s}{2B_N}\right) \cong 87\,\mathrm{dB}\,. \qquad (6.8)$$

6.4.1. Instantaneous dynamic range analysis

Similarly to Section 6.3.1, this section summarizes the results of the proposed digital receiver simulations using *ALTERA's DSPbuilder toolbox* for MATLAB Simulink software. The simulations were focused mainly on essential radio parameters – as defined in Chapter 2.

The fundamental block diagram of the digital receiver to be evaluated can be found in Figure 6.9. The particular parameters of the simulation were selected as follows.

- Parameters related to the digital modulations for the selected modes of operation have been set as they were derived in Section 3.4:
    - 2-CPFSK: 13.02 kBaud; modulation index h=0.5;
    - 4-CPFSK: 12 kBaud; modulation index h=0.25;
    - Modulation and matched filter, the square root Nyquist δ-filter with equivalent excess bandwidth of 28.4%, as derived in Section 3.3;
    - π/4-DQPSK, 8DPSK, 16-DEQAM: 17.3 kBaud;
    - Modulation and matched filter, the square root Nyquist δ-filter with equivalent excess bandwidth of 45%, as derived in Section 3.3;
    - Over-sampling factor N=10 samples per one modulation symbol.
- Parameters of the physical layer test frames as derived in Section 5.4:
    - Preamble length L_0=16 symbols;
    - Data payload of a given length for each frame has been generated using randomly seeded random generator (Matlab, simulink).
- The receiver processed bandwidth has been selected as:
    - For exponential modulations, the processed bandwidth (B_N≈10.9 kHz) has been set by the main channel selectivity FIR filter;
    - For linear modulations, the processed bandwidth has been defined by the receiver matched filter and can be approximated by $B_N=(1+\alpha)R/2$, where α is the equivalent excess bandwidth parameter and R is the symbol rate. (B_N≈12.5 kHz).
- Other parameters of the simulations
    - Correction of the symbol timing has been performed using the fractional interpolator having the Farrow structure of a linear interpolation as described in Section 5.6.
    - For exponential modulations the modified mathematic algorithm for digital frequency discrimination has been selected (Section 4.5).
    - Direction directed version of the decision directed TED as derived in Section 5.5 has been used. The step size parameter μ=0.1, unless otherwise noted.
    - The ADC noise floor has been simulated by an independent noise generator having the variance parameter set according to the measured

spectrum shown in Figure 6.10; 3 LSB bits which corresponds to the relative level of approximately 12 dB above the ideal quantization noise level.

- To compare the robustness of the proposed mode of operation, the same unwanted signal has been used. The A-M3 [1], consisting of an RF signal, modulated by an audio signal of 400 Hz with a frequency deviation of 12% of the channel separation.

The results of the essential radio parameters simulations are provided in Figure 6.13, Figure 6.14 and Table 6.1. In addition to the measurement procedure described in Section 6.3.1 the Table 6.1 gives also the signal-to-noise ratios in respective locations of the simulation. The SNR_{ADC} @ $SER=10^{-2}$ represents the input signal-to-noise ratio with respect to the whole Nyquist zone for selected level of symbol-error-rate of 10^{-2}.

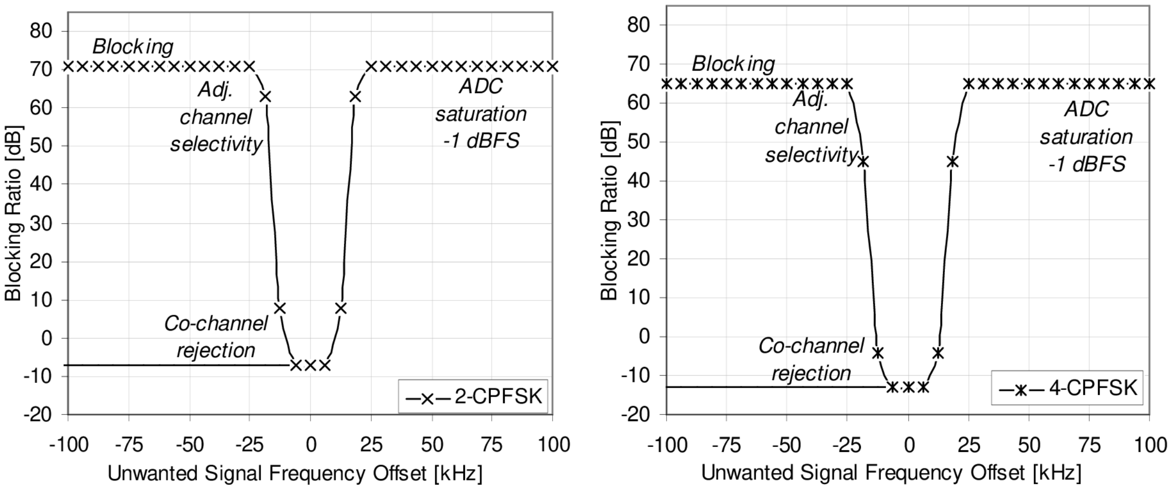

Figure 6.13: The results of the co-channel rejection, adjacent channel selectivity, radio blocking simulations of the digital receiver in mode of exponential modulation.

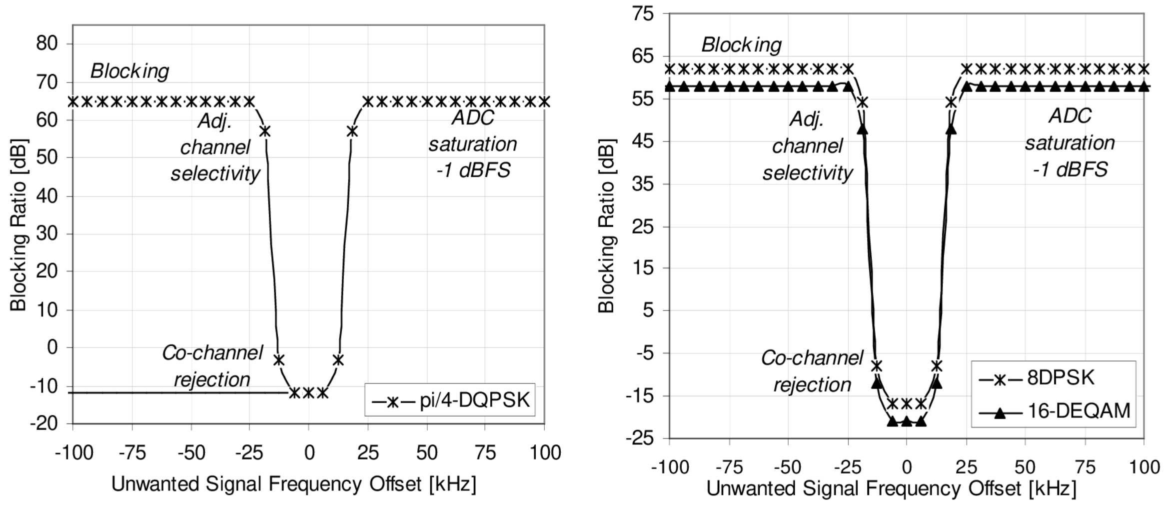

Figure 6.14: The results of the co-channel rejection, adjacent channel selectivity, radio blocking simulations of the digital receiver in mode of linear modulation formats.

The SNR_{ADC} @ $-3dB$ $Deg.$ represents the signal-to-noise ratio of the wanted signal and the simulated ADC noise signal that has been set for the degradation measurement without a presence of the interfering signal and without the inclusion of processing gain; and the processing gain influenced *SNR* ratio is finally the one seen by the digital demodulator within the processed signal bandwidth.

Table 6.1: Simulation results of the narrowband digital radio parameters in selected mode of operation.

Measurement bandwidth:			**Nyquist zone**			**Occupied Bandwidth**		**Nyquist zone**		
Modulation Format	**Symbol Rate**	**Mod. Parameter**	**ADC Noise Level**	**SNR_{ADC}, @ SER 10^{-2}**	**SNR_{ADC}, @-3dB Deg.**	**SNR**	**Co-channel Rejection**	**Adj. channel Select.**	**Block. Ratio**	**IDR**
[-]	**[kBaud]**	**[-]**	**[dB]**	**[dB]**	**[dB]**	**[dB]**	**[dB]**	**[dB]**	**[dB]**	**[dB]**
2CPFSK	13.08	h=0.5, α=0.28	18.0	-2.0	1.0	6.8	-7.0	71	71.0	71
4CPFSK	12.00	h=0.25, α=0.28	18.0	4.0	7.0	12.8	-13.0	65	65.0	65
π/4-DQPSK	17.30	α=0.45	18.0	3.0	6.0	11.5	-12.0	65	65.0	65
8DPSK	17.30	α=0.45	18.0	6.0	9.0	16.0	-17.0	62	62.0	62
16-DEQAM	17.30	α=0.45	18.0	11.0	14.0	19.5	-21.0	58	58.0	58

From the simulation results, it can be seen that the strictest limits required for the co-channel rejection (-8 dB) can be fulfilled fully only in the 2-CPFSK mode of operation. For the spectrally more efficient techniques particularly the 4-CPFSK and π/4-DQPSK this limit cannot be maintained without an additional forward-error-correction technique, however, it is reasonable to assume that with an acceptable amount of redundant information even the most enhanced forward error correction techniques prove to be short in delivering additional 4 to 5 dB in power efficiency. For even higher spectrally efficient modulation techniques the limit is far too severe to be fulfilled.

Two other parameters, in form of the adjacent channel selectivity, and radio blocking, determines the instantaneous dynamic range of the digital receiver. It can be seen from Figure 6.13, Figure 6.14 and Table 6.1, the more spectrally efficient modulation technique, the higher value of the *SNR* is required. And while the instantaneous dynamic range requirements are constant it drives the need for widening the efficient dynamic range of the whole digital receiver. Thus, it can be concluded that similarly to the sub-sampling architecture, the over-sampling digital narrowband receiver utilizing higher spectrally efficient modulation techniques fails to provide 70 dB of the adjacent channel selectivity and 84 dB of radio blocking in close vicinity of the nominal working frequency. However, compared to the sub-sampling architecture the digital radio architecture utilizing the narrowband IF over-sampling subsystem can reach 14 dB wider effective dynamic range for the system parameters chosen. This value directly contributes to the 14 dB increase in instantaneous dynamic range of the digital receiver in accordance with (6.4). Nonetheless, the selective analog front-end part is still inevitable to increase the robustness of the software defined narrowband radio receiver if the higher spectrum efficiency of the data transmission is required.

6.5. Analog front-end design notes

It is not the intention of this thesis to cover a complex task of the analog front-end part design for the narrowband radio receiver. As the analog front-end part influences the overall receiver performance significantly, at least, the most important design notes are included in this section.

To satisfy the design objectives without the performance degradation of narrowband radio receiver by the ADC noise, the preceding analog front-end part should provide enough gain for the thermal noise coming from the input low noise amplifier to become dominant over the ADC noise level.

Firstly, one can rewrite (2.1) to calculate the worst case *NF* [25] of the analog front-end part with regards to the demanded maximum usable sensitivity of the receiver as

$$NF\ [\mathrm{dB}] = S - 10\log(kT) - 10\log(B_N) - SNR_{req}\,, \qquad (6.9)$$

where SNR_{req} is the signal-to-noise ratio acquired from the system simulations, required for the specified BER level of the modulation technique in use and *S* is the demanded data sensitivity limit. The implications of this equation are straightforward. For the fixed limit of the data sensitivity, channel bandwidth and absolute temperature, the radio modem utilizing modulation and coding format which requires certain (higher) level of SNR would either does not fulfil the requested limit or the only way to accomplish this objective is to lower the *NF*. However, the *NF* cannot be lowered arbitrarily. Especially in a frequency bands below the 1 GHz where much of the industrial and radio broadcasting interference takes place, designing the analog front-end always creates a compromise between the robustness of the overall radio receiver and overall noise figure. This compromise usually yields noise figure values in range between 6 to 10 dB.

Secondly, the overall analog front-end gain G_{FE} can be estimated according to

$$G_{FE}\ [\mathrm{dB}] = \left(ADC_{FS} - IDR\right) - \left(10\log(kT) + NF + 10\log\left(\frac{f_s}{2}\right)\right). \qquad (6.10)$$

Here the ADC_{FS} represents the *full scale level of the ADC*; *IDR* is the instantaneous dynamic range of the digital receiver – including the ADC – found by the system simulation (e.g. Figure 6.14). In (6.10), the *IDR* parameter describes the ability of the digital receiver to process the incoming digital signal modulated by the selected mode of modulation in the presence of a strong interferer. It is evident that the wider the *IDR*, the less front-end gain is required and the better values of selectivity and blocking can be achieved only by the digital part of the receiver. If the overall value of the digital receiver *IDR* is lower that the SNR_{ADC} (Figure 6.2), its value should already include a sufficient gain margin to suppress the noise contributions of the ADC device. It is also important to notice that for a given value of the SNR_{ADC} (6.1), the instantaneous dynamic range of the digital receiver decreases with decreasing power efficiency of the selected modulation format (6.3).

Thirdly, a suitable anti-aliasing filter has to be chosen. It can be seen from Figure 6.8, Figure 6.13 and Figure 6.14 that notwithstanding that the digital filters can bear major part of the channel selectivity, the proposed architectures of the digital receiver do not reach required values of the instantaneous dynamic range. Thus, the use of anti-aliasing filters with steep band-pass response – typical for crystal and SAW filters – are still inevitable for the intended analog front-end system. This part can be seen as the main restrictive element in the narrowband radio receiver architecture that dominantly limits the flexibility of the whole equipment, especially when it comes to processed bandwidths applicable.

Last, but not least, a phase noise of the first local oscillator is of the prior importance as it influences the adjacent channel selectivity and the blocking ratio in close vicinity to the nominal frequency by a mechanism called reciprocal mixing [25], [6]. The strict limits of these parameters makes the design of the first local oscillator a challenging task, while the phase noise that would be required is below the -130 dBc/Hz at 20 kHz frequency offset. In Figure 6.15 there is an example of the radio blocking measurement of the over-sampling architecture using two different signal generators in the position of the first local oscillator. The phase noise of the first signal generator – integrated in the frequency band of the adjacent channel reaches approximately[13] -78 dBc, while of the second one , HP8640B, Appendix A, I.5, [94], reaches -86 dBc. In both cases the frequency of 509.15 MHz generated by the signal generators has been used.

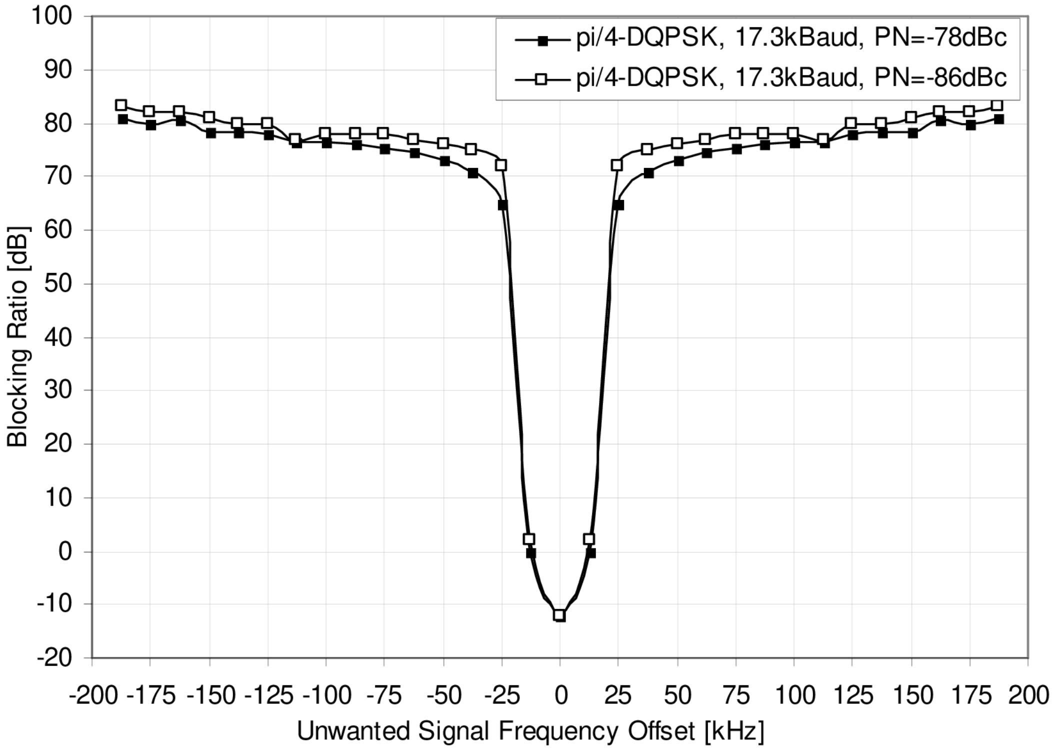

Figure 6.15: An example of the essential narrowband radio parameters influenced by the phase noise of its first the local oscillator by a reciprocal mixing.

It can be seen from this comparison that when using the signal generator having lower absolute phase noise level, the overall radio receiver can reach better values of adjacent channel selectivity and radio blocking parameter in a close distance to nominal channel frequency. While it is assumed that there is no practical way how to omit the influence on the instantaneous dynamic range measurement results altogether, the measurement results presented in the following chapters have been performed with a signal generator having the lowest phase noise available (HP8640B, Appendix A, I.5, [94]).

6.6. Measurement results

6.6.1. Sub-sampling architecture

The IF sub-sampling digital radio, as described in the Section 6.3, was adopted for the narrowband radio modem together with appropriate analog front-end part, Section 6.5. The software defined digital core was implemented in Altera's Cyclone II EP2C8T144I8 FPGA device [29]. Together with the transmitter part, proprietary Ethernet MAC and radio controllers the complete solution consumes 80% of LEs, 35% of memory bits, 60% of embedded multipliers and drives approximately 80 mW of power, while running at 25 MHz system clock.

---

[13] It is also a demanding task to measure such a low phase noise values precisely, while these values of phase noise are typically lower than the values achieved by measuring equipments Appendix. A.

Initial measurements of the essential radio parameters as specified in Section 2 were also carried out. Figure 6.16 presents the results of the maximum usable data sensitivity measurement of the complete radio receiver. It can be seen that the maximum usable sensitivity limit of -110 dBm demanded by [1] is fulfilled fully for 2-CPFSK, but only with a small margin for the 4-CPFSK modulation. It needs to be noted that the actual values of *BER* have been calculated from the *packet-error-rates* (*PER*) according to (6.11), where N_{bytes} is the number of bytes in the received packet

$$BER = 1 - \left(1 - PER\right)^{\frac{1}{8N_{bytes}}} \qquad (6.11)$$

Although the results are influenced by the synchronization, carrier signal level and frequency offset estimation errors, they reflect the complete radio system performance well.

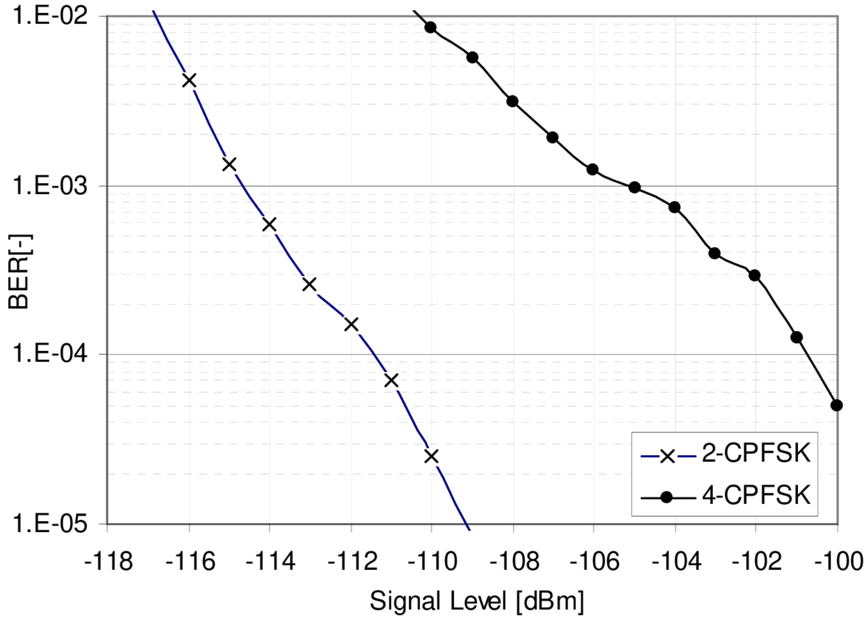

Figure 6.16: The result of the maximum usable sensitivity measurement of the narrowband receiver for 25 kHz channel bandwidth.

As a second, the essential radio parameters for the IF sub-sampling digital receiver as well as for the complete radio receiver solution have been measured and the results are shown in Figure 6.17. It can be seen, that the results for the software defined digital part differ from the one simulated (Figure 6.8) for less than 3 dB which can be judged acceptable for the practical realization. Moreover, it can be seen that the requirements of the standard [1] are met fully for 2-CPFSK mode of operation.

For 4-CPFSK modulation, the proposed digital receiver architecture, even with a selective front-end part, does not fulfil the essential radio receiver parameters, especially the co-channel rejection and radio blocking parameter describing the dynamic range of the receiver. It can be therefore concluded that although there is a possibility to use the sub-sampling technique in modern IF-sampling receivers in order to lower the required sampling frequency, the results clearly show that it cannot be lowered arbitrarily and it is necessary to use significantly higher sampling frequencies compared to the occupied signal bandwidth to widen the overall dynamic range of the narrowband receiver.

Although at this phase of the project only the exponential digital modulations were tested, it was supposed that the same difficulties would be faced when implementing higher order linear modulation formats. Therefore, the additional widening of the effective dynamic range of the digital receiver is necessary to utilize the narrowband radio channel more effectively. Since increasing the sampling frequency significantly increases price and consumed power, the described prototyping architecture based on sub-sampling technique cannot be judged suitable for the high performance narrowband radio device.

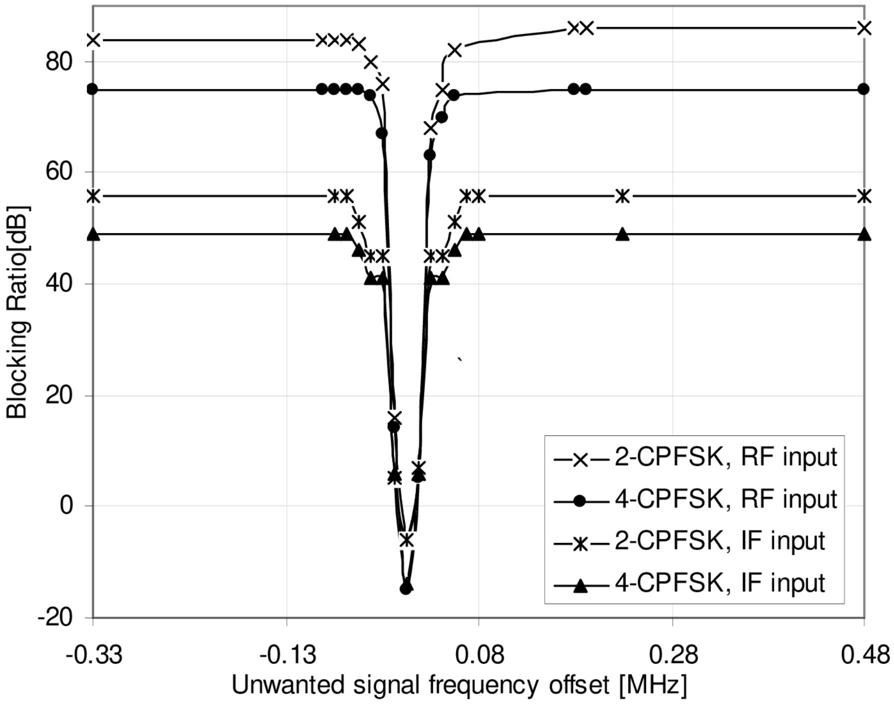

Figure 6.17: The result of the co-channel rejection, adjacent channel selectivity, radio blocking and desensitization measurements for the frequency band of one Nyquist's zone of 0,78125 MHz around the RF frequency of 409,025 MHz and around the IF frequency of 45 MHz. As a local oscillator the HP8640B, Appendix A, I.5, has been used.

6.6.2. Over-sampling architecture

The IF over-sampling digital radio architecture – as described in Section 6.4 and 6.5 – was also designed for the narrow band radio modem. The software defined digital core containing both modems for exponential and linear modulations were implemented in *Altera Cyclone III EP3C10F256I8 FPGA* device [95]. The essential radio parameters of the complete radio transceiver were measured and the results are presented in this section.

In Figure 6.18, there are power efficiency characteristics measured for 2-CPFSK, 4-CPFSK and π/4-DQPSK modes of operation. It can be seen that the *emf* sensitivity limit of +3 dBμV is fulfilled for all modes when running at the symbol rate of 10.4 kBaud. When higher symbol rates are selected, the 4-CPFSK losses its power efficiency significantly and for the symbol rate of 13.08 kBaud it lowers down to the very edge of the admissible data sensitivity levels. Further increase of the exponential modulation spectrum efficiency can be therefore considered impractical. On the other hand, when using the π/4-DQPSK, the radio receiver can still reach the data selectivity limit for 17.3 kBaud with a 2 dB margin. The power efficiency characteristics for lower symbol rates were added to the plot as well in order to compare the properties of the modulation formats at the same spectrum efficiencies. As can be seen, at the symbol rate of 10.4 kBaud, both modulation formats reach almost the same data sensitivity (-113dBm @ BER 10^{-2}). This is caused mainly due to the fact that there is higher frequency deviation used for 4-CPFSK at the lower symbol rates, thus the increase in power efficiency is not linear as for the π/4-DQPSK. Even from this comparison it is evident that the π/4-DQPSK mode of operation outperforms the 4-CPFSK at higher spectrum efficiencies.

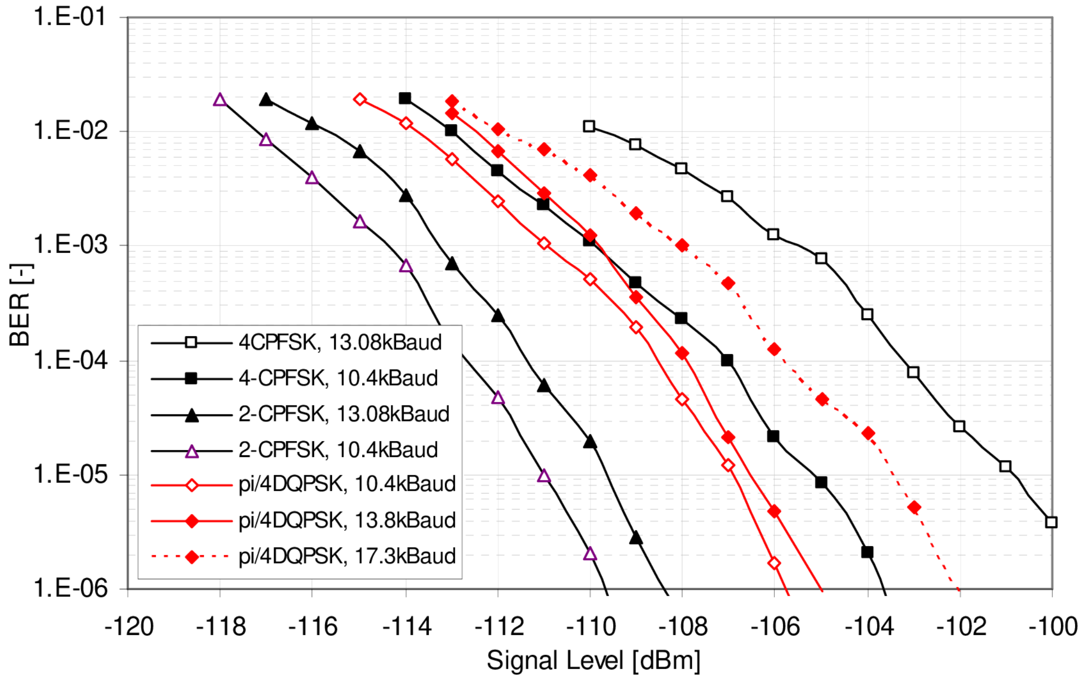

Figure 6.18: Results of the maximum usable sensitivity measurement of the narrow band receiver for 25 kHz channel bandwidth.

The second set of measurement results, shown in Figure 6.19 to Figure 6.21, describes the essential radio receiver parameters of the proposed IF over-sampling architecture. The particular values of the receiver parameters are collectively given in Table 6.2. It is important to note that the measurement results are encumbered with a measurement uncertainty of ±2 dB which is caused by *BER* estimation (6.11) as well as the inaccuracy of the measurement procedure itself. It already includes tolerances of the measurement equipments (Appendix A).

In accordance with the simulation results, only the 2-CPFSK mode of receiver operation fulfils the strict limit for the co-channel interference rejection. As it was concluded already in previous section, this limit – as required by [1] – is too severe and hinders the practical usage of spectrally more efficient modulation schemes while fulfilling limits of all essential radio parameters.

The decrease in power efficiency of the 4-CPFSK modulation at 13.08 kBaud causes the degradation of adjacent channel selectivity and while also the value of data sensitivity is near the requested limit, this mode can be judged the least suitable for the efficient narrowband channel usage.

By comparing the measurement results describing the instantaneous dynamic range of the sub-sampling and over-sampling architectures it can be concluded that the IF over-sampling architecture reaches substantially wider dynamic range which contributes to efficient narrowband channel usage.

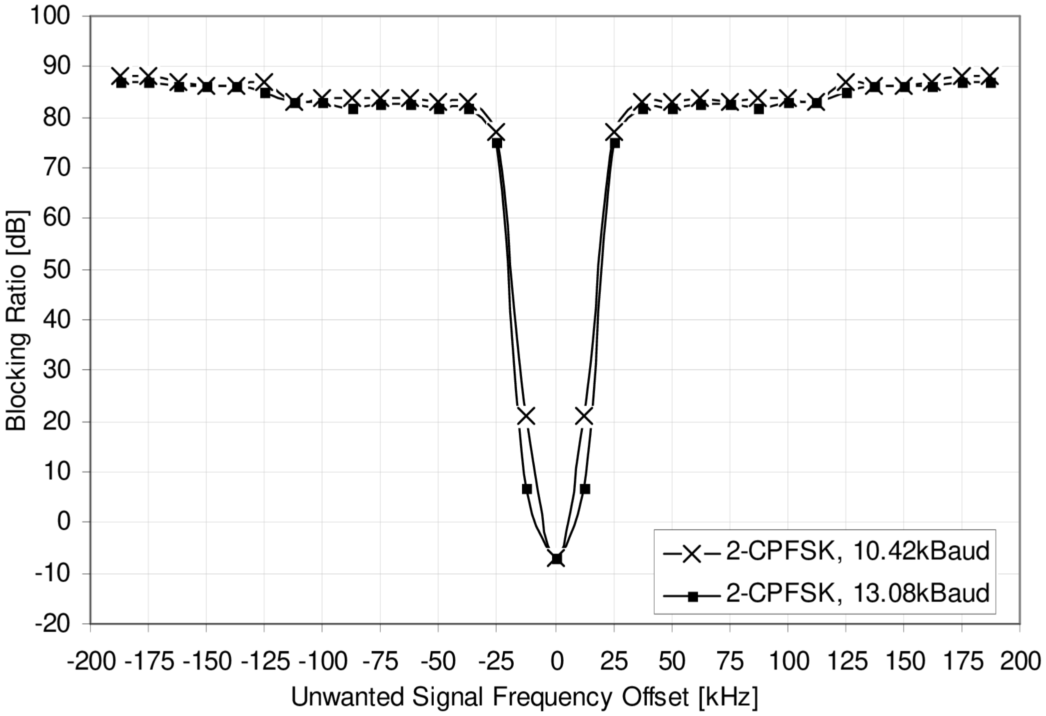

Figure 6.19: Result of the co-channel rejection, adjacent channel selectivity, radio blocking and desensitization measurements; RF frequency 439,1 MHz; 2-CPFSK modulation. As a first local oscillator the HP8640B, Appendix A, I.5, has been used.

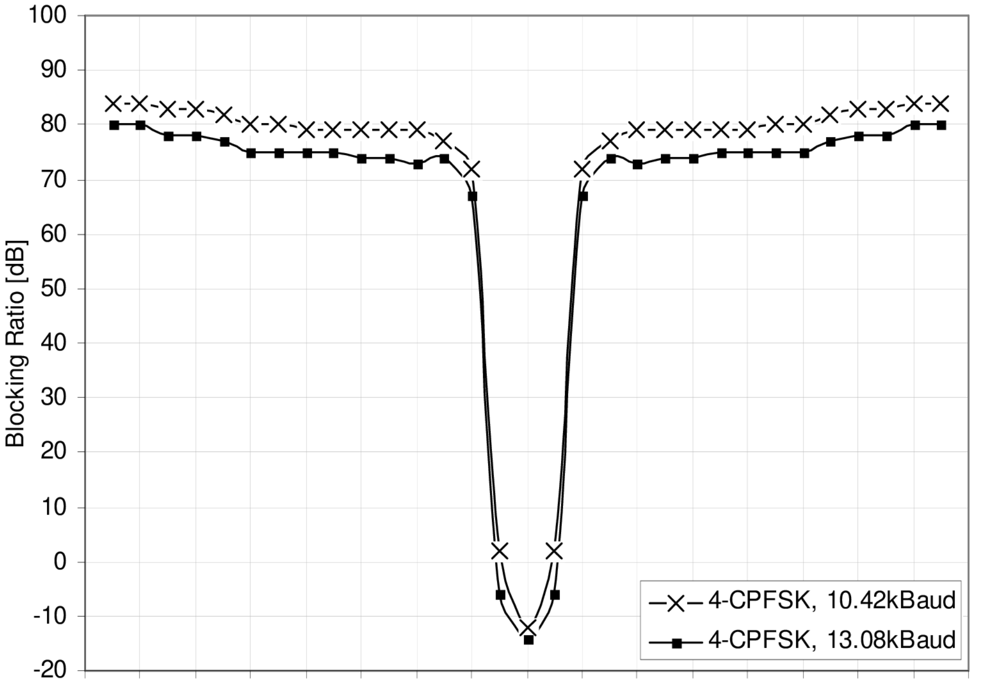

Figure 6.20: Result of the co-channel rejection, adjacent channel selectivity, radio blocking and desensitization measurements; RF frequency 439,1 MHz; 4-CPFSK modulation. As a first local oscillator the HP8640B, Appendix A, I.5, has been used.

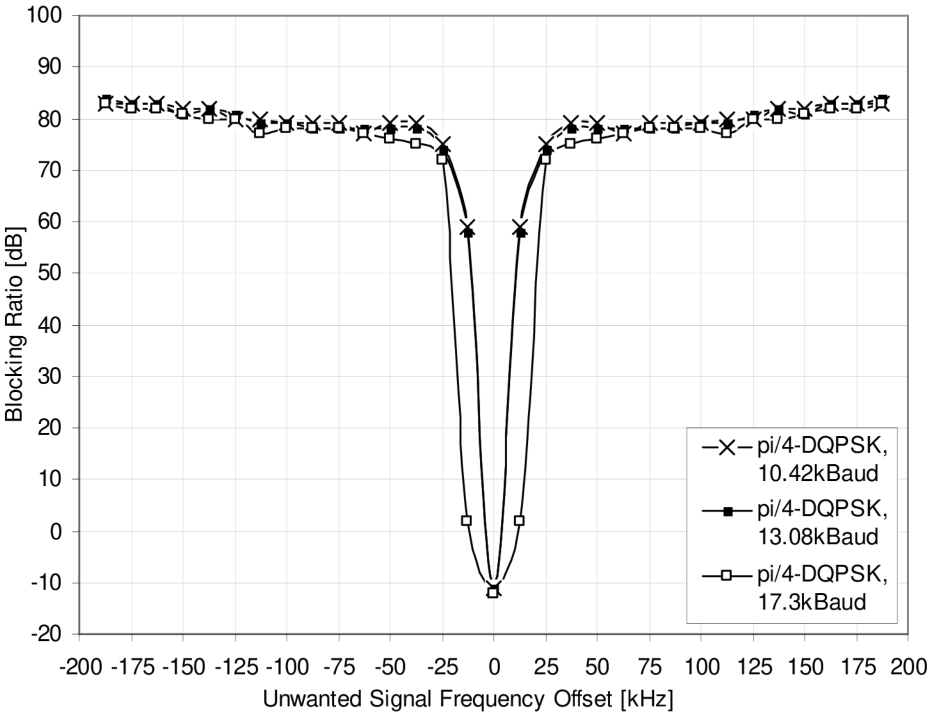

Figure 6.21: Result of the co-channel rejection, adjacent channel selectivity, radio blocking and desensitization measurements; RF frequency 439,1 MHz; π/4-DQPSK modulation.

Table 6.2: Measurement results of the narrowband digital radio parameters in selected mode of operation at nominal frequency of 439.1 MHz.

Modulation Format	Symbol Rate	Mod. Parameter	Data Sensitivity @ BER 10^{-2}	Co-channel Rejection	Adjacent channel Selectivity	Blocking Ratio @ 1MHz offset
[-]	[kBaud]	[-]	[dBm]	[dB]	[dB]	[dB]
2-CPFSK	10.42	h=0.75, α=0.28	-117	-7	77	96
	13.08	h=0.5, α=0.28	-116	-8	75	96
4-CPFSK	10.42	h=0.25, α=0.28	-113	-12	72	92
	13.08	h=0.22, α=0.28	-110	-14	67	87
π/4-DQPSK	10.42	α=0.45	-114	-11	75	92
	13.08	α=0.45	-113	-11	74	92
	17.30	α=0.45	-112	-12	72	90
Measurement uncertainty ±2 dB						

6.7. Efficient use of the narrowband radio channel

The measurement results presented in the previous section can be used to analyze the efficiency of narrowband radio channel utilization by direct comparison to the Shannon bound (Chapter 2.3). Referring to (2.1), (2.3) and (2.4) the E_b/N_0 that is required by the radio receiver in each particular mode of operation can be calculated as

$$\frac{E_b}{N_0}\,[\mathrm{dB}] = SNR_{req} - 10\log(\eta), \qquad (6.12)$$

where

$$SNR_{req}\,[\mathrm{dB}] = S - 10\log(kTB_N) - NF\,, \qquad (6.13)$$

and

$$\eta\,[\mathrm{bit/s/Hz}] = \frac{R_b}{B_N}\,. \qquad (6.14)$$

In (6.13) the NF of 8 dB and occupied bandwidth B_N=25 kHz is assumed. S is the particular level of the data sensitivity measured (Table 6.2) for $BER=10^{-2}$.

Although the results presented are based on measurement values, and thus, they are encumbered with systematic errors – either in NF estimation, BER calculation, measurement uncertainty, various algorithms imperfection etc. – the ambition is to compare the communication efficiency as close to the real application of the narrowband LMR as possible. It can be seen in Figure 6.22 that while for the 4-CPFSK modulation the distance from the Shannon bound is increasing significantly with only moderate increase in spectrum efficiency, it is not the case for π/4-DQPSK.

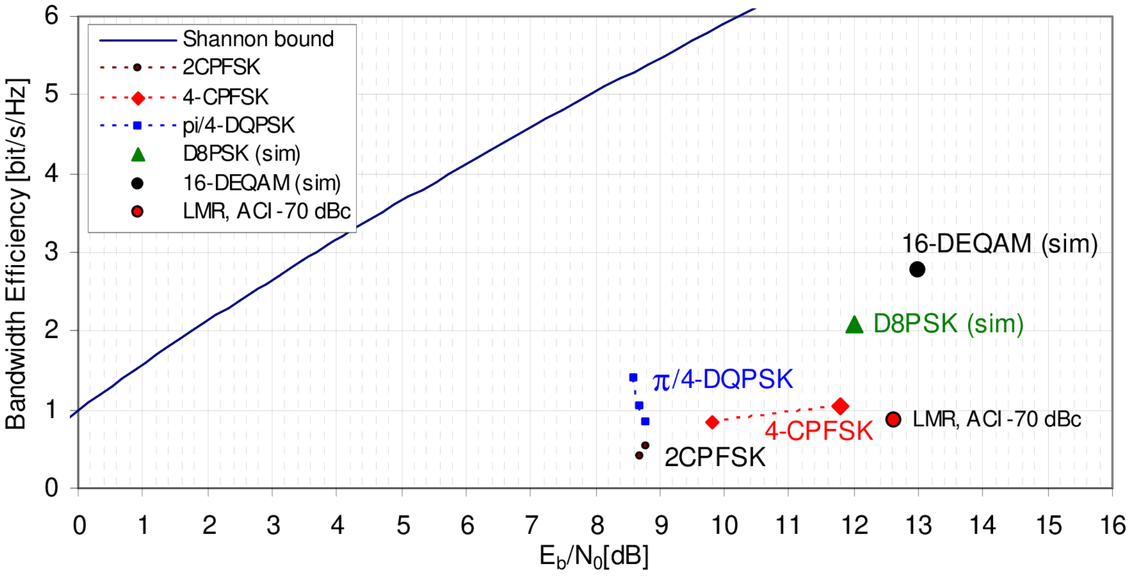

Figure 6.22: Comparison of the spectrum and power efficiency for the applicable modes of the narrowband LMR operation (Table 6.2). NF=8 dB, B_N=25 kHz, $BER=10^{-2}$.

With increasing the spectrum efficiency within the fixed bandwidth, the required value of E_b/N_0 remains almost constant and thus, the communication efficiency approaches towards optimal communication system. Therefore, it can be concluded that the LMR systems utilizing proposed mode of operation uses the assigned bandwidth more effectively. Compared to the up-to-date LMR systems – R_b=21.68 kb/s, B_N=25 kHz, S=-110 dBm ($BER=10^{-2}$), NF=8 dB is assumed – that were subject to ACI limit of -70 dBc the distance is even more evident. At the current state of the project, the D8PSK and 16-DEQAM modes have not yet been implemented, however when the simulated values of the spectrum and power efficiencies are compared in Figure 6.22 it can be seen that the communication efficiency is not increased compared to π/4-DQPSK mode of operation, even though the spectrum efficiency is higher.

Based on the above comparison it can be also concluded that the main ambition of the dissertation thesis presented *…to find a practical way how to combine efficient signalling techniques together with the modern digital methods for rapid frame and symbol synchronization in order to increase the efficiency of the narrowband radio channel usage allocated to the new generation of industrial narrowband LMR system…* has been reached successfully. The particular contributions of this dissertation project and practical recommendations towards meeting this objective are summarized in final chapter.

7 CONCLUSION AND FUTURE WORK

In this section, the preceding work towards meeting the main thesis objective is summarized. Several practical recommendations and possible future improvements are also presented.

The industrial narrowband LMR devices as considered in this dissertation project are subject to European standard ETSI EN 300 113 [1]. The system is operating on frequencies between 30 MHz and 1 GHz, with channel separations up to 25 kHz and is intended for private fixed or mobile radio packet switching networks. Data telemetry, SCADA, maritime and police radio service; traffic monitoring; gas, water and electricity producing factories are the typical system applications. Long distance coverage, high power efficiency and efficient channel access techniques in half duplex operation are the primary advantages the system relays on. Strict limits of adjacent channel power attenuation and robust radio receiver architectures with high dynamic range enable a system coexistence with various communication standards without the additional guard band frequency intervals.

As was shown by this dissertation work, the strict limits of this standard as well as the state of the technology hindered increasing the communication efficiency with which the system has used its occupied bandwidth. The key limiting factor that has been identified was the limit of adjacent channel power attenuation. Lessening the requirement from -70 dBc to -60 dBc in 2007 has opened up the closed door for implementation of the linear digital modulation techniques. However, additional modifications are needed either to the standard itself or to the up-to-date architectures of narrowband LMR devices to make the utilization of the more efficient modes of system operation practically realizable. Based on the dissertation work presented they can be summarized as follows.

Digital modulations for narrowband radio channel

- As it was shown in Section 3 and measurement results presented in Section 6.6, the higher level of admissible adjacent channel interference in addition to the proposed pulse shaping technique enable 10% raise in spectrum efficiency of the exponential digital modulation, from the value of 0.87 bit/s/Hz (21.68 kbit/s @ 25 kHz) to 0.96 bit/s/Hz (24 kbit/s @ 25kHz). However, when the overall power efficiency is of the primary application concern, the additional increase in frequency deviation can be recommended instead of increasing the modulation rate. Thus, the 2-CPFSK modulation having h=0.75 and resulting spectrum efficiency approaching 0.5 bit/s/Hz can be a suggested option.
- When higher symbol rates are selected, the 4-CPFSK losses its power efficiency significantly and therefore the distance from optimal system is increasing rapidly (Figure 6.22). Moreover, for the symbol rate of 13.08 kBaud it lowers down to the very edge of the data sensitivity limit -110 dBm. Further increase of the exponential modulation spectrum efficiency from the values currently being used can be therefore considered inefficient.
- From all the modulation formats studied, the π/4-DQPSK can provide the narrowband LMR system with communication efficiency closest to the optimal communication systems. The proposed solution based on this modulation technique can reach the spectrum efficiency of 1.5 bit/s/Hz. The data sensitivity limit required by [1] can also by fulfilled with margin of 2-3 dB.
- Additional increase in spectrum efficiency can be gained by D8PSK and 16-DEQAM modulation formats. However, compared to π/4-DQPSK, an increase

in overall communication efficiency cannot be expected, while there is a penalty in power efficiency characteristic. Without significant amount of redundant information in form of forward-error-correction coding, also the current (absolute) limit of data sensitivity -110 dBm, which does not take into account the spectrum efficiency of the mode of operation considered, cannot be met.

- As it was shown by the system simulations presented in Chapter 5.7.2, the robustness against multipath fading effects is becoming a critical issue when higher order modulation techniques are considered. Therefore, prior to the practical implementation of the spectrally more efficient modes of operation, an effective algorithm for narrowband radio channel equalization would be required. The multicarrier modulation technique such as FBMCM in combination with adaptive channel equalizer can be an option. It is assumed that in this case, the current network topology as well as the channel access techniques should be a subject of the further analysis.

Pulse shape filtering

- *The Nyquist δ-filters* derived in Chapter 3.3 provide the narrowband digital modem with higher adjacent channel attenuations required with only a half of the filter impulse response group delay compared to truncated raised cosine filters. The group delay parameter determines the digital filter order and more importantly, it is the main contributor to the signal propagation delay in a digital signal processing part of the modem. The resultant occupied bandwidth of the linearly modulated signal makes the usage of high symbol rates of up to 18 kBaud applicable while the shape of the main lobe positively affects the PAPR which remains very close to the optimum values simulated (Section 3.4). An exact symbolic definition of the Nyquist δ-filter in the frequency domain gives the designer scope to choose freely the filter parameters such as equivalent excess bandwidth, group delay and over-sampling parameters and derive coefficients for either the “normal” or the square root filter variants.
- *Nyquist (M) filters* as derived in [47] can also be recommended for practical implementation while the optimization design technique enables additional trade off between inter-symbol interference and out-of-band interference suppression.

Digital algorithms for frequency discrimination

- As was shown in Chapter 4, the algorithms for frequency discrimination represent a typical class of the non-linear signal processing tasks and with an exception of the digital phase locked loop with its combined feed-forward and feedback architecture they use approximation techniques and are limited by a nature of the signal sampling in time. In particular, the approximation of the derivation process by a discrete time differentiation yields to higher over sampling rates in order to reduce the approximation imperfection.
- Two main modifications to the more general formulations of the frequency discriminators have been proposed in Chapter 4. As was shown by the simulation results, the modifications improve the behavior of demodulators at low SNR levels that are important for the maximum usable data sensitivity of the narrowband LMR and in marginal operating conditions (e.g. the radio modem being blocked by a strong interferer).

- From all the studied algorithms the *normalized digital phase locked loop* utilizing the proposed *averaging filter* reaches the best results. However, it has the most demanding realization structure combining feedback and feed-forward architecture. The *modified mathematic algorithm* can be classified a preferable frequency discrimination algorithm for the narrowband LMR radio modems, since it can be effectively implemented by a feed-forward architecture and has the SNR penalty of 0.5 dB compared to the normalized DPLL algorithm with the averaging filter.

Rapid frame and symbol synchronization

In order to implement efficient frame and symbol synchronization algorithm in narrowband LMR system, the following recommendations can be derived based on Chapter 5.

- *Sample wise pattern correlator* in its simplified and effective form (5.18) and (5.37) for the exponential and linear modulation techniques respectively can be used as the frame synchronization algorithm as well as for the initial timing estimation. Further analysis of the autocorrelation properties of the various pseudo-noise and random sequences can result in even better synchronization performance than the one presented. However, based on the simulated and measured results it can be concluded that the algorithm is proved to provide efficient symbol synchronization in future narrowband LMR systems.
- *Decision directed timing estimate detector* in its unified realization structure based on (5.50) and (5.62) can be used to correct the sampling instant over the entire receiving frame. The proposed version of the algorithm does not require any redundant information and forms a low implementation complexity, all-digital solution.
- *Fractional interpolator with linear or parabolic interpolation polynomial* given by (5.83) and (5.85) respectively can be used as the main timing adjustment algorithm. As shown in Section 5.6, for the over-sampling factor exceeding 5 signal samples per modulation symbol, even the simplest interpolator with linear interpolation polynomial can be used without noteworthy system degradation.
- The results of the overall system simulations (Section 5.7.1 and 5.7.2) demonstrate that the proposed synchronization algorithm recovers frame and symbol synchronization with practically acceptable penalty in power efficiency – comparing to the optimally synchronized radio receiver – reaching 1 dB in an analyzed interval of the symbol-error-rates. The overall algorithm requires 16 known symbols to acquire the initial timing estimate. The algorithm can be used for all digital modulation formats studied and excess bandwidths down to 20%. The performance characteristics of the proposed synchronization algorithm can be taken as a benchmark for future synchronization algorithm enhancements.

Narrowband radio system architecture

Following practical recommendation can be derived based on the experimental part of this dissertation project, presented mostly in Chapter 6.

- For the practical design of the narrowband radio receiver with an IF sampling digital part the appropriate combination of the selective analog front-end together with the high performance digital receiver is still inevitable in order to improve the data sensitivity, adjacent channel selectivity and to extend the instantaneous dynamic range of the whole narrowband receiver.

- There were two possible *IF sub-sampling* (Section 6.3) and *IF over-sampling* (Section 6.4) architectures analyzed in this project in order to fulfil the design objective of narrowband radio receiver.
- By comparing the measurement results describing the instantaneous dynamic range of the sub-sampling and over-sampling architecture it can be concluded, that the IF over-sampling architecture reaches substantially wider dynamic range. The main reason can be seen in the efficient proprietary implementation of the higher sampling frequencies that are needed to widen the instantaneous dynamic range of the digital part.
- There is a possibility to use the sub-sampling technique in modern IF-sampling narrowband receivers, in order to lower the required sampling frequency. But, the sampling frequency cannot be lowered arbitrarily. It is necessary to use significantly higher sampling frequencies comparing to the occupied signal bandwidth to widen the overall instantaneous dynamic range of the narrowband receiver. While increasing the sampling frequency significantly increases price and consumed power of the digital part, the architectures based on IF sub-sampling technique can be classified impractical for the high performance narrow band radio device.
- Although the digital filters bear a major part of the channel selectivity, the proposed architectures of the IF sampling digital receiver do not reach the required values of instantaneous dynamic range in close and farther distance from the nominal carrier frequency. The use of anti-aliasing filters with steep band-pass response is still inevitable for the intended analog front-end system. This part can be seen as the main restrictive element in the narrowband radio receiver architecture that dominantly limits the flexibility of the whole equipment, especially when it comes to processed bandwidths applicable. This limitation is considered a main disadvantage of both proposed architectures.

Technical parameters of the narrowband receiver

- *Maximum Usable Data sensitivity (-110 dBm)*: limit can be fulfilled by the proposed narrowband radio receiver for spectrum efficiencies reaching 1.5 bit/s/Hz using π/4-DQPSK, and lower for 2-CPFSK and 4-CPFSK modulation formats. For additional increase in spectrum efficiency, the absolute limit of data sensitivity imposes an impractical constraint. It is therefore reasonable to advise the modification of the present standard [1], in order to make use of higher spectrally efficient modulation techniques by the LMR system operating in LBT mode possible. In this way, the spectrum efficiency of narrowband systems can be increased.
- *Co-channel interference rejection (0 dB to -8 dB)*: without additional forward-error-correction techniques this limit can be fulfilled only in 2-CPFSK mode of operation. As was concluded in Section 6.6, this limit is too severe and hinders the practical usage of spectrally more efficient modulation schemes while meeting limits of all essential radio parameters. Adequate lowering of the limit being subject to increased spectrum efficiency should be advised, without the risk of assigned spectrum misuse. As it was shown in Chapter 6.7, contrary can be expected the case, especially in π/4-DQPSK mode of operation.
- *Adjacent channel selectivity (70 dB)*: while this limit is met for 2-CPFSK mode of operation, it is becoming difficult to reach this limit with higher spectrally efficient modulation techniques 4-CPFSK, π/4-DQPSK. The limitation is caused mainly by two factors. Firstly, it is the limited instantaneous dynamic

range of the IF sampling digital radio part which can be improved using strictly selective analog front-end part while abnegating the flexibility of the overall radio construction. Secondly, it is the absolute level of the phase noise of first receiver local oscillator which cannot – or it is highly impractical to – be lowered to the limits that would be required for higher spectrally efficient techniques such as D8PSK and 16-DEQAM. Natural lowering of this limit with increasing spectrum efficiency of the mode of operation is therefore advisable. The absolute power level (e.g. -37 dBm) of the interfering signal that the radio receiver has to withstand while operating near (+3 dB) the specified data sensitivity limit would be the suggested modification to the present standard, without the risk of future communication system co-existence problems.

- *Blocking and desensitization (84 dB)*: the same holds true for the radio blocking and desensitization of the radio receiver in close vicinity (below 1 MHz) to the nominal carrier frequency. While typically, it is not critical to fulfill limit of this parameter at the frequency offsets exceeding 1 MHz, below this value, the residual level of the first receiver local oscillator phase noise is becoming a limiting factor. In any case, again the absolute power level (e.g. -23 dBm) of the interfering signal that the radio receiver has to withstand while operating near (+3 dB) the specified data sensitivity limit would be the suggested modification to the present standard, without the risk of future communication system co-existence problems.

REFERENCES

[1] ETSI EN 300 113-1 V1.6.2 (2009-11), Electromagnetic compatibility and Radio spectrum Matters (ERM), Part 1: Technical characteristics and methods of measurement. *European Standard*. ETSI, 11/2009.

[2] DANĚK, K. Efficient use of mobile radio channel II. In *Radioengineering*, June 2000, vol. 9, no.2, p.1-4. [Online] Cited 2010-10-02. Available at: http://www.radioeng.cz/fulltexts/2000/00_02_01_04.pdf

[3] JESUALE, N., EYDT, C. B. A Policy Proposal to Enable Cognitive Radio for Public Safety and Industry in the Land Mobile Radio Bands. In *2nd IEEE International Symposium on New Frontiers in Dynamic Spectrum Access Networks. DySPAN 2007*. 10.1109/DYSPAN.2007.16.

[4] NAVALEKAR, A. C. at al. Effects of Push-To-Talk (PTT) delays on CSMA based Capacity Limited Land Mobile Radio (LMR) Networks. In *ISWPC*, 2008, 978-1-4244-1653-0/08.

[5] R&TTE 1999/5/EC, Directive 1999/5/EC of the European Parliament and of the Council. In *Official Journal of the European Communities.* April 1999.

[6] DANĚK, K. *Efektivní využití rádiového kanálu pro přenos dat*, Dissertation Thesis, VUT Brno, 2001.

[7] PROAKIS, J., G. *Digital Communication, 4th edition.* New York: McGraw-Hill Higher Education, 2001.

[8] BUTCHER, A. B., KAMALI, B. Comparison of Doubinary and 4-Level CPFSK signals for Narrowband LMR applications. In *IEEE Trans. on Broadcasting 1999.* vol. 45, no. 2, June 1999, p. 177-186.

[9] BOBULA, M. *Use of Radio Channel 200 kHz for data transmission.* MSc. Diploma Thesis, University of Technology BRNO, 2006.

[10] SENGUL, E. A Spectrally Efficient PMR Systems Utilizing Broadcast Service. In *IEEE Trans. on Broadcasting 2005.*vol. 51, no. 4, December 2005, p. 493-503.

[11] NOURI, M. TEDS: A High speed digital Mobile Communication Air Interface for Professional Users – Part I: Overview of Physical Layer. In *Vehicular Technology Magazine, IEEE,* 2007, 10.1109/MVT.2006.343629.

[12] ETSI TS 100 392-2 V3.1.1, "Terrestrial trunked radio (TETRA); Voice plus Data (V+D); Part 2: Air Interface (AI). *Technical specification*, ETSI 10/2008.

[13] BOBULA, M., DANĚK, K., PROKEŠ, A. Implementation of Industrial Narrow Band Communication System into SDR concept. In *Radioengineering,* vol. 17, no. 4, December 2008. [Online] Cited 2010-10-02. Available at: http://www.radioeng.cz/fulltexts/2008/08_04a_086_092.pdf

[14] BURR, A. *Modulation and Coding for Wireless Communications.* Harlow: Pearson Education Ltd. 2001. 360 pages. ISBN 0 201 39857 5.

[15] DANĚK, K., *Moderní rádiový přijímač – kniha o jeho návrhu.* (in Czech),*" Modern radio receiver – the designer's handbook"*, Praha: BEN 2005. 215 pages. ISBN 80-7300-142-X.

[16] ERM TG DMR, *Suggestions and edits to ETSI EN 300113-1 V1.6.1.,* PE 20061208.

[17] WILSON, J. F. The TETRA System and its Requirements for Linear Amplification. In *IEE Colloquium on Linear RF Amplifiers and Transmitters,* April 1994.

[18] SHANNON, C., E., Communication in the Presence of Noise. In *Proceeding of the I.R.E.,* IRE New York, 1949.

[19] WYNER, A. D., SHAMAI S. Introduction to "Communication in the Presence of Noise" by C.E. Shannon. In *Proceeding of the IEEE,* vol. 86, no. 2, February 1998.

[20] SKLAR, B., Rayleigh Fading Channels in Mobile Digital Communication Systems Part I: Characterization. In *IEEE Communication Magazine 1997.* IEEE, July, 1997.

[21] SKLAR, B., Rayleigh Fading Channels in Mobile Digital Communication Systems Part II: Mitigation. In *IEEE Communication Magazine 1997.* IEEE, July, 1997.

[22] BOBULA, M. OFDM Performance Simulation for Narrow Bandwidth Radio Channel of 200 kHz. *Final technical report 2006.* Manipal Academy of Higher Education. MIT India. 2006.

[23] BOBULA, M., DANĚK. K., PROKEŠ, A., Simplified frame and symbol synchronization for 4–CPFSK with h=0.25. In *Radioengineering*, vol.17, no. 2, June 2008, ISSN 1210-2512. [Online] Cited 2010-10-03. Available at: http://www.radioeng.cz/fulltexts/2008/08_02_108_114.pdf

[24] BOBULA, M. FPGA Implementation of an SDDR Core for Radio Transceiver. In *STUDENT EEICT 2006*. vol. 2. VUT BRNO, 2006. p. 14 - 16, ISBN-80-214-3161-X.

[25] DWIVEDI, S., AMRUTUR, B., BHAT, N. Optimizing resolution of signals in a low-IF receiver. In *Symposium on Signals, Circuits and Systems, 2007*, ISBN: 1-4244-0969-1.

[26] MILLER, P., CESARI, R. Wireless communication: Signal conditioning for IF sampling, 24 pages., SLOD006A, [online] 08-11-2008, Available at: http://focus.ti.com/lit/ml/sloa085/sloa085.pdf

[27] KESTER, W., MT-001: Taking the Mystery out of the Infamous Formula, "SNR=6.02N+1,76dB" and Why You Should Care. [online] 08-11-2008, Available at: http://www.analog.com/en/analog-to-digital-converters/ad-converters/products/tutorials/CU_tutorials_MT-001/resources/fca.html

[28] DA DALT, N., HARTENECK, M., SANDER, CH., WIESBAUER, A., On the jitter requirements of the sampling clock for analog-to-digital converters. In *IEEE Trans. on circ. and sys.*, vol. 49, no. 9, pp. 1354-60, Sept. 2002.

[29] ALTERA Corp., 2. Cyclone II Architecture CII51002-3.1. [online] 2008-09-11, Available at: http://www.altera.com/literature/lit-cyc2.jsp

[30] SCHREIER, R., HENDRIKS, P. Low-Power IC Digitizes 300 MHz IF., Analog Dev., [online] 08-04-2009, Available at: http://www.analog.com/static/imported-files/tech_articles/AD9874_Microwave_RF_Article.pdf

[31] LOSADA, R., A., LYONS, R., Reducing CIC filter complexity. In *IEEE Signal proc. magazine,* July 2006.

[32] XILINX Inc. Distributed Arithmetic FIR Filter. V 9.0. Xilinx, Inc., April 2005, [online] 10-11-2008, Available at: http://www.xilinx.com/ipcenter/catalog/logicore/docs/da_fir.pdf

[33] YU, F. FPGA implementation of a fully digital FM demodulator. In *The ninth International Conference on Communications Systems*, ICCS 2004, 10.1109/ICCS.2004.1359416.

[34] SCHNYDER, F., HALLER, CH., *Implementation of FM Demodulator Algorithms on a High Performance Digital Signal Processor.* MSc. Diploma Thesis, Technological University Nanyang, 2002.

[35] FONSEKA, J., Baseband pulse shaping to reduce intersymbol interference in Narrowband M–ary CPFSK Signaling. In *Tenth Annual International Phoenix Conference on Computers and Communication,* 1991, CH2859-5/91/0000/0393.

[36] ETSI EN 301 166-1 V1.3.2 (2009-11), Electromagnetic compatibility and Radio spectrum Matters (ERM), Part 1: Technical characteristics and methods of measurement. *European Standard.* ETSI, 11/2009.

[37] RIMOLDI, B., QUINN, L., Coded Continous Phase Modulation Using Ring Convolutional Codes. In *IEEE Trans. on Comm.,* Vol 43, No. 11, November 1995, p. 2714 – 2720.

[38] MAW, R., DESMOND, T., Externally Encoded Space-Time Coded Systems with CPFSK. In *IEEE Int. Conference on Wireless Networks.* IEEE 2005, p. 1597-1602.

[39] MAO, R., FONSEKA, J., Nonlinear Multi-h Phase Codes for Full Response and Partial Response CPFSK Modulation. In *IEEE International Conference on Communication,* 1994, p. 363-368.

[40] ETSI EN 302 561 V1.2.1 (2009-12), Electromagnetic compatibility and Radio spectrum Matters (ERM), Land Mobile Service; Radio Equipment using constant or non-constant envelope modulation operating in a channel bandwidth of 25 kHz, 50 kHz, 100 kHz or 150 kHz; Harmonized EN covering essential requirements of article 3.2 of the R&TTE Directive. *European Standard*. ETSI, 12/2009.

[41] ALAGHA, S., KABAL, P. Generalized Raised-Cosine Filters. In *IEEE Trans. on Comm.* Vol. 47, No.7, July 1999, p. 989-997.

[42] BEAULIEU, C. N., et al., A "Better Than" Nyquist Pulse. In *IEEE Communications Letters.* Vol. 5, No.9, September 2001., p. 367-368.

[43] BOROUJENY, B. F., Nyquist Filters with Robust Performance Against Jitter. In *IEEE Trans. on Signal Processing.* Vol. 46, No. 12, December 1998., p. 3427-3431.

[44] CHATELAIN, B., GAGNON, F., Peak-to-Average Power Ratio and Intersymbol Interference Reduction by Nyquist Pulse Optimization. In *60th IEEE Vehicular Technology Conference,* 2004,VTC2004-Fall. p. 954-958.

[45] KRAGH, F., et al., Spectrally efficient digital modulation using new pulse shapes. In *Military Communications Conference, 2007.* MILCOM 2007 IEEE, 5 pages.

[46] HERMES, D., KRAGH F. A bandwidth efficient constant envelope modulation. In *Conference on Signals, Systems and computers, 2006.* ACSSC '06, 2006, p. 488-492.

[47] FARHANG-BOROUJENY, B. A universal square-root Nyquist (M) filter design for digital communication systems. In *Proceeding of the SDR 06 Tech Conference.* SDR forum 2006.

[48] HARRIS, J. F. On the use of windows for harmonic analysis with the discrete Fourier transform. In *Proceedings of the IEEE.* Vol. 66, No. 1, January 1978.

[49] BENJEBBOUR, A., et al., Nonparametric interference suppression using cyclic Wiener filtering: Pulse Shape Design and Performance Evaluation. In *EURASIP Journal on Wireless Com. and Networking,* vol. 2008, Article ID 243548, 2008, 14 pages.

[50] Mathworks Inc. *Digital filter design DSP blockset description.* [Online] Cited 2010-01-30. Available at: http://www.mathworks.com/access/helpdesk_r13/help/toolbox/dspblks/digitalfilterdesign.html

[51] JAN, J. *Digital Signal Filtering, Analysis and Restoration.*(in Czech) VUTIUM BUT, BRNO. 2002. ISBN 80-214-2911-9.

[52] ŽALUD, V. *Modern Radioelectronics* (in Czech), BEN Praha, 2000. ISBN 80–86056–47–3.

[53] FX919, 4-level FSK modem data pump, *CML Semiconductor product datasheet, July 1997.*

[54] FARHANG-BOROUJENY, B. *Signal Processing Techniques for Software Radios.* ECE Dep. University of UTAH. Salt Lake City, USA. 364 pages. Self published at http://www.lulu.com/

[55] REED, J., H. Software Radio: A Modern Approach to Radio Engineering, Prentice Hall, New Jersey, 2002. ISBN 0-13-081158-0.

[56] HOŠEK, J., An Overview of the wireless digital communication systems. (in Czech), [Online] Cited 2010-03-30. Available at: http://www.elektrorevue.cz/cz/clanky/komunikacni-technologie/0/prehled-modernich-bezdratovych-digitalnich-komunikacnich-systemu/

[57] SVENSSON, N., A., B. On Differentially Encoded Star 16QAM with Differential Detection and Diversity. In *IEEE Transaction on Vehicular Tech.* Vol. 44, No. 3, August 1995.

[58] YU, M., FEHER, K. π/4-FQPSK: An Efficiency Improved, Standardized π/4-DQPSK Compatible Modulation / Nonlinearly Amplified RF Wireless Solution. In *IEEE Trans. on Broadcasting 1996.*vol. 42, no. 2, June 1996, p. 95-101.

[59] CLARKE, R. *On Synchronization Issues in Wireless Mobile Digital Communications.* MSc. Diploma Thesis, University of Canterbury, Christchurch, 2002.

[60] PEIMIN, CH. *Timing and Frequency Synchronization Issues for Narrowband Wireless Communication Systems.* MSc. Diploma Thesis, University of California, Berkeley, 2002.

[61] CAIRE, G., ELIA, C. A new symbol timing and carrier frequency offset estimation algorithm for noncoherent orthogonal M-CPFSK. In *IEEE Trans. on Commun.,* Vol.45, No. 10, October 1997, p. 1314 - 1326.

[62] D'ANDREA A., MENGALI U., REGGIANNINI R. A digital approach to clock recovery in generalized minimum shift keying. In *IEEE Trans. on Veh. Tech.,* Vol.39, No. 3, August 1990, p.227-234.

[63] MORELLI M., MENGALI U. Joint frequency and timing recovery for MSK-type modulation. In *IEEE Trans. on Commun.,* Vol.47, No. 6, June 1999, p. 938 - 946.

[64] ZHAO Q. Advanced synchronization techniques for continuous phase modulation, *A Thesis Presented to School of El. and Computer Engineering,* Georgia, May 2006.

[65] YU Z., ZHAO M., LIU L., QIU P. A timing recovery scheme for pulse shaped 4-CPFSK with h-0.25. In *10th Asia-Pacific Conf. on Commun.*, September 2004 IEEE, p.343-346.

[66] YU Z., ZHAO M., LIU L. Joint frequency and timing recovery for pulse shaped 4-CPFSK with h-0.25., In *IEEE Vehicular Technology Conference,* April 2004, 0-7803-8521-7.

[67] YAFENG Z., ZHIGANG C., ZHENGXIN M. Modulation index estimation for CPFSK signals and its application to Timing Synchronization. In *10th Asia-Pacific Conf. on Commun.*, September 2004 IEEE, p.874-877.

[68] YAFENG Z., ZHENGXIN M., ZHIGANG C. A novel carrier recovery method for CPFSK demodulation. In *Communication Technology Proceedings, 2000.* WCC – ICCT 2000. 0-7803-6394-9.

[69] D'ANDREA A., MENGALI U., REGGIANNINI R., The modified Cramer-Rao bound and its application to synchronization problems. In *IEEE Trans. on Commun.,* Vol.42, No. 2/3/4, February 1994, p.1391 - 1399.

[70] GARDNER F.M., Interpolation in digital modems – Part I: Fundamentals, In *IEEE Trans. on Commun.,* vol. 41, March 1993, pp. 502–508.

[71] ERUP L., GARDNER F.M., HARRIS R. A., Interpolation in digital modems–Part II: Implementation and performance, In *IEEE Trans. Commun.,* vol. 41, No.6, June.1993, pp. 998–1008

[72] BOBULA, M., Design of the fractional delay interpolators based on Farrow structure. (in Czech), [Online] Cited 2010-06-13. Available at: http://www.elektrorevue.cz/cz/clanky/zpracovani-signalu/5/navrh-cislicovych-filtru-se-spojite-promennou-hodnotou-zpozdeni-na-bazi-farrowova-interpolatoru/

[73] FARROW, C.W., A Continuously Variable Digital Delay Element, In *Proc. IEEE Int. Symp. Circuits & Systems*, Espoo, Finland, 1988, s. 2641–2645.

[74] BABIC, D., LEHTINEN, V., RENFORS, M., Implementation of Farrow Structure Based Interpolators with Subfilters of Odd Length, In *International Symposium on Circuits and Systems 2004.* ISCAS'04, 0-7803-8251-X/04.

[75] CARSON, K.S., WU, Y.C., On the Design and Efficient Implementation of the Farrow Structure, In *IEEE Signal Proc. Letters*, vol. 10, no. 7, 2003.

[76] HARRIS, F.J., RICE, M., Multirate Digital Filters for Symbol Timing Synchronization in Software Defined Radios, In *IEEE Journal on Sel. Areas in Comm.*, vol. 19, no. 12, Dec. 2001.

[77] GHADAM, A., RENFORS, M., Farrow Structure Interpolators Based on Even Order Shaped Langrange Polynomials, In *Proceed. of the 3rd Intern. Symp. on Image and Sig. Proc. and Analysis* , 2003.

[78] BARTSCH, H. J., *Matematické vzorce*, "*Math equations*", (in Czech), Academia, Praha, 2006, ISBN 80-200-1448-9.

[79] FORT, A., WEIJERS, J., DERUDDER, V., A Performance and Complexity Comparison of Auto-correlation and Cross-correlation for OFDM Burst Synchronization. In *2003 IEEE Int. Conf. on Acoustics, Speech, and Signal Processing*, 0-7803-7663-3/03 ISASSP, 2003.

[80] SHIMA, M., J. *FM Demodulation Using a Digital Radio and Digital Signal Processing*. A thesis presented in partial fulfillment of the requirements for the degree of Master of Science. University of Florida, 1995.

[81] ARMSTRONG, E. H. A Method of Reducing Disturbances in Radio Signaling by a System of Frequency Modulation. In *Proceeding of the IEEE.* August 1984. ISSN 0018-9219.

[82] ANDRAKA, R. A Survey of CORDIC Algorithms for FPGA Based Computers. Andraka Consulting Group, Inc. North Kingstown, 1998. [Online] Cited 2010-07-17. Available at: http://www.andraka.com/files/crdcsrvy.pdf

[83] LAKSHMI, B., DHAR, A.S., CORDIC Architectures: A Survey. *VLSI Design*, Volume 2010, Article ID 794891, 19 pages. [Online] Cited 2010-07-17. Available at: http://www.hindawi.com/journals/vlsi/2010/794891.html

[84] DODLEY, J., P., ERVING, R., H., RICE, C.W., In-building software radio architecture, design and analysis., In *The tenth IEEE International Symposium on Personal, Indoor and Mobile Radio Communications,* PIMRC 2000, 10.1109/PIMRC.2000.881470.

[85] LAWTON, M., C., Sensitivity analysis of radio architectures employing sample and hold techniques. In *Radio rec. and assoc. syst. 1995,* Conf. publication No. 415, pp. 52-56.

[86] HAGHIGHAT, A., A review on essential and technical challenges of software defined radio. In *Proceedings MILCOM, 2002*,ISBN 0-7803-7625-0.

[87] OERDER, M., MEYR, H., Digital Filter and Square Timing Recovery, In *IEEE Trans. on Comm.*, vol. 36, no. 5, 1988, s. 605–612.

[88] AD9874, IF Digitizing Subsystem, *Analog Devices product datasheet 03/2003.,* [Online] Cited 2010-10-07. Available at: http://www.analog.com/static/imported-files/data_sheets/AD9874.pdf

[89] AD9237, 12-Bit, 20/40/65MSPS 3V Low Power A/D Converter, *Analog Devices product datasheet 05/2010.,* [Online] Cited 2010-10-07. Available at: http://www.analog.com/static/imported-files/data_sheets/AD9237.pdf

[90] CMX7163, QAM modem, *CML Microcircuits product datasheet 2010,* [Online] Cited 2010-10-27. Available at: http://www.cmlmicro.com/Products/Index.asp?/Products/WData/cmx7163.htm

[91] BOBULA, M., PROKEŠ, A., DANĚK, K. Nyquist Filters with Alternative Balance between Time- and Frequency-domain Parameters. In *EURASIP Journal on Advances in Signal Processing.* Volume 2010, Accepted for publication 2010-10-28.

[92] ASCHBACHER, E., et al. *Prototype Implementation of Two Efficient Low-Complexity Digital Predistortion Algorithms. ontributions to the power linearization using digital baseband adaptive predistortion*. In *EURASIP Journal on Advances in Signal Processing.* Volume 2008, [Online] Cited 2010-10-07. Available at: http://www.hindawi.com/journals/asp/2008/473182.html

[93] CMX998, Cartesian Feed-back Loop Transmitter, *CML Microcircuits product datasheet 01/2010,* [Online] Cited 2010-10-07. Available at: http://www.cmlmicro.com/products/innovate/docs/inv998_1.pdf

[94] 8640B Signal Generator, Operating And Service Manual Part NO. 08640-90197, Hewlett Packard, 1982.

[95] ALTERA Corp., *Cyclone III Device Handbook*, CIII5V1-3.3. [online] 2010-10-31, Available at: http://www.altera.com/literature/hb/cyc3/cyc3_ciii5v1.pdf

ABBREVIATIONS

A

ADC	Analog-to-digital conversion/converter
ACI	Adjacent Channel Interference
ACP	Adjacent Channel Power
AGC	Automatic Gain Control
AM-AM	Amplitude-to-amplitude conversion, distortion
AM-PM	Amplitude-to-phase conversion, distortion
A-M3	RF signal used for degradation measurement, 400 Hz modulation rate, 12% CS frequency deviation
AWGN	Additive White Gaussian Noise

B

BER	Bit-Error-Ratio (Rate)
BT	BT product, design parameter of the Gaussian filter, GMSK

C

CIC	Cascaded Integrator-Comb digital filter
2-CPFSK	Two State Continuous Phase Frequency Shift Keying (digital modulation format)
4-CPFSK	Four State Continuous Phase Frequency Shift Keying (digital modulation format)
CPM	Continuous Phase Modulation
CS	Channel Separation
CSMA	Carrier Sense Multiple (channel) Access

D

DA	Data Aided digital method (synchronization tasks)
DAC	Digital-to-Analog Converter, conversion
DC	Direct current, 0 Hz frequency
DDTED	Decision directed timing error detector
DDC	Digital Down Converter, conversion
8DPSK	8-state differentially encoded phase shift keying modulation
π/8-D8PSK	π/8-phase shift differential encoded 8-state phase shift keying modulation
16-DEQAM	Star constellation, 16-state differentially encoded quadrature amplitude modulation
DPLL	Digital Phase Locked Loop
DSP	Digital signal processing, processor

E

EDR	Effective Dynamic Range
ENOB	Effective Number of Bits
E_b/N_0	Bit-energy to Noise power spectrum density ratio, usually given in [dB]
emf	electromotive force

F

FBMCM	Filter Bank Multi Carrier Modulation
FIR	Finite Impulse Response (digital) filter
FFT	Fast Fourier Transform
FM	Frequency Modulation, analog frequency modulation
FPGA	Field Programmable Gate Arrays - electronic circuit

G

GMSK	Gaussian minimum shift keying (digital modulation format)
GSM	Global System for Mobile Communication

H

HT200	Highly Terrain fading radio channel model at 200 km/hour

I

I	In-Phase signal component

IDR	Instantaneous dynamic range
IF	Intermediate Frequency
IIR	Infinite Impulse Response (digital) filter
IS-95	Interim Standard
ISI	Intersymbol Interference

L

LBT	Listen-before-transmit (mode of operation)
LE	Logic Elements (ALTERA Corp.)
LMR	Land Mobile Radio (system)
LSB	Least Significant Bit (byte)

M

MCRB	Modified Cramer-Rao Bound
MSB	Most Significant Bit (byte)
MSE	Mean Square Error
MSE_{τ}	timing Mean Square Error
MSK	Minimum shift keying modulation, h=0.5

N

NCO	Numerically Controlled Oscillator
NDA	Non-Data Aided digital method, (synchronization tasks)
NF	Noise Figure in dB

O

OSR	Over-sampling Ratio [-], processing gain in [dB]

P

PER	Packet-Error-Rate, ratio
P_{out}	Transmitted output power in Watts or in [dBm]
PMR	Private Mobile Radio (system)
PN	Pseudo-noise, random sequence
PAPR	Peak-to-average power ratio

Q

Q	Quadrature signal component
16-QAM	16-state quadrature amplitude modulation
QPSK	quadrature phase shift keying modulation
$\pi/4$-DQPSK	$\pi/4$-phase shift differential encoded quadrature phase shift keying modulation
$\pi/4$-FQPSK	$\pi/4$-phase shift Feher quadrature phase shift keying modulation

R

RC	Raised Cosine (pulse shaping filter)
RF	Radio Frequency
RND	square-root Nyquist δ-filter

S

SAW	Surface Acoustic Wave analog filter
SDR	Software Defined Radio
SCADA	Supervisory Control and Data Acquisition systems
SNR	Signal-to-Noise ratio in dB
S/N	Signal-to-Noise ratio
SWPC	Sample Wise Pattern Correlation (synchronisation technique)

T

TETRA	Terrestrial Trunked Radio
TED	Timing Error Detector
TEDS	TETRA Enhanced Data Service
TU50	Typical Urban fading radio channel model at 50 km/hour

V

VHF	Very High Frequency range 30 MHz to 300MHz

LIST OF SYMBOLS

	A
$A(t)$	continuously variable signal amplitude
$A[i]$	variable signal amplitude, digital representation
a_0, a_1, a_2	parameters of generally defined Blackmann window
α	excess bandwidth parameter, roll-off factor, equivalent excess bandwidth
α_0	base excess bandwidth parameter, Nyquist δ-filter
α_k	sequence of modulation symbols (real or complex values)
	B
B	occupied bandwidth
B_N	receiver noise bandwidth
$b_l(i)$	Farrow coefficients
β	parameter of the "better" than Nyquist filter [42]
	C
$C_i(\mu_k)$	coefficients of the Lagrange polynomial interpolation
	D
δ	shift parameter of the Nyquist δ-filter
Δf	maximum frequency deviation of exponential modulation
Δf	overall frequency offset between transmitter and receiver
Δv	relative transmitter-receiver velocity
$\Delta\nu[i]$	Band limited noise signal at the differential demodulator output
$\Delta\phi(k)$	phase change in differential modulation
	E
E	mean value or expectation function
E_b	signal energy per one bit of information
E_S	signal energy per one modulation symbol
$e[k]$	error sample of the kth symbol
$\varepsilon[i]$	approximation imperfection
$\varepsilon^2_k[i]$	mean square error of the detected signal (at kth symbol)
	F
F_i	sampling frequency commensurate to the symbol rate
F_s	general sampling frequency, the same as f_s
f	frequency in general meaning
f_0	normalized cut-off frequency of the pulse shaping filter
f_d	Doppler shift frequency
f_s	sampling frequency
	G
$G(f)$	overall Nyquist filter frequency characteristic
$g(t)$	overall Nyquist filter continuous-time impulse response
G_D	digital filter group delay
G_N	noise improvement (gain) in [dB]
G_{FE}	analog front-end gain
	H
$H(f)$	square-root Nyquist filter frequency characteristic
h	modulation index of the exponential modulation
$h(t)$	continuous-time impulse response of the pulse shaping filter (transmitter

	part)
$h_a(t)$	continuous-time impulse response of the analog filter (Farrow interpolator)
$h_{PLL}[n]$	impulse response of the PLL filter
η	bandwidth (spectrum) efficiency
$\eta_{(TX)}$	overall transmitter power efficiency

I

i	general sample index in digital algorithm

K

k	Boltzmann's constant
k_{FM}	sensitivity constant of frequency modulator
k	index, counting modulation symbols
k	number of information bits per one modulation symbol

L

L	length of the digital filter impulse response
L_0	length of the preamble in symbol intervals, observation interval
λ_0	wavelength calculated at nominal frequency

M

M_N	noise margin
M	modulation order, number of modulation states
m	general signal sample index, the same as [i]
$m(t)$	modulation signal for exponential modulation
μ	step-size parameter of the adaptive timing estimation loop
μ_k	fractional interval in digital signal interpolation

N

N	oversampling factor, number of samples per modulation symbol
N	number of ADC bits (signal resolution)
N_0	noise power spectral density
N_O	digital filter order
N_{FFT}	length of the FFT algorithm
n	digital sample index within the specific interval
ν	frequency offset

Q

$q(t)$	phase pulse in CPM modulations
θ	Initial phase of the receive signal

R

R	symbol (Baud) rate
$R(\tau)$	correlation function
$R_{xx}(\tau)$	auto-correlation function of signal x
$R_{xy}(\tau)$	cross-correlation function of signal x and y
R_b	(gross) data rate
RX	short assignment of the receiver
$r(t)$	continuous -time baseband representation of the receive signal
ρ_{ISI}	relative level of residual ISI in [dB]
ρ_{SL}	relative level of impulse response side lobes level in [dB]
ρ_{ISI}	relative stop-band attenuation of the pulse shaping filters in [dB]

S

S	data sensitivity level in [dBm] or [dBµV]
$s(t)$	complex signal envelope, baseband signal representation

$s_I(t)$	in-phase modulated signal component
$s_Q(t)$	quadrature modulated signal component
$\Sigma-\Delta$	sigma-delta modulator
σ^2	mean squared deviation, variance

T

T	base modulation symbol time duration
T_S	sampling period
TX	short assignment of the transmitter
t	assigns time in general
τ	optimum symbol timing instant
τ_0	initial symbol timing estimate

U

$\upsilon(t)$	band limited continuous-time noise signal
$\upsilon[i]$	band limited noise signal, digital representation

W

$w(t)$	general assignment of window function e.g. rectangular window
$w(t)$	continuous-time AWGN noise signal

X

x	general input variable
$x[i]$	general input signal to the digital algorithm
$x_I[i]$	general input signal to the digital algorithm, In-phase component
$x_Q[i]$	general input signal to the digital algorithm, Quadrature component
$\xi[n]$	signal containing synchronization information
ξ_g	energy of the frequency pulse

Y

$y[i]$	general output of the digital algorithm
$y_{PD}[i]$	digital output of the phase detector (PLL system)
$\psi(t)$	continous phase of the exponentially modulated signal
$\psi[i]$	phase of the exponentially modulated signal, digital representation
$\sim\psi[i]$	estimate of the signal phase

LIST OF FIGURES

LIST OF TABLES

APPENDIX

A. List of instruments

I.1. FSP, R&S spectrum analyzer (calibrated), 9 kHz – 3 GHz, 1164.4391.03, *used for spectral analysis, ACI measurement, output power measurement.*

I.2. FSIQ, R&S vector signal analyzer (calibrated), 20 Hz – 3.5 GHz, 1119.5005.03, *used for modulation analysis, constellation plots, trajectories.*

I.3. E4438C, Agilent vector signal generator (calibrated), 250 kHz – 3 GHz, MY45091475, *used as a modulated signal reference and for generating test signals for general receiver tests.*

I.4. SML03, R&S signal generator (calibrated), 9 kHz – 3.3 GHz, 1090.3000.13, *used as a general purpose signal generator and for generating interfering signal for receiver degradation measurements.*

I.5. HP8640B, Hewlett Packard signal generator, 500 kHz – 1024 MHz, 2250A20733, *used as a reference receive signal oscillator for receiver degradation measurement due to the low level of phase noise [94],[6].*

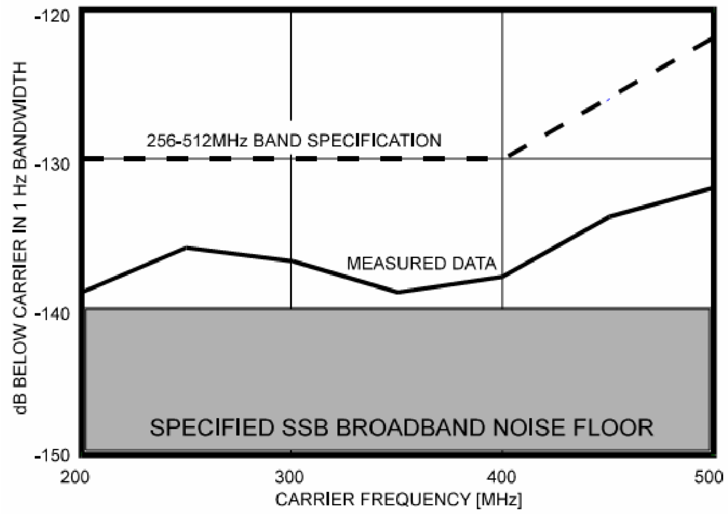

Figure A.1: Signal-to-Phase-Noise ratio specification of the HP8640B signal generator at the offset frequency of 20 kHz. Reprinted with permission [6].

I.6. APEX ATE 40/30, 30 dB (40 W, 50 Ω) signal attenuator, 051106*, used to lower down the transmitter output signal (ACI measurement), receiver test link.*

I.7. PE7015-40, PASTERNACK 40 dB signal attenuator (50 Ω), *used for essential radio parameters measurements.*

I.8. PE7033-2, PASTERNACK 0-80 dB in 1 dB steps signal attenuator (50 Ω), DC-2 GHz, *used for essential radio parameters measurements.*

B. Transmitted signal spectrum and ACI measurement

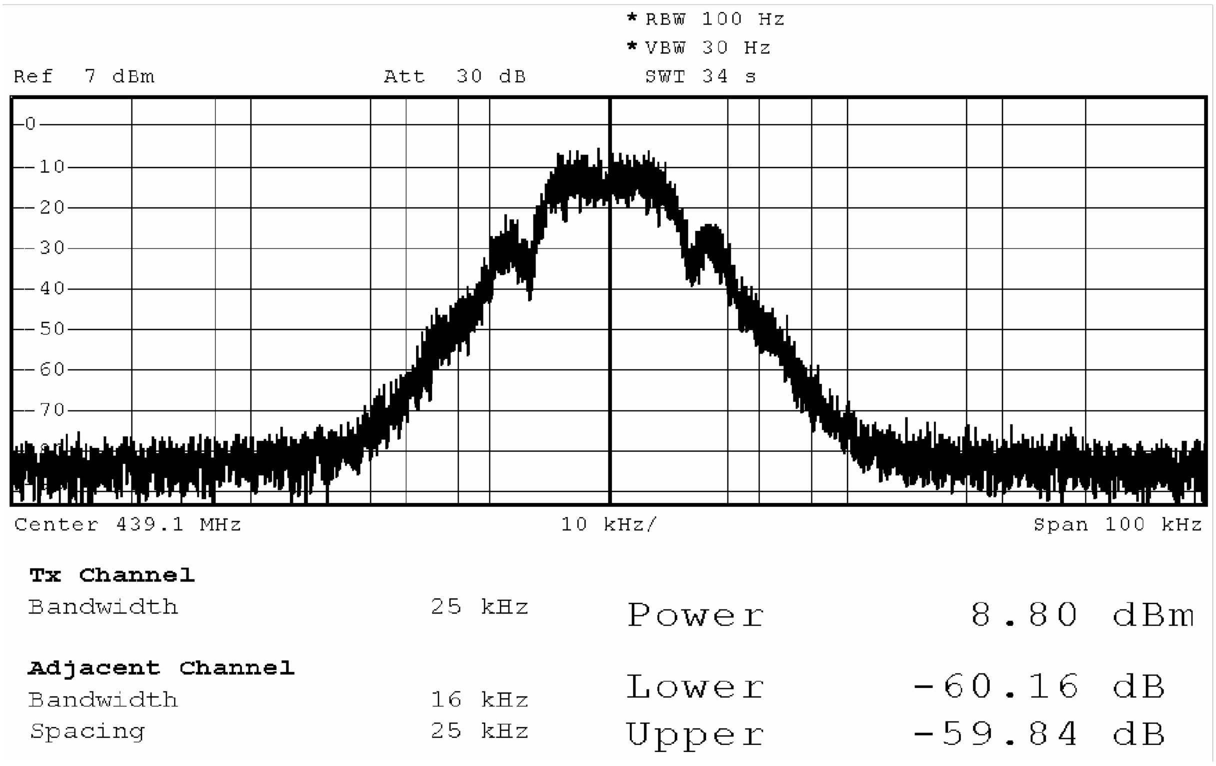

Tx Channel

Bandwidth	25 kHz	Power	8.80 dBm

Adjacent Channel

Bandwidth	16 kHz	Lower	-60.16 dB
Spacing	25 kHz	Upper	-59.84 dB

Figure B.1: 2-CPFSK modulation; 10.417 kBaud; modulation index (*h*~0.75). Square root Nyquist δ-filter (α=0.284). 30 dB attenuator used in series.

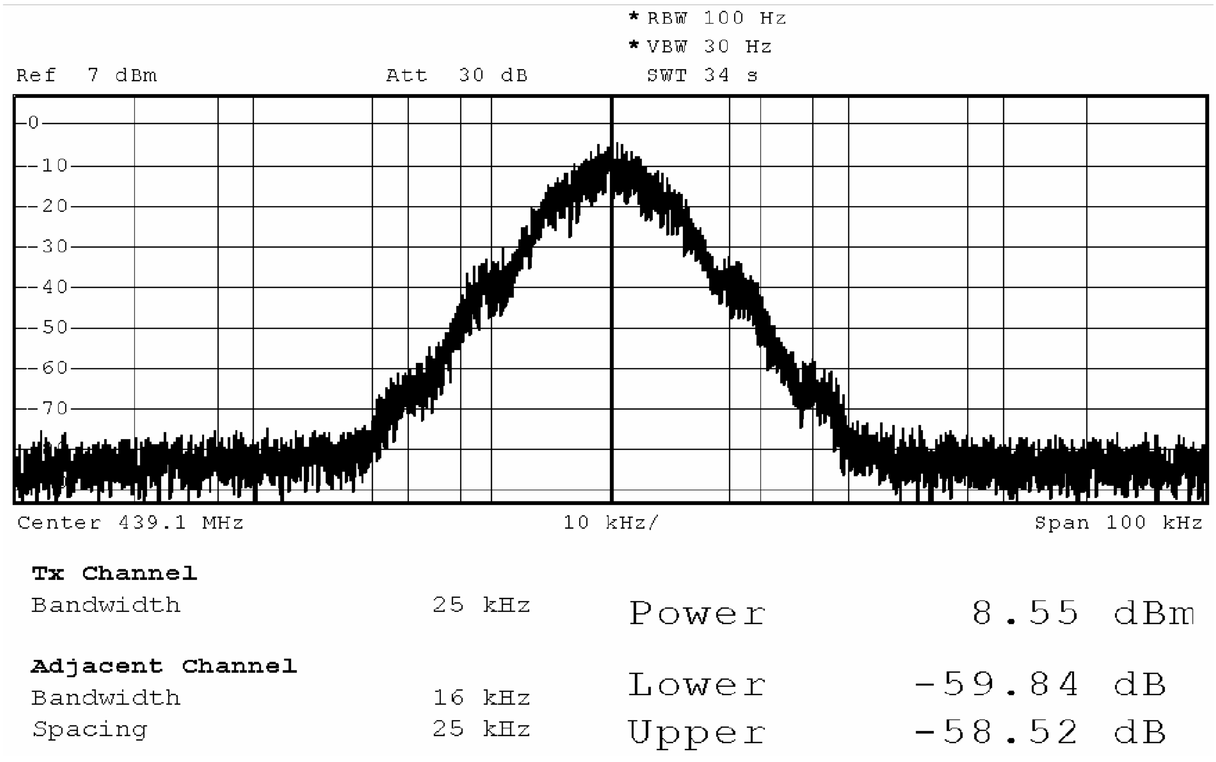

Tx Channel

Bandwidth	25 kHz	Power	8.55 dBm

Adjacent Channel

Bandwidth	16 kHz	Lower	-59.84 dB
Spacing	25 kHz	Upper	-58.52 dB

Figure B.2: 2-CPFSK modulation; 13.028 kBaud; modulation index (*h*~0.5). Square root Nyquist δ-filter (α=0.284). 30 dB attenuator used in series.

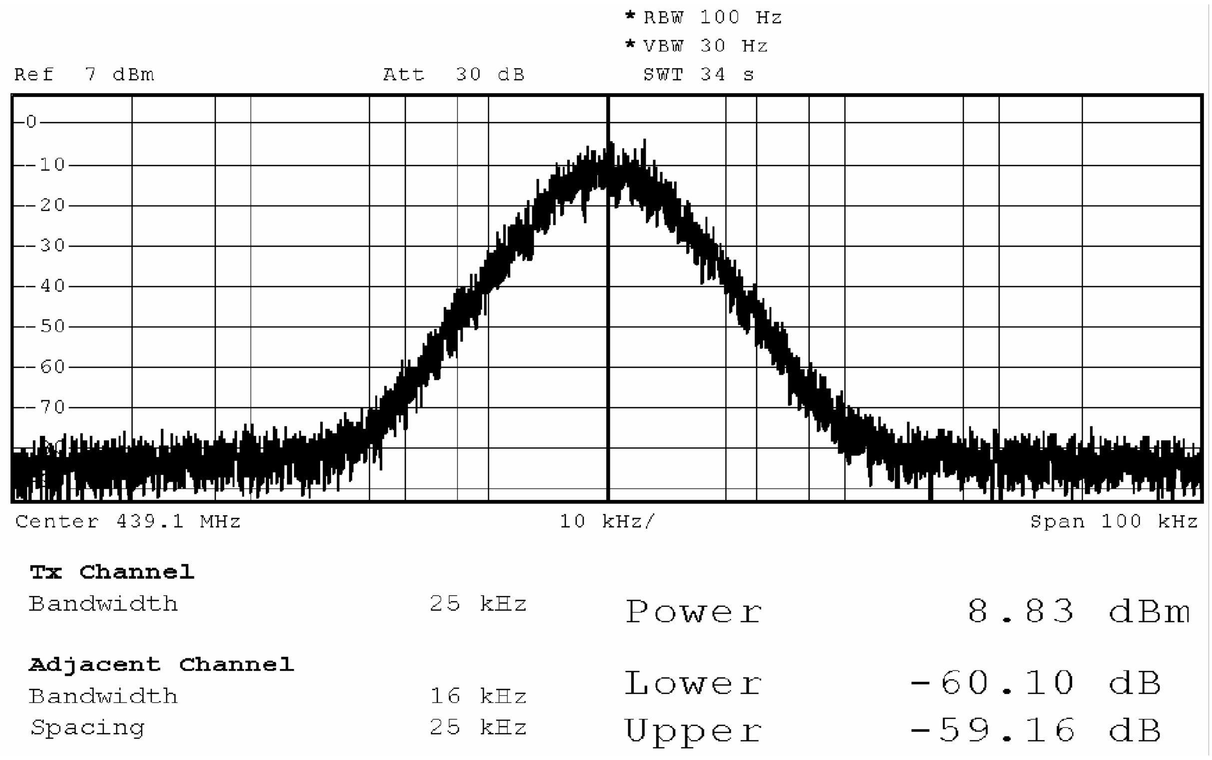
```
                                        *RBW 100 Hz
                                        *VBW 30 Hz
Ref  7 dBm               Att  30 dB      SWT 34 s

Center 439.1 MHz              10 kHz/                  Span 100 kHz

Tx Channel
Bandwidth                 25 kHz      Power          8.83 dBm

Adjacent Channel
Bandwidth                 16 kHz      Lower        -60.10 dB
Spacing                   25 kHz      Upper        -59.16 dB
```

Figure B.3: 4-CPFSK modulation; 10.417 kBaud; modulation index (h~0.25). Square root Nyquist δ-filter (α=0.284). 30 dB attenuator used.

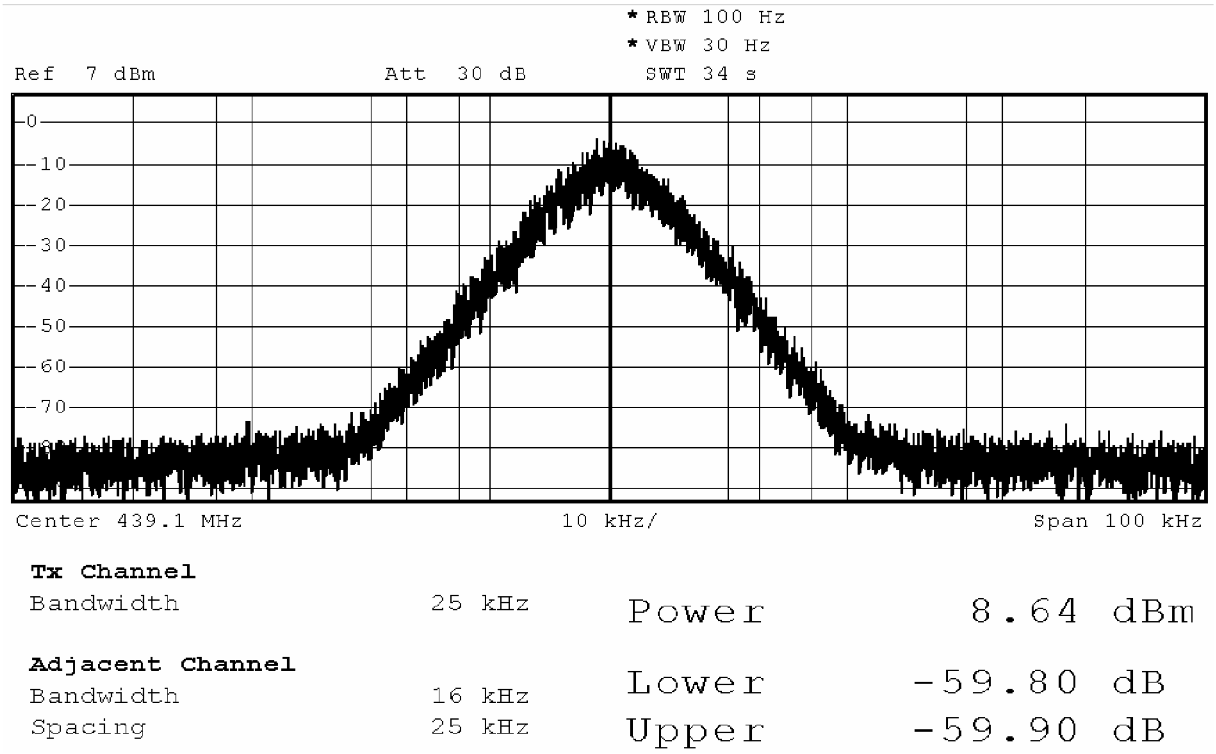
```
                                        *RBW 100 Hz
                                        *VBW 30 Hz
Ref  7 dBm               Att  30 dB      SWT 34 s

Center 439.1 MHz              10 kHz/                  Span 100 kHz

Tx Channel
Bandwidth                 25 kHz      Power          8.64 dBm

Adjacent Channel
Bandwidth                 16 kHz      Lower        -59.80 dB
Spacing                   25 kHz      Upper        -59.90 dB
```

Figure B.4: 4-CPFSK modulation; 13.028 kBaud; modulation index (h~0.5). Square root Nyquist δ-filter (α=0.284). 30 dB attenuator used.

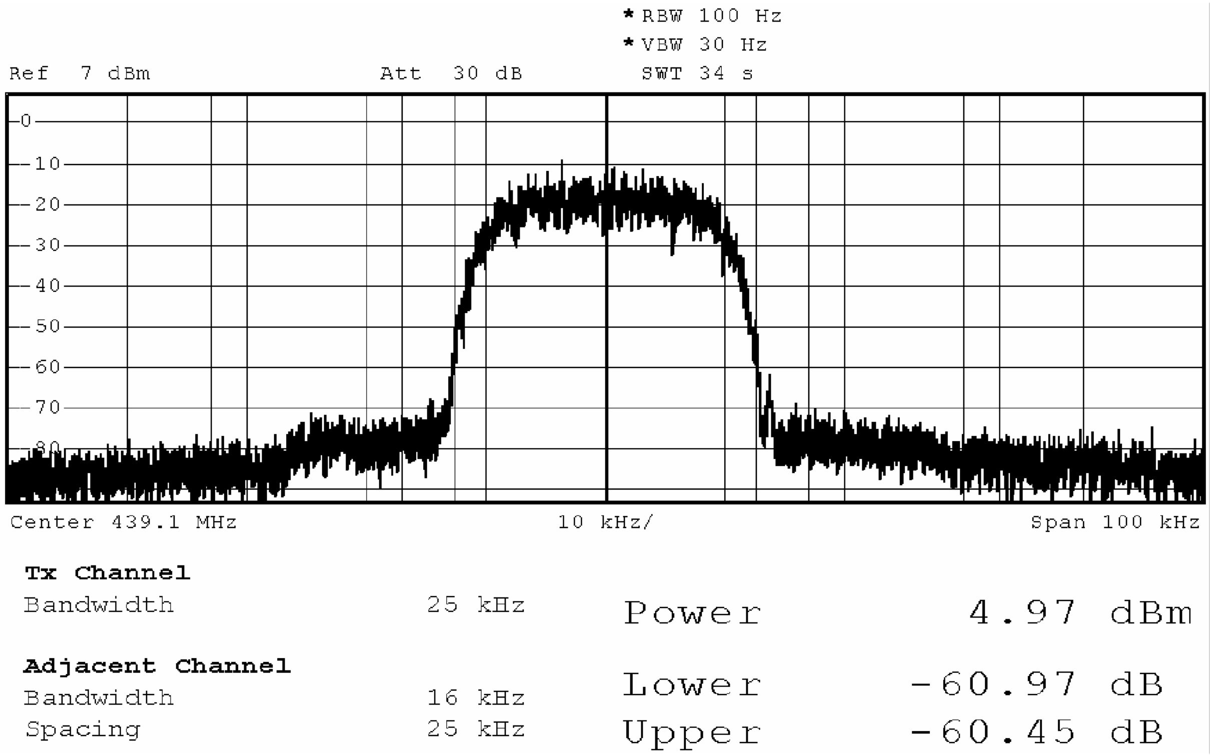

```
                                   *RBW 100 Hz
                                   *VBW 30 Hz
Ref  7 dBm          Att  30 dB      SWT 34 s

Center 439.1 MHz              10 kHz/                  Span 100 kHz

Tx Channel
Bandwidth                 25 kHz     Power            4.97 dBm

Adjacent Channel
Bandwidth                 16 kHz     Lower          -60.97 dB
Spacing                   25 kHz     Upper          -60.45 dB
```

Figure B.5: π/4-DQPSK modulation; 17.361 kBaud; Square root Nyquist δ-filter (α=0.45). 30 dB attenuator used.

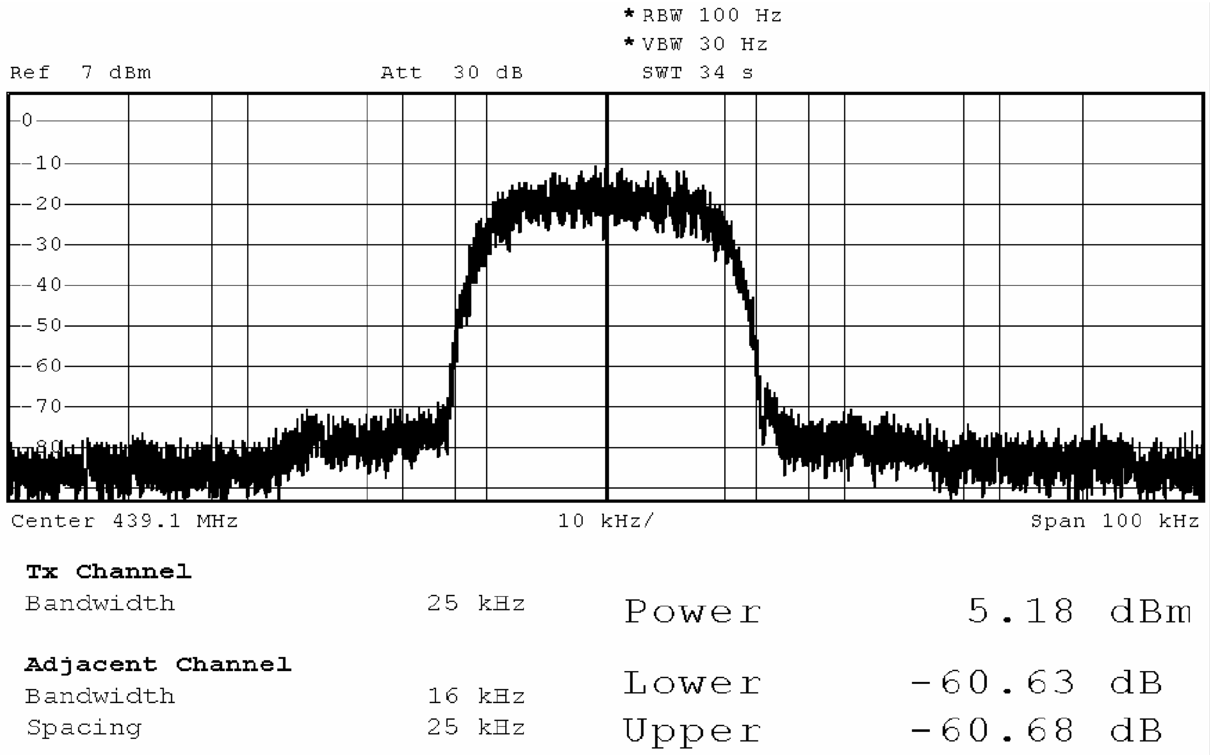

```
                                   *RBW 100 Hz
                                   *VBW 30 Hz
Ref  7 dBm          Att  30 dB      SWT 34 s

Center 439.1 MHz              10 kHz/                  Span 100 kHz

Tx Channel
Bandwidth                 25 kHz     Power            5.18 dBm

Adjacent Channel
Bandwidth                 16 kHz     Lower          -60.63 dB
Spacing                   25 kHz     Upper          -60.68 dB
```

Figure B.6: D8PSK modulation; 17.361 kBaud; Square root Nyquist δ-filter (α=0.45). 30 dB attenuator used.

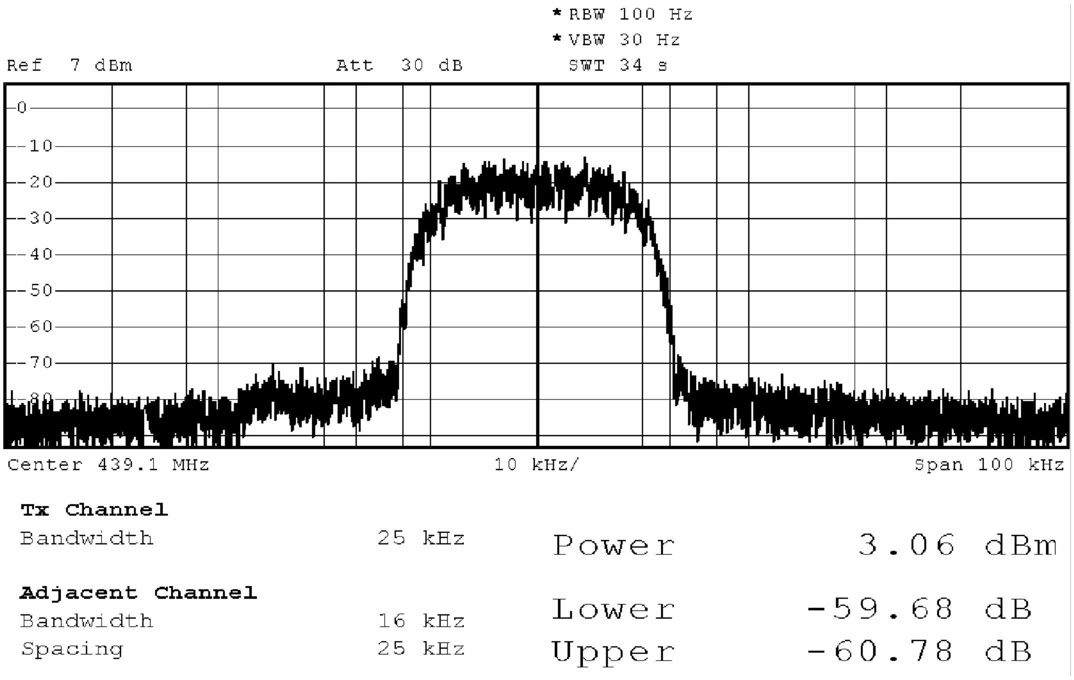

Tx Channel
Bandwidth 25 kHz
Power 3.06 dBm

Adjacent Channel
Bandwidth 16 kHz
Spacing 25 kHz
Lower -59.68 dB
Upper -60.78 dB

Figure B.7: Star 16-DEQAM modulation; 17.361 kBaud; Square root Nyquist δ-filter (α=0.45). 30 dB attenuator used.

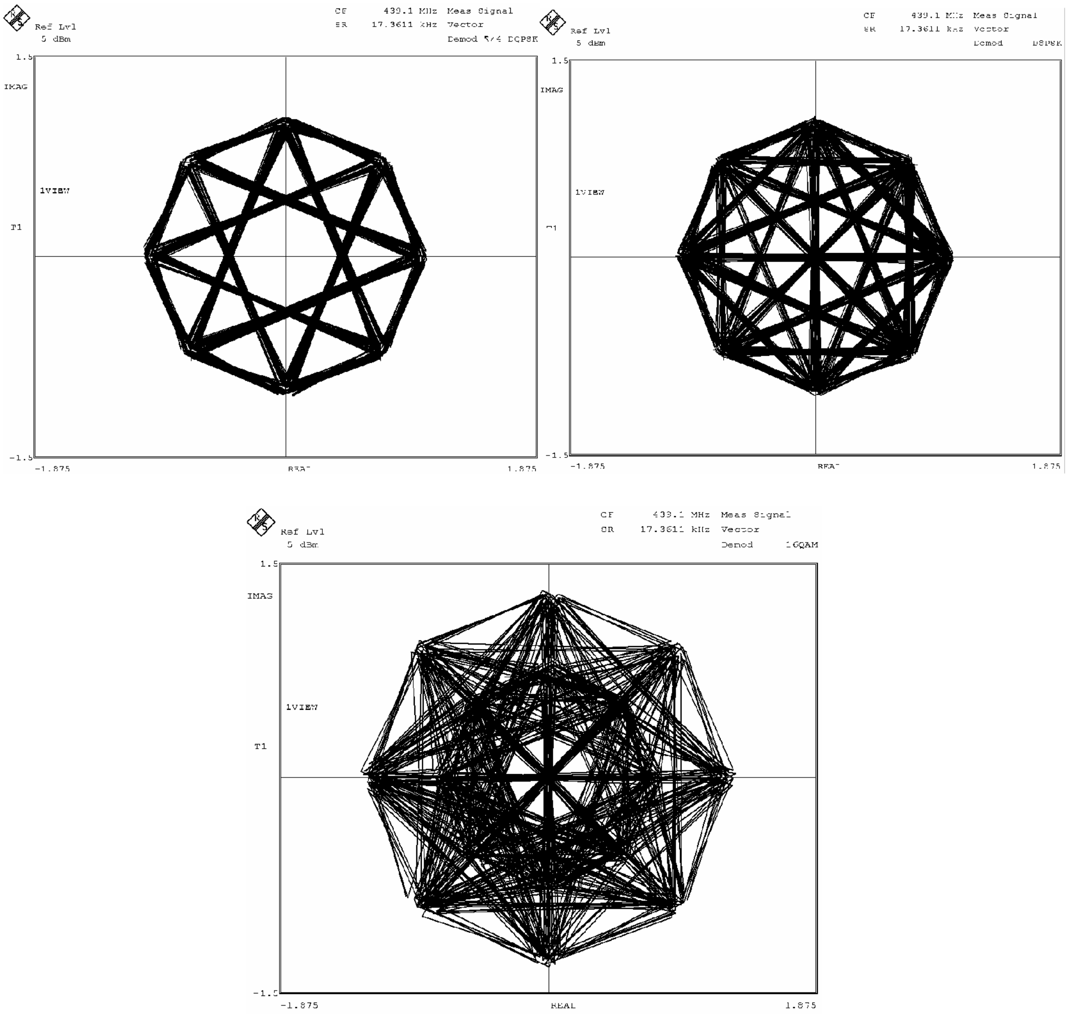

Figure B.8: Signal vector constellations π/4-DQPSK; D8PSK and 16-DEQAM modulation.

C. Programme routines – Maple

```
#  Algebraic Calculation for the Nyquist's Delta Filter Characteristics
#  This section describes the Nyquist's delta-filter, particularly its
#  time and frequency characteristics
#  The script can be used to calculate Nyquist's delta-digital filter
#  coeficients. Thesis Section 3.2.2
#
   ➢  restart;
   ➢  S[u] := 1-a[0]-a[1]*cos(Pi*(B*(1+alpha[0])-f-
      delta)/(2*B*alpha[0]))-a[2]*cos(2*Pi*(B*(1+alpha[0])-f-
      delta)/(2*B*alpha[0]));
   ➢  S[um] := 1-a[0]-a[1]*cos(Pi*(B*(1+alpha[0])+(f-
      delta))/(2*B*alpha[0]))-a[2]*cos(2*Pi*(B*(1+alpha[0])+(f-
      delta))/(2*B*alpha[0])); S[d] := a[0]+a[1]*cos(Pi*(B*(1-
      alpha[0])-f+delta)/(2*B*alpha[0]))+a[2]*cos(2*Pi*(B*(1-
      alpha[0])-f+delta)/(2*B*alpha[0]));
   ➢  S[dm] := a[0]+a[1]*cos(Pi*(B*(1-
      alpha[0])+(f+delta))/(2*B*alpha[0]))+a[2]*cos(2*Pi*(B*(1-
      alpha[0])+(f+delta))/(2*B*alpha[0]));
   ➢  delta := 1/2-B*(1-alpha[0])-2*B*alpha[0]*(Pi-
      arccos((1/4)*(a[1]-sqrt(a[1]^2+8*a[2]^2+4*a[2]-
      8*a[2]*a[0]))/a[2]))/Pi;
   ➢  G[d] := piecewise(abs(f) <= B*(1-alpha[0])-delta, 1, `and`(-
      B*(1-alpha[0])+delta > f, f >= -B), S[um], `and`(-B > f, f >= -
      B*(1+alpha[0])-delta), S[dm], `and`(B*(1-alpha[0])-delta <= f,
      f < B), S[u], B <= f and f < B*(1+alpha[0])+delta, S[d],
      B*(1+alpha[0])+delta <= abs(f), 0);
   ➢  alpha[0] := .3; T := 1; B := 1/(2*T); a[0] := 3/8; a[1] :=
      4*(1/8); a[2] := 1/8;
   ➢  evalf(delta); plot([G[d]], f = -1 .. 1, color = [black]);
      alpha[RC] := alpha[0]+delta;
   ➢  G[RC] := piecewise(abs(f) <= B*(1-alpha[RC]), 1, `and`(-
      B*(1+alpha[RC]) < f, f <= -B*(1-alpha[RC])),
      1/2*(1+cos(Pi*(f+B*(1-alpha[RC]))/(2*B*alpha[RC]))),
      `and`(B*(1-alpha[RC]) < f, f <= B*(1+alpha[RC])),
      1/2*(1+cos(Pi*(f-B*(1-alpha[RC]))/(2*B*alpha[RC]))),
      B*(1+alpha[RC]) <= abs(f), 0);
   ➢  plot([G[RC], G[d]], f = -1 .. 1, color = [black, red]);
   ➢  g[d] := (1/2)*Pi*(Int(G[d]*exp((I*2)*Pi*f*t), f = -1 .. 1));
   ➢  g[delay] := 4; N := 5; krok := 1/N; i := 0;
   ➢  for t from -g[delay] by krok to g[delay] do t; i := i+1;
      coef[i] := evalf(Re(evalf(g[d]))) end do; k := i;
   ➢  for i to k do print(coef[i]) end do;
```

```
#  Algebraic Calculation for the square root Nyquist's Delta Filter
#  Characteristics
#  This section describes the Nyquist's delta-filter, particularly its
#  time and frequention characteristics
#  The script can be used to calculate the square root Nyquist's delta-
#  digital filter coeficients
#
   ➢  restart;
   ➢  S[u] := 1-cos(Pi*(B*(1+alpha[0])-f-delta)/(4*B*alpha[0]))^4;
   ➢  S[um] := 1-cos(Pi*(B*(1+alpha[0])+(f-delta))/(4*B*alpha[0]))^4;
   ➢  S[d] := cos(Pi*(B*(1-alpha[0])-f+delta)/(4*B*alpha[0]))^4;
   ➢  S[dm] := cos(Pi*(B*(1-alpha[0])+(f+delta))/(4*B*alpha[0]))^4;
   ➢  delta := 1/2-4*arccos((1/2)*2^(3/4))*B*alpha[0]/Pi-B*(1-
      alpha[0]);
   ➢  G[d] := piecewise(abs(f) <= B*(1-alpha[0])-delta, 1, `and`(-
      B*(1-alpha[0])+delta > f, f >= -B), S[um], `and`(-B > f, f >= -
      B*(1+alpha[0])-delta), S[dm], `and`(B*(1-alpha[0])-delta <= f,
      f < B), S[u], `and`(B <= f, f < B*(1+alpha[0])+delta), S[d],
      B*(1+alpha[0])+delta <= abs(f), 0);
   ➢  alpha[0] := .25; T := 1; B := 1/(2*T); a[0] := 3/8; a[1] :=
      4*(1/8); a[2] := 1/8;
   ➢  evalf(delta);
   ➢  G[Rd] := sqrt(G[d]);
   ➢  plot([G[d], G[Rd]], f = -1 .. 1, color = [black, red]);
   ➢  alpha[RC] := alpha[0]+delta;
   ➢  G[RC] := piecewise(abs(f) <= B*(1-alpha[RC]), 1, `and`(-
      B*(1+alpha[RC]) < f, f <= -B*(1-alpha[RC])),
      1/2*(1+cos(Pi*(f+B*(1-alpha[RC]))/(2*B*alpha[RC]))),
      `and`(B*(1-alpha[RC]) < f, f <= B*(1+alpha[RC])),
      1/2*(1+cos(Pi*(f-B*(1-alpha[RC]))/(2*B*alpha[RC]))),
      B*(1+alpha[RC]) <= abs(f), 0);
   ➢  G[RRC] := simplify(sqrt(G[RC])); plot([G[RRC], G[Rd]], f = -1
      .. 1, color = [black, red]);
   ➢  g[Rd] := (1/2)*Pi*(Int(G[Rd]*exp((I*2)*Pi*f*t), f = -1 .. 1));
   ➢  g[delay] := 6; N := 6; krok := 1/N; i := 0;
   ➢  for t from -g[delay] by krok to g[delay] do t; i := i+1;
      coef[i] := evalf(Re(evalf(g[Rd]))) end do; k := i;
   ➢  for i to k do print(coef[i]) end do;
```

```
#  Algebraic Calculation for the "Better" than Nyquist Filter
#  Characteristics
#  This section describes the filter based on: A "Better Than" Nyquist
#  Pulse, Norman C. Beaulieu, IEEE 2001 [42].
#  The script can be used to calculate the digital filter coeficients

   ➢  restart;
   ➢  delta := 1/2-4*arccos((1/2)*2^(3/4))*B*alpha[0]/Pi-B*(1-
      alpha[0]);
   ➢  alpha[RC] := alpha[0]+delta;
   ➢  G[b] := piecewise(abs(f) <= B*(1-alpha[RC]), 1, `and`(-B*(1-
      alpha[RC]) > f, f >= -B), exp(ln(2)*(f+B*(1-
      alpha[RC]))/(alpha[RC]*B)), `and`(-B > f, f >= -
      B*(1+alpha[RC])), 1-exp(ln(2)*(-f-
      B*(1+alpha[RC]))/(alpha[RC]*B)), `and`(B*(1-alpha[RC]) <= f, f
      <= B), exp(ln(2)*(B*(1-alpha[RC])-f)/(alpha[RC]*B)), B <= f and
      f <= B*(1+alpha[RC]), 1-exp(ln(2)*(f-
      B*(1+alpha[RC]))/(alpha[RC]*B)), B*(1+alpha[RC]) <= abs(f), 0);
   ➢  alpha[0] := .60; T := 1; B := 1/(2*T); a[0] := 3/8; a[1] :=
      4*(1/8); a[2] := 1/8;
   ➢  evalf(delta);
   ➢  H[Rb] := sqrt(G[b]);
   ➢  plot([G[b], H[Rb]], f = -1 .. 1, color = [black, red]);
   ➢  G[RC] := piecewise(abs(f) <= B*(1-alpha[RC]), 1, `and`(-
      B*(1+alpha[RC]) < f, f <= -B*(1-alpha[RC])),
      1/2*(1+cos(Pi*(f+B*(1-alpha[RC]))/(2*alpha[RC]*B))),
      `and`(B*(1-alpha[RC]) < f, f <= B*(1+alpha[RC])),
      1/2*(1+cos(Pi*(f-B*(1-alpha[RC]))/(2*alpha[RC]*B))),
      B*(1+alpha[RC]) <= abs(f), 0);
   ➢  G[RRC] := simplify(sqrt(G[RC])); plot([G[RRC], H[Rb]], f = -1
      .. 1, color = [black, red]);

   ➢  h[Rb] := (1/2)*Pi*(Int(H[Rb]*exp((I*2)*Pi*f*t), f = -1 .. 1));
   ➢  g[delay] := 7;
   ➢  N := 5;
   ➢  krok := 1/N;
   ➢  i := 0;
   ➢  for t from -g[delay] by krok to g[delay] do t; i := i+1;
      coef[i] := evalf(Re(evalf(h[Rb]))) end do;
   ➢  k := i;
   ➢  for i to k do print(coef[i]) end do;
```

D. Enclosed DVD-ROM contents

- **00_document**
    - Directory contains documents related to the dissertation thesis, electronic version of the thesis, reviews and additional documents needed for thesis submission.
- **01_references**
    - Contains all the relevant references and publications, except the books.
- **02_figures**
    - Contains figures presented in the thesis.
- **03_tables**
    - Contains tables presented in the thesis.
- **04_matlab**
    - Contains matlab source codes and simulation files relevant to the topics described in the thesis.
- **05_maple**
    - Contains maple source codes relevant to the topics described in the thesis.
- **06_quartus**
    - Contains Altera Quartus II source codes relevant to the topics described in the thesis.